MEASURING THE NEUTRINO MIXING ANGLE θ_{13} WITH THE DOUBLE CHOOZ FAR DETECTOR

by

IGOR OSTROVSKIY

JEROME K. BUSENITZ, COMMITTEE CHAIR
ANDREAS PIEPKE
ION STANCU
NOBUCHIKA OKADA
JANET CONRAD

A DISSERTATION

Submitted in partial fulfillment of the requirements
for the degree of Doctor in Philosophy in the
Department of Physics and Astronomy
in the Graduate School of
The University of Alabama

TUSCALOOSA, ALABAMA

2012

Abstract

The neutrino mixing angle θ_{13} is the last one which value is still unknown. This dissertation presents an analysis suggesting a non-zero value of the θ_{13}. The analysis is based on four months of data taken with the far Double Chooz reactor anti-neutrino detector. Using only rate information yields a best fit value of $sin^2(2\theta_{13})$ equal to 0.0934±0.0785 (1 sigma). Incorporating information on the shape of the signal energy spectrum in the analysis results in a best fit value of 0.0849±0.0509 (1 sigma). Based on frequentist studies, $sin^2(2\theta_{13})$=0 is excluded at the 92.6% confidence level. The frequentist construction using $\Delta\chi^2$ as an ordering rule gives [0.0098, 0.1825] interval for $sin^2(2\theta_{13})$ at 90% C.L.

Acknowledgments

First of all, I want to thank my advisor, Jerry Busenitz, for helping, guiding, and tolerating me throughout these years. Thank you for trusting me to make my own choices and providing a lot of independence.

Next, to my favorite Double Chooz group ever: I can't thank enough Janet Conrad for her continuous support and kindness and for welcoming me during my visits to MIT. Thanks so much to Lindley Winslow. You got me started on analysis, and were it not for your drive and motivation, I would not have done half of the work I did. You are truly my foster postdoc, and I am grateful for our numerous discussions over the last couple of years. Kazuhiro Terao. Kazu. We were way ahead of the crowd many times and I will miss working with you. What am I going to do without our endless Skype chats, filled with a mixture of code debugging and complaints about the miserable fate of graduate students? With whom else can I drink a glass of beer at a bar in Paris, while video calling Brandon at the analysis meeting in the US?

I am also grateful to Mike Shaevitz for an opportunity to learn a lot about higher level analysis. Thanks to Camillo Mariani for welcoming me during my trips to Columbia University. It was great to stay at Nevis and share the experience of the first final analysis with you and Matt Toups and Arthur Franke.

My special gratitude goes to Tomokatsu Hayakawa for providing friendly support during one of the most difficult parts of my graduate experience.

Finally, I want to mention that I was pleased to find a helpful environment in the Univer-

sity of Alabama's physics department. Professor Andreas Piepke provided a lot of valuable feedback on the content of this thesis and corrected tons of missing/misplaced articles. The hardware part of this thesis would not have been possible without our skillful machinists, David Key, Joe Howell, and Mike Perrigin, as well as Danny Whitcomb and Jason Kuykendall from the electronics shop.

Contents

List of Tables

List of Figures

Part I

Introduction

Chapter 1

Neutrino oscillations

In this chapter we introduce the concept of neutrino oscillations and describe the parameters on which oscillations depend on and experiments that have measured them. Particular attention is given to the CHOOZ experiment and the limit it established on the third neutrino mixing angle, as improving on that measurement is the purpose of this research.

1.1 Standard Model context and properties of the neutrino

The essential goal of physics is to describe the full body of experimental observations in the form of a mathematical model that provides a description for observed phenomena using a set of fundamental equations. Today the model that is most successful in describing the vast majority of experimental results in particle physics is the Standard Model (SM).

The Standard Model is a relativistic quantum field theory, and for a field theory the "set of fundamental equations" is obtained by minimizing the action with respect to the fields [1]. The action is defined by the Lagrangian density[1], hence to define the Standard Model we must define its Lagrangian. To do that in quantum field theory, one postulates the

[1]We omit the word "density" for the sake of brevity from now on.

symmetries to be respected by the fields one wants to describe and formulates the minimum renormalizable Lagrangian for such fields. The symmetries that define the Standard Model are the local gauge symmetries SU(3)×SU(2)×U(1). [2]

The existence of a local gauge symmetry requires the existence of a gauge field, one for each generator of the symmetry group. Mathematically, gauge fields arise as additional terms that have to be added to the Lagrangian to realize the invariance under the local gauge transformation. These additional terms, in effect, describe new vector fields that interact with the existing fields. The quanta of the gauge fields, the gauge bosons, mediate their corresponding interactions.

The $SU(3)_C$ symmetry in the SM Lagrangian corresponds to the strong interactions, mediated by 8 gauge bosons, called gluons. The "C" subscript corresponds to the degree of freedom, called the "color" charge, and "3" corresponds to the number of possible states.

The fundamental particles that participate in the strong interactions are called quarks. There are three generation of quarks known today, with each generation consisting of two quarks having different quantum numbers (Table 1.1). Unlike the number of gauge bosons, which is dictated by the number of group generators, the number of fundamental fermions is not predicted in the SM. The "zoo" of particles consisting of two (mesons) or three (baryons) quarks, though, can be derived using group theoretical arguments. In fact, many baryons and mesons were predicted to exist before they were discovered experimentally.

The other two interactions described in the SM are the weak and the electromagnetic (EM) forces. EM processes can be described as an interaction of the electromagnetic current with photons (for example, Figure 1.1a). In a similar way, a weak process can be described as an interaction of the weak current with W^+,W^-, or Z^0 bosons. Weak currents associated with emission/absorption of $W^\pm$ bosons are called charged currents, and these currents change the charges of incoming particles (for example, Figure 1.1b). Neutral currents, on the other hand, leave the particles unchanged and are mediated by Z^0 bosons (Figure 1.1c).

[2]Other symmetries, such as global Lorentz and translational symmetries, are common to all relativistic theories.

Gauge bosons

$\boldsymbol{\gamma}$	**g**	**W**	**Z**
$I(J^{PC}) = 0, 1(1^{--})$	$I(J^P) = 0(1^-)$	$J = 1$	$J = 1$
$m < 10^{-18}$ eV	$m = 0$	$m \approx 80.4$ GeV	$m \approx 91.19$ GeV
$q < 10^{-35}$ e	SU(3) color octet	$q = \pm 1$	$q = 0$
$\tau = Stable$		$\Gamma \approx 2.1$ GeV	$\Gamma \approx 2.50$ GeV

Quarks

u	**c**	**t**
$I(J^P) = \frac{1}{2}(\frac{1}{2}^+)$	$I(J^P) = 0(\frac{1}{2}^+)$	$I(J^P) = 0(\frac{1}{2}^+)$
$m = 1.7 - 3.1$ MeV	$m = 1.29^{0.05}_{-0.11}$ GeV	$m = 172.9 \pm 0.6 \pm 0.9$ GeV
$q = \frac{2}{3}$ e	$q = \frac{2}{3}$ e	$q = \frac{2}{3}$
$I_z = \frac{1}{2}$	Charm = +1	Top = +1
		$\Gamma = 2.0^{+0.7}_{-0.6}$ GeV
d	**s**	**b**
$I(J^P) = \frac{1}{2}(\frac{1}{2}^+)$	$I(J^P) = 0(\frac{1}{2}^+)$	$I(J^P) = 0(\frac{1}{2}^+)$
$m = 4.1 - 5.7$ MeV	$m = 100^{+30}_{-20}$ MeV	$m = 4.19^{0.18}_{-0.06}$ GeV
$q = -\frac{1}{3}$ e	$q = -\frac{1}{3}$ e	$q = -\frac{1}{3}$ e
$I_z = -\frac{1}{2}$	Strangeness = -1	Bottom = -1

Leptons

e	$\boldsymbol{\mu}$	$\boldsymbol{\tau}$
$J = \frac{1}{2}$	$J = \frac{1}{2}$	$J = \frac{1}{2}$
$m \approx 0.510999$ MeV	$m \approx 105.658$ MeV	$m = 1776.82 \pm 0.16$ MeV
$q = -1$ e	$q = -1$ e	$q = -1$ e
$\tau > 4.6 \times 10^{26}$ yr	$\tau \approx 2.197\ \mu s$	$\tau = (290.6 \pm 1.) \times 10^{-15}$ s
$\boldsymbol{\nu_e}$	$\boldsymbol{\nu_\mu}$	$\boldsymbol{\nu_\tau}$
$J = \frac{1}{2}$	$J = \frac{1}{2}$	$J = \frac{1}{2}$
$m^{2(eff)}_{\nu_e} < (2eV)^2$	$m^{2(eff)}_{\nu_\mu} < (0.19MeV)^2$	$m^{2(eff)}_{\nu_\tau} < (18.2MeV)^2$
$q = 0$	$q = 0$	$q = 0$

Table 1.1: Basic properties of elementary particles [12]. Note that the upper limits on the masses of muon and tau neutrinos may be obsolete. Since we know that the mass splittings between all neutrino types are smaller than 1 eV, the tight bound on the electron neutrino, thus, applies to the other flavors too.

Although seemingly different at achievable energies, the EM and weak processes can be described as a manifestation of a single force, called the electroweak force. The theory of such a force is a local gauge theory based on the group $\mathrm{SU}(2)_L \times \mathrm{U}(1)_Y$ where the addition of the $\mathrm{U}(1)_Y$ group (different from $\mathrm{U}(1)_{EM}$, which is a subgroup of $\mathrm{SU}(2)_L \times \mathrm{U}(1)_Y$!) allows the EM current to be included in the framework. Note that the actual (massless) gauge bosons corresponding to the groups' generators are W^1, W^2, W^3 and B^0, while the $W^\pm$ are linear combinations of the W^1 and W^2, and the Z boson and the photon are the mixtures of W^3 and B^0:

$$\begin{aligned} W^\pm &= \frac{1}{\sqrt{2}}(W^1_\pm \pm iW^2_\pm) \\ Z &= cos\theta_W W^3 - sin\theta_W B^0 \end{aligned} \tag{1.1}$$

where θ_W is the Weinberg angle.

The fact that the $W^\pm$ and Z bosons are massive can be explained by the proposed Higgs mechanism. In the SM, the Higgs mechanism is a particular case of a spontaneous local symmetry breaking, realized by a scalar field that acquires a non-zero vacuum expectation value (a detailed description of the mechanism may be found in numerous sources, for example, in [2], or [1]).

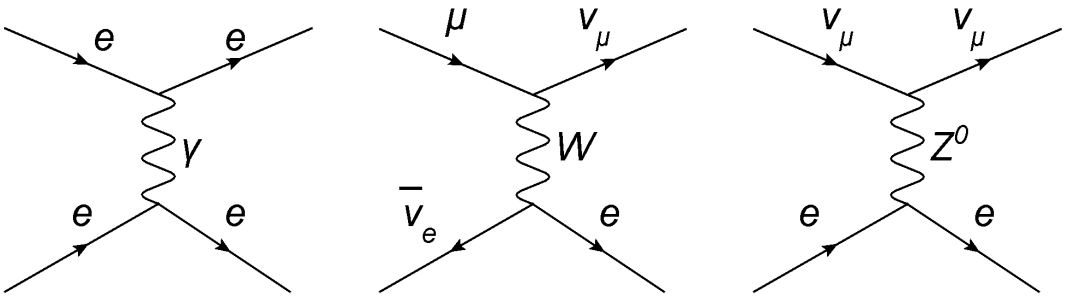

(a) EM process (Møller scattering)

(b) Charged current process

(c) Neutral current process

Figure 1.1: Examples of EM and weak currents.

Charged and neutral currents have lepton and hadronic components. Three generations

of leptons are known today (Table 1.1). As in the quark sector, each generation consists of two leptons. Each charged lepton has a corresponding chargeless partner, called the *neutrino*.

To summarize, the SM is a gauge theory describing 12 bosons that mediate strong and/or electro-weak interactions between 12 fundamental fermions. The existence of a possible Higgs boson would result in additional terms in the SM Lagrangian, coupling some of the particles to the Higgs field and providing a possible explanation of why particles that comprise matter are massive.

Note that these mass terms have the following form for charged fermions (dropping Hermitian conjugates for brevity)

$$L \sim -m\bar{\phi}_L\phi_R, \tag{1.2}$$

where $\phi_{L(R)}$ denotes left(right)-handed fermion fields, and m is the positive real mass constant that can be expressed in terms of the vacuum expectation value of the Higgs field and a coupling constant (the Yukawa coupling).

Since only left handed neutrinos have been observed, the original formulation of the SM contains only left-handed neutrino fields, and therefore, by default, the SM describes neutrinos as massless particles.

Experimental evidence acquired over the last few decades, on the other hand, points to significant discrepancies between observed and expected rates of different processes involving the neutrino, most of which could be reconciled assuming the neutrinos are massive particles that can participate in the phenomenon of neutrino oscillations. Before proceeding to the next section, which describes this idea, we mention possible avenues for incorporating neutrino mass in the theory.

1.1.1 Neutrino mass

Probably the "minimally invasive" way to incorporate neutrino mass into the Standard Model is to postulate that right-handed neutrinos do exist, and therefore neutrino fields can couple to the Higgs field in the same way other fermions do. The corresponding mass term, called the Dirac mass term, would then be of the same form as for other massive fermions - leptons and quarks (see Equation (1.2)). The problem is that experimental evidence suggests that the absolute value of neutrino mass, even though not zero, is very small compared to other fermions. In particular, tritium decay experiments limit electron anti-neutrino mass to be below 2 eV. Similarly, the observation of the cosmic microwave background and the density fluctuations, and other cosmological measurements, put a combined upper limit on neutrino mass around 0.5 eV [12], which is six orders of magnitude smaller than the electron mass. Such a small mass would require a coupling constant many orders of magnitude smaller compared to other leptons.

Another possibility to incorporate neutrino mass is associated with the fact that $\bar{\psi}\psi$ is not the only bilinear combination of fermions that is allowed by Lorentz-invariance. As was first considered by Ettore Majorana, one could replace the Dirac spinor in the Dirac equation by its charge conjugate and still retain relativistic invariance for such a massive fermion field. The Lagrangian corresponding to the Majorana equation has a mass term of the form [2]

$$L \sim -\psi^T C^{-1} \psi \tag{1.3}$$

where C denotes charge conjugation. The difference of this form of the mass term, compared to the Dirac one, is that it does not generally conserve charge (equivalently, it is not invariant under global transformation, $\psi \rightarrow e^{i\alpha}\psi$), unless the field in question is self-conjugate, i.e.

$$\psi = \psi^C \equiv C\bar{\psi}^T \tag{1.4}$$

In other words, the second type of mass term, called the Majorana mass term, requires that a particle is its own anti-particle. Since neutrinos are neutral, they, in principle, can be described by the Majorana mass term. Note that the Majorana mass does not require the right-handed neutrino. It is still not clear whether neutrinos are Majorana or Dirac particles, but significant experimental efforts to find this out are underway. One of the most promising approaches relies on the fact that, if neutrinos are Majorana, lepton number is no longer conserved, and such processes as neutrino-less double beta decays may occur[3]

Finally[4], it is also possible to have both Dirac and Majorana type terms present. This is particularly advantageous as it provides a natural explanation for the smallness of mass of the observed neutrinos. As can be shown [2], the combined mass term of Majorana and Dirac types (as usual, dropping hermitian conjugates) is:

$$L^{M+D} = -\frac{1}{2}(\bar{\nu}'_L)^C M^{M+D} \nu'_L, \tag{1.5}$$

where

$$\nu'_L = \begin{pmatrix} \nu_L \\ (\nu_R)^C \end{pmatrix} \quad M^{M+D} = \begin{pmatrix} 0 & m_D \\ m_D & M_R \end{pmatrix}, \tag{1.6}$$

m_D is the mass constant corresponding to the Dirac term[5] and M_R is the mass constant corresponding to the Majorana neutrino, which is assumed to be right-handed. Generally, the upper left element of the matrix is not zero. The zero value, however, is necessary for the see-saw mechanism. Expressing the mass term in mass eigenstates, instead of interaction eigenstates (diagonalization), one gets

$$L^{M+D} = -\frac{1}{2}\sum_{i=1,2} m_i \bar{\nu}_i \nu_i, \tag{1.7}$$

[3]Provided it is allowed kinematically.

[4]Of course, there are more theoretical possibilities for incorporating neutrino mass, but they will not be considered here.

[5]of the same order of magnitude as for other fermions

where $\nu_{1,2}$ are Majorana fields, and $m_{1,2} = \frac{1}{2}(M_R \pm \sqrt{(}M_R^2 + 4m_D^2))$. The mixing between weak and mass states is given by

$$\begin{aligned} \nu_L &= -i\cos\theta\,\nu_{1L} + \sin\theta\,\nu_{2L}, \\ (\nu_R)^C &= -i\sin\theta\,\nu_{1L} + \cos\theta\,\nu_{2L}, \\ tan2\theta &= \frac{2m_D}{M_R} \end{aligned} \tag{1.8}$$

If we now assume that the Majorana term is much larger than the Dirac one, $M_R \gg m_D$, we see that the theory predicts two Majorana particles

$$\nu_1 \approx i(\nu_L - (\nu_L)^C), \quad \nu_2 \approx (\nu_R + (\nu_R)^C) \tag{1.9}$$

one very light, $m_1 \approx \frac{m_D^2}{M_R}$, and the other very heavy, $m_2 \approx M_R$. The lightness of the observed left-handed neutrino is therefore explained by the possible existence of another right-handed Majorana state with mass that is much larger than the weak scale.

1.2 Oscillations

The neutrino was first experimentally detected in 1956 by Reines and Cowan [3]. Subsequent experiments performed in late 60's, notably the Homestake experiment in the US, the SAGE experiment in Russia, and the GALLEX experiment in Italy, followed by others, have measured the neutrino rate from the sun, and found a substantial discrepancy with expectation. As a possible explanation, the theory of neutrino oscillations was developed.

The idea is that neutrinos are observed as flavor eigenstates (ν_l), but propagate as mass eigenstates (ν_i). Each flavor eigenstate can be expanded as a superposition of mass eigenstates (and vice versa):

$$\nu_l = \sum_i U_{li}\nu_i \tag{1.10}$$

The matrix elements (U_{li}) are most commonly parametrized in the Maki-Nakagawa-Sakata-Pontecorvo (MNSP) form:

$$U_{MNSP} = \begin{pmatrix} 1 & 0 & 0 \\ 0 & c_{23} & s_{23} \\ 0 & -s_{23} & c_{23} \end{pmatrix} \begin{pmatrix} c_{13} & 0 & s_{13}e^{-i\delta} \\ 0 & 1 & 0 \\ -s_{13}e^{i\delta} & 0 & c_{13} \end{pmatrix} \begin{pmatrix} c_{12} & s_{12} & 0 \\ -s_{12} & c_{12} & 0 \\ 0 & 0 & 1 \end{pmatrix} \tag{1.11}$$

where s_{ij} and c_{ij} mean $\sin(\theta_{ij})$ and $\cos(\theta_{ij})$ respectively, θ_{ij} is the mixing angle between mass eigenstates i and j, and δ is a CP violating phase (If the neutrino is a Majorana particle, i.e. if it is identical to its antiparticle, two other CP phases become physical but are left out here from the MNSP matrix since they do not affect any properties of neutrino oscillations).

If at least one of the neutrino masses (denoted below as m_i) is different from the other neutrino masses, the relative phases of the mass wave-functions will periodically change with time, resulting in observable oscillations of flavor. Assuming an ultra-relativistic approximation, valid for all practical energies and experimental upper limits on neutrino mass, one can derive the general probability for neutrino flavor transitions as a function of distance from the source (L) and energy (E_i)

$$\nu_l(t) = \sum_i U_{li}\nu_i e^{-iE_i t/\hbar} \tag{1.12}$$

$$v \to c \Rightarrow t \to L/c, \quad \nu_l(L) = \sum_i U_{li}\nu_i e^{-iE_i L/c\hbar} \tag{1.13}$$

At the same time,

$$\nu_i = \sum_l U^*_{il}\nu_l \tag{1.14}$$

Hence

$$\nu_l(L) = \sum_{\beta=e,\mu,\tau} \left(\sum_i U_{li} e^{-iE_i L/c\hbar} U^*_{i\beta} \right) \nu_\beta \tag{1.15}$$

For a particular case of electron survival probability ($\nu_e \to \nu_e$) we square the corresponding

expansion coefficient:

$$
\begin{aligned}
P_{ee}(L,E) &= (\sum_i U_{ei} e^{-iE_iL/c\hbar} U^*_{ie})^2 = \\
&= (U_{e1}U^*_{1e}e^{-iE_1L/c\hbar} + U_{e2}U^*_{2e}e^{-iE_2L/c\hbar} + U_{e3}U^*_{3e}e^{-iE_3L/c\hbar})^2 \\
&= U_{e1}U^*_{1e}U^*_{e1}U_{1e} + U_{e2}U^*_{2e}U^*_{e2}U_{2e} + U_{e3}U^*_{3e}U^*_{e3}U_{3e} + \\
&+ U_{e1}U^*_{1e}U^*_{e2}U_{2e}e^{-i(E_1-E_2)L/c\hbar} + U_{e1}U^*_{1e}U^*_{e3}U_{3e}e^{-i(E_1-E_3)L/c\hbar} + \\
&+ U_{e2}U^*_{2e}U^*_{e1}U_{1e}e^{i(E_1-E_2)L/c\hbar} + U_{e3}U^*_{3e}U^*_{e1}U_{1e}e^{i(E_1-E_3)L/c\hbar} + \\
&+ U_{e2}U^*_{2e}U^*_{e3}U_{3e}e^{-i(E_2-E_3)L/c\hbar} + U_{e3}U^*_{3e}U^*_{e2}U_{2e}e^{i(E_2-E_3)L/c\hbar} = \\
&= (c^4_{13}c^4_{12} + c^4_{13}s^4_{12} + s^4_{13}) + c^4_{13}c^2_{12}s^2_{12}2\cos\left(\frac{(E_1-E_2)L}{c\hbar}\right) + \\
&+ c^2_{13}c^2_{12}s^2_{13}2\cos\left(\frac{(E_1-E_3)L}{c\hbar}\right) + c^2_{13}s^2_{12}s^2_{13}2\cos\left(\frac{(E_2-E_3)L}{c\hbar}\right)
\end{aligned}
\tag{1.16}
$$

Assuming different mass eigenstates were produced with equal momenta (p),

$$
\begin{aligned}
E_i - E_j &= \sqrt{p^2c^2 + m_i^2c^4} - \sqrt{p^2c^2 + m_j^2c^4} \approx \\
&\approx pc + \frac{m_i^2c^4}{2pc} - pc - \frac{m_j^2c^4}{2pc} = \frac{(m_i^2 - m_j^2)c^4}{2E}
\end{aligned}
\tag{1.17}
$$

and using the following identities:

$$
\cos\left(\frac{(m_i^2 - m_j^2)Lc^3}{2E\hbar}\right) = 1 - 2\sin^2\left(\frac{(m_i^2 - m_j^2)Lc^3}{4E\hbar}\right) = 1 - 2\sin^2\Delta_{ij} \tag{1.18}
$$

$$
s^2_{12}c^2_{12} = sin^2(2\theta_{12})/4 \tag{1.19}
$$

$$
sin^2(2A) = \frac{1 - cos(A)}{2} \tag{1.20}
$$

we get

$$[c_{13}^4 c_{12}^4 + c_{13}^4 s_{12}^4 + s_{13}^4 + c_{13}^4 sin^2(2\theta_{12})/2 + c_{12}^2 sin^2(2\theta_{13})/2 +$$
$$+ s_{12}^2 sin^2(2\theta_{13})/2] - c_{13}^4 sin^2(2\theta_{12}) sin^2(\Delta_{12}) -$$
$$- c_{12}^2 sin^2(2\theta_{13}) sin^2(\Delta_{13}) - s_{12}^2 sin^2(2\theta_{13}) sin^2(\Delta_{23}), \tag{1.21}$$

where terms in square brackets:

$$\frac{(1+cos(2\theta_{13}))^2(1+cos(2\theta_{12}))^2}{16} + \frac{(1+cos(2\theta_{13}))^2(1-cos(2\theta_{12}))^2}{16} +$$
$$+ \frac{(1-cos(2\theta_{13}))^2}{4} + \frac{sin^2(2\theta_{13})}{2} + \frac{sin^2(2\theta_{12})(1+cos(2\theta_{13}))^2}{8} =$$
$$= 1/16 \times (6 + 2cos^2(2\theta_{12}) + 2cos^2(2\theta_{13})cos^2(2\theta_{12}) + 4cos(2\theta_{13})cos^2(2\theta_{12}) -$$
$$- 4cos(2\theta_{13}) + 6cos^2(2\theta_{13}) + 8sin^2(2\theta_{13}) + 2sin^2(2\theta_{12}) +$$
$$+ 4sin^2(2\theta_{12})cos(2\theta_{13}) + 2sin^2(2\theta_{12})cos^2(2\theta_{13}) =$$
$$= 1/16 \times (16) = 1 \tag{1.22}$$

Hence, the electron neutrino survival probability is

$$P_{ee} = 1 - c_{13}^4 sin^2(2\theta_{12}) sin^2\left(const\frac{\Delta m_{21}^2 L}{E}\right) -$$
$$- c_{12}^2 sin^2(2\theta_{13}) sin^2\left(const\frac{\Delta m_{31}^2 L}{E}\right) -$$
$$- s_{12}^2 sin^2(2\theta_{13}) sin^2\left(const\frac{\Delta m_{32}^2 L}{E}\right), \tag{1.23}$$

where $\Delta_{ij}^2 = m_i^2 - m_j^2$ in units of $10^{-3} eV^2$, L has units of km, E has units of MeV, and the

constant is equal to

$$const = \frac{[J^2][m]}{c^4[J]} \times \frac{c^3}{4\hbar} = \\ = \frac{(10^{-3}[eV^2])[km]}{4 \cdot 2.99979 \cdot 10^8 \cdot 6.582119 \cdot 10^{-16} \cdot (10^6[MeV])} = 1.266 \tag{1.24}$$

Such "traditional" quantum mechanical treatment of neutrino oscillations in vacuum, essentially based on plane waves, is rather straightforward and often used to this day, as it gives the right answer in many practical applications. Yet it contains fundamental limitations, probably the most apparent one is the simultaneous assumption of definite momentum and localization of neutrino. It is also not generally justified to assume that different mass eigenstates composing a flavor state during emission all have the same momentum (or, in the alternative derivation, same energy) [4]. A more consistent approach would be to use either the wave packet description, or a quantum field-theoretical model.

A wave packet is a superposition of many individual plane waves ν_i, each with definite but slightly different frequency. As each wave is a solution to Schrödinger's equation, their linear superposition is as well, as long as they all have the same relation between angular frequency and the wave vector (dispersion relation). The more frequencies are involved in the composition, the more localized interference can be constructed.

Assuming the Gaussian form for the momenta distribution around mean p_i:

$$\psi_i(\mathbf{p}) = \frac{1}{\sqrt{2\pi}\sigma_{pP}} e^{-\frac{(\mathbf{p}-\mathbf{p_i})^2}{4\sigma_{iP}^2}}, \tag{1.25}$$

where σ_{pP} represents the spread during the production process, P, and is assumed to be the same for all mass states and along all directions. The average momentum p_i, on the other hand, is different for different mass states, as in general dictated by kinematics. The flavor

states after time t are then given by [5]:

$$\psi_l(t) = \sum_i U_{li} e^{-iHt} \int d^3p\, \nu_i\, \psi_i(\mathbf{p}) = \\ = \sum_i U_{li} \int d^3p\, \psi_i(\mathbf{p})\, e^{-iE_i(p)}\, \nu_i, \tag{1.26}$$

where $E_i = \sqrt{p^2 + m_i^2}$. The same states in the position representation:

$$\psi_l(t) = \sum_i U_{li} \int d^3x\, \psi_i(\vec{x})\, \nu_i(\vec{x}), \tag{1.27}$$

where now the spread function $\psi_i(\vec{x})$ is defined by

$$\psi_i(\vec{x}) = \frac{1}{(\sqrt{2\pi}\sigma_x)^{3/2}} e^{\left(i(\vec{p_i}\vec{x} - E_i t) - \frac{(\vec{x} - \vec{v_i} t)^2}{4\sigma_x^2}\right)}, \tag{1.28}$$

where σ_x is the width of the wave packet and v_i is the group velocity of i-th mass eigenstate [5]. Wave packet treatment readily quantifies two conditions necessary for oscillations to be observed:

- negligible decoherence due to wave packets separation

  As different mass states have different group velocities, their wave packets will eventually separate and can not interfere at the detection point. Hence an experiment aiming to observe oscillations better be placed closer than the coherence length, as was first pointed out in [6]

  $$L_{coh} \quad \propto \quad \frac{E^2}{\Delta m_{ij}^2} \sigma_x, \tag{1.29}$$

- uncertainty in position due to wave packet smearing is smaller than oscillation length

  $$\sigma_x < \frac{4\pi E}{\Delta m_{ij}^2} \tag{1.30}$$

  If rewritten in the momentum basis, this suggests that oscillations can be suppressed

by measurements attempting to identify what mass eigenstate is propagating.

Let's consider an example. C.W.Kim estimated [7] the uncertainties of packet localization for different typical neutrino sources. In particular, $\sigma_x \sim 10^{-11}$ m for the supernova neutrinos, and $\sigma_x \sim 10^{-6}$ m for the reactor neutrinos. Plugging in typical values of mass splitting ($\sim 10^{-3}$ eV^2) and neutrino energies ($\sim 10^6$ eV), we can estimate the coherence length to be of the order of $\gtrsim 10^8$ m for reactor neutrinos and $\gtrsim 10^4$ m for supernova neutrinos. From these rough estimates we can conclude that

- Experiments aiming to observe oscillations of reactor neutrinos are not expected to suffer from decoherence effect for all practical source-detector separations and up to very large mass-squared differences
- Different mass states of supernova neutrinos are likely to completely separate on their way to earth due to different group velocities.

The wave packet approach provides a more rigorous treatment, compared to the plane waves, but to describe the oscillation phenomena in the most consistent way one needs to include the production and detection processes in the same framework with the propagation. This is achieved with a quantum-field-theoretical (QFT) approach, sometimes also called "external" wave-packet theory. In the QFT approach, neutrino production, propagation, and detection are considered as a single process, which can be described by a Feynman diagram with the neutrino in the intermediate state. The amplitude of the combined process can then be computed according to the Feynman rules. Unlike the case of the wave packet treatment, where the oscillation probability has to be normalized by hand by imposing the unitarity condition, the oscillation probability for ultra-relativistic neutrinos derived from the QFT approach is automatically normalized [8].

1.3 Review of current knowledge

By now, different experiments have observed discrepancies in measured neutrino fluxes from the sun, earth's atmosphere (produced by cosmic rays), accelerators, and nuclear reactors, when compared with expectations of no oscillations or other non-standard physics. The idea of flavor oscillations allows one to reconcile such discrepancies, assuming existence of two practically decoupled oscillations in the "atmospheric", Δm^2_{32}, and "solar", Δm^2_{21}, quadratic mass splittings ranges with corresponding mixing angles (Table 1.2). Additional parameters may be needed to account for the possible existence of sterile neutrinos.

Parameter	Value
Δm^2_{21}	$(7.59 \pm 0.20) \cdot 10^{-5} eV^2$
$sin^2(2\theta_{12})$	0.87 ± 0.03
Δm^2_{32}	$(2.43 \pm 0.13) \cdot 10^{-3} eV^2$
$sin^2(2\theta_{23})$	> 0.92, proj. of 90% C.L. $sin^2(2\theta_{23}) - \Delta m^2_{32}$ contour
$sin^2(2\theta_{13})$	< 0.15, C.L.=90%

Table 1.2: Current status of neutrino oscillation parameters [12].

The solar mass splitting ($\Delta m^2_{\odot} = \Delta m^2_{21}$) is known to be positive, as the sign depends on the matter effects which strongly affect the neutrino oscillations in the sun. Since the notation of the mass eigenstates is arbitrary, one could always assign the second index to the more massive one. It is yet to be determined, though, if the third state is willing to comply with such notation. If the third state will be found to be more/less massive than the second one, which is referred to as "normal"/ "inverted" hierarchy, the atmospheric mass splitting has a positive/negative sign, respectively.

Sterile neutrinos, or neutrinos that do not participate in weak interactions, are speculated to exist to relieve tensions with results of the LSND experiment that reported an excess of electron anti-neutrinos in the muon anti-neutrino beam [13]. Such excess requires existence of yet another mass splitting inconsistent with the 3x3 MNSP matrix. The MiniBooNE

experiment was most recently performed to cross-check the LSND result[6], but while its neutrino data excludes at 98% C.L. the LSND result, its anti-neutrino data show an excess of electron flavor that is similar to LSND. To explain this result, however, more than one sterile neutrino is required [14]. In addition to that, a recent re-evaluation of the conversion procedure used to derive the reactor anti-neutrino flux [15] resulted in a systematic shift in the expected neutrino rate of roughly +3%. This creates tension with previous short-baseline ($<$ 100 m) reactor experiments (Bugey, Krasnoyarsk, Savannah river, Rovno, Goesgen, and ILL-Grenoble) and suggests a possible anomaly that, again, would require existence of a larger mass splitting ($|\Delta m^2_{new}| > 1.5eV^2(95\%C.L.)$) and a new (fourth) angle ($sin^2(2\theta_{new}) = 0.14 \pm 0.08(95\%C.L.)$).

Sterile neutrino controversy aside, the existence of three active flavors implies three flavor oscillations, hence the existence of another mixing angle in addition to the atmospheric and the solar ones. As of now, however, only an upper limit on the θ_{13} is known, established by the CHOOZ experiment [16] and also Palo Verde [17]. Recently, a few low-significance hints at a non-zero value appeared in several global analyses. For example, KamLAND [7] published an analysis that contains a joint fit for the solar mixing angle and mass splitting, and θ_{13} [19]. The publication contains best-fit values for different data combinations and analysis approaches (Figure 1.2). In case of three-flavor analysis it includes data from CHOOZ, solar (chlorine [20], gallium [21], Borexino [22], SNO [23], [24], and Super-Kamiokande [25]), and long baseline (K2K and MINOS) experiments [26], obtaining $sin^2 2\theta_{13} = 0.035^{+0.050}_{-0.028}$. This value corresponds to 79% C.L. for non-zero θ_{13}.

When this thesis was already in preparation, another result, announced by T2K, provided a new indication of a non-zero value of the last mixing angle. T2K is an off-axis long baseline experiment that uses the Super-Kamiokande detector to search for appearance of electron neutrinos in the predominantly muon neutrino beam, generated at the J-PARC accelerator

[6]KARMEN and Bugey experiments, conducted earlier, limited the parameter space but did not exclude LSND results.

[7]KamLAND is a reactor experiment that successfully measured parameters of solar oscillations [18] providing a clear resolution of the observed deficit of solar neutrinos

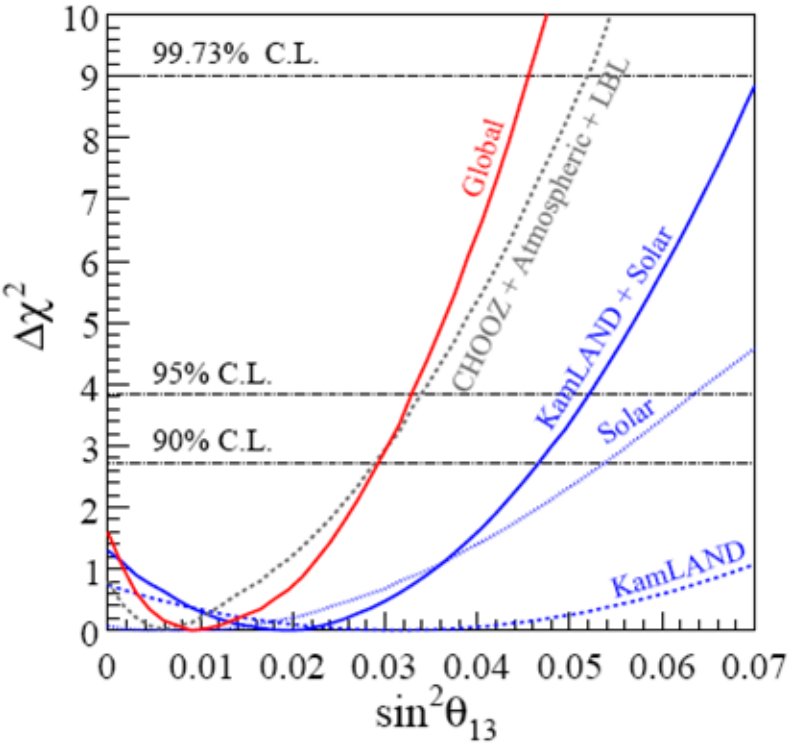

Figure 1.2: Chi-square profiles for different combinations of oscillation data [19].

complex [27]. In Summer 2011, T2K reported observation of six events passing all selection criteria for electron neutrinos. The background expectation value was 1.5±0.3 (syst.) events, providing a 2.5σ significance of excess. Assuming no CP violation, the corresponding 90% C.L. interval is $0.03(0.04) < \sin^2(2\theta_{13}) < 0.28(0.34)$ for the normal (inverted) mass hierarchy [28].

The T2K' announcement was almost immediately followed by a statement from the MINOS experiment, which updated its appearance analysis and disfavored a zero value of θ_{13} at the 89% confidence level [29].

In spite of the existing exciting results, it is neccessary to continue working towards a more precise measurement of the last mixing angle. The motivation for improving our knowledge about θ_{13} is further reinforced by the fact that another parameter of the MNSP matrix, namely the CP violating phase, which is now completely unknown, can only be measured if θ_{13} is not too small. Practically speaking, if $sin^2 2\theta_{13} > 0.001$, the next generation off-axis

long base line experiments, in particular LBNE, can achieve 3σ sensitivity for about 50% of the total physical parameter space for the Dirac CP phase [30].

1.4 Approaches to measure the last mixing angle

Increasing sensitivity to θ_{13} is possible using reactor neutrinos and accelerator neutrino beams.

Accelerator neutrino experiments use a proton beam interacting with a fixed target, producing copious amounts of pions and kaons. The secondaries decay (in flight or at rest) into muons and neutrinos, resulting in mostly muon type neutrino emission. [8] Using magnetic horns allows one to focus charged secondaries, producing an intense neutrino beam. Reversing polarity of the horn results in a predominantly anti-neutrino beam, opening an opportunity to detect differences in oscillation probabilities for neutrinos and anti-neutrinos, and hence probe the CP violating phase and sign of the atmospheric mass splitting. With accelerator experiments one can pick an L/E term to be in the range of atmospheric oscillations by choosing the energy of the initial beam and distance between the detector and accelerator[9]. Moreover, locating the detector at a particular angle off-axis with respect to the beam allows to select neutrinos with narrower energy distribution, peaking near the oscillation maximum of the muon-to-electron neutrino oscillation probability. Having fewer high energy neutrinos in the off-axis beam also reduces the large background associated with neutral current interactions [31]. Concrete examples of the current off-axis accelerator experiments are T2K [27], that has already produced its aforementioned first result [28], and NOνA [32], that is expected to start operations with its far detector soon.

It is clear that current long-baseline accelerator experiments provide a rich physics program. Along with the main goal of θ_{13} measurement using the $\nu_\mu \rightarrow \nu_e$ appearance channel, they can provide additional increase in accuracy of atmospheric oscillation parameters in

[8] Typical contamination by electron type neutrinos is on the order of 1%.

[9] Since the distances are on the order of hundreds of kilometers, the experiments are called long-baseline experiments.

the ν_μ disappearance channel, and even have sensitivity to the Dirac CP violating phase and the sign of the Δm^2_{32}. The downsides are large costs associated with beam constuction and operations, need for very large far detectors, and a complicated analysis involving the disentangling of correlations and degeneracies between parameters [33].

On the other hand, reactor experiments allow for a clean and relatively simple measurement of θ_{13} as a single parameter.

1.4.1 Reactor neutrino experiments

In this subsection we explain basic principles and techniques behind reactor experiments and describe the two previous experiments that provided a constraint on θ_{13}, namely, CHOOZ and Palo Verde. The CHOOZ experiment will be described in greater detail, as it was very similar and offered a lot of guidance for the Double Chooz and other current generation experiments, now in preparation.

1.4.1.1 Basic technique

Nuclear reactors are abundant sources of electron anti-neutrinos. The non-zero value of θ_{13} would lead to oscillation of electron anti-neutrinos into other flavors as they travel away from reactor. As the majority of emitted neutrinos have energy not exceeding 8 MeV, observation of the appearance of a neutrino of different flavor is not possible due to kinematic restriction of the production of a much heavier charged lepton. On the other hand, a detector that contains a target consisting of a large number of hydrogen atoms can detect electron anti-neutrinos via the inverse beta-decay (IBD) reaction and search for their disappearance. Given the average energy of electron anti-neutrinos emitted by the reactor and the value of the atmospheric mass splitting, placing the detector about 1.5-2 km from the reactor would maximize the sensitivity to oscillations.[10] Plugging the previously measured parameters (Table 1.2) into the electron neutrino survival probability (equation (1.23)) substantially

[10] $sin^2(1.267 \cdot 2.43[10^{-3}eV^2] \cdot 1.95[km]/3.5[MeV]) \approx 1$

simplifies it, leaving a single term that dominates at this distance

$$P_{ee} = 1 - \sin^2 2\theta_{13} sin^2 \left(\frac{1.267 \Delta m^2_{atm} L}{E_\nu} \right) \tag{1.31}$$

Reactor experiments are therefore ideal for measuring this parameter and can provide complementary input to long-baseline accelerator experiments, helping them to reduce ambiguity due to parameter correlations.

Detection method

The core volume of a typical detector contains an accurately measured amount of hydrogen atoms as a target for anti-neutrinos emitted by the reactors. An anti-neutrino that hits a hydrogen atom has a small but well-known probability to participate in the inverse β-decay (IBD) reaction, leaving behind a positron and a neutron (Figure 1.3):

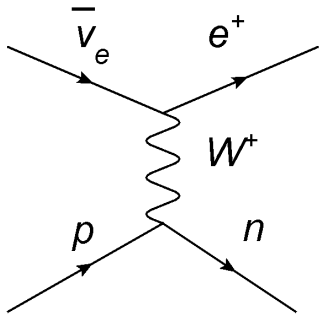

Figure 1.3: Feynman diagram of the IBD reaction.

IBD threshold

The threshold for the IBD reaction can be easily estimated:

$$E = E_\nu + E_p = E_\nu + m_p \quad \text{and} \quad \vec{p} = \vec{p_\nu} + \vec{p_p} = \vec{p_\nu} \tag{1.32}$$

The total invariant mass of the system is then

$$M^2_{\nu p} = E^2 - p^2 = (E_\nu + m_p)^2 - E^2_\nu = m^2_p + 2 m_p E_\nu, \tag{1.33}$$

where m_ν is ignored.

That should be at least as big as $M^2_{e^+n}$. The invariant mass of the positron+neutron is most easily calculated in the center-of-mass (CM) frame, where their kinetic energy is zero

$$M^2_{e^+n} = 2m_{e^+}m_n + m_n^2 + m^2_{e+} \tag{1.34}$$

$$M^2_{\nu p} = M^2_{e^+n} \Rightarrow E_\nu^{min} = \frac{2m_{e^+}m_n + (m_n^2 - m_p^2) + m^2_{e^+}}{2m_p} \tag{1.35}$$

First term: $1.0014 \cdot m_{e^+} = 0.511$ MeV

Second term: $\frac{(m_n^2 - m_p^2)}{2m_p} = 1.2942$ MeV

Third term: $\frac{m^2_{e^+}}{2m_p} = O(10^{-4})$ MeV

The threshold energy is then 1.805 MeV in the lab frame. Taking into account the velocity of CM with respect to the lab frame ($V = \frac{p_\nu}{E_\nu + m_p}$), $E_\nu^{min} = 1.803$ MeV in the CM frame.

IBD cross-section

The cross section of the IBD reaction is given below:

$$\sigma(E_{e^+}) = \frac{2\pi^2\hbar^3}{m_e^2 f \tau_n} p_{e^+} E_{e^+} (1 + \delta_{rec} + \delta_{WM} + \delta_{rad}), \tag{1.36}$$

where τ_n is mean neutron lifetime, f is the neutron decay phase-space factor, $\delta_{rec}, \delta_{WM}, \delta_{rad}$ are the energy dependent recoil, weak magnetism, and radiative corrections respectively, p_{e^+} is positron momentum, and E_{e^+} is total positron energy, which is approximately related to the anti-neutrino energy in the following way:

$$E_{e^+} \approx E_{\bar{\nu_e}} - (m_n - m_p) - \frac{1}{m}[E_{e^+}(E_{e^+} + m_n - m_p) + \frac{(m_n - m_p)^2 - m_e^2}{2}], \tag{1.37}$$

where m is the nucleon mass.

The last term in Equation (1.37) takes into account neutron recoil energy. While small, when coupled with the rapid fall of the anti-neutrino flux with energy, it decreases the

positron yield by several percent [38]. The recoil correction (to the cross section, not energy) is negligible. The correction for weak magnetism, caused by the difference between magnetic moments of neutron and proton, decreases the cross section by 2% for 5 MeV positrons. The first order radiative correction increases the cross section ≈1.5% near the threshold and ≈0.7% at 5 MeV. More details can be found in [15, 38].

Uncertainty on the IBD cross-section, mostly stemming from uncertainty on the neutron life-time, is at the sub-percent level, and is a subdominant error in reactor experiments.

Signature in the detector

The positron produced by the IBD reaction will most likely thermalize and annihilate into two gammas (annihilation into more gammas is possible, but is less likely[11]). The kinetic energy of the positron and the energy of annihilation gammas can be detected, for example, through light produced by the scintillation process.

The other product of the reaction, the neutron, will thermalize after a few collisions with hydrogen and carbon atoms and will get captured. The capture gammas will produce a detectable signal as well.[12]

Thermalization of a positron will occur almost immediately ($\sim 10^2$ picoseconds) and annihilation will follow shortly (∼0.1 nanosecond if it occurred at rest or from a short-lived state of the positronium). The ortho state of positronium has a longer lifetime, ∼0.1 microseconds, however its lifetime may be reduced in the matter due to interaction with electrons of the medium. In fact, as has been measured [39], positronium is formed before annihilation in about 50% of the cases and its lifetime in the main component of the Double Chooz scintillator (dodecane) is ∼3 nanoseconds.

Thermalization of a neutron will happen rather quickly as well (nanoseconds to a few microseconds) but the capture can occur on a time scale of tens and hundreds of microseconds,

[11] Unless two gamma decay is suppressed by conservation law, as is the case, for example, of decay of ortho-positronium, whose spin (S=1) forbids decay into two gammas.

[12] While the kinetic energy of the neutron is too small (∼10-100 keV) to pass a typical trigger threshold, it will be added, in quenched form, to the prompt energy deposition.

depending on the composition of the medium.

The positron (prompt) and the neutron (delayed) induced signals create a distinct coincidence signature in the detector that allows one to discriminate the IBD reaction against much more abundant uncorrelated background events.

Neutrino production

Electron anti-neutrinos are generated in the reactor by β-decays of unstable fission fragments. The dominant role in neutrino production is played by the fissions of four isotopes: U-235, Pu-239, U-238, and Pu-241. When a nucleus undergoes fission the resulting fragments have the same ratio of neutrons to protons as the parent nucleus, which makes these lighter nuclei unstable and prone to getting rid of the excess neutrons by undergoing a series of beta decays. Each time a beta decays occurs, an electron anti-neutrino is emitted. There are roughly six neutrinos emitted per fission, but only 1-2 of them will have energy above the threshold of the IBD reaction.

The actual amount and energy spectrum of the neutrinos emitted by three of the four isotopes (apart from U-238) was inferred from measurements conducted at ILL, Grenoble, back in the eighties. Targets of the individual fissile isotopes were irradiated by thermal neutrons to induce fission, and the electrons emitted in the subsequent beta decays were analysed in a precise beta-spectrometer to obtain a cumulative energy spectrum. Anti-netrinos from a beta decay are kinematically related to electrons in a straightforward way, but on a branch by branch level. Since only cumulative electron spectra could be measured, a conversion procedure had to be developed and applied to obtain the resulting anti-neutrino spectra. A typical reactor neutrino spectrum above IBD threshold is shown in Figure 1.4. The uncertainty of the procedure was reported to be 1.9% for normalization, and a few percent on energy dependent shape error, correlated between energy bins [34]. Since thermal neutrons do not induce fission in U-238, no measurement were performed and, so far, a theoretical spectrum is used for this isotope. The associated uncertainty is larger, but the contribution of U-238 to overall number of fissions is on the level of 8%.

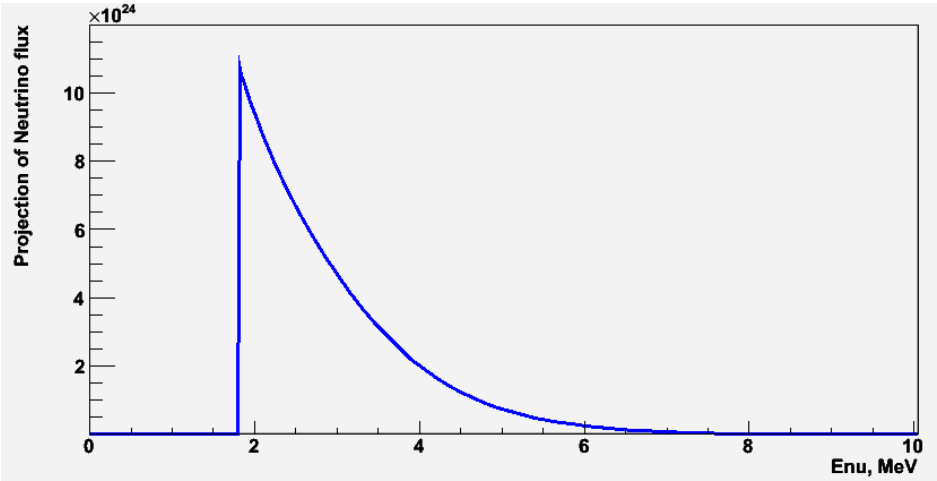

Figure 1.4: Reactor anti-neutrino energy spectrum (part above IBD threshold shown).

We can see that to know the emitted number and energy spectrum of reactor anti-neutrinos one needs to know the fission rates of individual fissile isotopes. The rates should be known as a function of time, because of the burn-up effect.[13][14] The typical time dependence of fission rates during fuel cycle is illustrated on Figure 1.5, as simulated by the DRAGON simulation code [35].

The typical accuracy on individual fission rates achieved with dedicated Monte Carlo codes is on the order of 5% (correlated between isotopes). Fortunately, one can constrain the overall number of fissions with better accuracy by monitoring thermal power output from the reactor. Several methods exist, the most accurate one involving calculation of the heat balance around the steam generator (for pressurized water reactors). With proper techniques, requiring accurate measurement of the water flow and temperature, steam enthalpy and moisture content, coolant cycle heat gain and losses, etc., one can constrain the overall number of fissions to better than one percent [36].

Putting the different pieces together, the expected rate of anti-neutrinos in the detector

[13]The relative fission fractions of different fissile isotopes evolve with time, with uranium concentration decreasing and plutonium accumulating.

[14]Additional small corrections may be needed to account for the residual anti-neutrino emission from long-lived fission fragments, which was not measured at ILL, small displacement of the average position of neutrino production inside the reactor core, small anti-neutrino emission from spent fuel storage, etc.

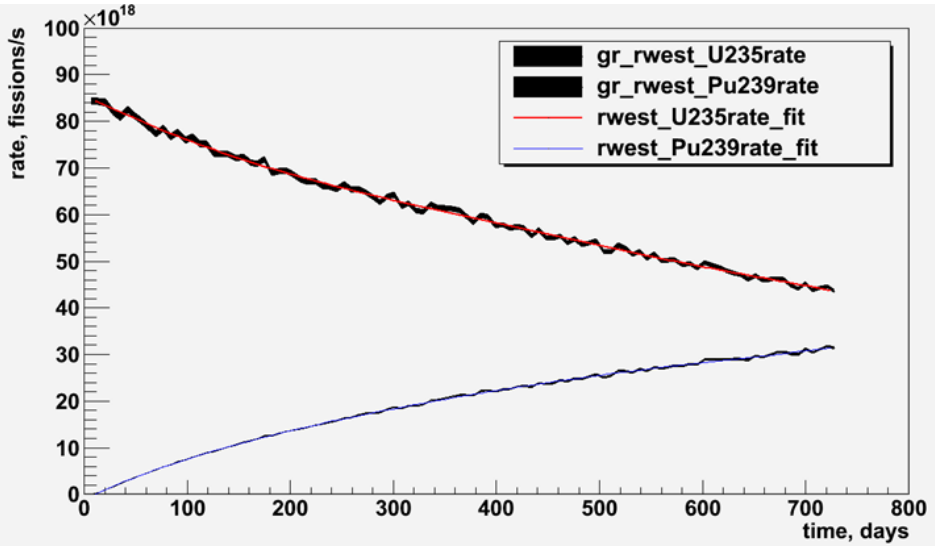

Figure 1.5: Fission rates as a function of time for U-235 and Pu-239 isotopes.

is

$$\frac{dN_\nu}{dE_\nu dt} = \sum_i N_p \epsilon \sigma(E_\nu) \frac{P_{ee}(E_\nu, \Delta m^2_{atm}, L_i)}{4\pi L_i^2} P_i^{th} \sum_j \frac{\alpha_{ij} S_{ij}(E_\nu)}{E_j}, \tag{1.38}$$

where N_p is the number of free protons, ϵ is the detection efficiency[15], L_i is the distance between i-th reactor and the detector, P_i^{th} is the instantaneous power of i-th reactor, S_{ij} is the reference spectrum of electron anti-neutrinos emitted by isotope j, P_{ee} is the electron neutrino survival probability, σ is the cross-section of the IBD reaction, α_{ij} is the fractional fission rate of isotope j, and E_j is the energy released in one fission of isotope j. Index i runs through all reactors, and j runs through the fissile isotopes. It is also useful to define the mean cross-section per fission as:

$$\langle \sigma_f \rangle = \sum_j \alpha_j \int_0^\infty S_j(E_\nu) \sigma(E_\nu) dE_\nu \tag{1.39}$$

Backgrounds

The inverse β-decay signature in the detector is two energy depositions O(1MeV) within

[15]Note that if the detection threshold is not low enough to accept all prompt positrons, the efficiency becomes energy dependent, which is undesirable.

a short time window (ca. 0.1 msec). The neutrino event can be faked by random coincidences and correlated backgrounds.

- Accidentals

  Gammas from naturally occurring isotopes, mainly U238/Th232 chains and K-40, may fake the prompt (positron) signal by depositing energy in the sensitive volume. The natural gamma background increases very quickly towards low energies. As was mentioned, one wants to set the prompt event threshold as low as possible, hence it is important to minimize the impact of natural radioactivity. Careful choice of materials, strict cleaning procedures, and passive shielding provide effective reduction of this source of single events.

  Contribution to neutron-like singles can come from background neutron captured in the detector or a bremsstrahlung gamma from a cosmic muon passing nearby.

  This background can be accurately measured by looking at coincidences at large capture times, since accidentals are distributed randomly, while real captures decay almost exponentially in time. Therefore, in a reactor experiment aimed at measuring θ_{13}, the uncertainty associated with this type of background is not significant, provided due consideration was given during selection of detector materials and construction.

- Correlated backgrounds

  The main source of correlated background is fast neutrons produced by cosmic muons not passing through the detector but traveling nearby. Such neutrons can then wander into the sensitive volume unvetoed, mimic the positron signal through proton recoils, and afterward get captured, composing the delayed event.

  Another source of correlated background is radioactive nuclei created by muons passing through the sensitive region. It is known from previous experiments that the most troublesome are Li-9, whose β-decay is accompanied by neutron emission in 50% of

the cases and He-8, having 15% chance to emit a neutron. The long life-time of these isotopes (100-200 ms) makes vetoing every muon impossible.

Reactor experiments are thus usually located underground, in order to reduce the muon flux. For typically available overburdens and reactor powers, signal-to-background fractions on the order of 10 or more are achievable.

We now describe two actual reactor experiments that provided a constraint on the value of the θ_{13}

1.4.1.2 CHOOZ and Palo Verde

In the early 1990s, an anomalous ratio of muon to electron neutrinos originating in the Earth's atmosphere was observed in several experiments [10, 11]. While the absolute flux of atmospheric neutrinos is difficult to predict accurately, the ratio of muon to electron neutrinos is naively expected to be about 2, and more detailed simulations can derive the ratio to a few percent accuracy [16].

In the framework of neutrino oscillations, observation of a smaller ratio could be explained either by $\nu_\mu \leftrightarrow \nu_e$ or by $\nu_\mu \leftrightarrow \nu_\tau$ transitions.

The former possibility motivated CHOOZ and Palo Verde experiments to look for a disappearance signal using reactors neutrinos, due to their high intensity and purity.

CHOOZ

The CHOOZ experiment was located in an underground laboratory about 1 km from the CHOOZ nuclear power plant. The plant consists of two reactors providing 4.25 GWth each. Reactor thermal power was monitored by two methods: the first one is based on the heat balance of the steam generators and had a claimed precision of 0.6%. The second

[16] Cosmic rays consist primarily of protons, which will interact in the atmosphere to produce pions. Pions will decay into muon anti-neutrinos and muons that, in turn, will decay into electrons and both electron anti-neutrinos and muon neutrinos, giving rise to the expected ratio.

one was provided by external neutron flux measurement and was less precise (1.5%). The laboratory was located inside a mountain under 300 meters water equivalent (m.w.e.) of rock overburden and had a 7 m pit that housed the detector. The detector was installed in a cylindrical steel vessel 5.5 m in diameter and 5.5 m deep. To decrease the impact of natural radioactivity of the rock, the steel vessel was surrounded by 75 cm of low radioactivity sand and covered by 14 cm of cast iron. The detector (Figure 1.6a) consisted of three concentric regions:

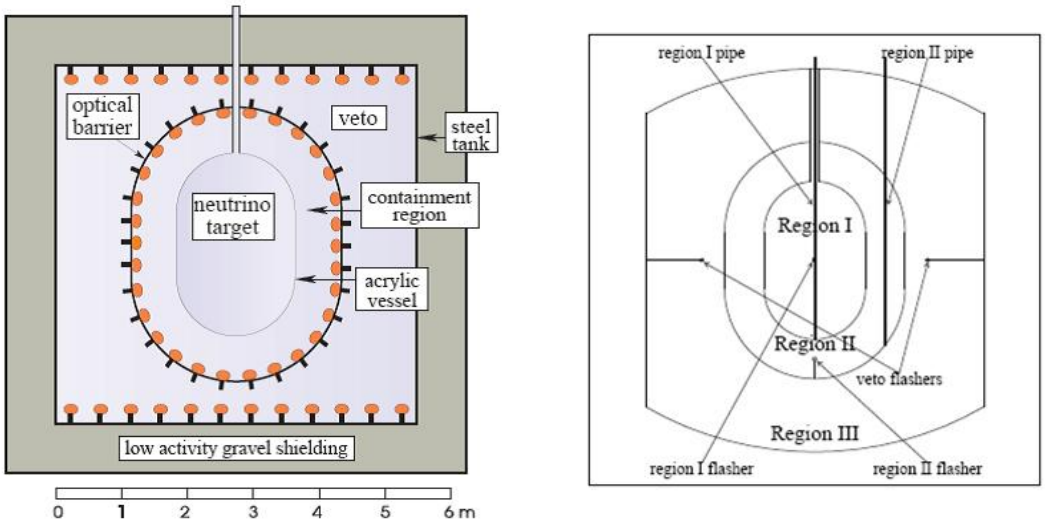

(a) detector schematics

(b) calibration systems

Figure 1.6: The CHOOZ detector.

- 8 mm thick acrylic target vessel filled with 5 tons of scintillator loaded with 0.09% of Gd by weight ("Region I") The vessel had a chimney of 70 mm in diameter to provide access for filling pipes, calibration sources and temperature/pressure sensors.

- 17 ton 70 cm thick intermediate region that housed 192 8" photomultiplier tubes (PMTs), used to protect the target from PMT radioactivity and to contain neutron capture gammas ("Region II") The support for the PMTs was provided by an opaque plastic structure called "geode". The total coverage of the Region II PMTs was 15%. This region was filled with unloaded liquid scintillator.

- an outer 90-ton optically separated active cosmic-ray muon veto shield (80 cm thick) equipped with two rings of 24 8" PMTs ("Region III"). This region was also filled with unloaded scintillator.

The CHOOZ detector was, essentially, a low-energy high-resolution liquid scintillator calorimeter. To calibrate the detector, six light flashers were installed in the three regions together with calibration pipes (Figure 1.6b) used to deploy neutron (Cf-252 and AmBe) and gamma (Co-60) sources.

The neutrino detection was based on the delayed coincidence between the prompt positron and delayed neutron signals, described above.

The experiment was taking data from 12 March 1997 till 20 July 1998 and had the total live time of ≈340 days. The unique feature of the CHOOZ experiment was that the reactor complex was new and subject to frequent stops. Because of that, for a large part of the experiment the reactors were off (40% of the live time was acquired with both reactors off, and at least 80% of the live time only one of the two reactors was on). That provides a great opportunity for a) measuring the correlated backgrounds and b) conducting a neutrino oscillation test at two slightly different baselines.

At the same time, the experiment stopped taking data when it became clear that neither reactor would resume normal operation for at least one year [16]. Another reason why CHOOZ was not able to continue the experiment was due to the optical properties of the scintillator progressively deteriorating, which was most probably related to oxidation by nitrate ions (Gd was dissolved in the scintillator in the form of a nitrate salt). That required repeated calibrations to trace the degradation of photo-electron yield and would make it difficult to run the experiment longer.

The data events acquired by CHOOZ can be separated into several classes, as illustrated on Figure 1.7:

- Neutrino candidates

- Backgrounds, which could further be categorized as follows:

  A) events with $E_{e^+-like} < 8MeV$ and $E_{n-like} > 12MeV$

  B) events with $E_{e^+-like} > 8MeV$ and $E_{n-like} > 12MeV$

  C) events with $E_{e^+-like} > 8MeV$ and $6 < E_{n-like} < 12MeV$

  D) events with $E_{e^+-like} < 8MeV$ and $E_{n-like} < 6MeV$

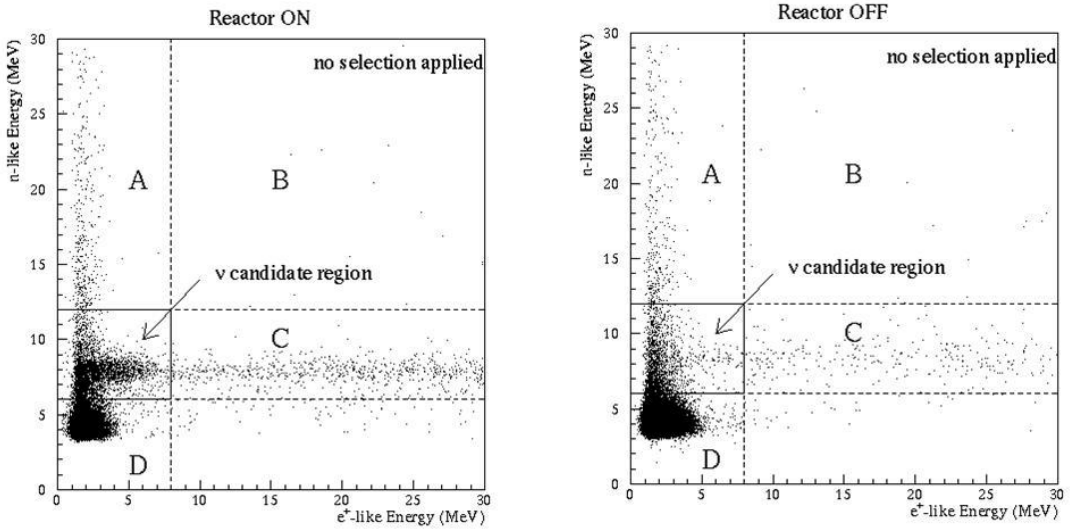

(a) reactor on (b) reactor off

Figure 1.7: Prompt versus delayed energy depositions. A preliminary cut on total charge (roughly corresponding to 4 MeV) in the neutron-like (delayed) event is applied to remove most of the radioactive background.

The regions A) and D) were measured to have an inter-event time distribution consistent with accidental coincidences of uncorrelated backgrounds. They can be largely eliminated by applying fiducial volume cuts to remove areas close to the PMTs (i.e. requiring prompt and delayed events to be a certain distance away from the geode surface[17]) and events with large prompt-delayed separation.

The region D) has an exponential inter-event time distribution with a lifetime of $2.8 \pm 0.4\mu s$, which is comparable to a muon decay at rest. Both muon and Michel electrons deposit more energy than reactor neutrinos, so these events were rejected by energy cuts.

[17] d_{prompt} and $d_{delayed}$, respectively

The region C) shows a clear 8 MeV peak in the delayed energy deposition consistent with neutron captures on Gd. The inter-event time distribution can be described as exponential with $30.5 \pm 1.0 \mu s$ lifetime, also in agreement with Gd capture time. It is thereby attributed to the spallation neutrons produced by muons that interact outside the detector. These neutrons are a source of correlated background, since their thermalization also produces a prompt signal which can mimic the one of the positron, and are more difficult to eliminate. Yet, since the muon spallation process usually generates more than one neutron, a cut on neutron multiplicity can be used to decrease the impact of this correlated background.

The final set of cuts employed during analysis of CHOOZ data was the following:

1. Energy cut on prompt event: $E_{prompt} < 8MeV$

   This upper limit accepts majority of positrons ($> 99.95\%$).

2. Energy cut on delayed event: $6 < E_{delayed} < 12MeV$

   While the lower cut introduces some inefficiency due to few Gd capture gammas escaping the active region, it optimizes the signal to noise ratio by removing residual low energy uncorrelated background.

3. Fiducial cut on prompt event: $d_{prompt} > 30cm$

4. Fiducial cut on delayed event: $d_{delayed} > 30cm$

5. Relative distance between events: $d_{e^+n} < 100cm$

6. Inter-event time separation: $2 < \delta t_{e^+n} < 100\mu s$

   The lower time cut was needed to reduce effects of the signal overshoot related to the AC coupling of the PMT bases and front-end electronics (FEE) [16, p.25].

7. Neutron multiplicity: $N_n = 1$

The efficiency of the positron cut was determined taking into account variations of the neutrino spectrum with time due to burn up effect, increase in the trigger threshold with

time due to scintillation aging, position dependence of the energy threshold (measured with Co-60 source along the z-axis and predicted using Monte Carlo elsewhere). Fiducial volume and inter-event distance cut efficiencies were determined using Monte Carlo and were found to be almost independent of the scintillator degradation.

The neutron capture efficiency was factorized into the fraction of captures on Gd (defined as ratio of neutron captures on Gd to the total captures), the 6 MeV cut fraction (defined as ratio of neutron captures with energy above 6 MeV to the total number of Gd captures), and the time cut (from 2 to 100 μs). The Gd captures fraction was determined for Cf-252 neutrons ($\approx$2 MeV mean energy, or $\approx$20 cm pathlength) using a tagged sources and extrapolated to the IBD neutrons ($\approx$ 50 keV energy, or $\approx$ 6 cm pathlength) with Monte Carlo. Similarly, the time delay cut was studied with AmBe source data and MC. The inefficiency of the 6 MeV cut was also found using calibration data and cross-checked with MC.

The neutron multiplicity has a potential for rejecting neutrino events if spurious triggers (e.g. due to uncorrelated gamma events) occur along with the positron-neutron pair. Possible scenarios were considered and the efficiency was estimated analytically, using known rates of singles events and time acceptance window.

The efficiency of each cut, along with its estimated uncertainty, is presented in the Table 1.3 [18]. The final positron spectrum, after application of all selection cuts is presented on Figure 1.8a superimposed with the expected spectrum obtained using Monte Carlo under assumption of no oscillations. The measured versus expected ratio, averaged over energy (Figure 1.8b) is

$$R = 1.01 \pm 2.8\%(stat) \pm 2.7\%(syst) \tag{1.40}$$

The break down of normalization systematics is listed in the Table 1.4. The major one is associated with reactor anti-neutrino flux.

Several methods were used to derive exclusion limits from the data. Below we summarize

[18] We note here that the Double Chooz experiment, guided by the CHOOZ experience, incorporated several improvements in the design that allows it to avoid some of the cuts and hence decrease the systematic uncertainty.

Cut	Efficiency, %	Rel.error, %
average positron energy	97.8	0.8
positron-geode distance	99.9	0.1
neutron capture	84.6	1.0
capture energy containment	94.6	0.4
neutron-geode distance	99.5	0.1
neutron delay	93.7	0.4
average neutron multiplicity	97.4	0.5
positron-neutron distance	98.4	0.3
average combined value	**69.8**	**1.5**

Table 1.3: Efficiency of the neutrino selection cuts [16].

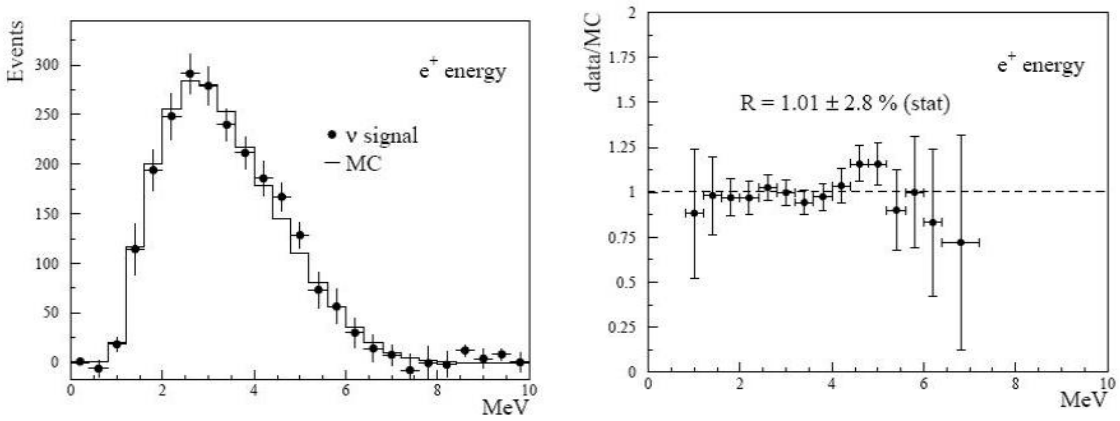

(a) measured and predicted spectra

(b) measured/expected ratio

Figure 1.8: Final measured positron spectrum. The reactor-off subtracted spectrum is compared to the MC prediction.

the most sensitive method that took advantage of both normalization and shape information (individually for each reactor): A chi-square function was constructed between background-subtracted data and prediction, with statistical and systematic errors related to the neutrino spectrum absorbed inside a covariance matrix (systematic errors associated with neutrino spectrum prediction assumed to be uncorrelated for simplicity). The absolute normalization uncertainty (Table 1.4) and the energy scale calibration factor (1.1%, resulting from measured width of hydrogen capture line and observed drift of Gd capture line) were added as pull terms.

The global minimum was found to be $\chi^2_{min} = 5.0$ (probability of 96%) for the best-fit

Parameter	Rel.error, %
mean cross section per fission	1.9
number of protons	0.8
detection efficiency	1.5
reactor power	0.7
energy released per fission	0.6
combined	**2.7**

Table 1.4: Overall systematic uncertainty on normalization in CHOOZ [16].

parameters $sin^2(2\theta) = 0.23$, $\Delta m^2 = 8.1 \cdot 10^{-4} eV^2$, and pulls on normalization and energy scale of 1.012 and 1.006 correspondingly. The non-oscillation hypothesis fit data well also, with $\chi^2 = 5.5$ (probability of 93%) and pulls of 1.008 and 1.011, respectively.

To determine the 90% exclusion plot a Feldman-Cousins approach was used [37]. The resulting plot is shown in Figure 1.9 together with curves obtained by other two methods and the region allowed by Kamiokande data for the $\nu_\mu \rightarrow \nu_e$ oscillations. The explanation of the atmospheric anomaly by oscillation between electron and muon neutrinos is thus excluded at maximal mixing for Δm^2 more than $7 \cdot 10^{-4} eV^2$, and at large Δm^2 for $sin^2(2\theta) > 0.1$.

Palo Verde

Palo Verde explored the same parameter space as CHOOZ experiment and obtained similar, though somewhat less restrictive countours, due to larger systematic uncertainties on trigger and event selection efficiencies and background estimates.

The experiment was performed at the Palo Verde Nuclear Generating Station in Arizona that consists of three reactors with total power 11.63 GW [17]. The detector was located at a shallower site (32 m.w.e), compared to CHOOZ, and consisted of 66 acrylic cells filled with 11.34 tons of Gd-loaded liquid scintillator. The active volume was monitored by PMTs separated by an oil buffer. The outermost layer of the detector was an active muon veto, comprised of tanks of liquid scintillator providing 4π coverage. A water shield was also placed between the active volume and the muon veto on the four long sides of the detector.

The exclusion plots obtained with two different analysis methods are shown in Figure 1.10.

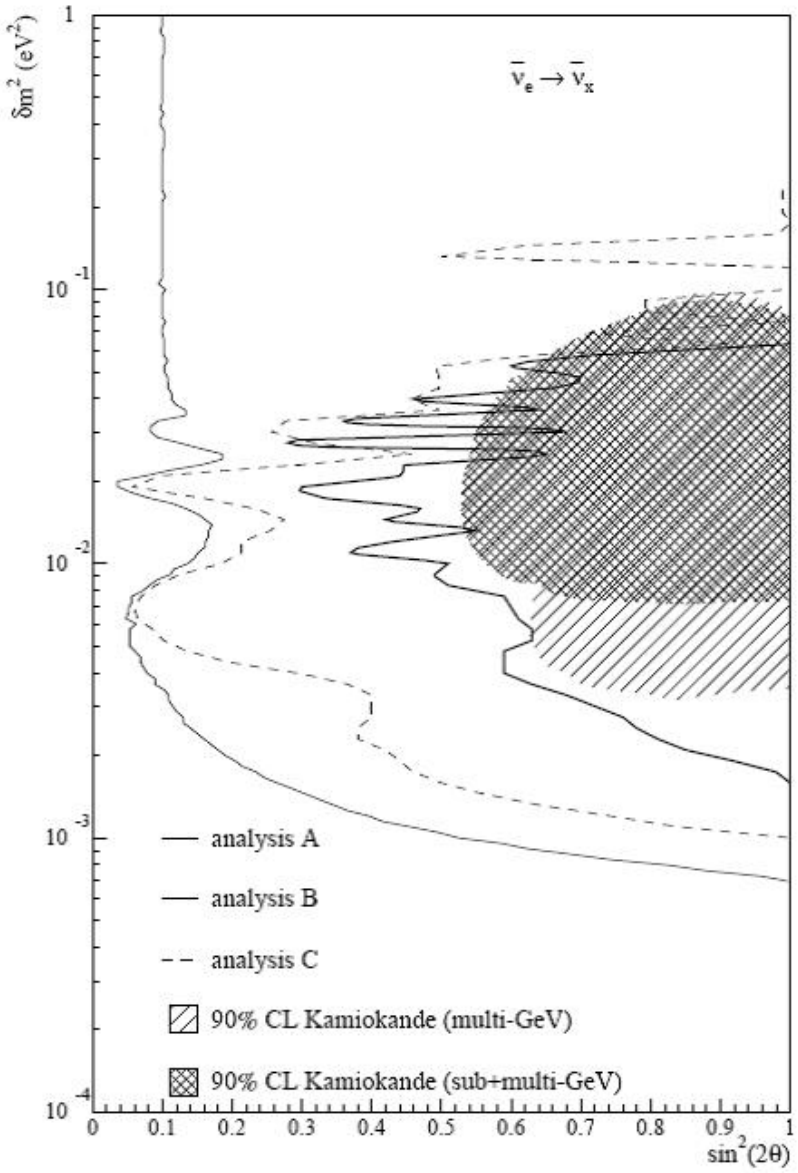

Figure 1.9: 90% C.L. contours obtained by CHOOZ (excluded) and Kamiokande (allowed). For description of analyzes B and C see [16].

1.4.1.3 Current generation reactor experiments

As can be seen from the Table 1.4, the dominant source of the systematic uncertainty in the CHOOZ experiment comes from the normalization of the reactor anti-neutrino flux. In order to improve the sentivity of reactor experiments to θ_{13} this source of systematics has to be

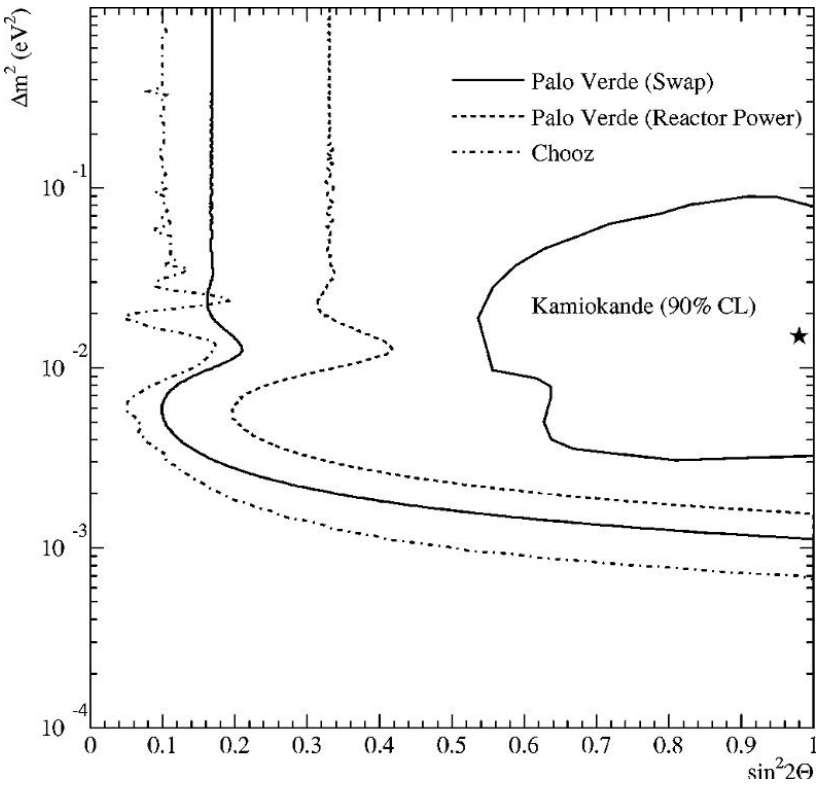

Figure 1.10: 90% C.L. contours obtained by Palo Verde. CHOOZ and Kamiokande (allowed) limits are also shown. For the description of analysis methods, see [17].

reduced. The way to do that, first discussed by Mikaelyan and Sinev [40], is to place another detector near the reactor cores, where the oscillations are not expected to develop yet. This "near" detector would effectively calibrate the actual flux emitted by the reactors, removing the absolute normalization uncertainty. The remaining error comes from understanding the relative differences between the far and near detectors, therefore they should be made as identical as practical.

The near/far detector approach was adopted by three new experiments - Double Chooz (France), Daya Bay (China), and RENO (South Korea). The next chapter is dedicated to the description of the Double Chooz experiment. The two other experiments are described in [41] and [42].

Chapter 2

Double Chooz

The Double Chooz (DC) experiment uses the existing underground hall near the CHOOZ-B nuclear power station in France that housed its predecessor, CHOOZ, which established the current best limit on the mixing angle. DC incorporates several improvements that will allow us to significantly improve the sensitivity and reach the limit $sin^2(2\theta_{13}) < 0.03$ at 90% C.L. after three years of data taking. The improvements are listed below:

- Reduced systematic error

  The CHOOZ error was dominated by reactor uncertainties (Table 1.4). DC will have an additional ("near") detector installed close to the reactor cores specifically to measure the non-oscillated neutrino flux and thus drastically reduce errors on core powers and production cross sections. The detector will be made as identical as possible to reduce systematics in detection efficiency and target mass. The detector induced uncertainties will also be decreased by using

  1. Calibration using the same sources for the different volumes of both detectors
  2. An Improved design requiring fewer selection cuts in order to simplify the analysis.

     The addition of another region (between Regions II and III) that is filled with non-scintillating liquid effectively shields the inner detector from the radioactiv-

ity in the PMTs glass, reducing the accidental backgrounds and allowing to avoid "positron-geode distance", "neutron-geode distance", "positron-neutron distance" cuts, and lowering the minimum accepted positron energy cuts (see Table 1.3)

3. More accurate measurement of target free protons

   The error on the number of free protons takes contributions from target mass uncertainty and chemical composition of the scintillator (the ratio of hydrogen to carbon atoms). The H/C ratio was dominating the error on the number of free protons in CHOOZ. Using the same batch of scintillator for both detectors cancels this error. Similarly, measuring the mass of the both targets using the same method and equipment reduces the error.

4. Increased statistics

   Both far and near DC detectors will have twice the sensitive volume of CHOOZ, thus increasing the event rate. Moreover, a more stable formulation of the Gd loaded scintillator will allow the experiment longer to run longer.

5. Similar detection efficiency systematics

- Lower backgrounds

  As described in the next section, special consideration was given to reducing both uncorrelated and correlated backgrounds to further decrease the impact on the systematic error.

2.1 The far detector

2.1.1 Detector design

The far detector is located 1115 m from the west and 998 m from the east core of the CHOOZ nuclear power plant. It is housed in an underground laboratory built inside the mountain providing about 300 m.w.e. overburden and decreasing the cosmic muon rate, compared to

the surface value, by a factor of ≈300 to a value of ≈0.4 $m^{-2}s^{-1}$ [16]. A bird's-eye view of the nuclear plant area and the layout of the far lab are shown in Figure 2.1 The detector consists of several concentric cylindrical vessels resembling a Russian doll (Figure 2.2).

Figure 2.1: Double Chooz experiment location.

2.1.1.1 Mechanics, liquids, and vetoes

Target volume (TV)

The "heart" of the detector is the target vessel (2.30 m diameter, 2.46 m height) made of 8 mm thick acrylic sheet. The acrylic is of a special type manufactured by Evonik Röhm GmbH to provide good mechanical stability, resistance to scintillator chemistry, and absense of UV luminescence. The thickness is kept as small as practical to minimize dead materials. The mass of the target vessel itself is ≈430 kg. The target volume is filled with 10.2 m^3 of

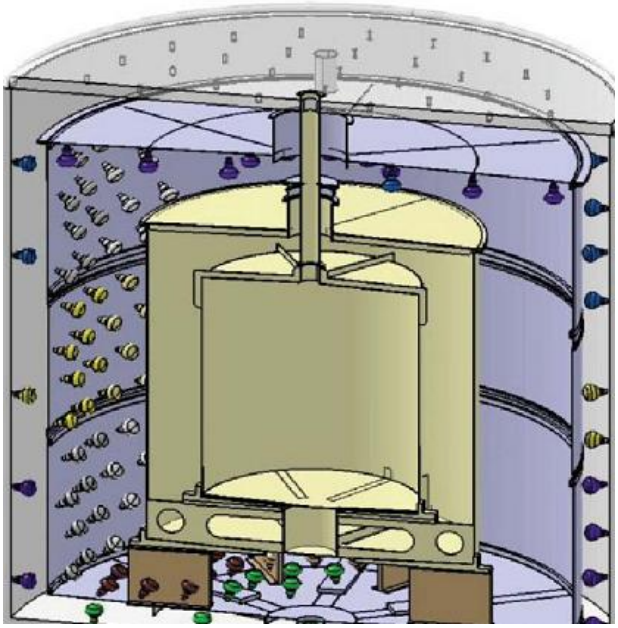

Figure 2.2: Schematic diagram of the Double Chooz detector.

liquid scintillator. Like all other volumes, the target has a chimney. The target chimney, extending roughly four meters above the target lid, provides access inside the sensitive volume for the calibration devices. Approximately two meters of the chimney are made of the same acrylic as the vessel itself. The target scintillator fills part of the chimney, but its diameter is just 15 cm, so very few events will occur in its volume, making the associated error small (0.3% associated systematics). The scintillator is a mixture of 80% n-dodecane as the main solvent, 20% aromatic solvent (PXE), and additions of 0.007 g/cm^3 of fluor (PPO), and $20 \cdot 10^{-6}$ mg/cm^3 of wavelength-shifter (Bis-MSB). The admixture of dodecane reduces the light yield, but improves the chemical compatibility with the vessel and increases the number of hydrogen atoms, providing abundant interaction medium for the reactor anti-neutrinos. The total concentration of hydrogen and carbon atoms in the target is[1] $6.53 \cdot 10^{22}$ cm^{-3} [44] and $3.51 \cdot 10^{22}$ cm^{-3} correspondingly [45].

The target liquid also contains 0.123 wt.% of Gd (about 1 mg/cm^3) as a part of the Gadolinium-β-dikenotane complex. Gd is a good choice for neutrino detection for the fol-

[1] or 13.60±0.04 wt.%, or $8.124 \cdot 10^{25}$(±0.3%) H/kg [44]

lowing reasons:

1. Very high cross-section of thermal neutron capture: 254 kbarn at 0.0253 eV on Gd-157 (15.65 atomic % natural abundance) and $\sim$ 61 kbarn at 0.0253 eV on Gd-155 (14.80 atomic % natural abundance). Other isotopes of Gd contribute as well and are modeled in the Monte-Carlo simulation.

2. The cascade of capture gammas totals around 8 MeV (compare with 2.232 MeV capture on hydrogen), placing it well above natural radioactivity, which does not extend above 2.6 MeV (Tl-208). However, unlike capture on hydrogen, there are several gammas emitted per capture on each isotope with a complicated and imperfectly known spectrum that makes it less usable for energy calibration.

3. The capture time on Gd is practically exponential with $\sim$ 30 μs lifetime, compared with $\sim$ 200 μs capture time on hydrogen, which further aids in background rejection

The price to pay is the complicated chemistry and multiple restrictions on material compatibility needed to maintain the Gd compound in solution for the duration of the experiment. The Gd scintillator technology we use was researched and developed specifically for Double Chooz by our collaborators at Max Planck Institute for Nuclear Physics (MPIK), Heidelberg.

Gamma-Catcher (GC) volume

The target is embedded in a larger acrylic cylinder of 3.392 m inner diameter and 3.55 m inner height. Its mass is $\approx$1450 kg. It is filled with slightly different liquid scintillator and does not contain the Gd compound. Its formulation (30% dodecane, 66% Ondina909 oil [2], 4% PXE, 2g/L PPO, and $20 \cdot 10^{-3}$ mg/L bis-MSB) was tuned to match the light yield and density of the target volume scintillator so as to increase the uniformity of the detector response and ensure the safety of the fragile acrylic modules, correspondingly. The main purpose of the GC is to contain inside the sensitive region the energy released in prompt

[2]Data sheets for Ondina909 and Ondina907 are available on the Shell Chemicals website

and delayed events by capturing the part of gamma radiation that may "leak out" from the target volume. Separating the sensitive region into two volumes allows us to avoid the fiducial volume cut and hence reduce the systematic uncertainty on the number of target protons available for the IBD reaction.

Buffer volume

The GC, in turn, rests inside a cylinder that is 5.516 m in diameter and 5.674 m in height, called the Buffer. The Buffer is made of pickled and passivated stainless steel SS304L. The 390 10" inner detector photomultiplier (PMT) tubes are attached to the walls of the Buffer. Natural radioactivity (U/Th chain, K-40) in the PMT glass was a substantial source of uncorrelated accidental background in the CHOOZ experiment, so special consideration was given to selecting the cleanest possible batches of glass for the production of the Double Chooz PMTs. However, the main reduction of this background comes from the fact that the Buffer vessel is filled with non-scintillating liquid (mixture of 47.2% CobersolC70 [3] and 52.8% Ondina917 oils), hence the Buffer effectively shields the sensitive detector from radioactivity originating in the photo-detectors.

Inner Veto

The Buffer sits inside another steel vessel - Inner Veto (IV). The IV is 6.50 m in diameter and 6.85 m in height. It contains its own 78 8" PMTs and is filled with liquid scintillator (48.4% LAB, 51.6% CobersolC70, 2g/L PPO, 20 mg/L bis-MSB). It allows one to detect the energy depositions created mainly by cosmic muons passing through the detector. During analysis, the muon like events can be tagged to either ignore the subsequent activity in the inner detector, so as to to reduce the muon induced backgrounds (that are usually of a correlated type) or, conversely, to study the physics following a muon, for example to select a sample of spallation neutrons that can be used for calibration purposes. Apart from muons, the IV may be sensitive to the fast neutrons produced by the muons interacting outside the

[3]Data sheet is available on the HRC Chemicals website

detector, i.e. in the rock.

Steel shielding

To further suppress the backgrounds, 15 cm thick steel shielding surrounds the detector. The shielding not only absorbs the gamma radiation originating in the rock, but also provides roughly one interaction length for the fast neutrons, thus helping reduce, to some extent, the correlated backgrounds. The steel shielding was demagnetized to avoid negative impact on the PMTs.

Outer veto

Several layers of scintillator panels covering a large surface above the steel shielding provide redundancy and further increase the efficiency of muon tagging, also allowing to tag and track the "near-miss" muons. The outer veto in the far detector has an active area of 6.4 x 12.8 square meters (limited by the lab dimensions) and consists of 44 different plastic scintillator sub-modules arranged in two layers. One layer (36 sub-modules) is installed over the IV vessels, while the second layer (8 sub-modules) is installed on the top of the lab, approximately 2.5 meters above the IV. The vertical separation provides tracking capability [43].

2.1.2 Inner detector PMTs and light properties

Energy released in a physics event, for example during thermalization and annihilation of prompt positrons, or during Compton scattering and the photo-effect of neutron capture gammas, is transformed into light. Transformation occurs mainly by scintillation, but Čerenkov and bremsstrahlung mechanisms are involved also.

The produced light then travels in the detector eventually reaching the photo-detectors. On its way it can scatter elastically (Rayleigh scattering, sub-dominant effect in Double Chooz) or get absorbed and be lost or get re-emitted again with a softer wavelength. All these processes are modeled in the Double Chooz Geant-4 based offline software (DOGS).

Implementation of some of the processes was substantially modified from the default Geant-4 treatment to represent the effects more accurately and increase flexibility.

Many parameters affecting the above phenomena, such as refractive indices, re-emission probabilities, emission and absorption spectra, quenching constants, and many more, were measured in dedicated laboratory experiments. Where no good defaults exist, the actual detector data, in particular calibration data, can be used to constrain the parameter space as will be described later.

Scintillation in Double Chooz

In the Double Chooz liquids there are three organic chemicals that are mainly responsible for the production of light:

- PXE

  Aromatic compound (phenyl-o-xylylethane) serves as a solvent with high density ($0.988 g/cm^3$) and high flash point ($145°C$), which is advantageous from safety and self-shielding points of view. The solvent is responsible for the bulk of energy absorption. The excited molecules of PXE then transfer the energy to the fluor, either through radiative or non-radiative mechanisms. The existence of non-radiative transfer is advantageous for us, as the light absorption is high at the PXE emission peak.

- PPO

  Excited molecules of PPO (2,5-diphenyloxazole) will fluoresce to return to the ground state. Due to the Stokes shift between absorption and emission spectra, the emitted photon has a larger wavelength, so it is not very likely to be absorbed by PPO again. The emission spectrum (Figure 2.3, red curve) is still not soft enough to be in the optimal photo-cathode quantum efficiency region of the Double Chooz photo-detectors, neither is it in the region where the overall attenuation length is large enough for the light to effectively reach the photo-detectors in the first place.

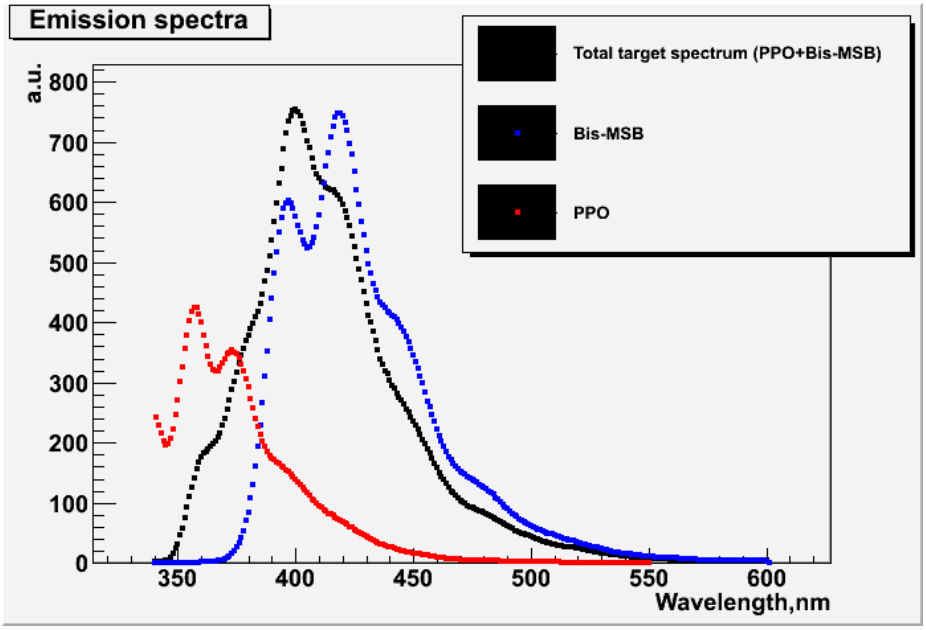

Figure 2.3: Emission spectrum of the target scintillator. Individual components are shown, as used in the DC Monte-Carlo simulation.

- bis-MSB

  Fortunately, the absorption band of 1,4-bis[2-(2-methylphenyl)ethenyl]-benzene (bis-MSB) matches well the emission profile of PPO, so the resulting spectrum is effectively shifted further, yielding peaks at 420-430 nm [50], where the photo-cathode sensitivity is maximum (Table 2.1), and the total attenuation length is of the order of meters (Figure 2.4)

Quenching effect

Not all excited scintillator molecules will fluoresce to return to the ground state. The denser the energy deposition by an incoming particle, the larger the probability of non-radiative de-excitation. The effect was quantified by Birks [46] with a phenomenological equation:

$$\frac{dS}{dr} = \frac{A\frac{dE}{dr}}{1 + kB\frac{dE}{dr}}, \tag{2.1}$$

which relates the specific fluorescence, $\frac{dS}{dr}$, to the stopping power $\frac{dE}{dr}$. A and kB are constants. The latter is called "Birks" constant, and is an important parameter in scintillator

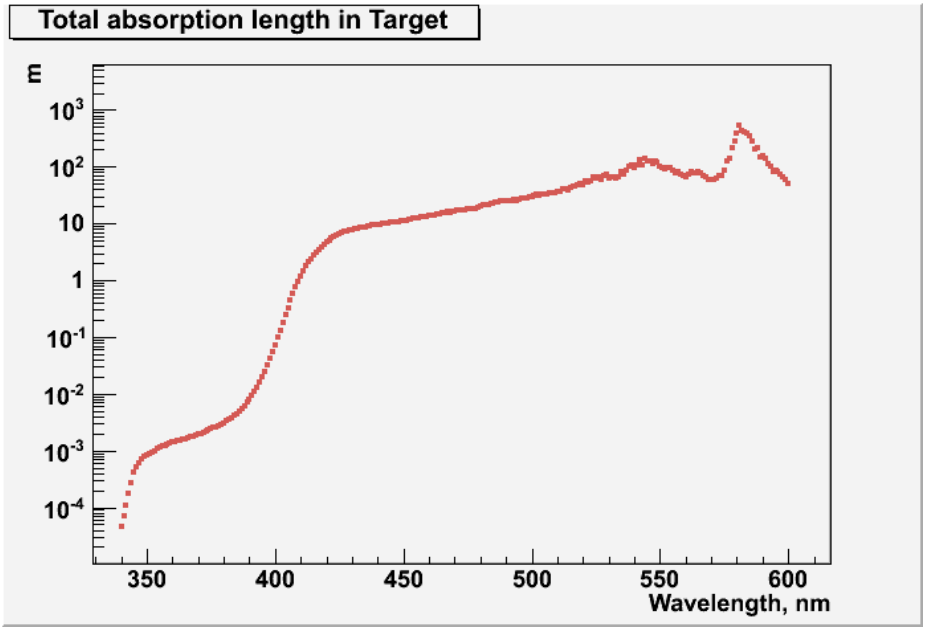

Figure 2.4: Total absorption length of the target scintillator. As calculated by DC Monte-Carlo simulation from components' extinction coefficients measured by MPIK.

experiments.

Čerenkov

Čerenkov light is emitted by a charged particle if its velocity in a medium exceeds the speed of light in the medium, c/n, where c is the speed of light in vacuum, and n is the refractive index of the medium. Emission of the Čerenkov light occurs in a cone with a half angle given by:

$$cos\theta = \frac{1}{\beta n(\lambda)}, \tag{2.2}$$

where β is the speed of the particle divided by the speed of light in vacuum. The number of Čerenkov photons emitted by a charged particle of charge z per unit length per unit wavelength λ is:

$$\frac{d^2N}{dxd\lambda} = \frac{2\pi\alpha z^2}{\lambda^2}(1 - \frac{1}{n^2(\lambda)\beta^2}), \tag{2.3}$$

where α is a fine structure constant $= \frac{e^2}{\hbar c} = \frac{1}{137}$. Hence, unlike scintillation, Čerenkov radiation is continuous. Also note that Čerenkov radiation intensifies towards shorter wavelengths making it an important contributor to the total light in the UV region.

Bremsstrahlung

Also called "braking radiation", bremsstrahlung is emitted by charged particles when they change velocity. The classic example is the X-rays produced by electrons impacting on the anode of an X-ray tube [4]. In a scintillator experiment like Double Chooz, bremsstrahlung may lead to losses in visible energy for charged particles, but in practice it is a subdominant effect, only relevant for higher energy electrons.

To detect the light produced in the inner detector, DC utilizes 390 photomultiplier tubes. The tubes were developed by Hamamatsu Photonics K.K. based on the model R7081 (Figure 2.5a). The PMTs are 10" in diameter that, combined with the total number of tubes, translates into coverage of ca. 13%. The PMTs have bi-alkali photo-cathode with a quantum efficiency (QE) value of ∼25% and wavelength dependence that matches well the emission spectrum of our wavelength shifter, bis-MSB [47] Combining estimates for QE and coverage gives a photon detection efficiency of ∼3%. Given that target and GC scintillators were initially measured to emit ca. 6500 photons per MeV of deposited energy (measured in the lab to ∼15% absolute accuracy) one expects an energy resolution better than $7\%/\sqrt{MeV}$. This estimate only includes the effects of geometry and photon statistics. In reality the resolution may be worse due to dark noise and other effects.

The PMTs are powered by positive (to reduce dark current) high voltage using CAEN S.p.A modules SY1527LC and A1535P. The values of the HV are tuned to provide a gain of $\sim 1 \cdot 10^7$. Other important characteristics of the inner detector PMTs are listed below in Table 2.1. A typical single photo-electron (SPE) charge distribution is shown in Figure 2.6. Each PMT has a mu-metal magnetic shield and sits inside the support structure (Figure 2.5b) that provides an interface with the Buffer. The location and orientation of individual PMTs were chosen with help of dedicated MC studies to provide as homogeneous a detector response as possible.

[4] Note, though, that only the continuous component of the X-rays is due to bremsstrahlung, the spikes in the spectrum are due to atomic level structure of the target material.

Unfortunately, an unexpected effect of spontaneous light emission ("light noise") was observed from the PMT bases, which was traced to luminescence from some of the resistors on the PMT base. While the collaboration considers to use a black cover for the near detector PMTs, which will prevent light noise from reaching the photo-cathode, in the first physics run with the far detector we dealt with this additional source of background by

- Identifying a subset of the inner detector PMTs that are most likely to emit the light noise and switching them off (14 out of a total 390 inner detector PMTs were chosen for the first physics run)
- Reducing the voltage on the remaining tubes to lower the probability of noise emission (the voltage was reduced so that the average gain was 5/6 of the original value)
- Using the multiplicity condition at the hardware trigger level, as the light noise is mostly registered by the PMT from which it was emitted
- Applying an analysis cut on the ratio of the maximum charge observed in a PMT in the event to the total amount of charge on all PMTs during the event (MQTQ). Other options are being investigated.

Property	Value
Wavelength region	300 nm - 650 nm
Photo cathode	Bialkali
Peak wavelength	420 nm
Diameter	253 mm
Number of dynodes	10
Glass weight	ca. 1150 g
HV to 10^7 gain	from 1150 V to 1650 V
P/V ratio	min 2.5
TTS (FWHM)	max 4.4 ns
Dark count rate	max 8 kHz
QExCE	min 20.8 %

Table 2.1: Basic characteristics of inner detector PMTs.

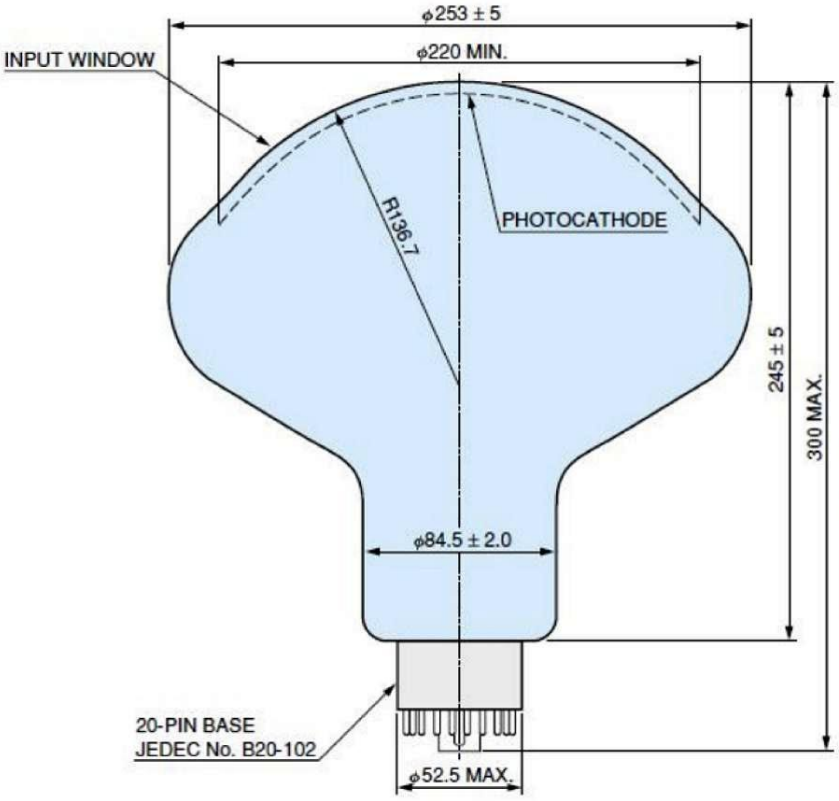

(a) R7081 schematics

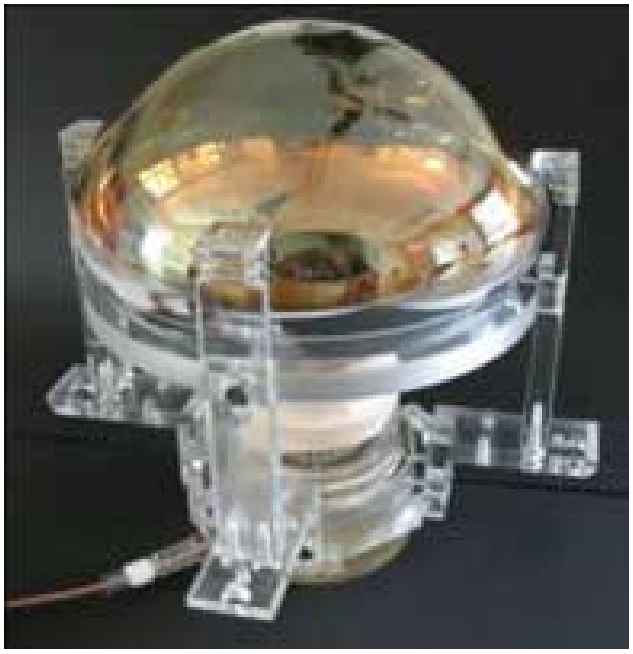

(b) Picture of the PMT inside an acrylic support structure. The mu-shield is not shown

Figure 2.5: Double Chooz inner detector PMT.

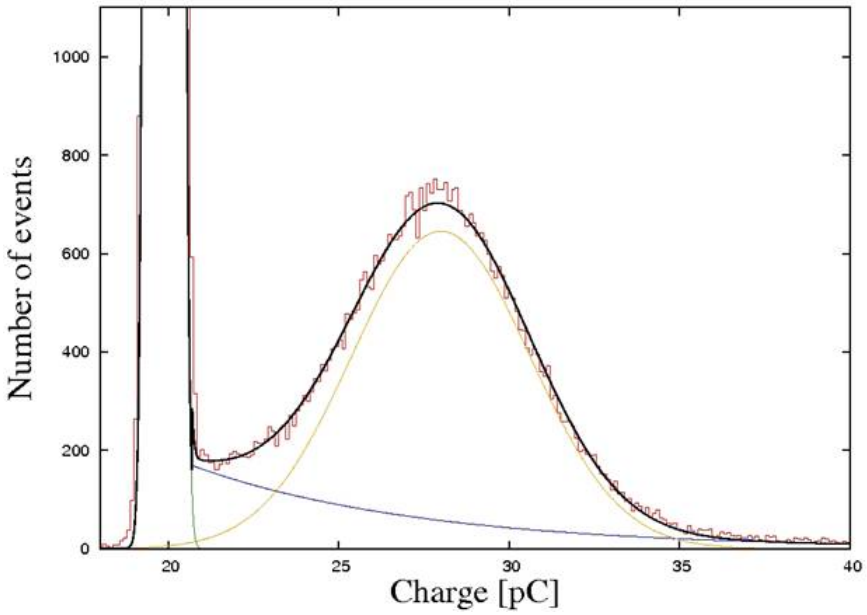

Figure 2.6: SPE charge spectrum. Red - raw data, green - Gaussian fit to pedestal. The SPE spectrum is fit by the sum of an exponential (blue) and a Gaussian (orange). Black - combined fit[48].

2.1.3 Inner detector electronics

When a photon hits a PMT's photo-cathode it has a chance of producing a photoelectron (p.e.). The high voltage applied between the cathode and the anode is divided progressively between intermediate dynodes (10 in our case), so the p.e. traveling towards anode is very likely to hit the first dynode and remove several electrons which, in turn, will go further and at each step hit a dynode removing several more electrons, creating an ever increasing flow that eventually reaches anode and produces a measurable signal.

Front End Electronics (FEE)

The signal is decoupled from the positive high voltage using a passive splitter and fed into the front end electronics that serves several important tasks:

- Summing signals from several PMTs together and stretching the summed signal for the analog trigger
- Reducing the noise and restoring the baseline
- Amplifying smaller, neutrino-like, signals to match the dynamic range of the flash analog-to-digital converters (νFADCs)
- Attenuating larger, muon-like, signals to match dynamic range of μFADCs

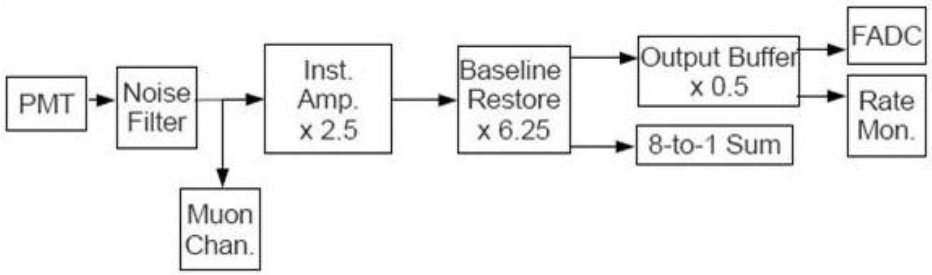

Figure 2.7: Schematic diagram of the neutrino FEE channel.

Figure 2.7 shows the circuit schematic for the neutrino channel of the Double Chooz FEE. Typical single photo-electron (SPE) signals from PMTs are 4-5mV, which is too small

to be read by the waveform digitizers. The FEE amplifies these signals by a factor of 7.8, in multiple stages [49]

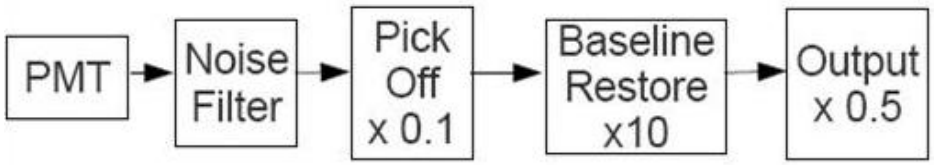

Figure 2.8: Schematic diagram of the muon FEE channel.

Figure 2.8 shows the diagram of the muon channel. It attenuates the same signal from the PMT, and outputs the signal to dedicated muon electronics. The signals go through the same baseline resoration circuitry as the signals in the neutrino channel. The muon channel has a gain of 0.55. There is a single output of this signal to the muon electronics [49]

FADCs

The output of the neutrino FEE channels is passed to dedicated CAEN VX1721 flash ADCs that were developed by CAEN SpA in collaboration with APC (AstroParticule et Cosmologie, Paris). Each module (Figure 2.9) has 8 analog input channels with a dynamic range of 500 mV (8 bit resolution). The 500 MHz sampling rate translates into 2 ns timing resolution.

Figure 2.9: CAEN VX1721

Each channel has 2MB memory split into pages. The number of pages is adjustable. In case of 1024 pages, each one can store 2048 samples for a total of 4 μs of digitized data. Until the trigger is asserted, the FADC continuously writes data in the current page (indicated by the "write index"), i.e. 2049th sample will be written as the first one of the same page. On a first clock after the trigger detection (all FADCs receive a 62.5 MHz clock from the trigger), the last ADC sample is written into the current write index and the write index is incremented so the subsequent samples are written into the next page, while the first becomes available for read-out (Figure 2.10). The earliest page that has not yet been read out through the VME bus is marked by the "read index". As long as the write index never catches up with the read index from the previous cycle, the system will have zero dead time. If the write index is just below the read index, for example if the FADC writes to the 1024th

page and the 1st page has not yet been read out, the trigger is disabled, causing a dead time [50]. Notes:

1. Only a part of the page could be read out if necessary, and during normal physics data taking of the first run the read out window is 256 ns, which is a compromise between data volume and ability to collect all light produced in an event.

2. The data read out from the FADC buffers into the VME crate controllers can optionally be processed by a software based data reducer that decides how much information to store. For the first period of data taking the data reducer is switched off.

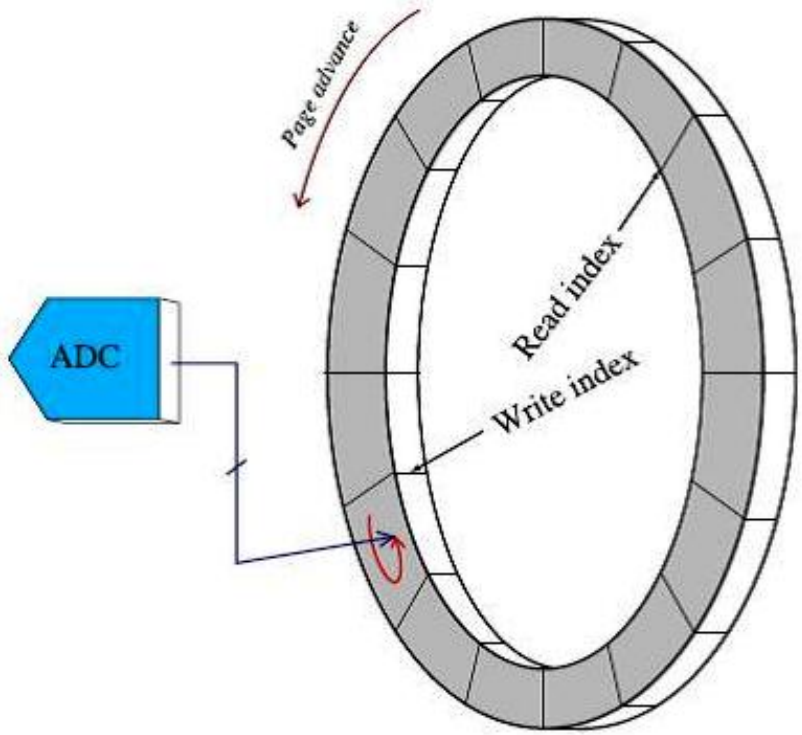

Figure 2.10: Operation of the digitizer as a FIFO [50].

Trigger

Double Chooz uses a two stage approach for the trigger system. The first level is implemented in hardware and is based on the analog sums of the PMT signals. Assertion of the hardware trigger leads to a read-out of the data. The second, software, trigger can then be used to further reduce the amount of data. The level-1 trigger is implemented on four trigger boards, two for the inner detector, one for the inner veto, and one trigger master board.

The ID trigger board takes up to 18 inputs (Figure 2.11), with each input being an analog sum of 16 PMTs formed by the FEE (each FEE board has 8 inputs that are summed, then the output of the two FEE boards are summed together to further reduce the number of trigger inputs, and finally the summed signal of each 16 channels is stretched to ensure all individual PMT signals overlap). The PMTs whose signals go into the first ID trigger board are chosen such that they are near PMTs whose signals go to the other ID trigger board, so the two boards receive information about the same part of the detector (so there are effectively two groups of the PMTs, each belonging to one of the trigger boards). This allows one to use one board to monitor performance and efficiency of the other.

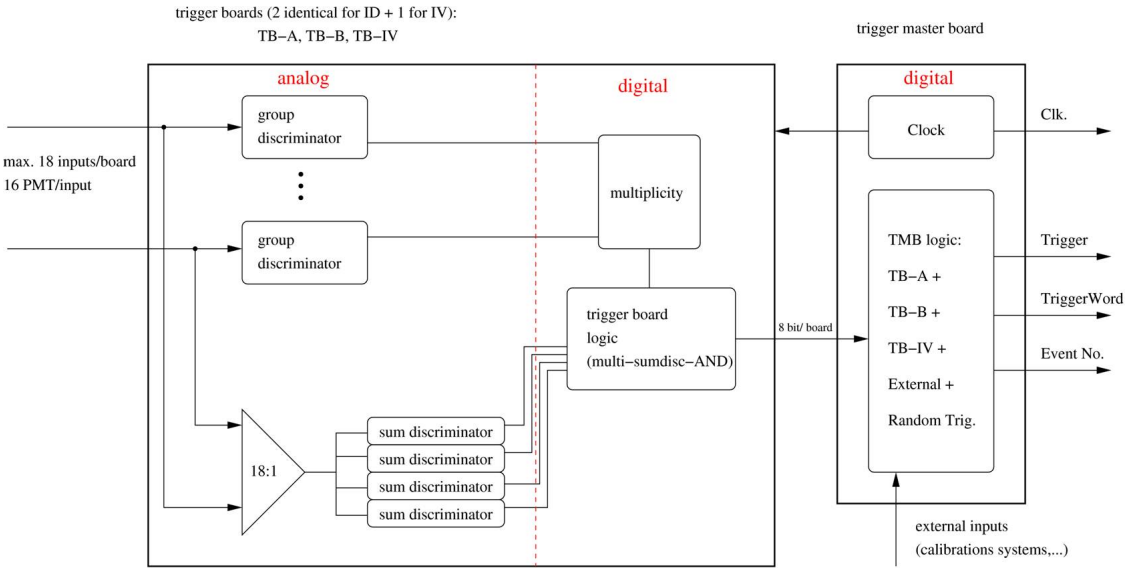

Figure 2.11: Schematic diagram of the Level-1 trigger.

All 18 inputs for a trigger board are summed together and the sum is compared with

four (programmable) discriminators which establishes four trigger thresholds. The schematic diagram is shown in Figure 2.12

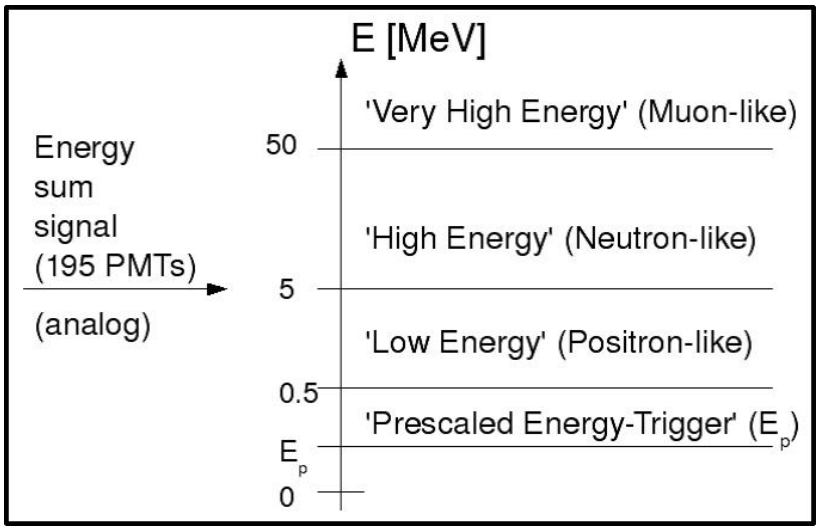

Figure 2.12: Diagram of the threshold levels. The levels are established by the trigger board programmable discriminators [51].

The four trigger thresholds are:

- Prescaled

  Prescaling means that the system triggers only once every N events that satisfy the threshold. That allows to probe the lowest energy region where the event rate is high and could not be otherwise sustained. The prescale trigger is important, for example, for studies of trigger efficiency and low energy part of the background. The scaling factor of 1000 is used now.

- Low ("Neutrino-like")

  This is a normal neutrino physics threshold and is set to be below the minimum positron signal of 1.022 MeV.

- High ("Neutron-like")

  This threshold is set to be below the energy released in the gamma cascade following neutron capture on Gd of 8 MeV allowing one to trigger on a neutron.

- Very High ("Muon-like")

  This is the highest energy threshold and is set to be only exceeded by a cosmic muon.

Apart from that, each input channel (taking signals from 16 PMTs) is divided into two separate signal lines, high and low group thresholds, to allow for a trigger condition based on multiplicity, which helps to reduce impact of noisy individual PMTs. The six threshold levels used in the first data taking period are listed in Table 2.2.

The trigger board logic unit contains eight programmable lines based on AND and OR operations and their result is encoded in a 8 bit trigger-word passed to the trigger master board. The status of the logic lines defines the inner detector trigger conditions listed in the Table 2.3

Threshold	Value (∼MeV)
Prescaled	0.2
"Neutrino-like"	0.35
"Neutron-like"	5
"Muon-like"	50
Group threshold low	0.25 (70% of "Neutrino"-like)
Group threshold high	0.25 (70% of "Neutrino"-like)

Table 2.2: Trigger discriminator thresholds for the inner detector [52].

For now, the high group threshold is not used for any trigger condition, so its value is kept at the same value as the low one, so the stability of the threshold could be monitored by comparing rates of the two.

logic line	event type	condition
0	ID rescaled event	prescaled threshold active
1	ID neutrino-like event	neutrino-like threshold active and multiplicity ≥ 2
2	ID neutron-like event	neutron-like threshold active
3	ID muon-like event	muon-like threshold active
4-7	not used	

Table 2.3: Inner detector trigger conditions [52].

The trigger master board receives trigger-words from each of the three trigger boards. In addition to that, seven more external (digital) channels are connected to it:

1. ID LED trigger
2. IV LED trigger
3. Tagged calibration source trigger
4. 470 nm laser trigger
5. 365 nm laser trigger
6. Dead-time Monitor

   The dead-time monitor produces two triggers every second, asynchronous to the clock, separated by $\sim$2 μs.
7. Outer veto

2.1.4 Calibration systems and sources

When both far and near detectors will be operational, the dominant source of systematic uncertainty will be the differences in detector responses between the two detectors (energy scales and efficiencies of selection cuts). Even in the far only phase it is important to make sure the detector related uncertainties are understood well enough not to contribute substantially to the overall error budget. To that end, several dedicated embedded and deployable calibration systems were developed. They are described below, with particular attention given to the wire source deployment system and untagged radioactive sources.

2.1.4.1 Untagged sources

The determination of efficiency and energy scale is possible with untagged neutron and gamma sources designed and fabricated for Double Chooz at the University of Alabama[5].

The sources are very small, so as to reduce absorption of emitted radiation and shadowing of the light by the materials of the deployment system and the capsule itself. In fact, the AmBe source may be one of the smallest composite neutron sources available. Fabrication of the AmBe sources is described in detail in appendix A.

The same source can be used in all active regions of both detectors to allow cross-calibration, The source design provides two levels of encapsulation to increase reliability of activity containment and interface with the deployment systems. The drawing of the outer encapsulation is presented on Figure 2.13, along with the picture of the AmBe source. The components of the outer encapsulation are fabricated to tight tolerances and high quality at a micro-machining shop.[6]

Inner encapsulation for all sources but AmBe is made of stainless steel SS304. The capsule containing radioactive material is closed with M0.6 screw which is then welded shut

[5]In particular, the author's contribution is the design of the inner and outer encapsulation for the untagged sources and the interface between the sources and the guide tube wire driver, as well as fabrication of AmBe neutron source.

[6]http://www.medicalmicromachining.net/index.asp

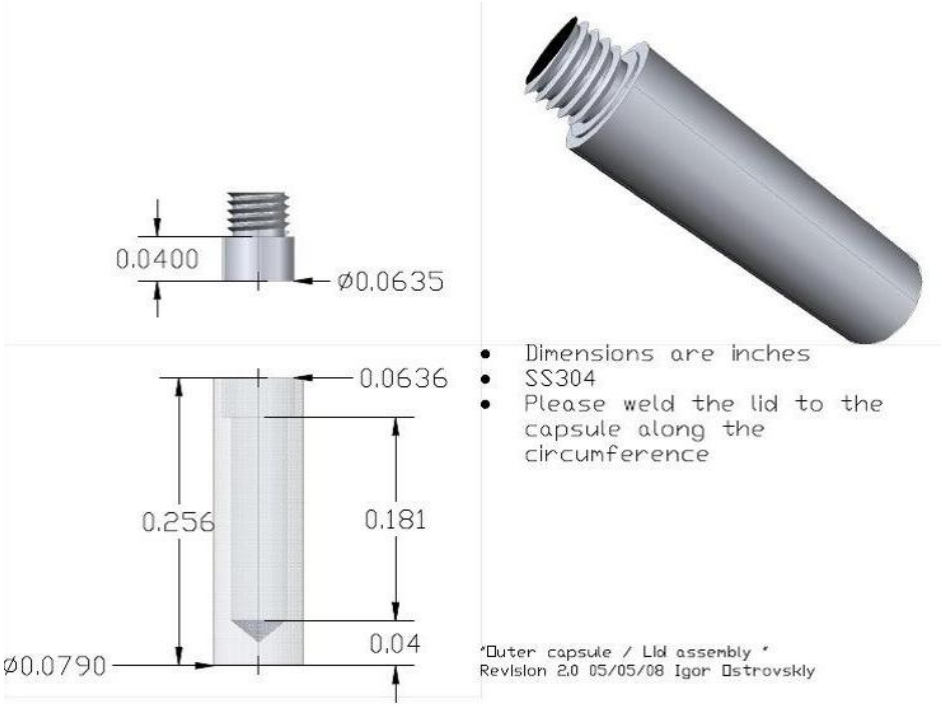

(a) Outer capsule and lid assembly

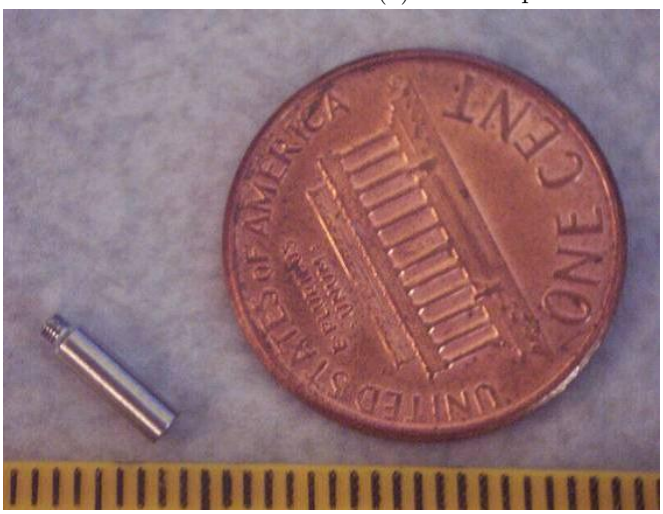

(b) AmBe source next to a penny

(c) AmBe source inner capsule (tungsten)

Figure 2.13: Double Chooz untagged source. Ruler notches are mm.

by electron beam welding, just like the outer encapsulation. The inner capsule for the AmBe sources is made of tungsten, to provide an order of magnitude decrease in the rate of 59.5 keV gammas, and is glued with epoxy adhesive.

After the outer capsule is welded, all sources are leak tested in accordance with ISO 9978 by soaking the sources in nitric acid solution (typically, 5%, or ≈1M) at elevated temperature for several days. The soak liquid is then counted with a HPGe spectrometer to establish limits on possible gamma activity released by the source. Typically, limits on the order of few mBq at 90% C.L. can be obtained for isotopes with prominent gamma lines, such as 663 keV from Cs-137, 1173 keV and 1333 keV from Co-60. Slightly weaker but still satisfactory limits are expected for Ge-68 (511 keV radiation is also produced by pair-production associated with cosmic muons, hence the background in this region can be higher, depending on the existence/performance of a muon veto) and for Am-241, whose lower energy gamma is in the region where the background of the germanium detectors are higher, while their efficiency is relatively lower and more uncertain.

Due to the absence of prominent mono-energetic gamma lines from Cf-252 it is difficult to establish a tight limit using gamma spectroscopy for this isotope. At the same time, a much smaller amount of activity released in the sensitive region of the detector can be tolerated in this case, due to the correlated signature of multiple neutron emission - a 100 mBq of Cf-252 leaked into target volume translates into ≈12 events/day, or 20% background. To improve the limit on Cf-252 activity contained in the soak solution an alpha detector set-up was put together and successfully used, as described in the appendix B.

The following sources were made at the University of Alabama:

- Am-Be

  Am-241 emits an alpha particle that can interact with a Be-9 nucleus to produce C-13 in an excited state, which de-excites by neutron emission. The energy spectrum of AmBe neutrons extends up to, approximately, 11 MeV, and has an average of, approximately, 4 MeV. In roughly 60% of the cases, the neutron emission will leave the C-12 nucleus

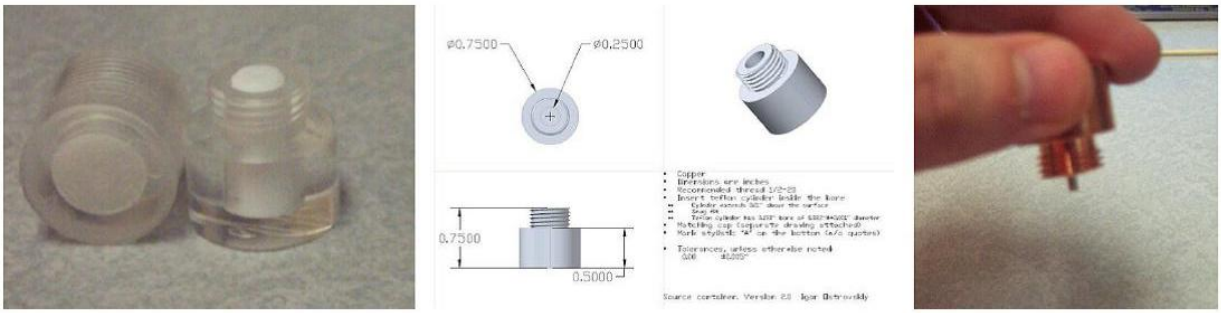

Figure 2.14: Storage containers for untagged sources.

in its first excited state, which will then de-excite by a single 4.43 MeV gamma. The emission of a mono-energetic gamma following a neutron is advantageous as it allows one to, essentially, "tag" the neutron emission and use the source to determine the absolute neutron efficiency. It might also be possible to use the gamma for energy calibration, though one would have to deal with significant distortions of the peak position and width caused by the neutron depositing its kinetic energy through recoil protons.

- Ge-68

  Ge-68 decays by electron capture to Ga-68, which β^+-decays to stable Zn-68 (in ca. 3% of cases, there is a 1.077 MeV gamma emission from an excited state of Zn-68). The annihilation gammas from this source correspond to the minimum prompt signal for IBD reaction, thus allowing to calibrate the efficiency of the trigger threshold at different positions to make sure all IBD positrons are accepted.

- Cf-252

  Cf-252 emits several neutrons with average multiplicity of 3.76, known to ≈0.3 %. It can be used to study neutron efficiency at different positions, in particular close to the boundary between target and gamma catcher. The neutron energy spectrum of Cf-252 is softer than the one of the AmBe source and has an average of approximately 2.1 MeV.

- Cs-137

  Cs-137 emits 0.662 MeV mono-energetic gamma that can be used to calibrate scintillator energy scale

- Co-60

  Co-60 emits 1.17 and 1.33 MeV gammas

When not in use, the sources are stored in individual containers (Figure 2.14) in a dedicated safe outside of the lab.

The outer encapsulation of the sources contains a threaded part that allows attachment of the same source to different calibration systems. The thread is a M1.4x0.2 right-handed fine thread manufactured using a milling technique for improved quality. A matching source connector that provides the interface between sources and the calibration systems is shown on Figure 2.15.

As can be seen from Figure 2.15a, the connector has an additional outer thread that is used to screw the so called protective cap on top of the source, as an additional level of protection against loosing the source inside the deployment system. The cap uses left-handed M2.5x0.45 thread. The fully assembled connector with the cap on is shown in Figure 2.16.

To test the reliability of the threaded connection the following exercise was performed: A source was screwed and un-screwed from the connector by four different people for a total of 1000 times. The threaded connection become looser due to normal wear but no other thread damage was observed. The source was then attached to the full-scale prototype of the deployment system and successfully deployed without the protective cap on.

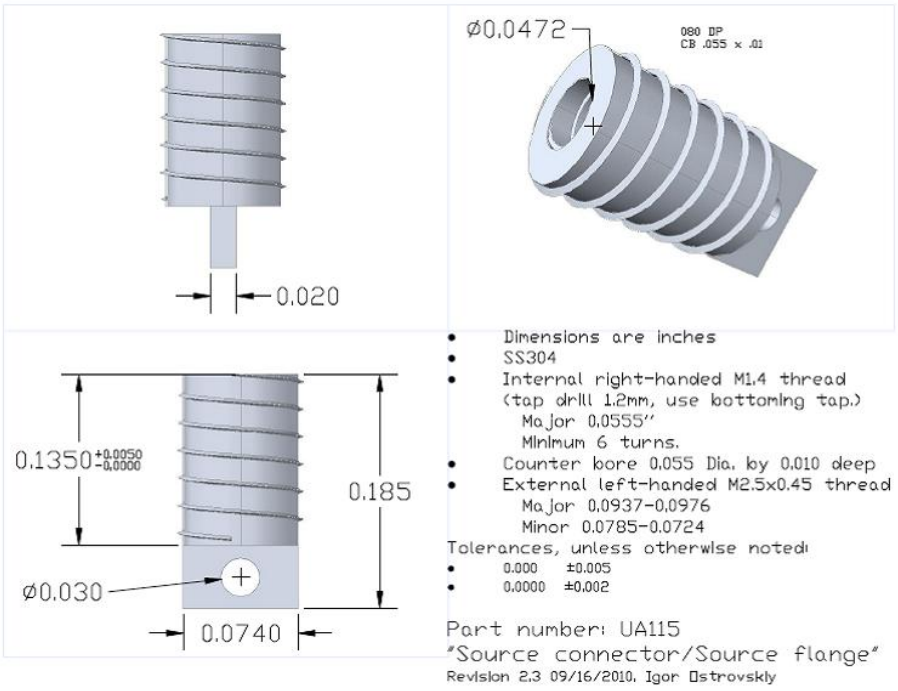

(a) Source connector drawings

(b) Picture of a source attached to the connector

Figure 2.15: Source connector.

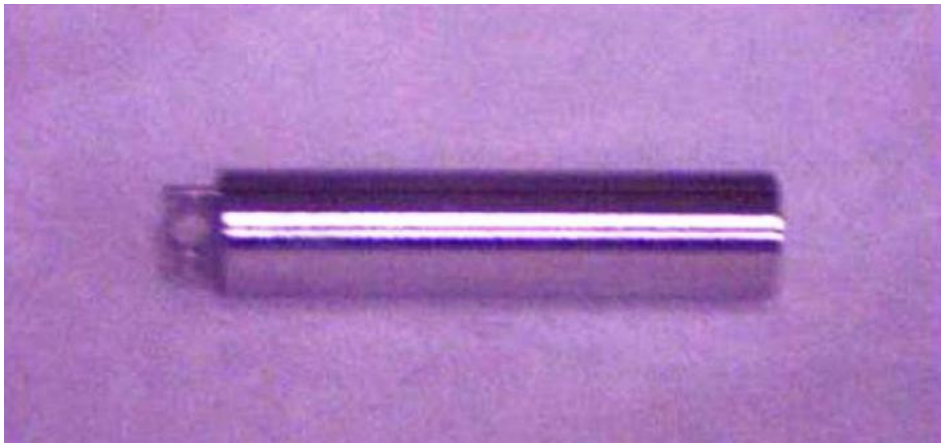

Figure 2.16: Protective cap attached to the source connector.

Other calibration tools

- Tagged Cf-252 source[7]

  A tagged Cf-252 source was successfully used in the CHOOZ experiment to measure absolute neutron efficiency to $\approx 0.6\%$ [53] It is foreseen to deploy a similar device in Double Chooz, although the source was not made in time for the first physics run.

  The CHOOZ source consisted of an ionization chamber with Cf-252 isotope deposited on the external surface of the cylindrical anode. The chamber was filled with Argon (1 atm) and few percent of carbon dioxide. Use of the ionization chamber allowed to detect fission fragments and easily discriminate against alpha decays of Cf-252 that emit roughly 30 times less energy. The signal from the chamber anode constituted an electronic "tag", indicating the a fission has occurred, and hence neutrons were emitted.

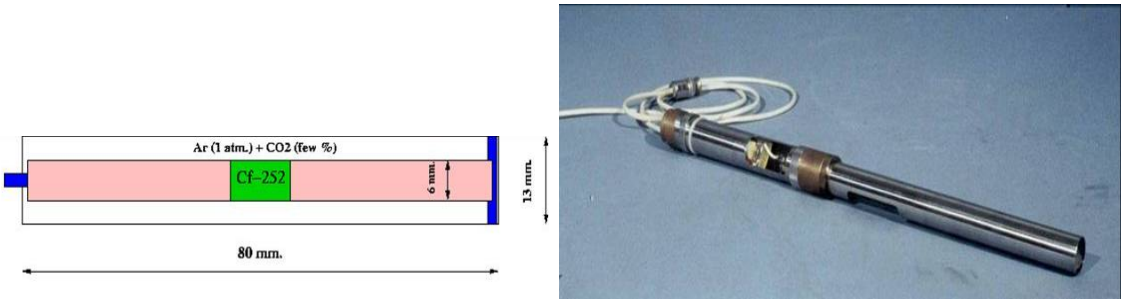

(a) tagged Cf-252 source diagram (b) tagged Cf-252 source picture

Figure 2.17: Tagged Cf-252 source [53].

- Laser diffuser ball

  Two lasers are used to calibrate the PMTs response and optical properties of Double Chooz scintillators. A 470nm blue laser is used mainly for determination of PMT time offsets and speed of light, while a 380 nm UV laser is used to obtain PMT gains and also charge likelihoods (important input for vertex reconstruction). The light produced by the laser heads is guided through the optical fiber into the diffuser ball

[7]The tagged Cf-252 source is provided by the Kurchatov Institute, Russia.

that is deployed inside the target vessel along the vertical axis. The diffuser balls are 80 mm spheres with 53mm long necks made of 4 mm (for blue laser ball) and 6mm (UV laser ball) thick acrylic [54] . The diffuser ball to be used with the UV laser is filled with the Double Chooz target scintillator mixture, while the one to be used with the blue laser is filled with GE silicon sealant gel. The size and the diffusing material are chosen to achieve better than 5% anisotropy of light, which is important for reliable measurements of time offsets (the size is also constrained by the available clearance of the target chimney)

Figure 2.18: Blue laser diffuser ball [54].

- Central LED flasher

  A battery powdered hermetically sealed blue LED was deployed before the filling at the center and along the Z axis of the empty target vessel to calibrate PMT time offsets independently of the speed of light, as the latter is accurately known for the air. The flasher automatically cycles through eight light levels, putting out 128 pulses at each level before moving to the next one [68].

  The data were used to extract time offsets to about 0.5 ns precision, but, unfortunately, a problem was discovered that causes the time offsets to fluctuate up to 8 ns upon reboot of the read-out processors. Before the official physics run was started, the problem was resolved, but the constants extracted from the dry deployment of the central LED could no longer be relied upon.

Figure 2.19: Central LED flasher [68].

- Inner detector light injection system (IDLI)

  The IDLI is an embedded calibration system that is used daily to inject a known amount of light in the detector and monitor stability of the inner detector PMTs gain and timing. There are three LEDs that emit light of different wavelengths: 385 nm, which will get absorbed by the GC scintillator and then re-emitted, 425 nm, which can be partially absorbed by either GC or TV scintillators, and 475 nm, that will mostly pass directly through both scintillators to the PMTs.

  The light from the LEDs is transported inside the detector either through polymer optical fibers terminating in a diffuser, spreading the light over the angle of about 22 degrees, or using quartz fibers providing a more narrow (about 7 degrees) so called "pencil" beam. While diffused light is important for PMT linearity measurements and general optical properties of all three inner detector liquids combined, the pencil beams are located such that different liquids can be probed independently (Figure 2.20) [56]

  There are a total of 32 diffused and 14 pencil light injection points in the Buffer. The inner veto PMTs are calibrated using a stand alone embedded inner veto light injection system (IVLI) that is similar to the IDLI, and is not described here.

To deliver deployable calibration devices inside sensitive volumes of the detector, several calibration systems exist:

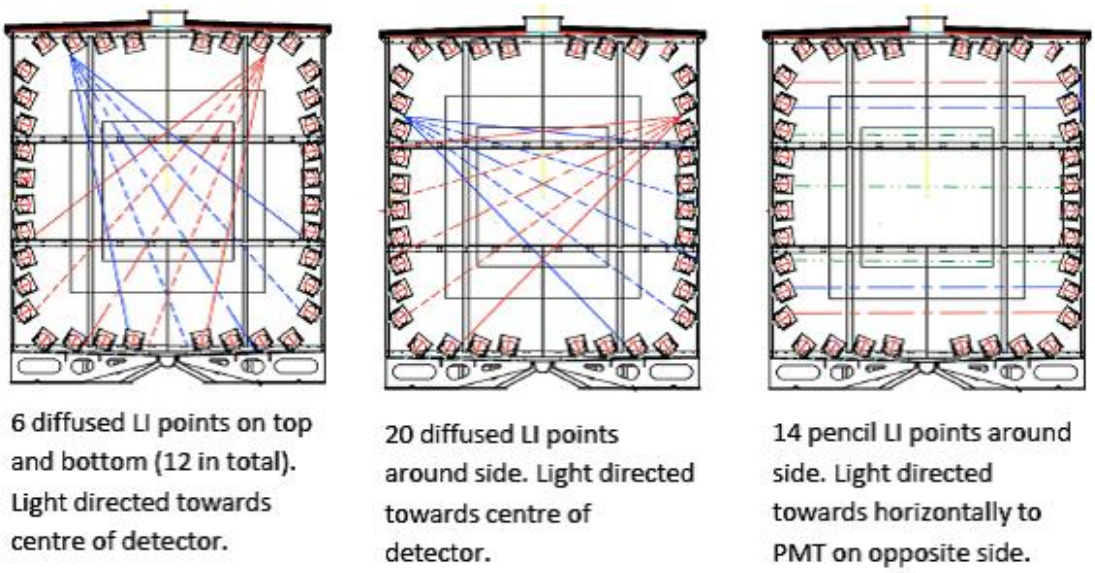

Figure 2.20: Inner detector light injection illustration [56].

Z-axis fish line

The Z-axis fish-line performs computer controlled deployments from inside a glove-box in a clean tent above the detector. The system can be used with untagged sources, the tagged Cf-252 source, and with the LED flasher and laser diffuser ball for determining gains, time offsets, etc.

The Z-axis fish-line system is comprised of a stepper motor with a driver, a deployment cable mounted on a guide pulley with independent position encoder and interchangeable spool (different for untagged sources and laser ball), and an acrylic weight to which different devices are attached through their interfaces (Figure 2.21) The system also contains a friction brake.

The default cable used in the Z-axis system is a 1/32" stranded (7x7 strands) stainless steel rope [57]. The rope is electropolished and then coated with FEP-Teflon to reduce exposure of the target scintillator to the stainless steel.

The untagged sources are attached to the weight interface using a steel source rod that has a tapered shape to minimize shadowing of light and absorption of source radiation, while still being mechanically stable.

Figure 2.21: Picture of the Z-axis fish-line system [57].

The Z-axis system is controlled via laptop using Java based software.

Articulated arm

The articulated arm will be used to deploy the untagged calibration sources off-axis, providing full volume calibration in the target. The system consists of a telescopic support rod, a pivot, and a segmented arm [58]. The source is attached to the last segment of the arm via a rod interface. During deployments the telescopic rod is extended down along the Z-axis, while the segmented arm is hold vertically, attached to the rod by a pivot. Once the pivot reaches the top of the target vessel, the segmented arm can be rotated from its vertical position up by pulling a cable.

To increase positional accuracy, a multidirectional light pulsing device (optical finder) can be incorporated as an additional segment in the arm. When deployed together with the source, it will provide a check on the position of the arm independent of the motor encoders. The optical finder consists of three LEDs whose light is reflected by the prisms to produce 3 pairs of back-to-back light pulses. Calculating the centroids of the triggered PMTs (weighted

by the charge) along the three orthogonal directions will allow to infer the optical finder's location to better than 5 mm [59]

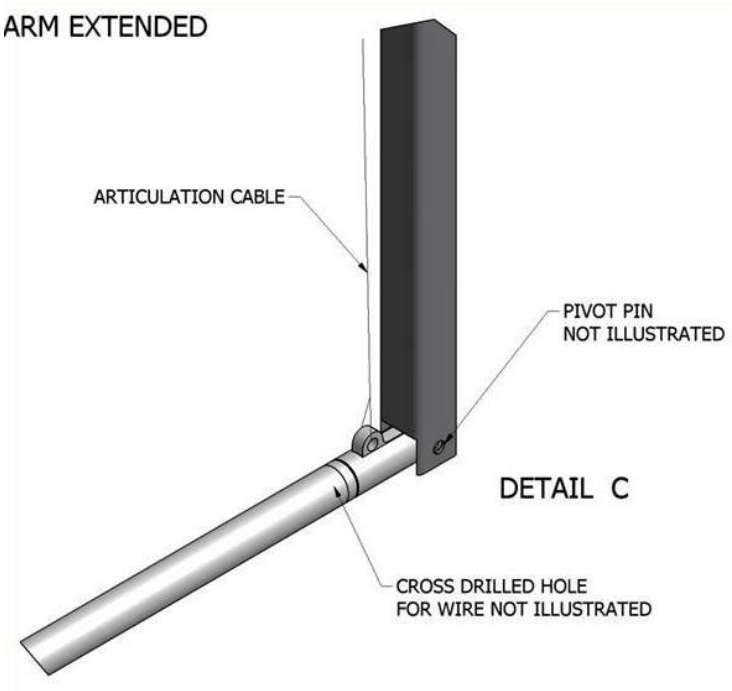

Figure 2.22: Schematic view of the articulated arm [58].

While design and testing of the articulated arm is practically completed, it was not used during the first physics run of the Double Chooz.

2.1.4.2 Gamma Catcher guide tube

The guide tube (GT) is a calibration system allowing deployment of radioactive sources inside the gamma catcher. It was designed and tested at the University of Alabama, where full scale prototypes of the tube and the path along the detector chimney were made (Figure 2.23) and extensively used to assist in design, validation, and practice of installation and operation decisions. The guide tube is located between target and gamma catcher vessels, both of which are made of a thin acrylic sheet (8 mm of target and 12 mm for GC) and are quite fragile. Integration of the guide tube with the vessels was a task that carried substantial risk to the experiment, which was addressed at all stages, from the design to fabrication to installation. Only approved components were used in the guide tube, and all GT components that are exposed to liquid scintillator were a) certified by the Saclay Nuclear Research Center (Saclay) to be chemically compatible with the GC liquid, and b) radio-assayed at the low background facilities. The first measurement was done at Oroville, USA, then the samples were sent to the deeper and more sensitive facility at LNGS, Gran Sasso. Unfortunately, the earth quake interrupted normal operations, so the samples were re-routed to the HADES underground lab near Geel, Belgium. Some of the auxillaury components, such as the wire and the capsules, were also later counted at the HPGe detector in Saclay and MPIK Heidelberg.

A appendix C contains a detailed desciption of the guide tube system and associated components.

The guide tube was assembled and successfully integrated with the actylic vessels (Figure 2.24) on November 02, 2009.

The first radioactive source deployment in Double Chooz was performed during Summer 2011 (Figure 2.25), demonstrating safe operation of the system during several days of deployments.

(a) guide tube prototype

(b) another prototype in the high-bay area

Figure 2.23: Full scale prototype of the guide tube system.

(a) Integration with the acrylic vessels

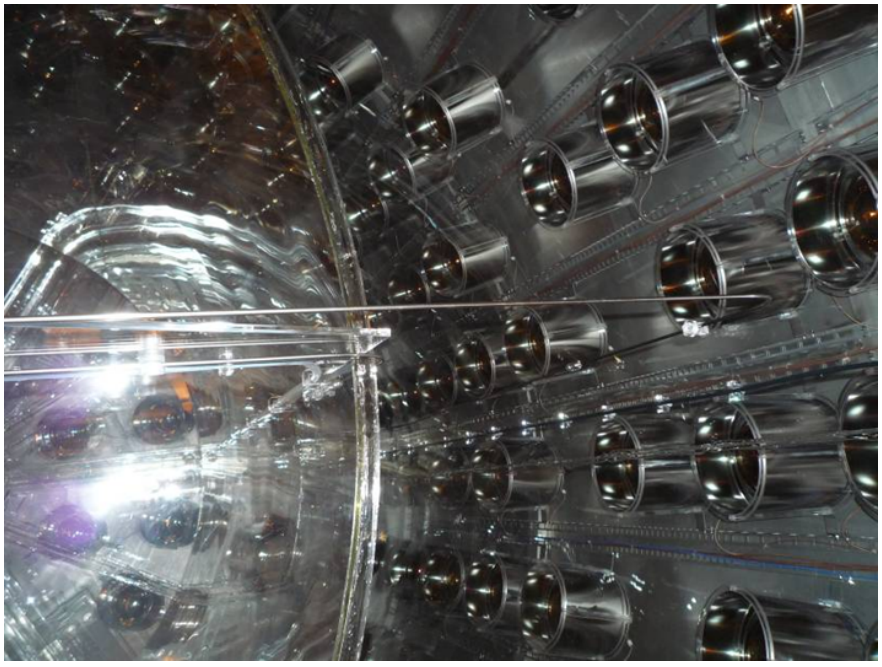

(b) Guide tube between target and GC. Rim of the TV lid clearly visible

Figure 2.24: Installation of the guide tube in the far detector. The people on the picture are I.Ostrovskiy (standing) and P.Starzynski (sitting).

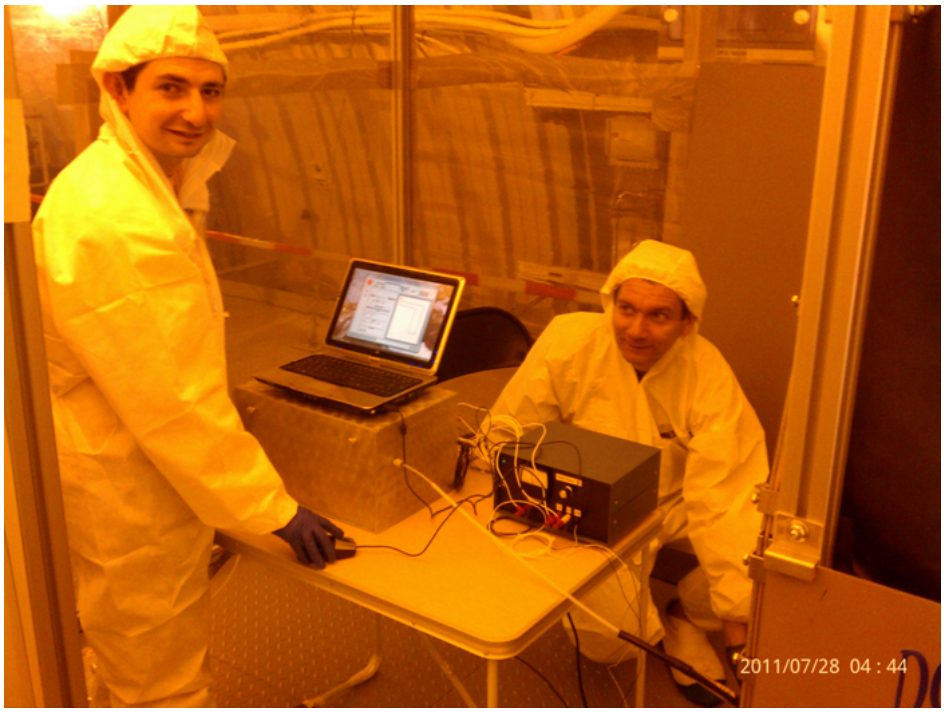

Figure 2.25: Preparations for the first source deployment. The people on the picture are I.Ostrovskiy (standing) and Z.Djurcic (sitting).

Part II

Detector Performance and Calibration

The Double Chooz far detector has started accumulating physics data on April 13, 2011. During normal data taking, several hours of physics runs are alternated with calibration runs taken with embedded light injection systems, which provide continuous monitoring of PMT gains and timing and overall stability of the detector. The physics data can be used as well to characterize detector performance and monitor important characteristics.

In the next few chapters we will derive some of the important detector parameters that had to be understood before proceeding to the final analysis. But first, we describe the event reconstruction used in Double Chooz.

Chapter 3

Data processing and event reconstruction

Upon assertion of the trigger all the waveforms, which are continuously accumulated by the flash ADC cards, are read out onto disk. These waveforms are, essentially, arrays of voltage levels spanning 256 ns (in steps of 2 ns) of the signal at each PMT at the time of the trigger. An example of the inner detector PMT waveform taken from a low energy gamma source event is shown on the Figure 3.1a. This particular waveform contains a pulse whose amplitude is characteristic of a single photoelectron.

The data files in their original binary format are automatically picked up by a processing code that converts them into the ROOT based "RAW" files that follow the format of the Double Chooz software (DOGSification process). The "RAW" files contain not only the waveforms, but also the relevant information about the trigger and the run configuration. Moreover, already during DOGSification, several routines are run that perform initial pulse reconstruction and data quality checks, and that information is stored in the "RAW" files as well. The binary and the DOGSified files are copied from the on-site computers to the Tier-1 computing facility at Lyon, France, through a high-speed internet connection. The disks on the on-site computers are continuously cleaned up from the old files by an automated

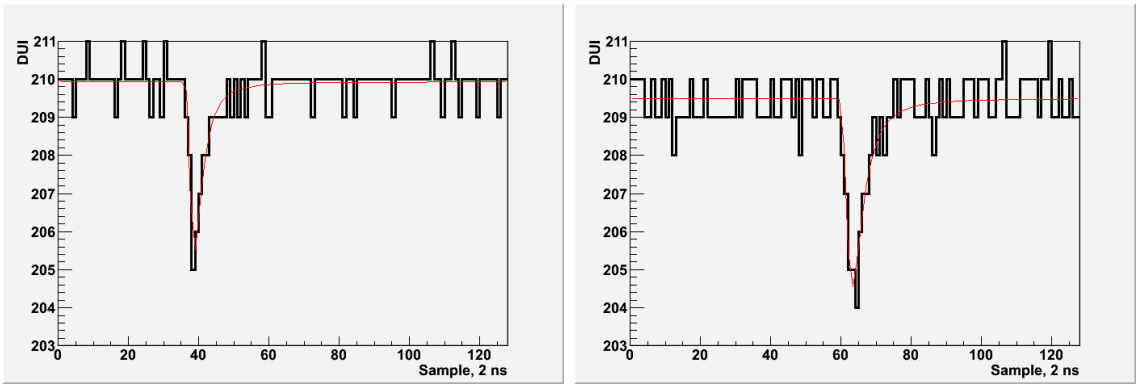

(a) Data (b) MC

Figure 3.1: The waveform of a single photo-electron in the data and MC. The pulses obtained from a low energy gamma source data/MC at the detector center. The spe shape is quite well described by the Landau distribution (the fit to the baseline+Landau is shown in red). DUI, or digital unit of intensity, is equivalent to 78 microA.

script, to prevent disk overfills. The DOGSified data is further processed by a series of reconstruction algorithms, the most important ones being RecoPulse, and RecoBAMA. This step constitutes the so called "common trunk" processing, or CT, that provides the basis for the multiple possibilities of higher level analyzes. The CT data files are permanently stored on tape at the Lyon cluster. A MySQL database contains information about location, processing status, description of the data, and other relevant information for each file.

Note that the Monte Carlo side of the Double Chooz software follows essentially the same path. After the particle interactions, light production and propagation to the PMTs are modeled by the Geant-4 based code, the read-out simulation (RoSS) steps in and produces the waveforms in the same format of RAW files as for the data. The CT processing is then applied to reconstruct the simulated waveforms, again using the same algorithms. Figure 3.1b shows a single photo-electron pulse extracted from the simulation of the low energy gamma source.

3.1 RecoPulse

The RecoPulse algorithm that is run as a part of the CT is a highly tunable framework that supports different types of pulse reconstruction. The RecoPulse performs the three following functions:

- Baseline subtraction
- Pulse charge calculation
- Calculation of pulse timing characteristics

The baseline[1] can be estimated either from an actual physics signal by looking at the first few samples in the beginning of the readout window (floating baseline), or by looking at the whole window in a special externally triggered event (external baseline). Based on the experience with the first data, both methods were found to have certain disadvantages. The external baseline method, while normally more accurate, as expected, suffers from bias if the external trigger event occurred after a large, muon-like, event. On the other hand, the floating baseline method is more stable against baseline fluctuations after a muon, but depends on the position and shape of the pulse, and is not valid for pulses that are broad and occur at the beginning of the readout window. To get the best of the two approaches, a hybrid scheme is used for the first physics run. Namely, numbers for both methods are computed, and if the RMS of the floating baseline is found to be more than 0.5 DUQ[2] larger than the RMS of the external baseline, the former one is considered unreliable, and the external baseline is used. Note that having the floating baseline as a default avoids reliance on a hard-coded definition of a muon-like signal. The first 8 samples (16 ns) of the readout window are used for the floating baseline estimation in the first physics run.

For the pulse charge reconstruction the following method is used by default: The algorithm calculates the pulse integral in a fixed-size time window, then "slides" the window to

[1]The term "baseline" is used inter-changeably with the term "pedestal" in Double Chooz experiment.
[2]digital unit of charge

analyze another part of the waveform. The window position that has the maximum integral is assumed to contain the pulse. In principle, the algorithm then reiterates and searches for possible other pulses in the waveform, until the the maximum integral in a window falls below the threshold. The threshold is defined as follows [63]:

$$Q_{min} = n_\sigma \cdot \sigma_{ped} \cdot \sqrt{WS}, \tag{3.1}$$

where WS is the analysis time window, in terms of number of samples, n_σ is the number of the pedestal RMS, σ_{ped}[3]. However, the default size of the sliding window was set to 112 ns, which is almost half of the full readout window, reducing the capability of individual pulse reconstruction. The large size of the sliding window was chosen due to observed long tails in the data pulses, so as to reduce the charge losses and improve the linearity of charge reconstruction.

For each found pulse, the RecoPulse computes the following timing characteristics:

- Start time

  By default, the start time corresponds to 30% of the maximum amplitude before it is reached. Other definitions, e.g. time when pulse goes above user-defined threshold, can be selected

- End time

  The end time corresponds to 20% of the maximum amplitude, after it was reached.

- Maximum amplitude time

  Time corresponding to maximum of the pulse

- Rise time

  This time is defined as the difference between the maximum amplitude and start times

[3]By default, a 5 sigma deviation is used as the threshold.

- Fall time

  The fall time is defined as the difference between the end and maximum amplitude times

In addition to the calculated raw quantities of pulse time and charge, the RecoPulse may apply a time offset correction and gain calibration, if the calibration constants are available either in MySQL database, or in ASCII file.

3.2 RecoBAMA

It is obviously advantageous to know the localization of the energy deposition inside the detector. The event' vertex can be inferred from the hit time and/or charge distributions among the PMTs (both available after RecoPulse). The basic idea behind many vertex reconstructions is simple - a point-like energy deposition in a scintillator detector may be considered as a source of isotropic light propagating towards PMTs at the speed of light in the medium c_n and delivering a certain amount of charge q at time t on the i-th PMT. In the ideal case, a light flash occurring at the center of an empty spherical detector will produce a uniform distribution of PMT hits, each carrying the same charge at the same time on all PMTs. While an event shifted off-center will deliver more charge, and sooner, to some PMTs than to others. One can then quantify the expectation to observe a hit of a certain charge at a certain time for each PMT as function of the event location and compare the expectation with the observed distribution of hits. By performing a minimization between the expected and observed hit distributions one can estimate the location of the vertex. In our ideal case, the likelihood of observing the charge q is simply proportional to the solid angle subtended by the PMT to the vertex location, while the timing of the pulse is directly proportional to the distance between the vertex and the PMT.

In the reality, however, the situation is much more complicated. First of all, only an average number of emitted photons is known, resulting in the fluctuation of the detected

number of photons following Poisson statistics. Moreover, the pulses from individual PMTs may take different time to propagate through the different lengths cables and internal delays in the electronic circuits. This creates a need for the so called "T0 calibration", which would equalize the time offsets of different PMTs and correct the raw pulse time reported by the RecoPulse. Second of all, the time profile of the light emission by a scintillator is not a delta-function, and has a sharp rise and then decays exponentially with one or more time constants. The light propagation itself suffers from exponential attenuation, reflections or scattering at the boundaries between different media inside the detector. To make things worse, the speed of light is wave-length dependent and may generally differ in different media. Third of all, individual optical photons hitting the PMT photocathodes are not guaranteed to produce a photoelectron. The probability may vary from PMT to PMT, and also depends on the angle of incidence and particular location on the cathode surface. Furthermore, the physics of the PMT is not trivial either. For example, electrons propagating from the photocathode to the dynodes may either miss the first dynode, and result in pulse arriving earlier than usual (prepulse), or back-scatter and arrive later (late pulse). Finally, there is always smearing due to the intrinsic transit time spread, the slewing effect (dependence of pulse time on the amount of charge), etc.

It is how the individual approaches deal with these complications that determines the performance of the vertex reconstruction. The Double Chooz software contains several packages that implement different types of vertex reconstruction. The de facto standard one is the RecoBAMA[4]. Instead of complicating the analytical expression for the expected time and charge distribution (likelihoods), for example by adding terms describing exponential attenuation of light by the media, or using Poisson statistics to account for randomness of the expected number of p.e., RecoBAMA uses look-up tables[5] for the expected time and charge likelihoods, and for the effective solid angle. Clearly, the best way to populate the look-up tables is by using the data from a well characterized light source of varied intensity

[4]This algorithm was developed by I.Stancu, now at the University of Alabama.
[5]One table for all PMTs is used currently.

located at various positions. However, if the Monte Carlo simulation does a decent jobs at describing the detector geometry, light production and propagation, the PMT physics etc., the tables based on the simulation may provide a reasonable compromise. In fact, for the first run the CT version of RecoBAMA was relying on the look-up tables obtained with the DOGS simulation. Examples of the time and charge likelihoods are shown in Figure 3.2 and Figure 3.3.

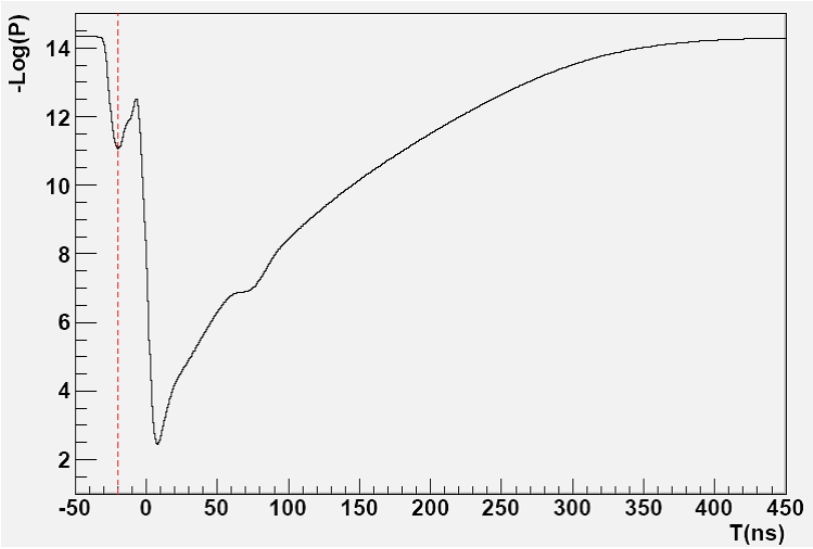

Figure 3.2: Example of the time likelihood used in RecoBAMA. Negative log-likelihood value of observing a pulse at a given time is given as a function of time. The red dashed vertical line shows the position of the prepulse. The function corresponds to the predicted charge of 1 p.e. and is generated using Test-07 version of DOGS [69].

The performance of the reconstruction algorithm can be evaluated by plotting the distribution of the reconstructed vertex position from a point-like source located at a known position inside the detector. Figure 3.4 shows the vertex distribution of Co-60 events at the detector center.

A typical spread in the reconstructed position obtained with out-of-the-box RecoBAMA is about 12 cm for a Co-60 source[6] (for each dimension). There are indications of systematic biases on the order of cm between reconstructed and deployment positions (Figure 3.5). At this point the source of the bias is not clear. Further tuning of the code, in particular speed

[6]The spread is estimated as a sigma of a Gaussian fit to the vertex distribution. Note that the energy deposition by gammas is not point like, which is likely to contribute to the observed spread.

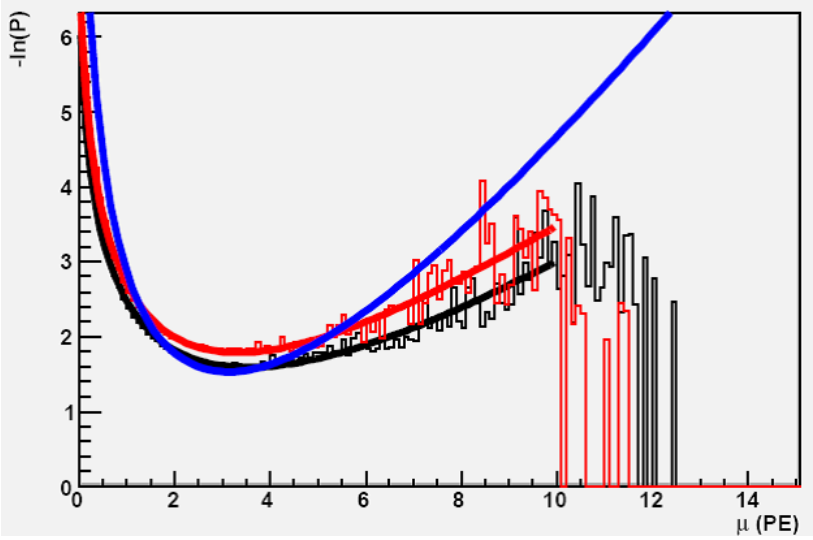

Figure 3.3: Example of the charge likelihood used in RecoBAMA. Negative log-likelihood value of observing a pulse of a given charge is given as a function of charge. The functions correspond to the mean charge of 3-3.1 p.e. The blue curve shows the function produced with the MC. The black curve shows the function extracted from the Ge-68 calibration source data using the default RecoPulse. The red curve is the same as black, only using older version of RecoPulse, which had shorter integration window. The three functions are similar [70].

of light constants, data-driven likelihood tables, is expected to improve the performance even further.

In the next chapter we concentrate on the rate and spectra of singles events and accidental coincidences in the far detector, because the author of this thesis contributed this analysis to the US cluster's part of the collaboration-wide comparison.

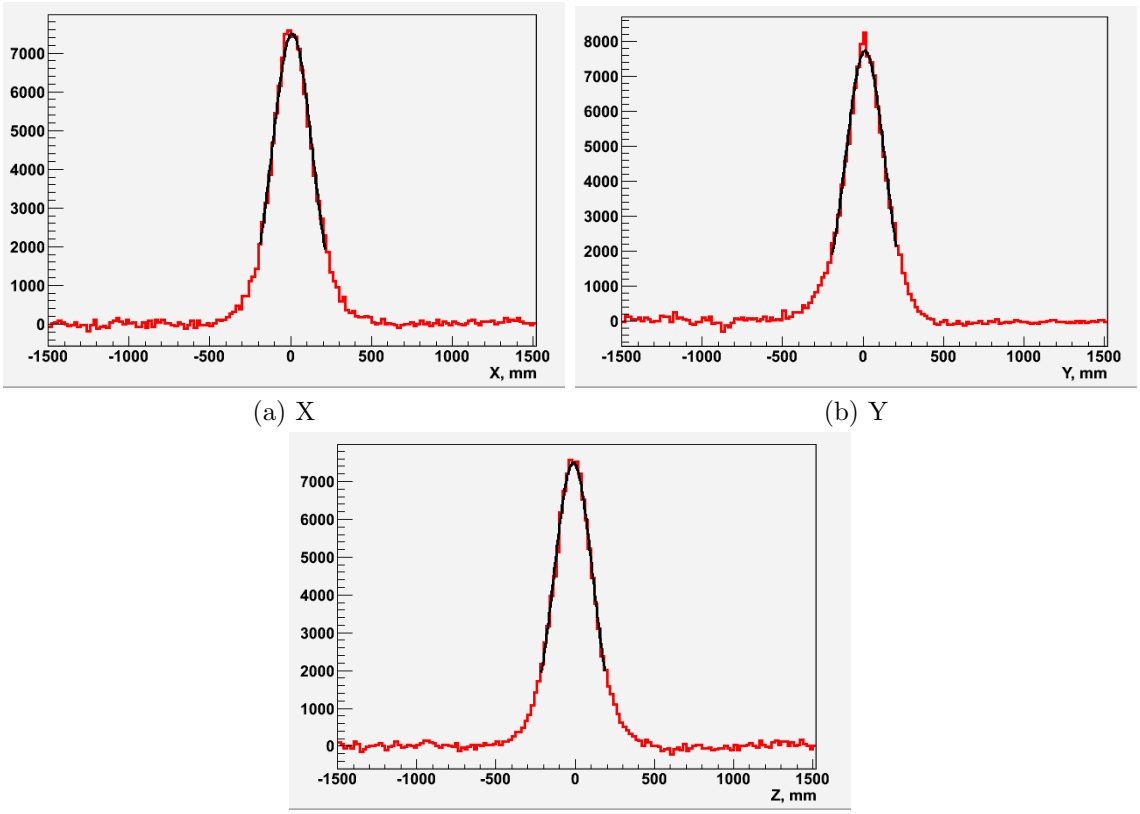

(a) X (b) Y

(c) Z

Figure 3.4: The vertex distribution for Co-60 events. Source was positioned at the detector center. The histograms are background-subtracted. The black line shows a Gaussian fit, with a typical width of 12-13 cm.

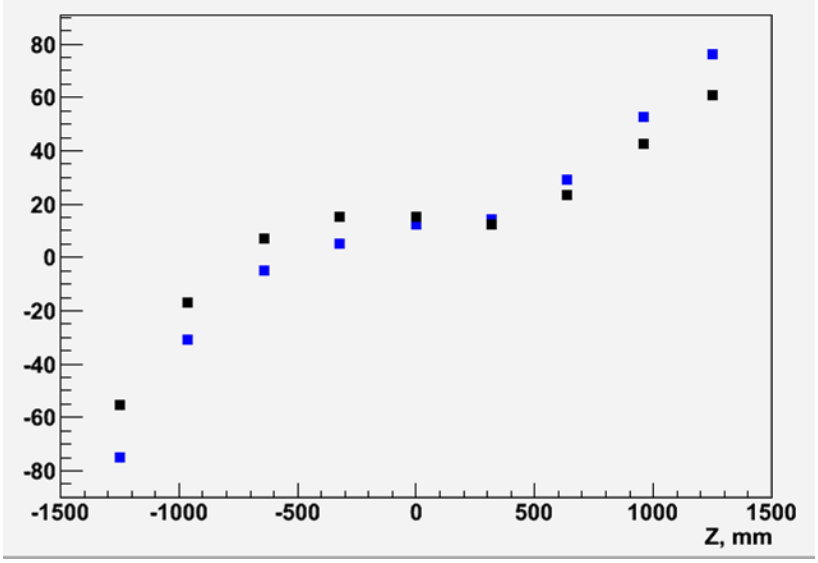

Figure 3.5: The difference between expected and reconstructed Z positions. The difference, in mm, is shown as a function of Z for Co-60 (black) and Cs-137 (blue) sources.

Chapter 4

Characteristics of single events and accidental coincidences in the far detector

The singles background consist of events that trigger the detector randomly, as opposite to the correlated events, e.g. IBD coincidence. The main source of singles is natural radioactivity contained in the detector materials and liquids, and in the rock of the cavern. Single events can form a random coincidence, mimicking an IBD event, and thus need to be understood and characterized. A singles rate which is too high may prevent a reactor neutrino experiment from maintaining the trigger threshold at a level low enough to accept all prompt positrons of the IBD reaction, hence introducing an energy dependent inefficiency. Furthermore, the singles spectrum may contain structures due to radiation of known isotopes with well defined energies, and therefore may be used as a free source of natural calibration. Finally, stability of the singles spectrum and rates can also be indicative of the detector performance.[1]

[1]Provided the associated radio-isotope concentrations are constant in time, which is practically true for such isotope as K-40 (1.29 billion years half-life).

4.1 Singles

The analysis of the singles rates was performed separately in the energy window corresponding to the prompt and delayed part of the IBD event. A preliminary rough energy scale was agreed upon to facilitate this analysis and to allow for inter-cluster comparisons. The conversion from total reconstructed charge to an energy-like variable, *MeV, was performed by a single factor derived from the position of the hydrogen capture peak, associated with captures of neutrons produced by the spallating muons passing through or near the detector. A prompt energy window, corresponding to the energy range of positron events, was defined between 0.7 to 12 *MeV. A delayed energy window, corresponding to captures of IBD neutrons on Gd isotopes, was defined as 6 to 12 *MeV.

To separate singles events from other sources of backgrounds the following cuts were applied:

1. light noise cut

   To exclude events that are likely to be attributed to a flash of light originating at a single PMT, the ratio of maximum charge per PMT to total charge in an event was required to be less than 8% (MQTQ < 0.08). The MQTQ cut effectively selects events associated with relatively isotropic light production, illuminating many photo-tubes at the same time. For this analysis, the values of total and maximum charges used in the MQTQ calculation were found without excluding waveforms flagged as abnormal.

   The distribution of MQTQ values for events in the Gd energy window is shown in Figure 4.1.

2. muon veto cut

   Any event occurring within 1 ms after a muon-like event was excluded from consideration. The muon-like event is defined by an energy deposition in the inner veto exceeding 10000 digital units of charge (DUQ). The muon-like events themselves were

excluded as well. The energy spectrum of the inner veto is shown in the Figure 4.2.

3. external triggers cut

   This last cut was taking care of special events associated with external trigger signals (see 2.1.3) Relevant external triggers always present in the physics data are the 1Hz trigger and the dead time monitor.

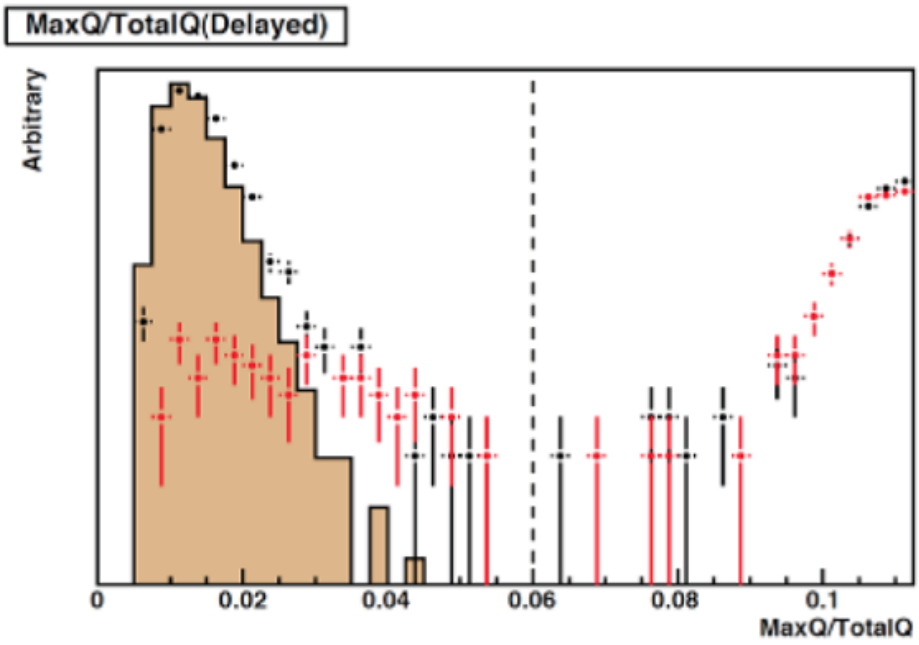

Figure 4.1: The MQTQ distribution for Gd-like events following a muon. The black data points are Gd-like events occurring from 4 to 100 microsecond after a muon. The red data points correspond to the events in the same time window, but shifted by 1 second from the muon (off-time window). The hatched gray area is a MC simulation of the Gd signal. The simulated signal is located well below the 8% percent level (MQTQ¡0.08), while the majority of the non-isotropic light is above the cut. The vertical dashed line shows more aggressive, 6%, cut that still provides about 0.1% leakage of the true events [65]

The obtained spectra for prompt and delayed energy windows corresponding to the first 40 days of data are shown in Figure 4.3

To get the rates we need to calculate the livetime. In case of singles events, one determines the total runtime by either summing all fixed rate 1Hz external triggers present in the data, or by summing last trigger time stamps from each run, and one then subtracts the deadtime due to muon veto cut, which is equal to the muon rate times veto window duration. The

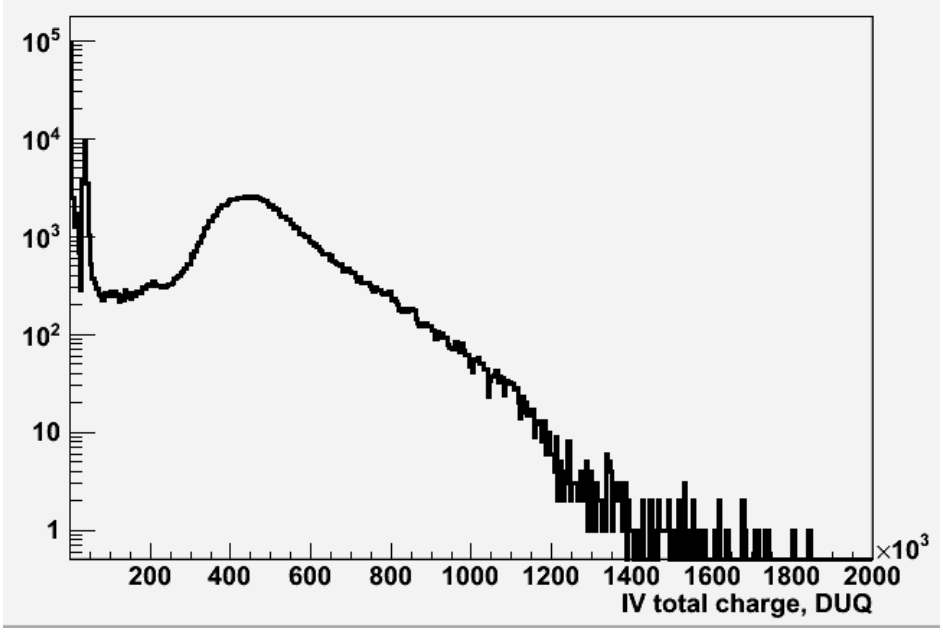

Figure 4.2: The charge distribution of IV triggers. The loose cut at 10000 DUQ cuts away triggers most obviously associated with natural radioactivity.

trigger clock has a resolution of 16 ns, therefore the relative systematic error in the total live time correction for single triggers is $1.6 \cdot 10^{-5}/\sqrt{n}$, where n is the number of 1-ms veto intervals, which is negligible (we ignore the second-order effect of a muon veto followed by another muon veto starting before the end of the first one). The 1 Hz trigger issued by the trigger board has an actual frequency of 0.999997456 Hz for a perfect 16 ns clock period, which is negligibly different from 1Hz. More information on associated uncertainties can be found in [64].

The total livetime (hours per day) and the deadtime fraction are plotted on Figure 4.4. Note that the deadtime plot, essentially, corresponds to the muon rate scaled by a factor of a 1000. The Double Chooz muon rate is therefore around 45 Hz.

We now can plot the rates of the single events in the detector as a function of time.

The average rate of prompt-like singles is 9.58 Hz with an RMS of 0.09 Hz. The rate is quite stable and is in good agreement with the Double Chooz proposal [50]. The delayed-like events have the average rate of 0.04 Hz with an RMS of 0.02 Hz. The average value of the rate is about twice as small than what was expected in the proposal. The rate shows a

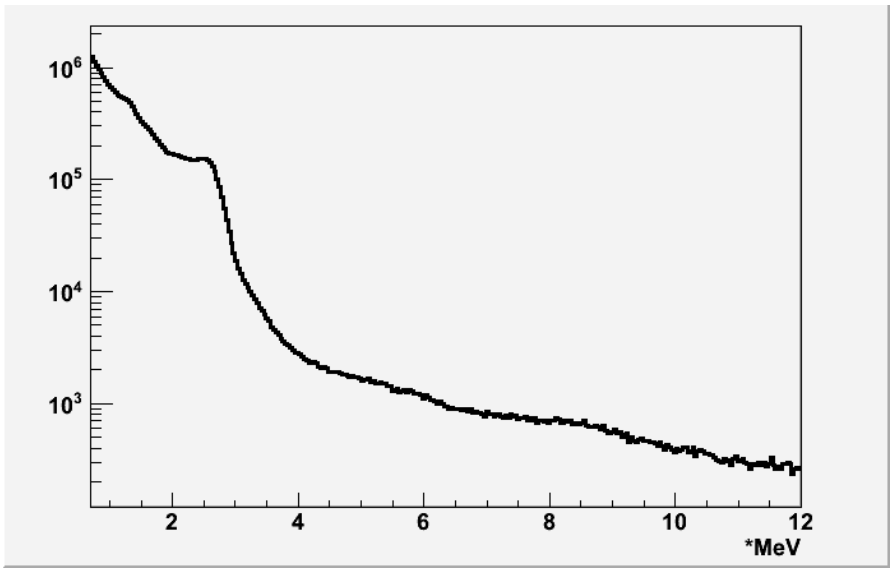

(a) Prompt-like

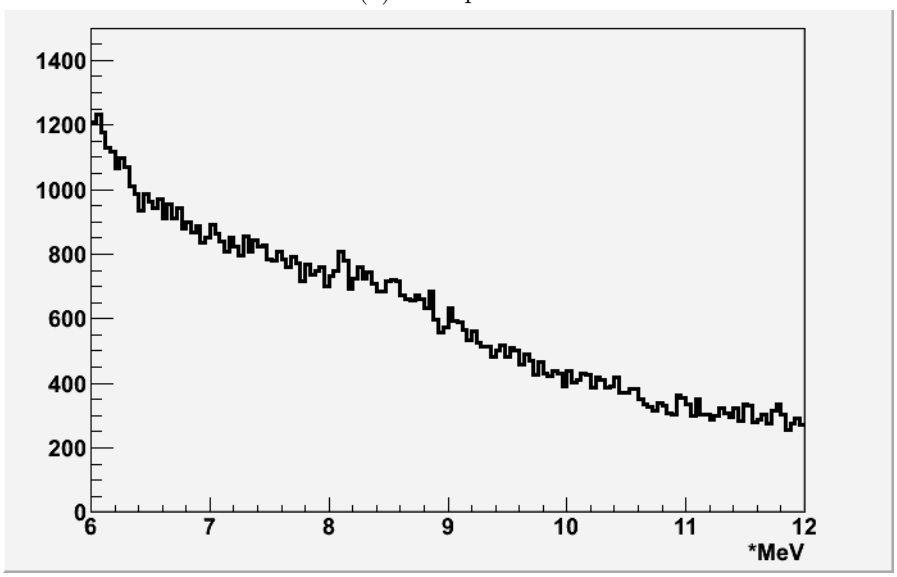

(b) Delayed-like

Figure 4.3: The spectra of single events in the detector.

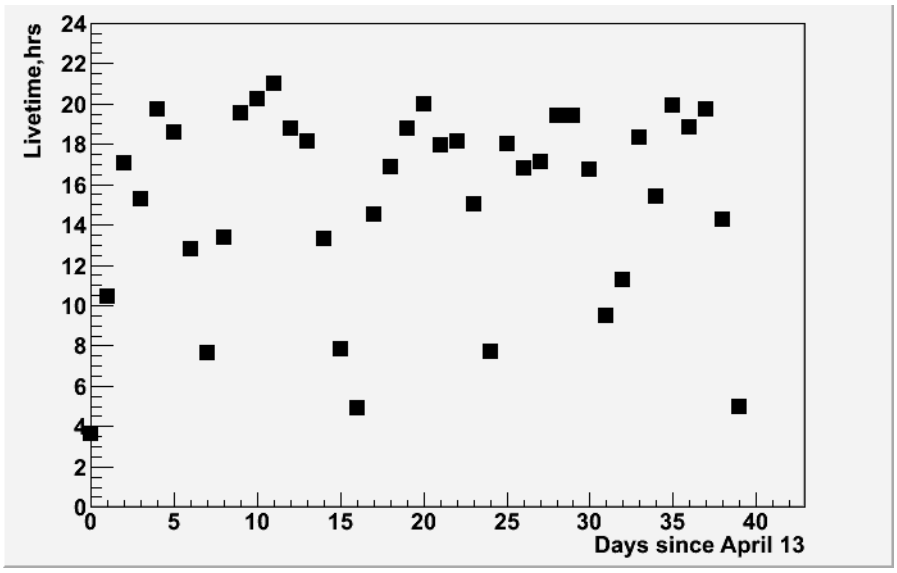

(a) Livetime, hrs per day

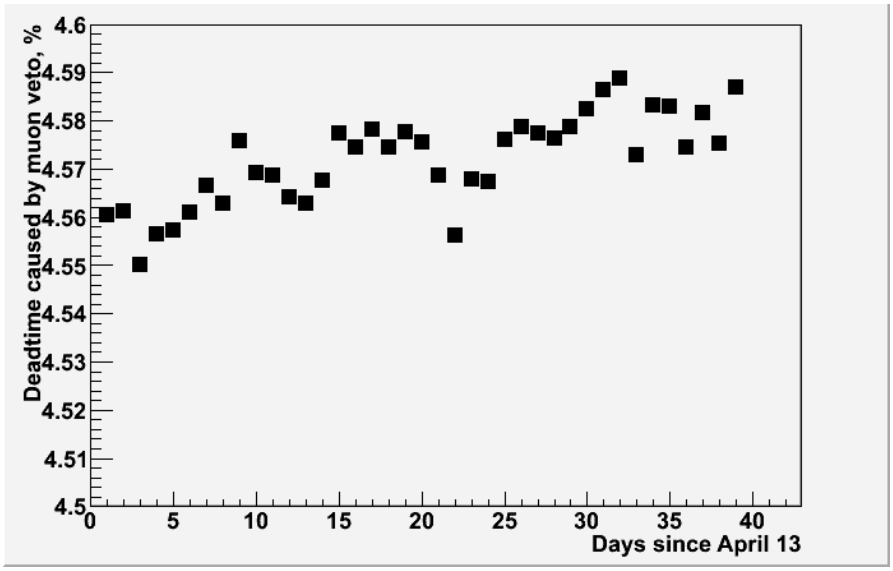

(b) Deadtime, %

Figure 4.4: The livetime and deadtime.

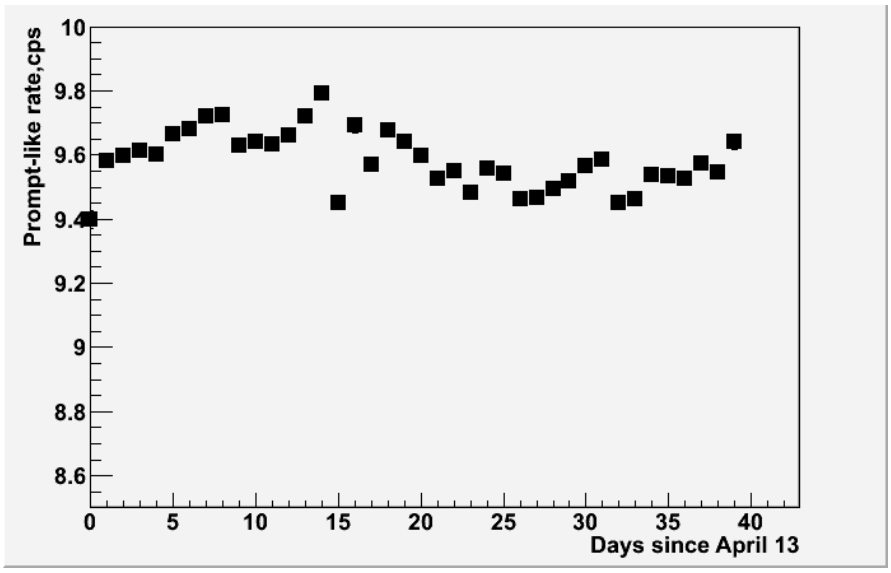

(a) Rate of prompt-like events, cps

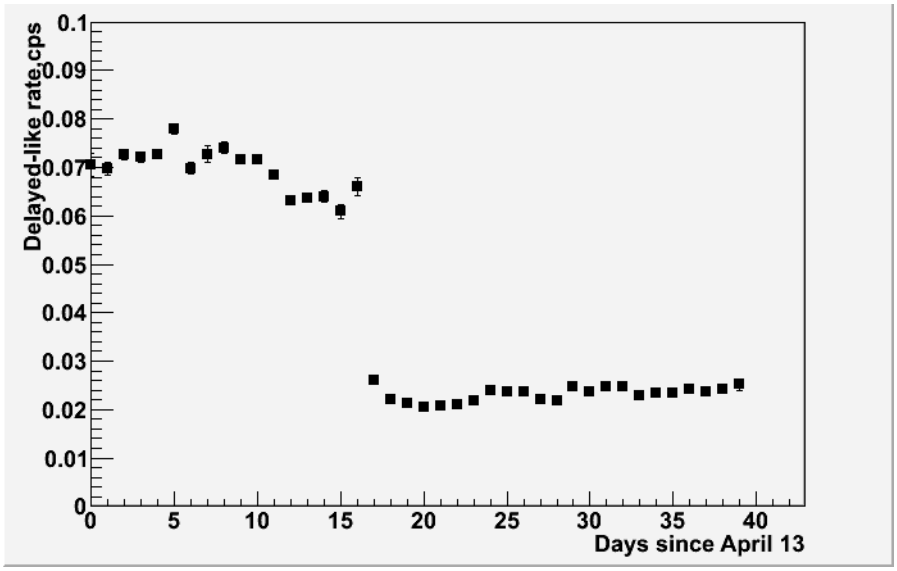

(b) Rate of delayed-like events, cps

Figure 4.5: The rate of singles events. Associated error-bars are small.

distinct drop around days 16 and 17 that is discussed below.

The singles spectrum 4.3a shows structures around 2.6 and 1.4 MeV. These are due to the presence of two common natural radioactive isotopes - Tl-208 and K-40, correspondingly. Tl-208 is a member of the Th-232 decay chain. K-40 is naturally present in grease or sweat secreted by human skin, and one way for it to enter the detector is due to handling of the components without gloves. This isotope is also ubiquitous due to long lifetime.

To amplify the relative signal from these mono-energetic emitters, we apply an additional vertex cut to isolate the region of the detector that is more likely to host these contaminants.

In case of K-40, we cut around the chimney of the target vessel, by applying the following additional cut:

$$\rho < 200 \text{ mm}, 1200 < z < 1900 \text{ mm}$$

RecoBAMA vertex reconstruction was used. The resulting spectrum of K-40 candidates is shown in Figure 4.6.

The vertex cut results in significant amplification of the K-40 signal. The peak sits on top of a Compton continium. Extracting the position of the peak by a Gaussian plus exponential functions (shown in Figure 4.6 in red) provides a natural calibration point. The integral of the Gaussian curve, corresponding to the rate K-40 events, can be used to monitor stability of the detector in this range (Figure 4.7).

In case of Tl-208 we apply the vertex cut around target walls:

$$900 < \rho < 1300 \text{ mm}, |z| < 1300$$

The resulting spectrum is shown in Figure 4.8.

The peak sits on top of a Compton continuum. We attempt to extract the position of the peak by fitting the right edge with a Gauss function. Before dedicated radioactive calibration sources were available, the Tl-208 and K-40 peaks served as natural calibration lines. Moreover, plotting the position of the Tl-208 peak as a function of time provides an

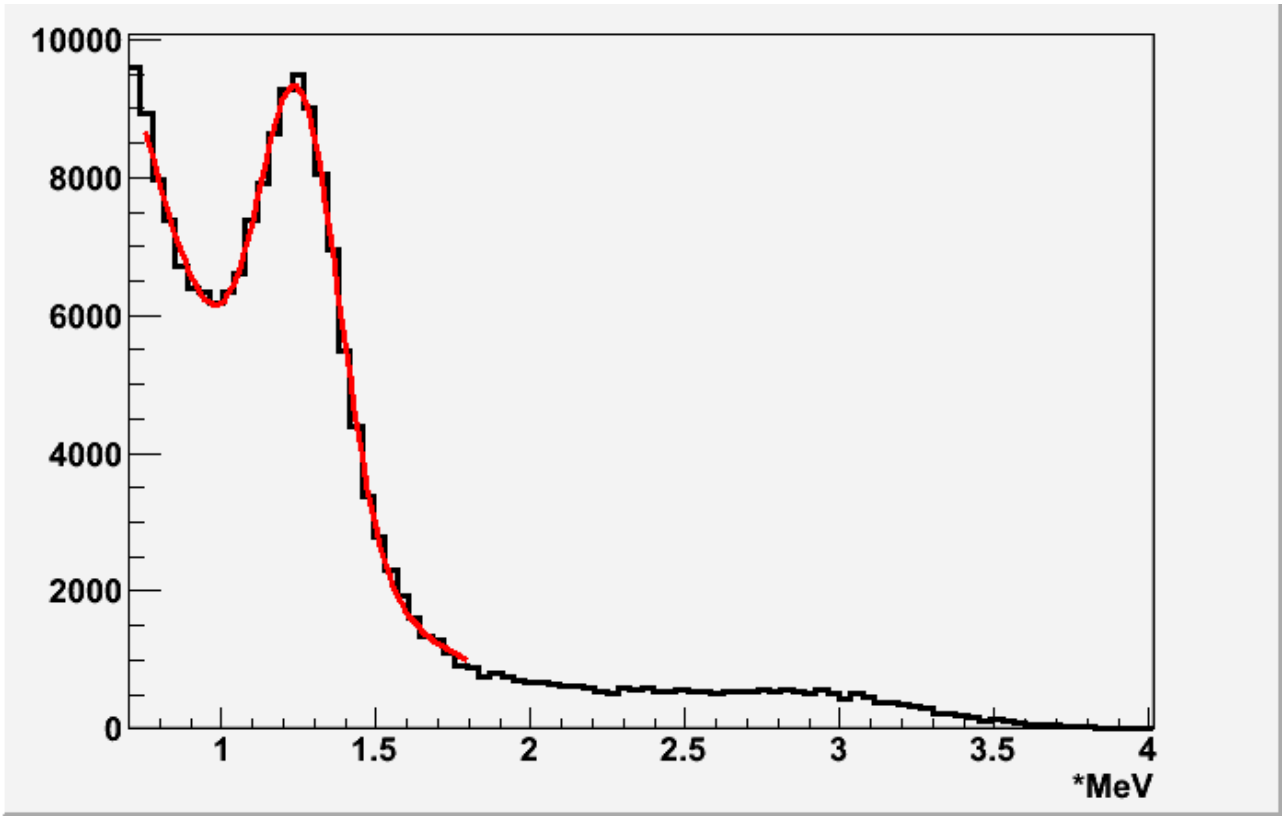

Figure 4.6: The K-40 signal around the chimney. The red curve is a Gaussian+exponential fit.

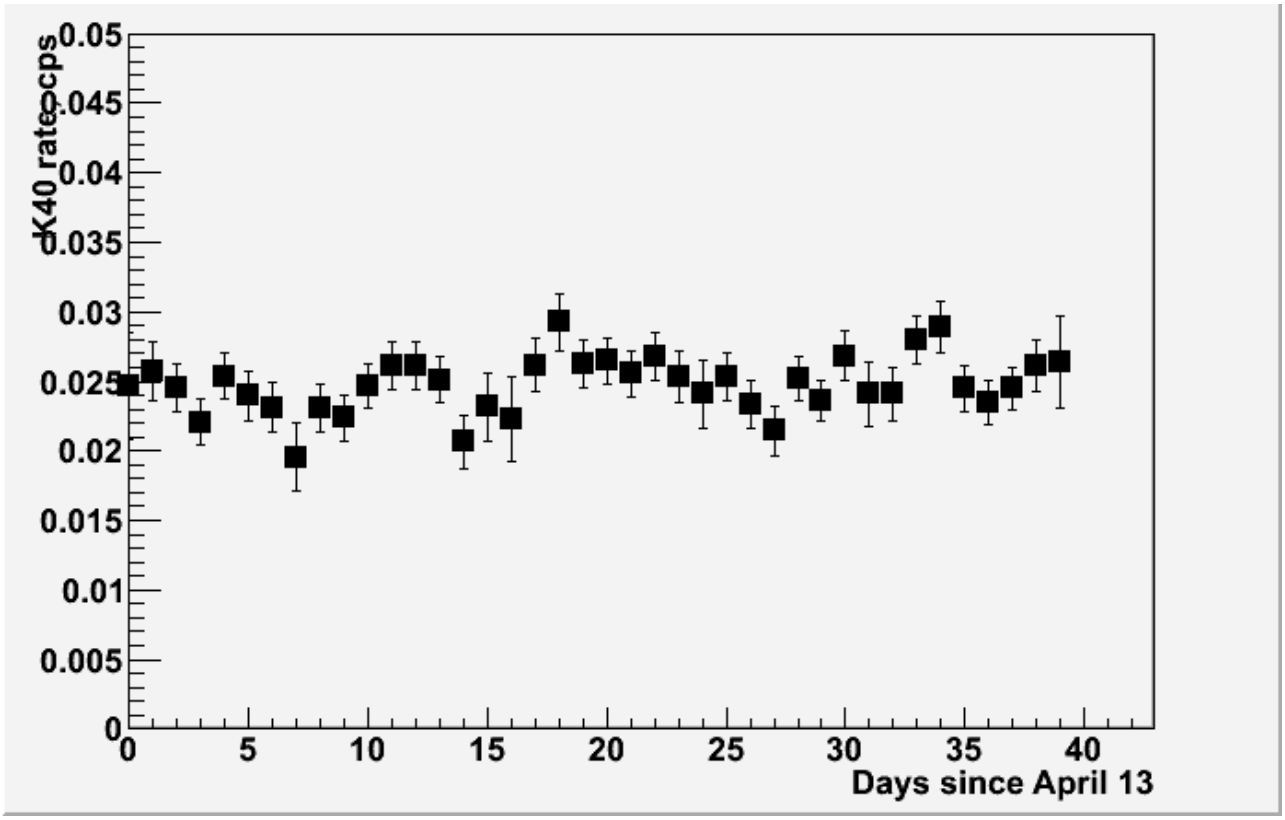

Figure 4.7: The rate of K-40 events as a function of time.

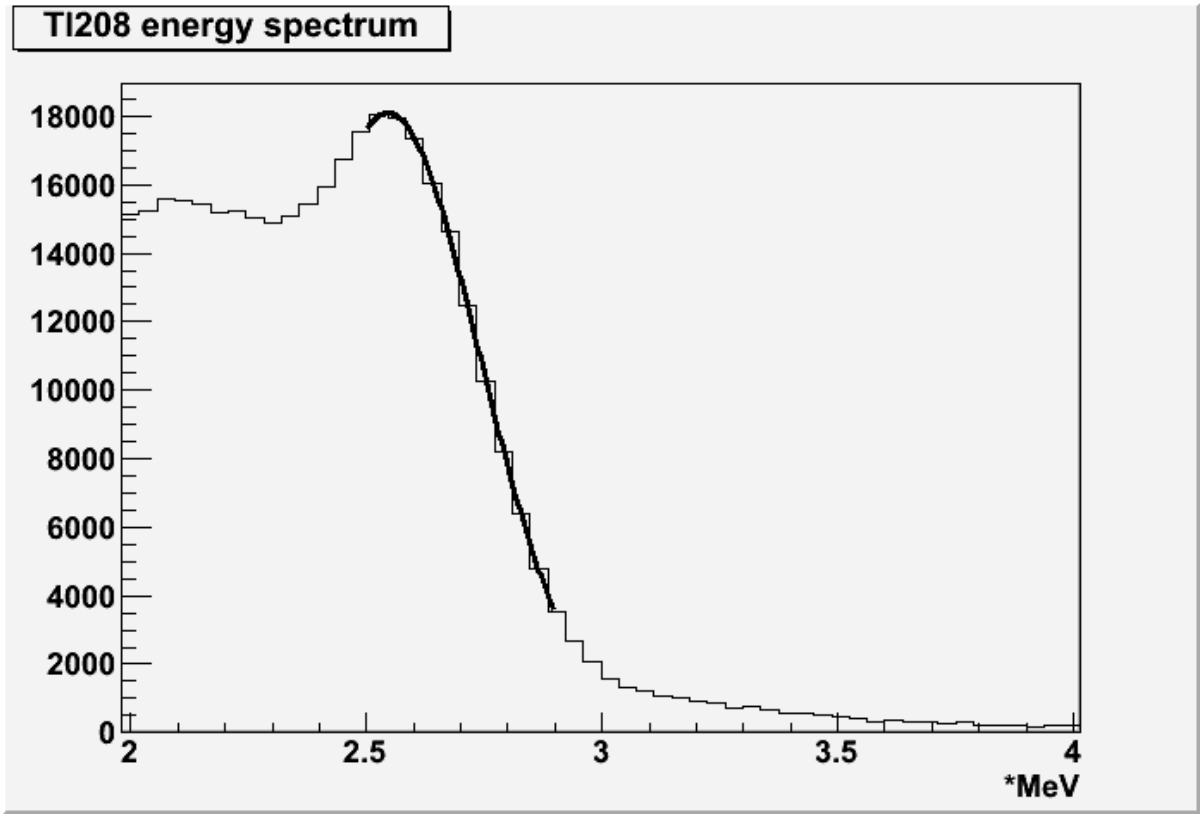

Figure 4.8: The Tl-208 signal around the target walls. Gaussian fit shown in thick black.

additional way to monitor the stability of the detector. Figure 4.9 shows the mean position of the Tl-208 peak. It experiences a shift around day 16 since the beginning of the data taking. This result is in good agreement with the independent analysis of the hydrogen capture peak position [64]. As was mentioned before, the drop in the rate of the delayed-like singles is also seen at about the same time. The drop is associated with a power outage which occurred at the same time, which may have resulted in slight shift in the PMT gains. The outage could also affect the pattern of the light noise and hence be responsible for the drop observed in the rate of delayed-like singles. The improved definition of the light noise cut, used in later analyses, confirmed this expectation and resulted in stabler and substantially smaller rates of delayed-like singles.

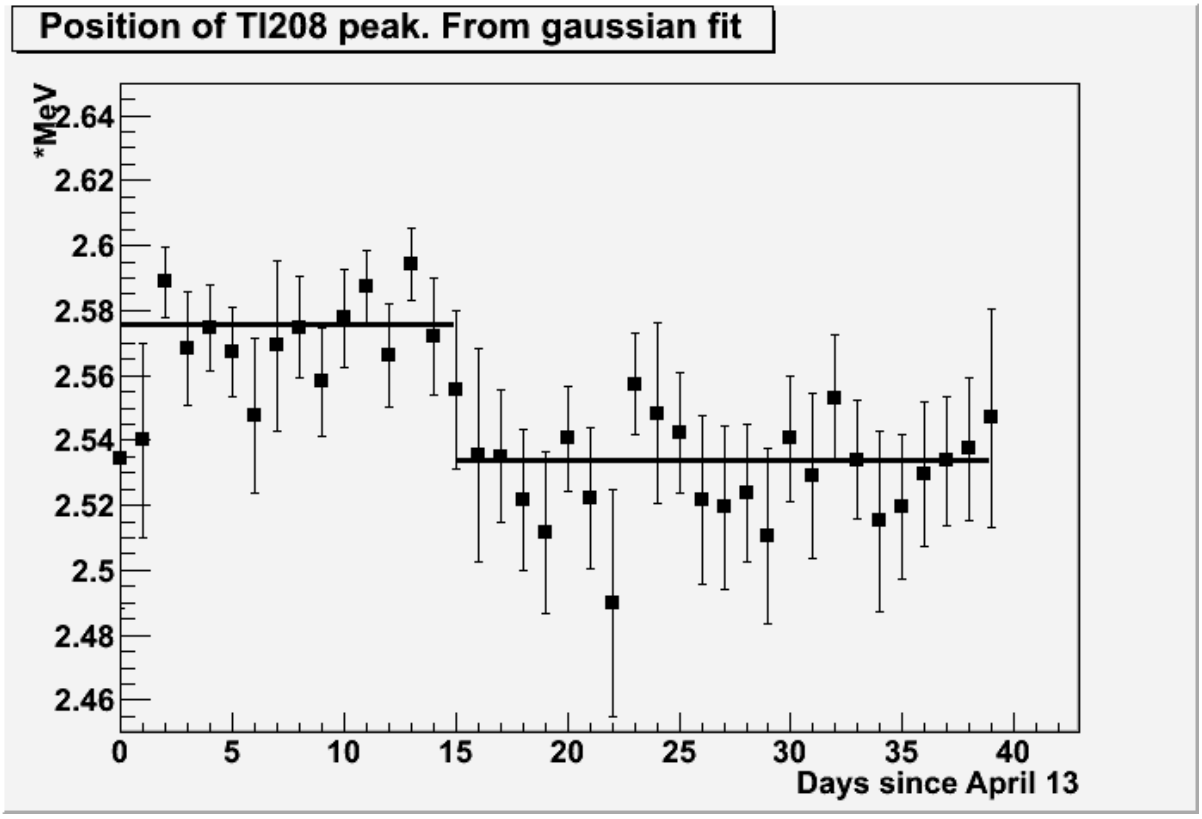

Figure 4.9: The position of the Tl-208 peak. The position is extracted from a Gaussian peak as a function of time. The black lines correspond to two constant fits. 1.6% drop is observed around days 15 and 16.

4.2 Accidentals

Two single events may mimick an IBD coincidence if they occur within the 100 μs time window. The rate of accidental coincidences can be calculated using rates of singles in the prompt and delayed energy windows, extracted in the previous section:

$$R_{accidental} = R_{prompt} \times (1 - e^{-R_{delayed}\delta}), \tag{4.1}$$

where δ is equal to 100 μs.

Substituting the mean values for the prompt and delayed rate, found in the previous section, the expected rate of accidentals is 3.31 events/day.

Due to the fact that the rate of accidental coincidences is independent of time, while the true IBD delayed event can only occur within first few hundred microseconds, one can directly extract the rate of accidentals from the data. To do that, one performs the same event selection as one would use for the neutrino events, only shifting the position of the time coincidence window far enough to ensure that no true coincidences can occur. This is called the "offtime" window method. The rate and spectrum of coincidence events in a 100 μs time window, shifted by +1 ms is shown on Figure 4.10

The prompt spectrum is dominated by low energy events, associated with the radioactive isotopes in the componenents of the detector and rock surrounding the lab. The mean rate of accidental events is found to be 3.20 events per day, with an RMS of 3.12 event per day, which is consistent with simple estimation (4.1). Note that the numbers will be updated in the final analysis section. Due to continuous improvement in the candidate selection criteria and light noise rejection algorithms, the final numbers improve subsantially.

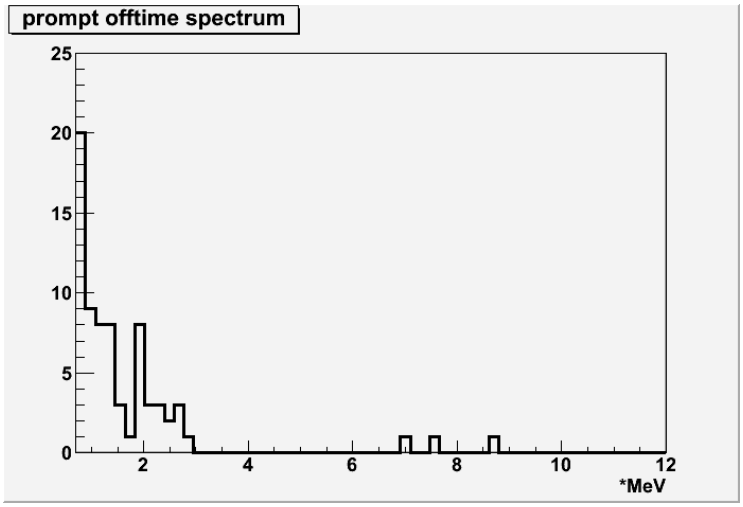

(a) Prompt spectrum

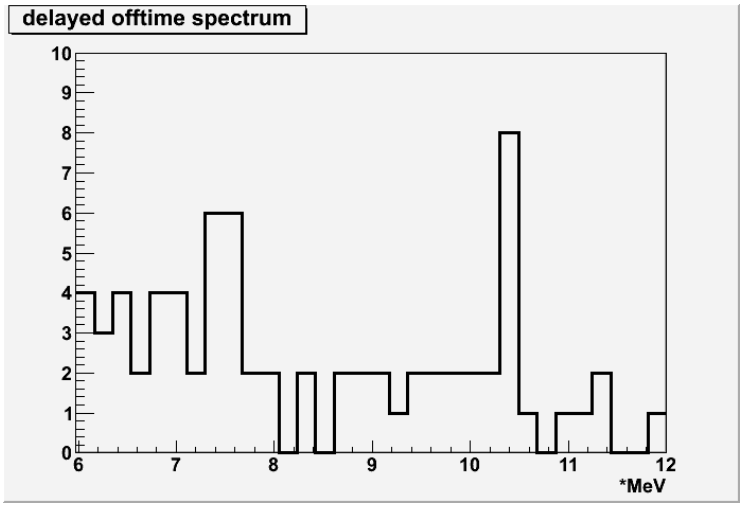

(b) Delayed spectrum

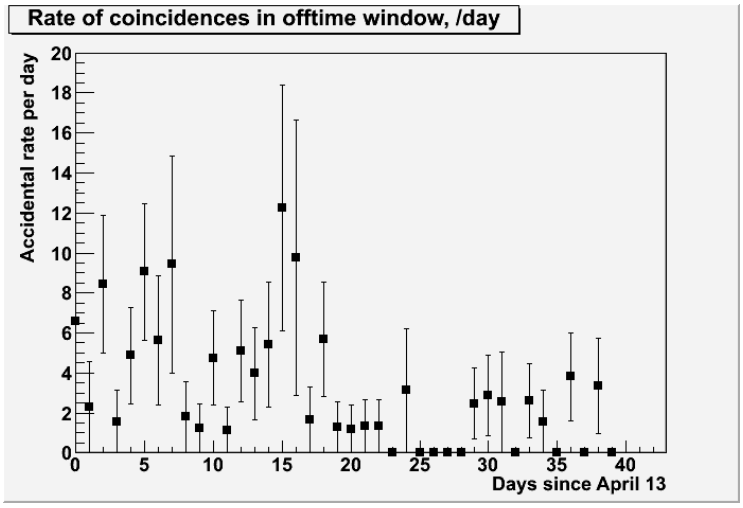

(c) Rate per day

Figure 4.10: The rate and spectrum of accidental coincidences. As determined with the offtime method.

Chapter 5

PMT gain and timing

5.1 Gain

We want to convert the reconstructed charge into a corresponding number of photoelectrons for two reasons:

1. As we saw in the previous chapter, the amount of charge corresponding to the same energy deposition occuring in the same spot inside the detector is not precisely constant in time (Figure 4.9)

2. The amount of charge corresponding to a photoelectron (*gain*) may depend on the total charge due to non-linearity effects. The non-linearity arises as a natural property of the scintillator response (e.g. quenching effect), but also due to charge-dependent losses and systematics in pulse reconstuction and electronics effects. In case some of the effects are not properly accounted for in the Monte Carlo simulation, one can perform a charge-dependent gain calibration to remove the discrepancy.

The time-dependent gain calibration for the first physics run was obtained using the inner detector light injection system (IDLI), described earlier. The gain is extracted by fitting the

charge distribution for low intensity light[1] events by the following function:

$$F(x) = \sum_{n=1}^{2} \frac{N e^{-\mu} \mu^n}{\sqrt{2\pi}\sigma_n n!} e^{\frac{x-na}{\sigma_1\sqrt{n}}^2} \tag{5.1}$$

where x - charge, DUQ, N - normalization factor, n - the number of photoelectrons (one and two photoelectron events are taken into account by the fit), μ - mean number of photoelectrons, σ_1 - width of the single p.e. peak, a - gain (DUQ/p.e.) An example fit is shown in Figure 5.1.

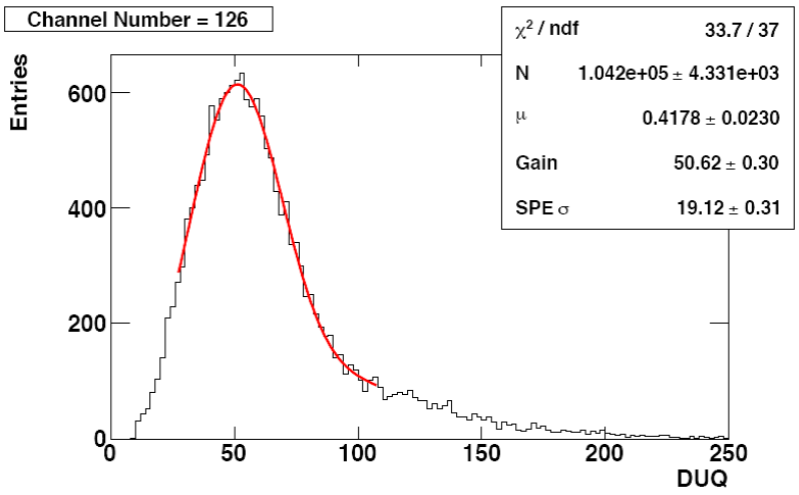

Figure 5.1: An example of gain extraction using the IDLI data. One and two p.e. are taken into account by the fitting model[66].

Extraction of the gain for individual PMTs was found to be difficult due to pedestal shifts upon power cycling of the readout processors. The effect affects relative gains, but the mean gain is rather stable. It was therefore decided to apply a mean gain calibration to all PMT channels for the first physics run. The mean gain is periodically calculated and averaged over 5 day periods. The average gain constant is then automatically applied during the CT data processing. An example of the gain time evolution is shown in Figure 5.2. Apart from the abrupt change due to a power cut in the lab, the gain constant shows a raising trend.

[1]Light intensity is a compromise between low contamination by multiple p.e. events and statistics.

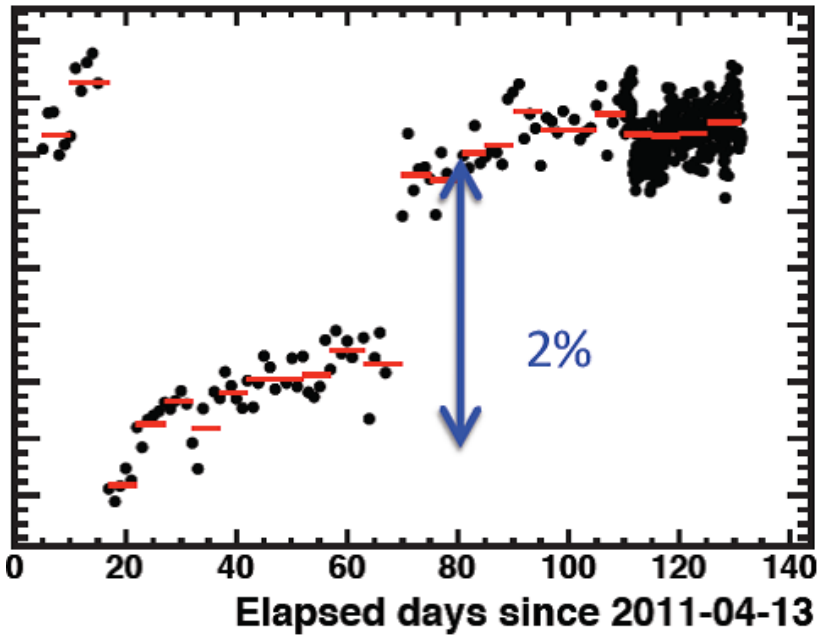

Figure 5.2: Mean gain as a function of time [67].

5.2 T0s

As was discussed earlier, it is neccessary to correct the raw pulse time for the time offsets of individual PMTs. This is done in the RecoPulse that applies the T0 correction by adding a constant to the raw pulse timing. The best way to derive the T0s is by injecting very short light pulses at the center of the detector. Using a light wavelength that does not excite the scintillator is advantageous, as it removes complications associated with the non-trivial time profile of the scintillator light emission. Morever, if one can perform the calibration in the empty detector, the determination of the time offsets will be decoupled from imperfect knowledge of the speed of light in the scintillator. The attempt on the latter was indeed performed before the far detector was filled [68]. However, the previously mentioned artifact of the electronics, present at the time, resulted in instabilities of the time offset upon power cycling on the order of several ns, reducing the reliability of the calibration. For the first physics run, the time-dependent relative time offsets for all PMTs were determined using

inner detector light injection data. For that purpose, high intensity light from 8 LEDs[2] was injected periodically between physics runs to cover all PMTs. The pulse time (maximum amplitude time) was corrected for event-to-event trigger differences using external trigger signals ("base" time) and then fitted to extract the "observed" time for the "target" PMTs. An example of the fitted time distribution is shown in Figure 5.3. The target PMTs are selected as follows:

- For the Buffer wall LEDs, the PMTs should be located on the wall and the opening angle between the LED and the PMT should be less than 45 degrees.
- For the top and bottom LEDs, the opening angle between the LED and the PMT should be less than 45 degrees

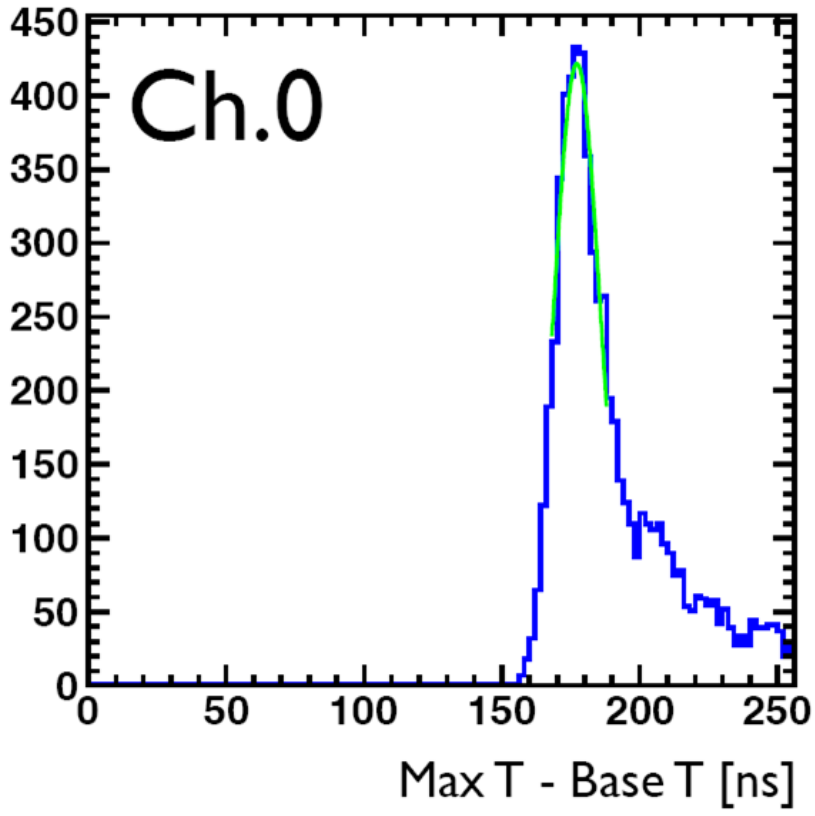

Figure 5.3: The PMT pulse time distribution. The distribution is corrected using the external trigger. The event time is found by fitting the peak as shown [66].

[2] 2 on top, 4 on the wall, and 2 at the bottom of the Buffer.

The observed event time is then plotted as a function of distance between LEDs and PMTs, individually for each of the eight LEDs. The plots are fitted by linear functions, and the mean slope value is extracted. The individual plots are the re-fit while keeping the slope fixed to the mean value. Finally, the relative time offsets are extracted by subtracting the fit-based expected time from the observed time for each PMT. An example of the observed pulse time versus the distance between a PMT and one of the light injection points is shown in Figure 5.4 before and after the T0 calibration.

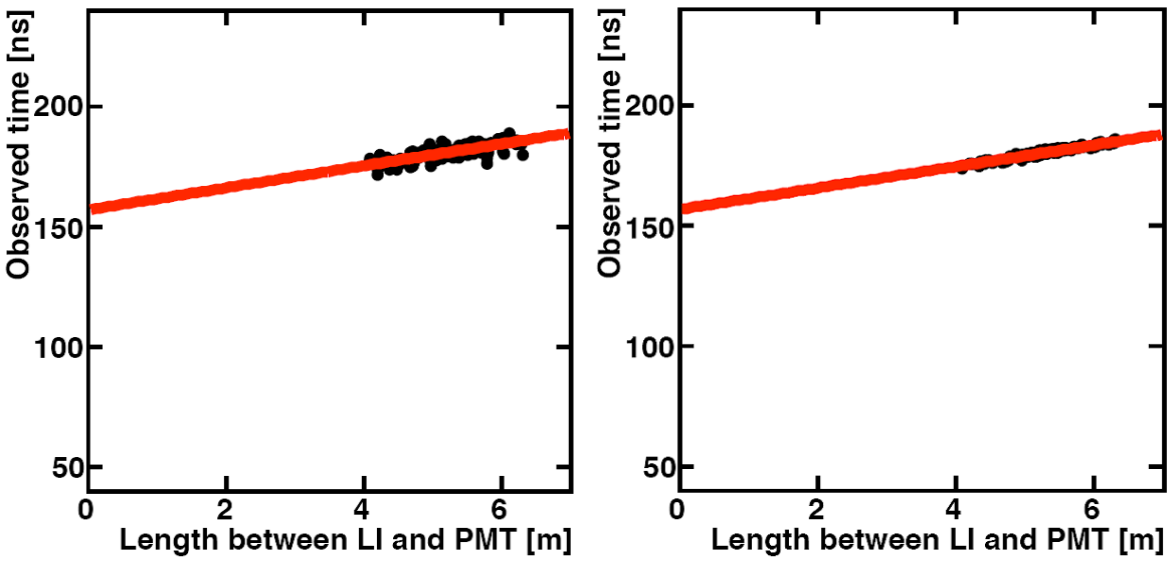

(a) Before calibration (b) After calibration

Figure 5.4: The PMT pulse time before and after calibration. The PMT pulse time is shown as a function of the distance between PMT and light source. Red line shows a linear fit (slope is an effective speed of light in the detector). [71].

The time offsets for individual PMTs are evaluated periodically and are automatically applied during CT data processing.

Chapter 6

Detector response

The final analysis performed by the Double Chooz collaboration relies on a Monte Carlo simulation to predict the prompt energy distribution of IBD positrons. The error of the prompt spectrum prediction gets contributions from the uncertainty of the reactor anti-neutrino energy spectrum and the simulation of the detector response. To understand the uncertainty of the detector response simulation we first compare the calibration source data with the Monte Carlo prediction. Figure 6.1 shows the ratio of the peak positions in the data and MC. The ratio deviates from one by several percent at the target center. The peak positions are extracted by phenomenological single or double Gaussian fits (examples are illustrated in Figure 6.2). It is believed that the discrepancy is due to effects not modeled in the current Monte Carlo. It is possible to adjust the MC parameters, in particular quenching constants and light yields, such that the agreement between the peak positions reaches the level of 1-2%. However, the required parameter values are far away from the ones measured in dedicated laboratory experiments. Since we also know that the data are affected by a non-linear loss of charge due to effects that are not yet completely understood, compensating for such effects by artificially increasing the quenching constants was decided to be undesirable. Therefore, for the first analysis we compensate for absense of the additional non-linearity in

the MC with correction functions instead of adjusting the parameters of the MC simulation.[1]

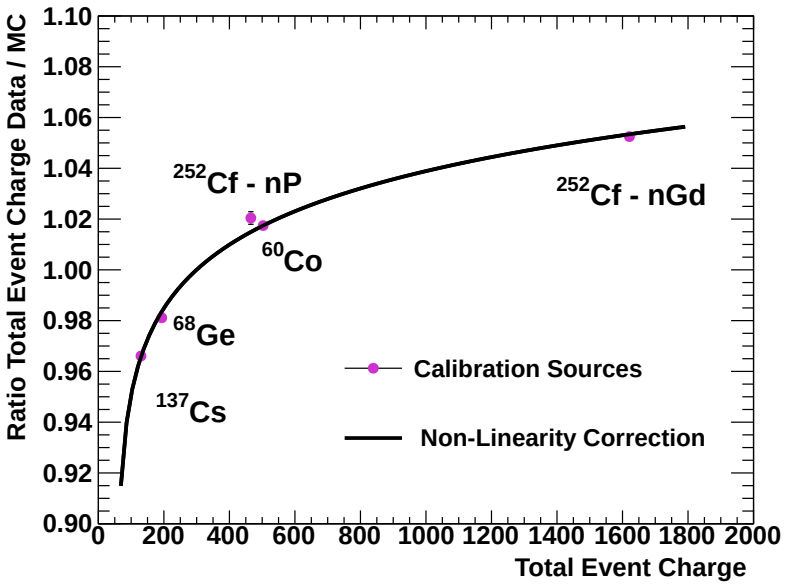

Figure 6.1: Discrepancy between data and MC at the detector center. The ratio of peak positions in the data and MC is plotted as the function of the peak position, in p.e. The solid line is the correction function, cor1.

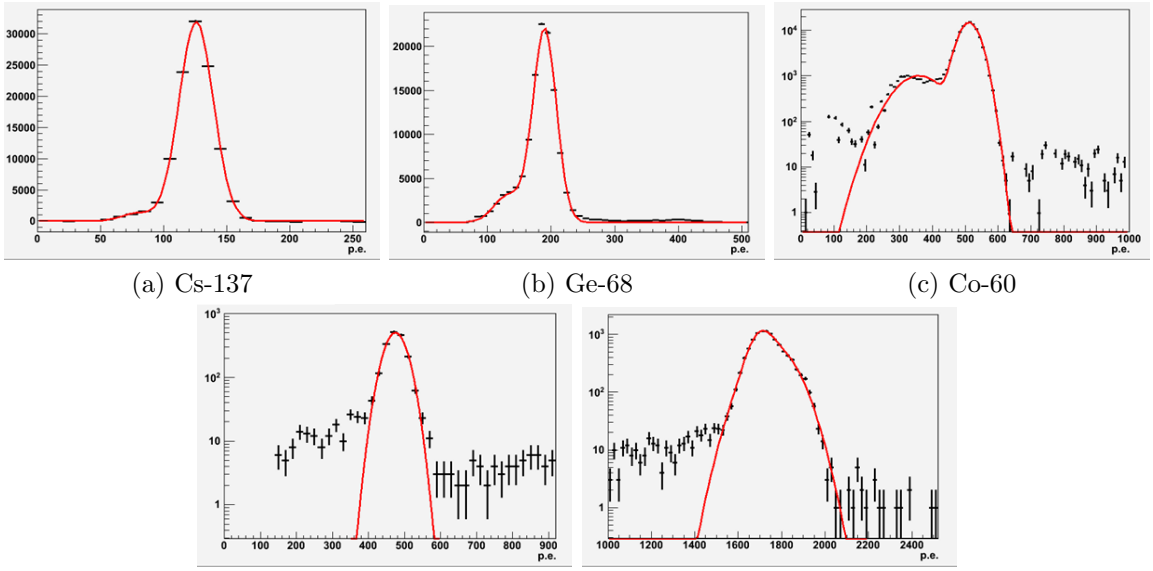

(a) Cs-137 (b) Ge-68 (c) Co-60

(d) H capture (e) Gd capture

Figure 6.2: Examples of peak position extraction. The data charge distributions (black) are fit by a single or double Gaussian (red). The X axis is total event charge (p.e.).

[1]The correction functions used in the first analysis were derived by the author of this thesis.

6.1 The correction functions

The correction function shown in Figure 6.1 has the following form:

$$cor1(p.e.) = 0.0286966 \times \ln(p.e. - 56.1478) + 0.842321, \tag{6.1}$$

where $p.e.$ is the number of photo-electrons in a MC event, ln is natural logarithm. The parameters are found by a Minuit fit. The reduced chi-square of the fit is equal to $\sim$4. This could indicate that the errors on the individual points are underestimated, or that the model is inadequate. Only the Gaussian fit errors are used as an uncertainty on each peak position. This ignores the systematic uncertainty on the peak position extraction and, thus, underestimates the error. Additionally, one can apply the function derived using data at the target center to the gamma catcher region. Figure 6.3 shows the ratio of peak positions in the data and MC in the middle of the gamma catcher guide tube (half-way between the target and the gamma catcher walls). The same correction function that fits the non-linear difference between the data and MC in the target, apparently, works reasonably well in the gamma catcher. Note that the two regions have different scintillators, and the corresponding quenching constants are different by more than 50%. The fact that the correction function applies to the both regions is indicative, though not conclusive, that the correction function may, indeed, describe the additional source of non-linearity adequately.

Application of the correction allows one to reconcile the MC prediction with the data at the target center. However, the data and MC also demonstrate different position dependence. Figure 6.4 shows the ratio of the full-absorption peak position as a function of the Z coordinate along the vertical axis for the Cs-137 source. The Co-60 source has very similar dependence.

The second, Z-dependent, correction function shown in Figure 6.4 has the following form:

$$cor2(Z) = 0.998201 - 9.51483 \times 10^{-6} \cdot Z - 3.25985 \times 10^{-8} \times Z^2, \tag{6.2}$$

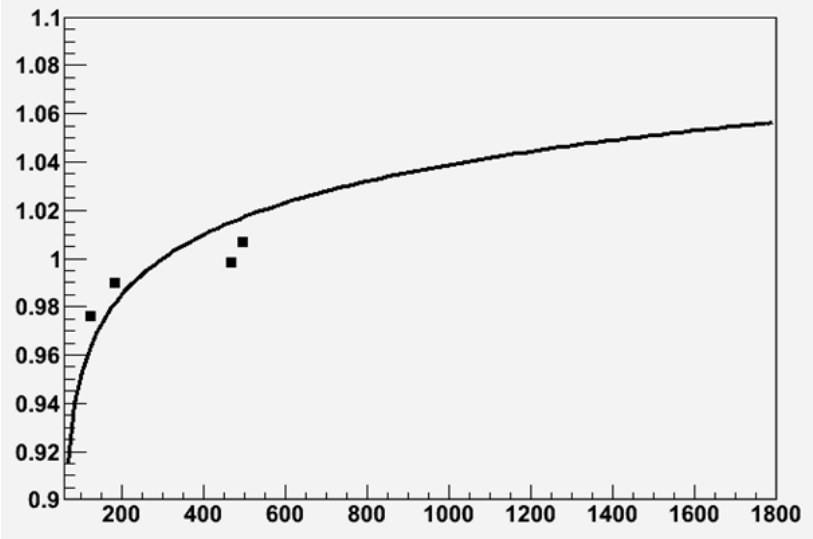

Figure 6.3: Discrepancy between data and MC in the gamma catcher. The ratio of peak positions in the data and MC is plotted as the function of the peak position, in p.e. The solid line is the correction function, cor1. X axis is total event charge, (p.e.).

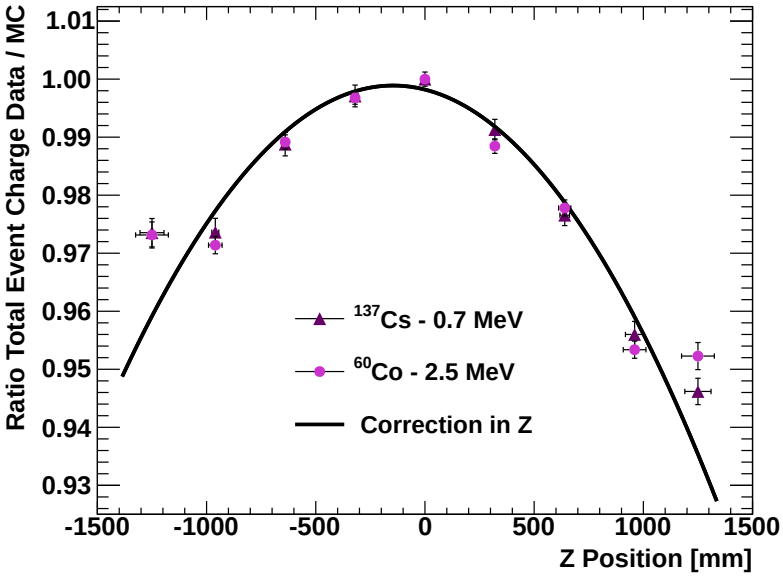

Figure 6.4: Discrepancy between data and MC along the Z-axis of the detector. The ratio of peak position in the data and MC is plotted as the function of Z in *mm*, for the Cs-137 (black points) and the Co-60 (blue points). The solid line is the correction function, *cor*2. Uncertainties of individual points include apparent differences between reconstructed and deployment source position

where Z is the vertex coordinate in mm. The parameters are found by a Minuit fit. The reduced chi-square of the fit to Cs-137 data is χ^2/ndf=3.3, and to the Co-60 data is χ^2/ndf=4.9.

6.2 Performance and parameter error matrix

Application of the correction functions removes the dependence on the errors of the Monte Carlo parameters. The relevant errors become those of the correction functions themselves. The errors of the function parameters are reported by Minuit in form of the covariance matrix. Since we perform the two fits for the $cor1$ and $cor2$ independently (to obtain the plot on Figure 6.4 the peak positions in the data and MC were made to match at the detector center) we obtain two covariance matrices that contain information about errors and correlations between parameters corresponding to each function independently of another function. The parameter matrix is then a 6x6 symmetric block-diagonal matrix

$$M_p = \begin{pmatrix} 2.562\cdot10^{-6} & -0.01536 & -1.678\cdot10^{-5} & & & \\ & 1.015\cdot10^{2} & 0.1019 & & & \\ & & 1.102\cdot10^{-4} & & & \\ & & & 8.397\cdot10^{-7} & -2.646\cdot10^{-11} & -1.29\cdot10^{-12} \\ & & & & 1.863\cdot10^{-12} & 4.174\cdot10^{-16} \\ & & & & & 4.846\cdot10^{-18} \end{pmatrix} \tag{6.3}$$

The first block corresponds to the correction function $cor1$, the second one to the $cor2$.

Note that

- The diagonal elements are the squares of the individual parameter errors, including the effects of correlations with other parameters
- The parameters of the first function are strongly (anti-)correlated with each other, which could be a sign that there are more free parameters than can be determined from the data (although, none of the correlation coefficients, which can be trivially computed for the matrix, is equal to one, or minus one)

We now check the predictive properties of our correction model. If the residual discrepancies are inconsistent with the error matrix (6.3), we can artificially increase the matrix elements. As long as the contribution of the detector matrix is not limiting the sensitivity of the final fit, the matrix expansion can be tolerated.

We first note that the reduced chi-square of both correction fits are larger than one, most likely because we only included statistical errors on the peak positions. We compensate for that by multiplying the first and the second matrices by 4 and 4.9, respectively. The matrix will be expanded further to account for the fact that the model may not be perfectly adequate. Note that the expansion can be achieved either by expanding all matrix elements at once (in other words, preserving the correlations), or by adding an uncorrelated error (equivalently, only increasing diagonal elements). Probably, the optimal way is to combine the two methods. The model clearly has predictive power (Figure 6.3), so the correlations returned by the fit are likely not spurious. At the same time, adding an uncorrelated error provides a safeguard against possible imperfection of the model, which may not be recognized immediately. It also takes a much smaller expansion factor in order to incorporate the necessary error. However, for the first analysis the correlations were preserved during the matrix expansion. The question about optimal expansion strategy continues to be discussed in the collaboration.

We now compare the data and the MC for the spallation neutrons and the sources outside

of the target region. In general, it is clear that the correction function helps, but the residual discrepancies remain. With more studies one could further optimize the correction function. However, based on our sensitivity studies, we can tolerate a large safety factor applied to the parameter matrix, so we prefer to conservatively enlarge the matrix to absorb the largest observed deviation.

The figures below show back to back comparisons of the source data and the spallation neutron data with both uncorrected and corrected Monte-Carlo predictions.

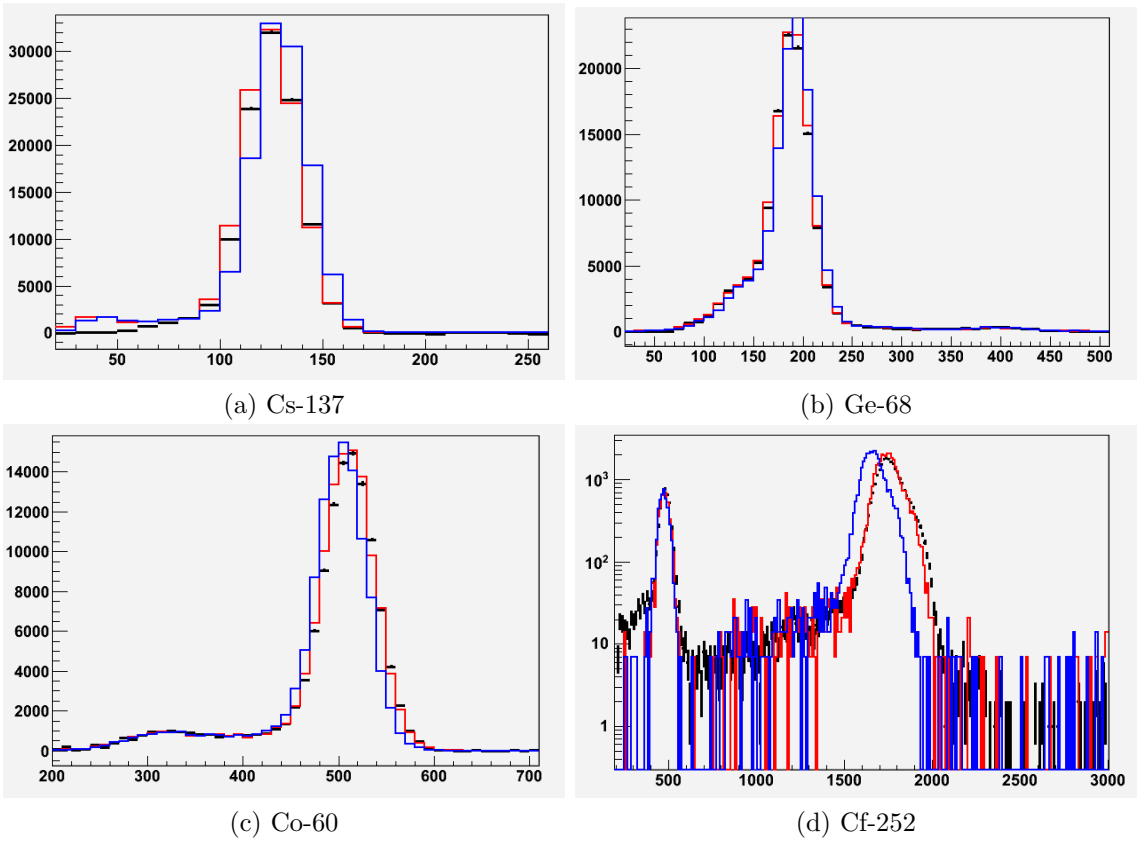

(a) Cs-137

(b) Ge-68

(c) Co-60

(d) Cf-252

Figure 6.5: Comparison of calibration data with MC in the target. The data (black) is show together with uncorrected (blue) and corrected (red) MC prediction at the detector center. The X axis is the total event charge (p.e.).

Note: The spallation neutron check was found to contain a sub-optimal implementation of the correction function. Instead of using the truth information about the Z position, as prescribed, the reconstructed vertex information was used. This likely introduced an additional spread, in particular in the regions close to the boundaries of the sensitive volume.

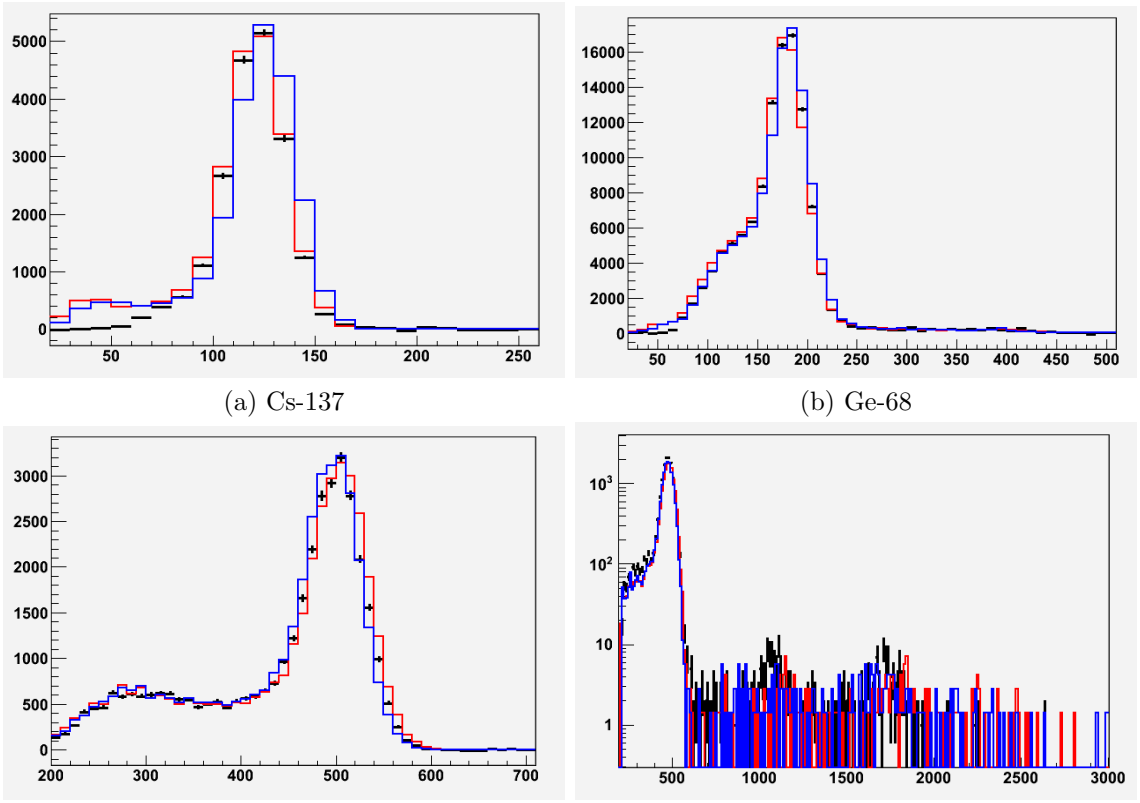

(a) Cs-137

(b) Ge-68

(c) Co-60

(d) Cf-252

Figure 6.6: Comparison of calibration data with MC in the GC. The data (black) is shown together with uncorrected (blue) and corrected (red) MC prediction midway between target and gamma catcher walls at the equator level. The X axis is the total event charge (p.e.).

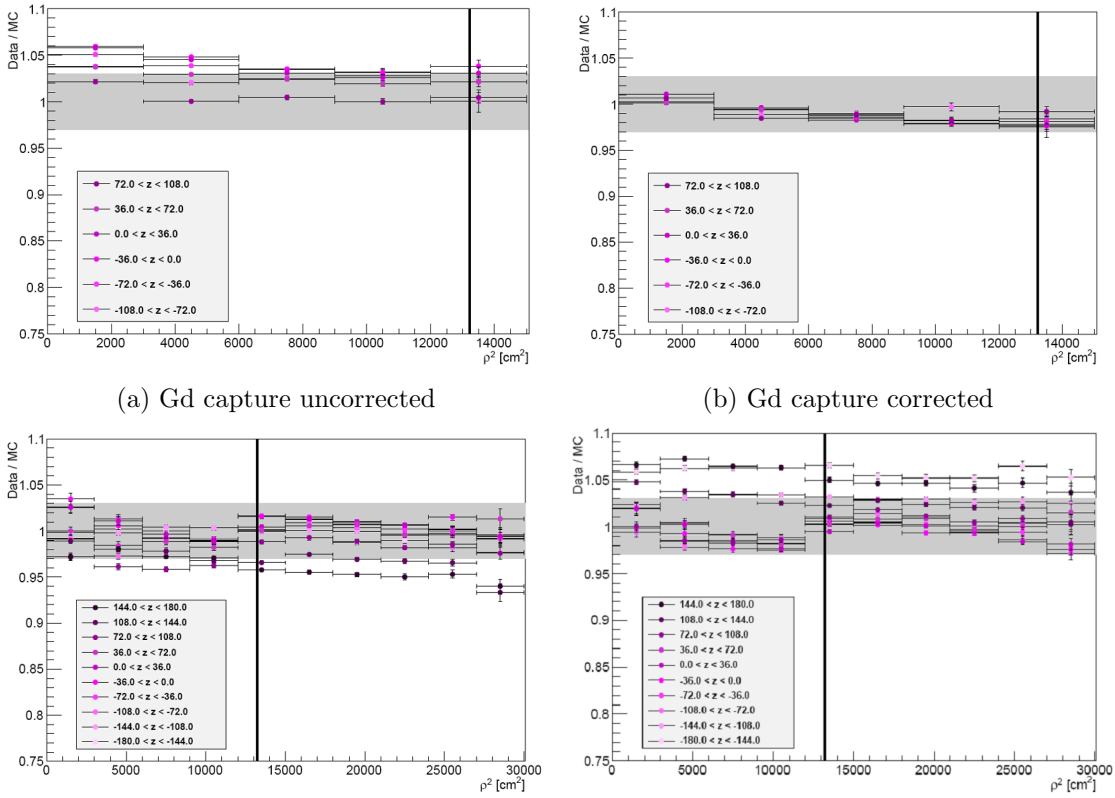

(a) Gd capture uncorrected

(b) Gd capture corrected

(c) H capture uncorrected

(d) H capture corrected

Figure 6.7: Ratio of spallation neutrons capture peaks positions in the data to MC. Ratios of peak positions are evaluated at different Z coordinates and different distances from the center. According to the spallation neutron map, the ratios of Gd peaks are improved in all positions and ratios of hydrogen peaks for all but extreme Z positions close to the top and bottom of the gamma-catcher.

The Gd peak position is less affected by this additional vertex reconstruction uncertainty, because Gd captures are confined to the central region of the sensitive detector (target vessel). This does not undermine the importance of the independent cross-check of the correction functions performance, but alerts us to the fact that the other two checks (using calibration peaks and using the hydrogen and Gd peaks from the actual neutrino candidates) are more reliable. Nevertheless, we will quite conservatively include a ≈7% uncertainty at the extreme Z positions by expanding the parameter matrix accordingly (see Figure 6.8 and Figure 6.9a).

To find out the correspondence between the size of the matrix elements and the uncertainty of the peak position prediction, we draw multiple correlated parameter sets from the matrix. Each set provides a slightly different prediction, and the histogram of multiple predictions has a shape close to a Gaussian curve, with the spread corresponding to the prediction error. Generally, the spread depends on the position and energy. Figure 6.8 shows the spread obtained with a safety factor of 7 (i.e. matrix elements multiplied by another factor of a 49) for the Ge-68 peak position at Z=1330.4 mm.

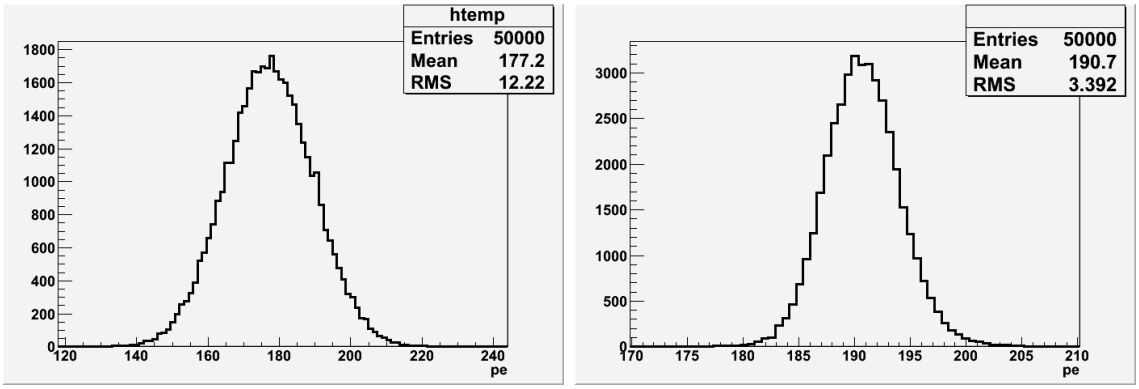

(a) Spread at Z=1330.4 mm (b) Spread at Z=0 mm

Figure 6.8: Uncertainty of the MC prediction for the Ge-68 peak position. The spread at each position obtained with 50,000 draws from the enlarged matrix of the correction function parameters. As expected, the spread increases with an increased Z coordinate.

Repeating this exercise at different Z positions and for different energies, we can obtain the following Figures (6.9a and 6.9b), illustrating the level of error on the energy scale that is included in the enlarged parameter matrix. These errors will later be propagated into the

uncertainty of the prompt spectrum prediction.

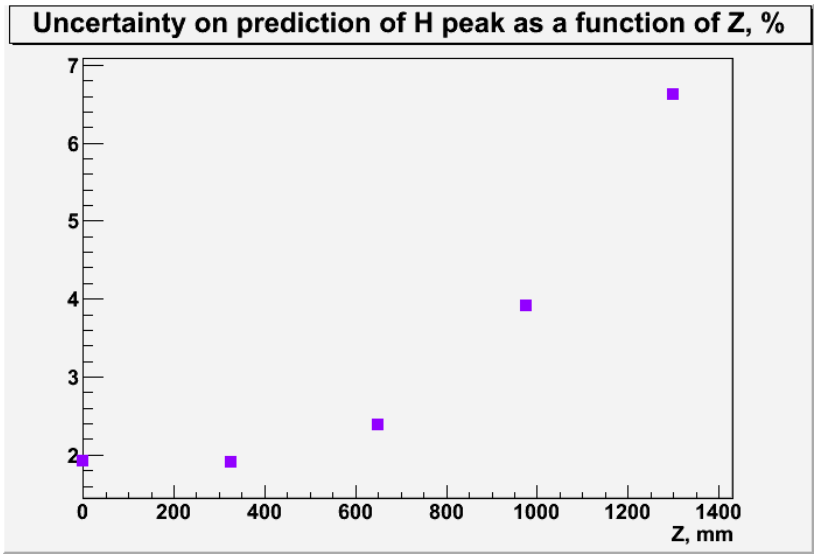

(a) Spread of H peak prediction vs. Z

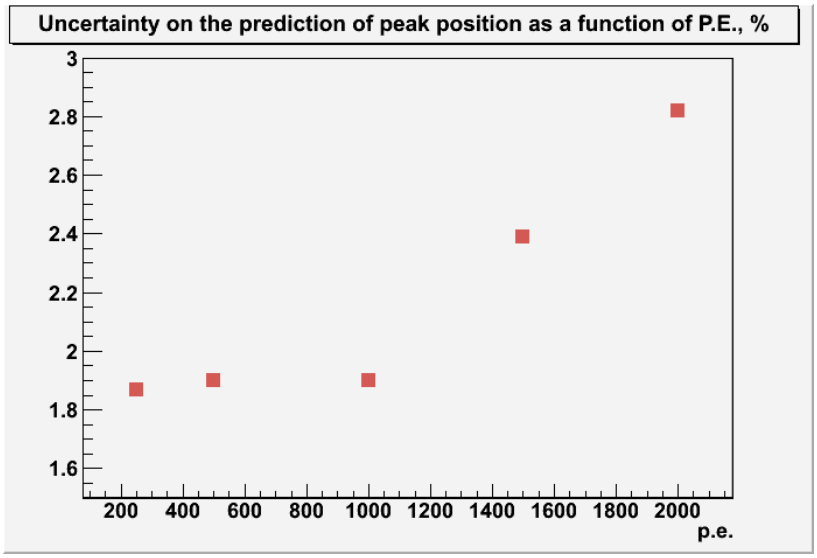

(b) Spread of peak prediction vs. energy

Figure 6.9: Uncertainty of the MC prediction as a function of Z and energy. The Z scan is performed for hydrogen peak. The energy scan is performed at the target center.

As a final cross-check, the positions of the hydrogen and Gd peaks were compared in the neutrino data and corrected Monte Carlo. The neutrino selection was performed with all standard cuts, but the delayed energy one, which was lowered to accept hydrogen captures. The study [73] finds a 0.45% agreement between the positions of the hydrogen capture peaks, and a 0.99% agreement between the positions of the Gd capture peaks, if one uses a

strict target vertex cut ($\rho < 1$ m, $|z| < 1.1$ m). Relaxing the cut to include portions of the gamma-catcher ($\rho < 1.4$ m, $|z| < 1.3$ m) results in 2.7% and 1.5% agreement between data and MC in the H and Gd peak positions correspondingly. This result demonstrates that the amount of uncertainty incorporated into the enlarged parameter matrix (Figure 6.9) is conservative. This result is also, arguably, more informative than the spallation neutron check, because it does not suffer from systematics on peak position extraction due to large background and baseline instabilities following a muon. Furthermore, it has an advantage over the calibration data/MC comparisons, because it is not limited to particular positions and shows a properly averaged response. The author of this thesis repeated a neutrino based check without using the individual event vertex cut, instead using a cut on the prompt-delayed distance (<300 mm). Data and MC were found to agree to 0.86% for Gd and to 1.1% for hydrogen. Figure 6.10 shows the obtained charge distributions.

We conclude the section by noting two technical aspects of the Monte-Carlo error propagation technique[2] used above:

- When making random draws from the enlarged parameter matrix, a fraction of the draws will have the first parameter of the cor1 function larger than the prompt threshold. Figure 6.11 illustrates the uncertainty on the prediction of the Ge-68 peak position obtained by including and excluding the draws with the first parameter exceeding the peak position. While one could reject these draws from the sample, the author decided to accept all draws while calculating the matrix for the first result. Such, "wild" draws are responsible for an asymmetry in the spread of the prediction of the peak positions (Figure 6.11). The average error asymmetry, defined as a difference between the central value prediction and the mean of the random predictions, is maximum around 1 MeV (∼1% skewed towards higher energies), and quickly decreases at higher energies. When propagating the uncertainty of the correction functions to the prediction

[2]To avoid confusion, we state that "Monte-Carlo" was used in the above statement to refer to the way of propagating the errors in the case of multiple correlated parameters, not the fact that the technique happened to be applied to the errors of the Monte-Carlo simulation of the detector response.

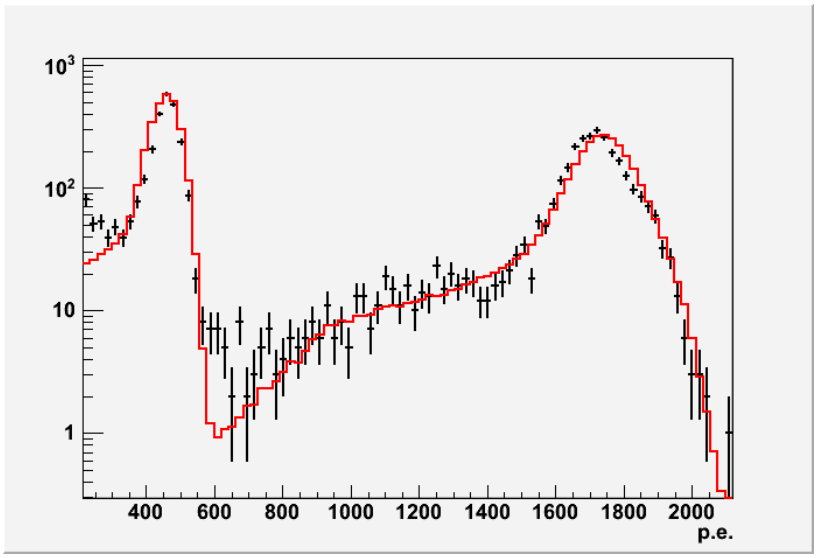

(a) Log scale

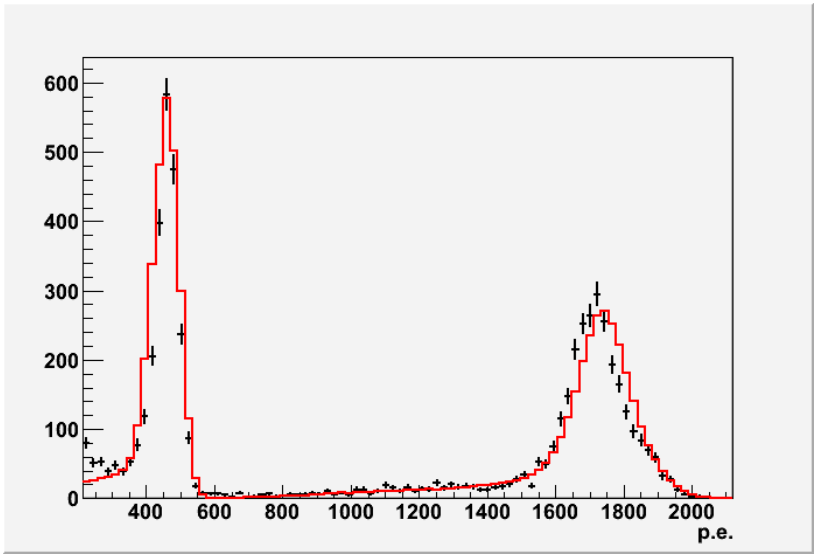

(b) Linear scale

Figure 6.10: The delayed energy distribution for neutrino candidates. The data (black) points are overlaid with the corrected MC (red).

of the prompt energy spectrum, discussed in the final fit chapter, the apparent effect of the wild draws is to increase the variance of the matrix (see an example below). Therefore, not excluding the wild draws is conservative. However, there is a concern that an asymmetry of the random draws may impact results of a fit that takes into account the energy spectrum shape. In practice the effect is small, even for much larger asymmetries. The above can be illustrated by the following simple example.

- Assume a spectrum consisting of 2 energy bins
- Calculate an error matrix using the following estimator:

$$M_{ij} = \frac{1}{N} \sum_{N} (p_i^n - p_i^{cv})(p_j^n - p_j^{cv}) \tag{6.4}$$

  where M_{ij} - the error matrix, N - number of random draws from the enlarged parameter matrix, $p_{i/j}^n$ - the i/j bin content of the prompt histogram corresponding to a random draw, $p_{i/j}^{cv}$ - the i/j bin content of the prompt histogram corresponding to the central value prediction.

- Consider a case when random draws are completely symmetric around the central value. For example, one random draw results in a shift (p_{ij}^n-$p_{i/j}^{cv}$) in each of the two bins equal to -2 events, and another draw produces a shift equal to +2 events in each bin. The diagonal elements of the matrix (variances) are then

$$M_{11} = M_{22} = \frac{2 \cdot 2 + (-2) \cdot (-2)}{2} = 4, \tag{6.5}$$

  which corresponds to an error of ± 2 events in each bin.

- Now consider a case when random draws for the first bin are not symmetric. Say, the first draw results in a shift equal to -2 events in the first bin, while the second

draw produces a shift of +3 events in the first bin. The variance is then

$$M_{11} = \frac{3 \cdot 3 + (-2) \cdot (-2)}{2} = 6.5, \tag{6.6}$$

which corresponds to an error of ±2.55 events in the first bin. The error in the second bin is still ±2 events. Note that in the final fit these errors correspond to the histogram obtained with the central value prediction. Similarly, we can find that the correlation between bins is equal to 100% for the symmetric case, and 98% for the asymmetric one. The total variance of the matrix, equal to the sum of all elements, is, again, larger for the asymmetric case. In the above example, a 50% asymmetry in random draws results in the correlation decrease of 2%. In our real situation, not excluding the wild draws produces an asymmetry that is a) several times smaller, and b) significant only in the limited energy region where there are not many events.

For the next iteration of analysis, we will probably decide upon an optimal condition to reject the wild draws, and will therefore obtain a smaller matrix. Alternatively, one can use an uncorrelated error during the matrix expansion. The required expansion factor is smaller, hence reducing or eliminating the wild draws altogether.[3]

- It was suggested [72] that the the parametrization of the correction functions should be adjusted such that all the parameters values were O(1). While this is clearly a good idea that eliminates possible machine accuracy issues, it was decided not to modify the matrix generation and event selection codes due to fear of introducing bugs at the last minute. To convince ourselves that the machine accuracy was not limiting in this case we perform the following check. Using both the original and adjusted parametrization

[3]Some time after the first Double Chooz result was released at the LowNu conference and this dissertation was already in preparation, the final fit was repeated with a couple of detector response error matrices enlarged in different ways that avoid the wild draws. As long as the total error included in the matrices was not very different from the error of the original matrix, the fit results were consistent.

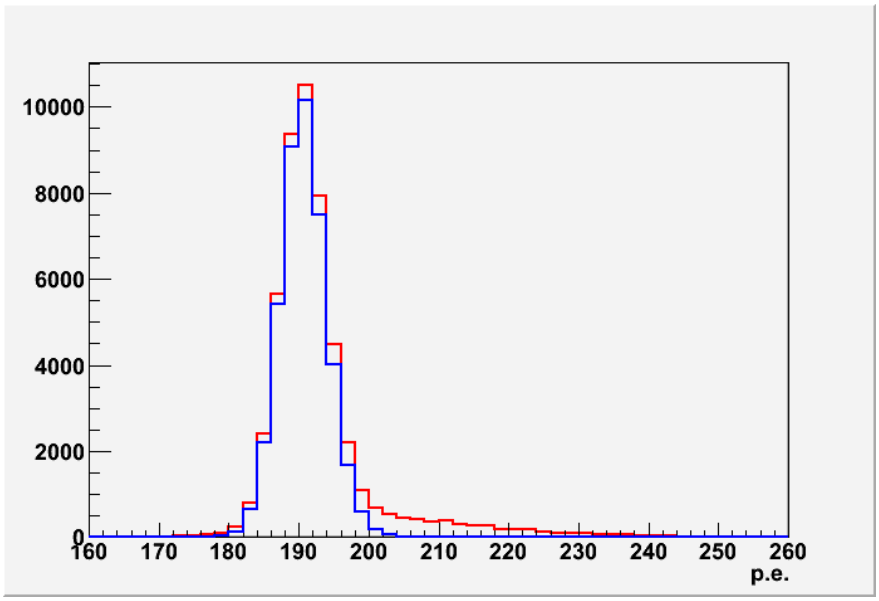

Figure 6.11:]
Effect of whild random draws on uncertainty distribution. The uncertainty on the prediction of the Ge-68 peak position at the center including (red line) and excluding (blue line) random draws with the first parameter of cor1 exceeding the peak position. Including the wild draws increases the RMS of the distribution and will result in a larger variance of the final fit error matrix.

and the corresponding error matrices we evaluate the uncertainty on the prediction of the Ge-68 capture peak at Z=500 mm by drawing multiple random parameter sets from each matrix. Figure 6.12 shows that the spread in the predictions is equivalent for both the original and adjusted correction functions, indicating that the round-off errors are not limiting the performance of the original parametrization.

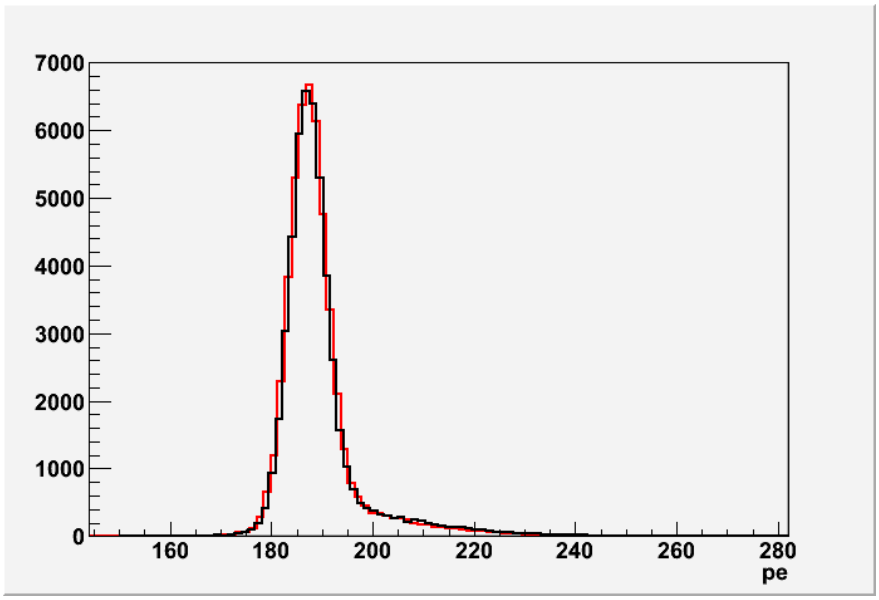

Figure 6.12: Original versus adjusted paramtrization. The uncertainty on the prediction of the Ge-68 peak position at Z=500. mm using the original (black line) and adjusted (red line) parametrization of the correction functions are shown. The adjusted parametrization has all parameter values close to 1 to avoid round-off errors during error matrix calculations. Both curves are consistent indicating that the machine accuracy is not limiting the computations using the original parametrization.

Part III

Final Analysis

The goal of the Double Chooz experiment is to measure the value, or put a limit, on the neutrino mixing angle θ_{13}. A non-zero value of the third mixing angle would manifest itself as a decrease in the rate, and, to a smaller degree, distortion in the spectrum of the detected neutrinos. In the first run, the expected values for the flux and the spectrum are based on the reactor information. The first Double Chooz disappearance analysis, based on 4 months of data, is presented in the next chapters. We will describe the criteria used to select the IBD candidates, characterization of the backgrounds, and the prediction of the positron rate and spectrum. The last part of the dissertation will be concluded by the description of the final analysis framework and the obtained results.

Chapter 7

Neutrino detection and its efficiency

The inefficiency of the neutrino detection is associated with hardware effects, such as trigger threshold and dead time, and analysis cuts. The efficiency of most of the cuts can be found using Monte-Carlo simulations. The difficult part is understanding the systematic uncertainty associated with imperfect modeling of underlying processes by the simulation, as compared to actual data.

7.1 Selection criteria and cuts

Below we list the final neutrino selection criteria used in the first Double Chooz analysis and describe the efficiency of individual cuts:

- First, general quality cuts are applied to any trigger as follows:
  - not an external trigger
  - has more than 0.5 MeV[1],
  - MQTQ < 0.09

[1]The conversion from reconstructed charge to the MeV variable is done by a single factor, 214 p.e./MeV, derived from the position of the hydrogen capture peak at the detector center. The same factor is used for the Monte-Carlo, after the MC charge is corrected as described in the previous chapter

  - RMS of pulse start times in the triggered PMTs is less than 40 ns[2]
  - separated from a preceding muon by at least 1 ms[3]

- The prompt event is defined by the following conditions:
  - Inner veto charge < 10000 DUQ
  - Energy between 0.7 and 12 MeV
- The delayed event is defined as:
  - Inner veto charge < 10000 DUQ
  - MQTQ < 0.06
  - Energy between 6 and 12 MeV
- The delayed event should coincide with the prompt in the time window between 2 and 100 μs. No spatial correlation cut is applied.
- The following multiplicity cuts are also applied:
  - The prompt candidate should be isolated from any valid preceding triggers by at least 100 μs.
  - The time coincidence window can contain only one delayed candidate. Existence of additional valid trigger in the time window causes the coincidence to be thrown out.
  - The time window from 100 to 400 μs following the prompt event must be void of valid triggers

The multiplicity cuts described above were introduced to eliminate hints of neutron capture peaks in the prompt energy spectrum (the same hint can be observed in the published CHOOZ prompt spectrum).

[2]This condition was recently found to be effective improvement in the light noise rejection strategy

[3]Muon is defined as an event with total charge in the Inner Veto more than 10000 DUQ, or energy in the inner detector more than 30 MeV

In the Monte-Carlo approach to the final fit, the efficiency of the cuts is naturally accounted for by performing the same selection on the Monte-Carlo event sample as was applied to the data. The relevant quantities are the discrepancies between data and MC due to imperfect modeling of the underlying processes. These discrepancies can be evaluated by comparisons of calibration data and MC, and are then included as systematic errors. In case some process is not modeled in the MC adequately, or at all, a correction factor can first be applied. For example, the MC sample does not contain muon events, therefore the amount of selected MC IBD candidates needs to be corrected for the muon veto applied to the data sample. To the first order, the muon veto decreases the MC live time by the number of muons tagged in the data sample, times 1 ms veto window. As we saw previously 4.1, this correction is on the order of 4.5% (the exact numbers based on the full official data set will be summarized at the end of the chapter). The second order effect is associated with muons overlapping within a single window. This increases the MC live time by a small fraction of a percent. Another second order effect is due to the fact the prompt and delayed events are correlated, which reduces the MC live time by a small fraction of a percent.[4]. As was discussed previously (Section 4.1), the systematics associated with calculating the dead time effects is negligible.

The MQTQ light noise cut, as was shown previously 4.1, rejects a fraction of a percent of physics events. For the delayed part of an event, a more stringent cut can be tolerated, as can be seen from the corresponding distributions (Figure 7.2). The newer cut that takes advantage of another characteristic signature of light noise events, namely the large spread in start times between the PMTs, is also highly efficient. As can be seen on Figure 7.1, only a fraction of a percent of physics events is rejected by the cut.

One of the most significant sources of inefficiency are the delayed time and energy cuts (neutron capture cuts). In the next section we evaluate the systematic errors associated with

[4]In case of exponential inter-event time distribution, when the time between successive muon vetoes is much larger than the capture time constant, as is the case, the efficiency for the delayed events decreases by a small fraction of a percent [64]

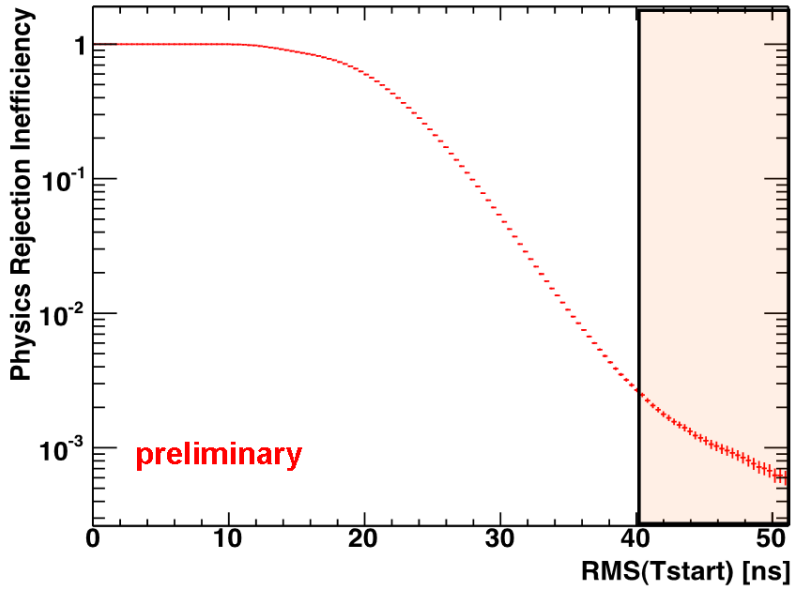

Figure 7.1: Distribution of RMS(Tstart) for physics events.

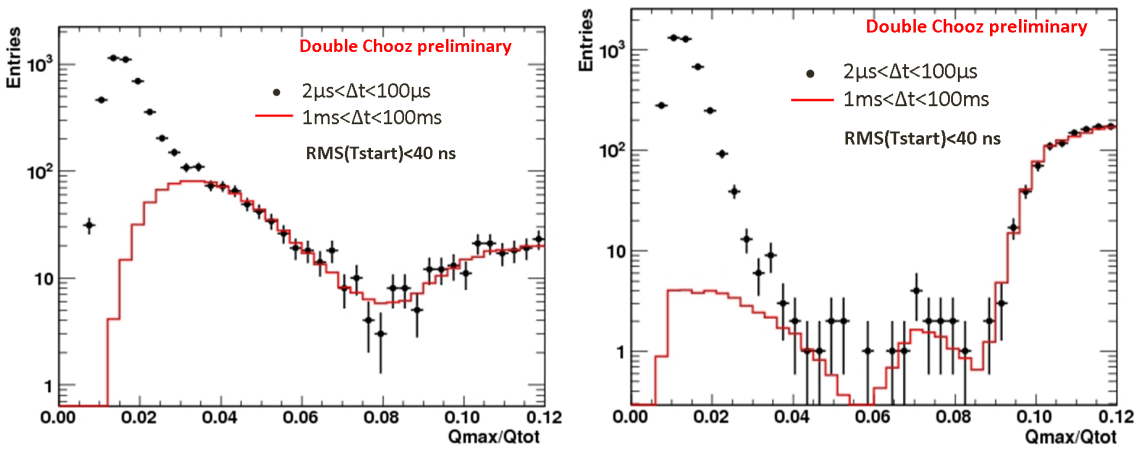

(a) Prompt (b) Delayed

Figure 7.2: Distribution of MQTQ variable. The distribution is shown for neutrino candidates (black) and accidentals (red) in the prompt (left) and delayed (right) energy windows.

the neutron detection efficiency.

7.2 Neutron efficiency

The neutron detection efficiency can be factorized into three terms:

$$\epsilon_n = \epsilon_{Gd} \cdot \epsilon_{\Delta T} \cdot \epsilon_{\Delta E}, \tag{7.1}$$

where ϵ_{Gd} is the fraction of neutron captures on Gd, $\epsilon_{\Delta T}$ is the fraction of neutron captures within the coincidence window, and $\epsilon_{\Delta E}$ is the fraction of Gd captures in the energy range between 6 and 12 MeV.

7.2.1 Time cut efficiency

To evaluate the agreement between data and MC we use Cf-252 calibration data collected along the Z-axis inside the target and at different positions in the GC guide tube.

Both data and MC samples were analyzed the same way. After generic data quality cuts, triggers were searched for a prompt candidate consistent with Cf-252 fission gamma cascade. The prompt candidate was required to be isolated from previous triggers by 1 ms. The prompt low energy cut was set as high as 7 MeV, resulting in a clean sample of Cf-252 fission tags, virtually free of accidentals contamination. The delayed candidates were collected in the 700 μs after a prompt, and were subjected to loose (1 MeV) energy cuts to avoid rejecting neutrons. Figure 7.3 shows the time distribution of delayed events consistent with Gd captures[5] relative to a prompt in the data and MC for the Cf-252 source positioned at the detector center.

The obvious difference between data and MC distributions is in the region between 0 and 10 μs, with the data events showing a depression compared to the MC. The likely explanation

[5]Gd captures selected by requiring the delayed energy be between 4 and 25 MeV, while for Hydrogen captures the region between 1 and 3 MeV is used

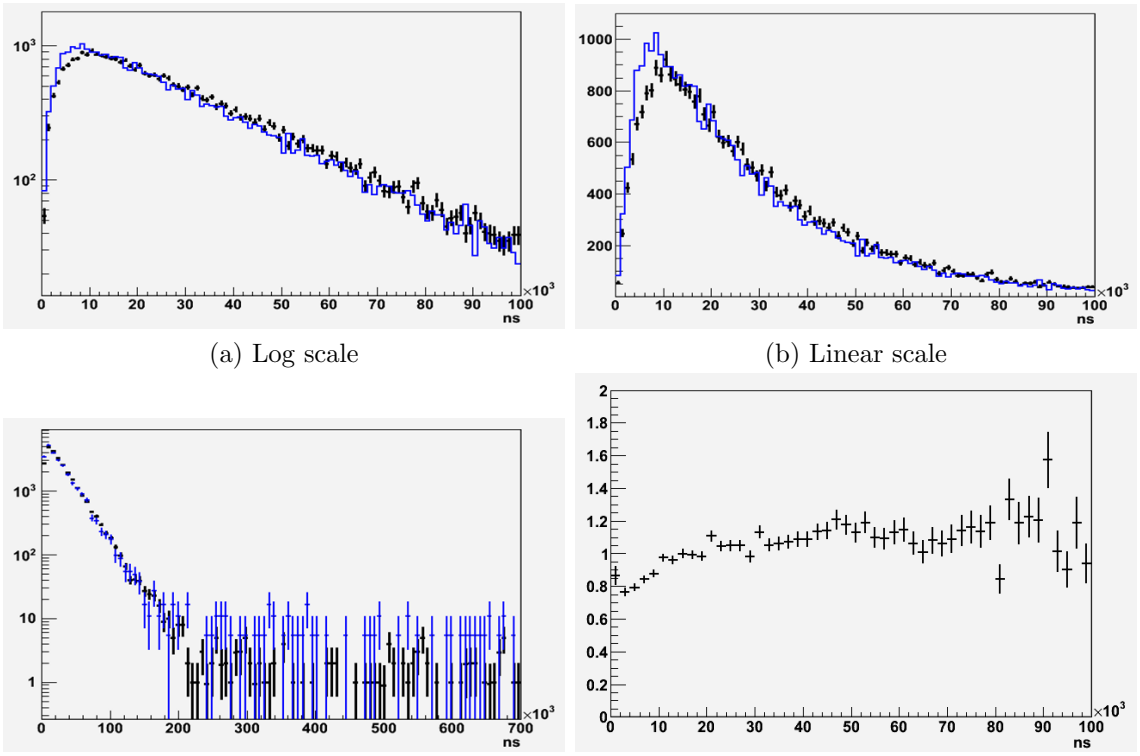

(a) Log scale

(b) Linear scale

(c) Full scale

(d) Data/MC ratio

Figure 7.3: Inter-event time distribution for Gd captures. MC (blue) distribution is normalized to the total number of events in the data (black) at the target center.

is the imperfect modeling of the neutron thermalization process in the MC. A concern was raised, however, that the depression may be a sign of trigger inefficiency at short inter-event times. To investigate the effect we can perform two checks. First, we can plot the inter-event time distribution of hydrogen captures. This plot is shown in Figure 7.4. Also, we can plot the inter-event time distribution for Gd captures relative not to the prompt event by to the first captured neutron. If the first neutron is also required to get captured at least 20 μs after the prompt event, the resulting distribution should contain only neutrons already thermalized. This plot is shown in Figure 7.5.

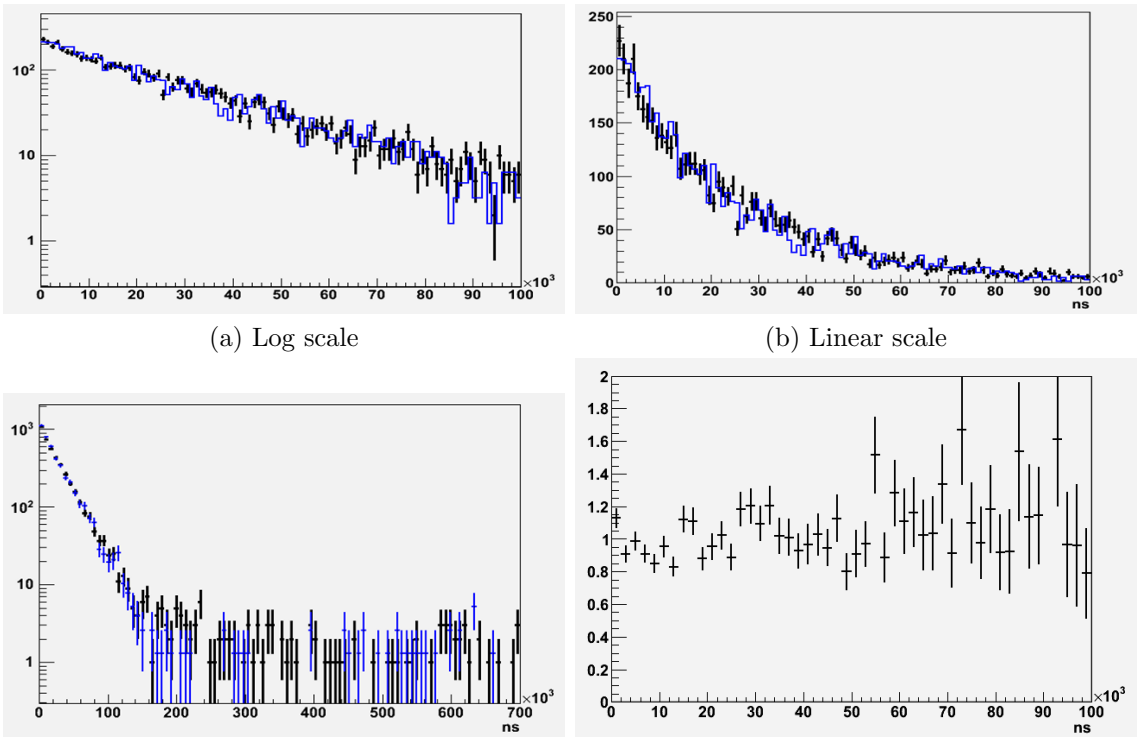

(a) Log scale

(b) Linear scale

(c) Full scale

(d) Data/MC ratio

Figure 7.4: Inter-event time distribution for H captures. MC (blue) distribution is normalized to the total number of events in the data (black) at the center.

The Figures 7.4 and 7.5 suggest there is no issue with registering triggers with short inter-event times in the data. The likely cause of the deficit in the captures on Gd at short inter-event times is imperfect modeling of thermalization and/or capture cross-section for epithermal neutrons, or related physics. In fact, an alternative physics list developed by one of the collaborators, that includes a more detailed treatment of molecular bonds and their

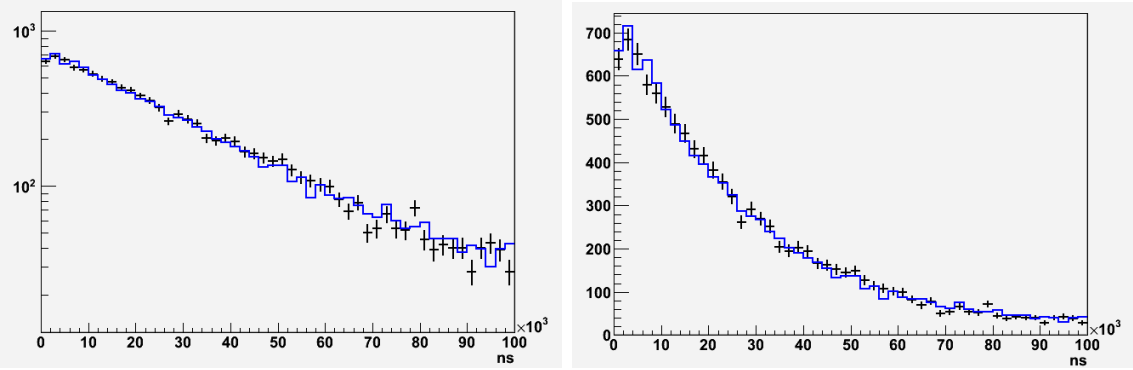

(a) Log scale (b) Linear scale

Figure 7.5: Inter-event time distribution relative to the first capture. The distribution of Gd captures at the center is plotted for relative to the first capture, which is required to occur at least 20 microsecond after a prompt. MC (blue) distribution is normalized to the total number of events in the data (black). No deficit of data events at short inter-event times is observed.

impact on the neutron cross-sections, shows significantly better agreement between data and MC at short inter-event times. The code, however, appeared to have its own imperfections, so for the first analysis the default Geant4 treatment was used.

We then calculate the efficiency of the Δt cut at different positions along the Z-axis in the target and along the ρ direction in the Gamma-Catcher, and evaluate the differences between data and Monte-Carlo. The efficiency is defined as the ratio of number of captures on Gd in the [2, 100] μs interval to the [0, 200] μs interval.

To decouple the effects of the capture time distribution from other issues related to the spill-in current and fraction of captures on Gd, which are discussed next, we weight each point by the relative fraction of captures in the Gd energy window at a given position (Figure 7.6). If the spill-in current is not modeled perfectly in the Monte-Carlo, the resulting discrepancy in the number of selected events can be compensated by a correction factor. Neutrons originating close to the boundary between target and gamma-catcher respond differently to the selection cuts, in particular to the Δt cut. Neutrons injected in the gamma-catcher have a longer lifespan, compared to neutrons emitted in the target, and are thus more strongly discriminated by the cut. The discrepancy between data and MC at these points can therefore come from a) imperfect modeling of the capture time distribution, and b)

imperfect modeling of other parameters affecting fraction of neutrons participating in spill-in (geometry factors, concentration of Gd atoms, etc.). Since b) is taken care of by a separate correction corresponding to different numbers of selected events in the boundary region, it was decided to decrease the relative weight of events occurring close to the boundary region, so as to avoid double-counting of errors. The relative fraction of captures in the Gd energy window drops when approaching the gamma-catcher boundary, and was used as a natural weighting function.

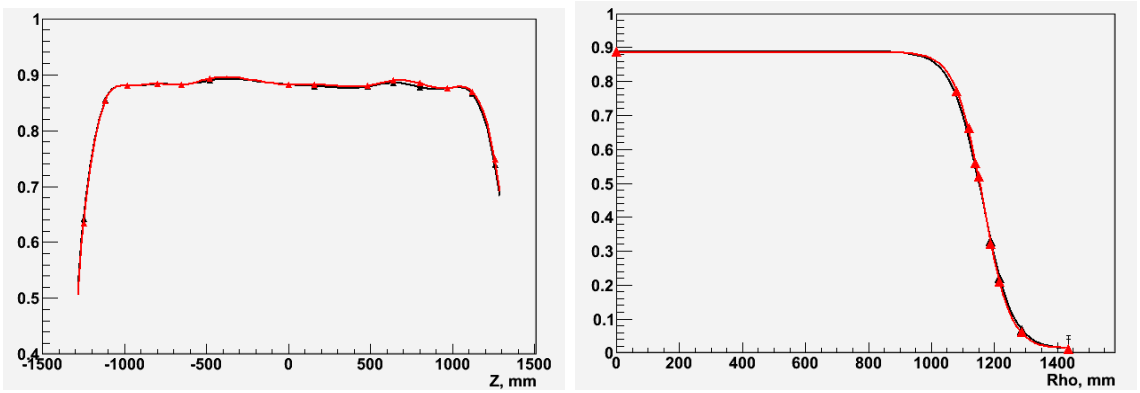

(a) Z-axis (b) Rho

Figure 7.6: The time cut efficiency. The efficiency of the time cut in the data (black points) and MC (red point) evaluated along the Z-axis inside the target and along the Rho direction in the Gamma-Catcher. The averaging is performed by integration of the spline function (Z-axis) and hyperbolic tangent fit (GC), shown as solid lines.

To calculate average differences between data and Monte-Carlo along the Z-axis we perform spline interpolation and integrate the curves in the target region:

$$\delta\epsilon_Z = \frac{\int_{-1250}^{1250} SP_{data}dZ - \int_{-1250}^{1250} SP_{MC}dZ}{\int_{-1250}^{1250} SP_{data}dZ}, \tag{7.2}$$

where SP - cubic spline. The average relative difference along the Z-axis is 0.21%.

To calculate the average difference along the rho direction we parametrize the observed dependence using hyperbolic tangent function, which fits the data points very well. In case of the Monte-Carlo, we can simulate points inside the target, which are not accessible for the currently available calibration systems, to validate the chosen parametrization and further

constrain the parameters. The average efficiency is then found by performing the integration in cylindrical coordinates in the target region:

$$\delta\epsilon_{Rho} = \frac{\int_0^{1150} \mathrm{Tfit}_{data} r dr - \int_0^{1150} \mathrm{Tfit}_{MC} r dr}{\int_0^{1150} \mathrm{Tfit}_{data} r dr}, \tag{7.3}$$

where Tfit - hyperbolic tangent fit function. The average relative difference along the Rho direction is 0.33%.

To combine the uncertainty along the Z and the Rho directions we can assume the numbers are 100% correlated, although that may be overly conservative. The combined uncertainty of 0.5% was used for the ΔT cut in the first analysis.

7.2.2 Gd capture fraction

The fraction of neutron captures on Gd is calculated as follows:

$$\epsilon_{Gd} = \frac{N_{Gd}}{N_{Gd} + N_H}, \tag{7.4}$$

were N_{Gd} and N_H - total numbers of neutron captures on Gd and Hydrogen, respectively. Figure 7.7 shows back to back comparison of data and MC delayed charge distribution for the Cf-252 source, combined for several positions along the Z-axis around the detector center. The delayed energy distribution shows the following characteristic features:

- Hydrogen captures around 2.2 MeV
- Gd captures around 8 MeV
- Double Gd+Gd captures around 16 MeV
- Double Gd+H captures around 10.2 MeV

Other effects that could result in a loss of a neutron, such as capture on carbon and neutron decay, are ignored as sub-dominant here.

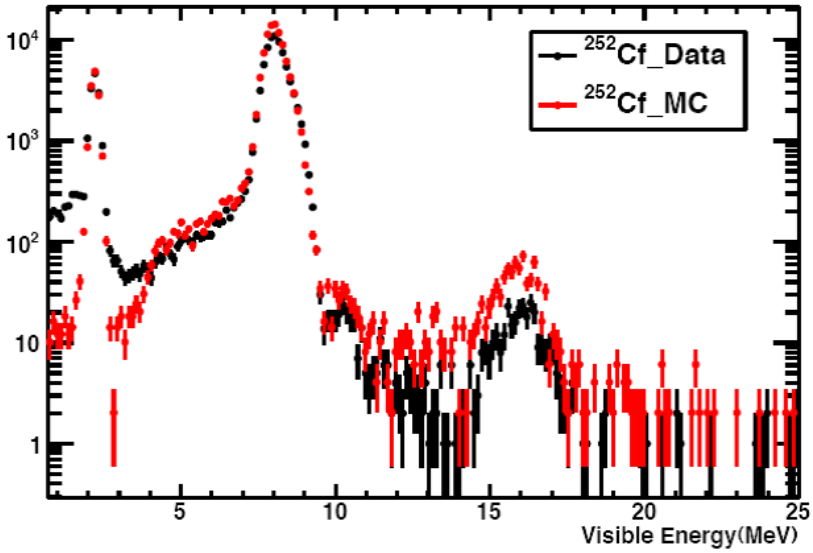

Figure 7.7: Cf-252 delayed energy distribution. The delayed energy distribution in the data (black) and MC (red) obtained with a Cf-252 source at several positions near the target center.

The four peaks were fit to extract the number of events corresponding to Gd and Hydrogen captures. The examples of the fits are shown in Figure 7.8.

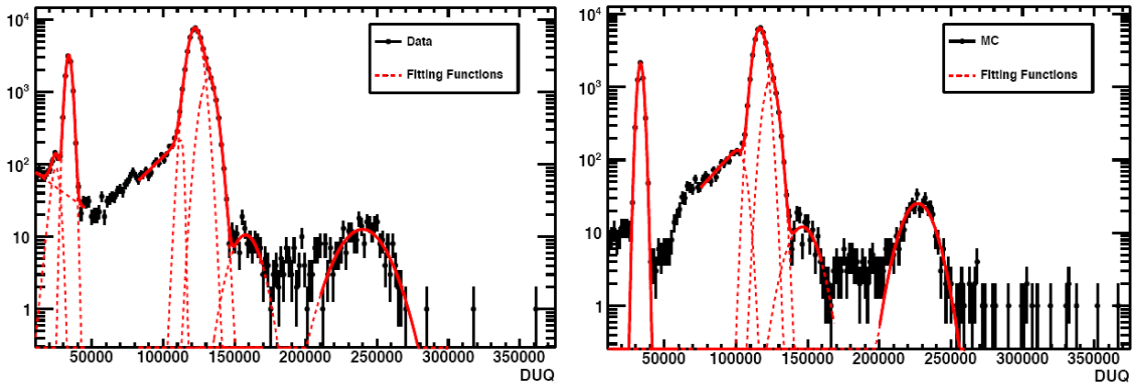

(a) Data (b) MC

Figure 7.8: The Gd fraction fit examples. The examples of the fits performed to extract the number of captures on Gd and Hydrogen.

To evaluate the robustness of the result the fit was performed independently using slightly different ways. Below we highlight the differences and choose the uncertainty that envelops the spread in the results obtained with the data:

1. Fitting the background under the Hydrogen peak by an exponential function results

in $\epsilon_{Gd} = 0.857 \pm 0.003$

2. Fitting the background under the Hydrogen peak by a sum of an error function and exponential gives $\epsilon_{Gd} = 0.856 \pm 0.003$

3. Using a loose prompt energy cut during event selection (E_{prompt} >0.7 MeV) results in $\epsilon_{Gd} = 0.860 \pm 0.0022$

4. Using a tight prompt energy cut during event selection (E_{prompt} >7.0 MeV) gives $\epsilon_{Gd} = 0.865 \pm 0.0023$

5. Fitting the Gd peak by a double Gaussian to take into account contributions of Gd-155 and Gd-157 isotopes results in $\epsilon_{Gd} = 0.862 \pm 0.002$

6. Not using individual fits for the two isotopes gives $\epsilon_{Gd} = 0.862 \pm 0.003$

The number that covers all the results above is 0.860 ± 0.005. In case of the MC the number is 0.880 ± 0.005. We then assign a correction factor of 2% to the Monte-Carlo to account for the difference in the central value. The associated relative error is 0.58% [74].

7.2.3 Energy containment efficiency

Gd emits a cascade of gammas totalling around 8 MeV. Placing a cut at 6 MeV safely isolates the neutron captures from the natural radioactivity and captures on Hydrogen, but also introduces some inefficiency due to escape of some of the gammas from the active region (gamma leakage). Modeling of the Gd cascade is a difficult task, and if the gamma energy and multiplicity distribution is not perfectly represented in the Monte-Carlo, different fraction of events will be rejected by the 6 MeV cut in the data and MC (imperfections in the geometry and materials definition may contribute as well). To evaluate the agreement the number of captures in the energy region between 6 and 12 MeV relative to the number of captures in the region between 4 and 12 MeV was calculated both for data and Monte-Carlo [75].

Figure 7.9 shows the energy containment efficiency for the Cf-252 source as a function of Z position in the target.

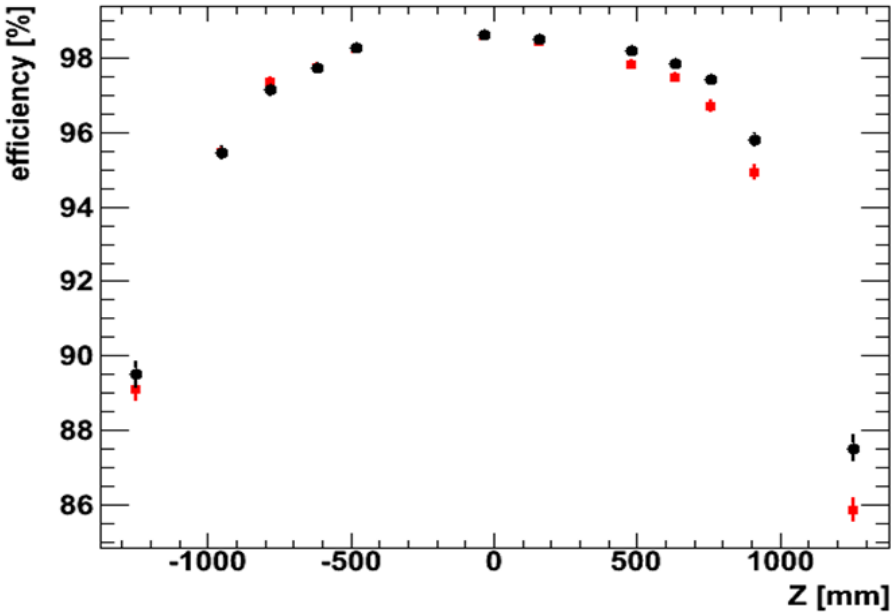

Figure 7.9: Energy containment efficiency. The plot shows energy containment efficiency in the data (black) and MC (red) along the Z-axis [75].

The mean discrepancy was found using a weighted average of target and guide tube data. An uncertainty of 0.6% [74] was assigned, which includes the contribution from the spread due to different weighting procedures. An alternative way would be to consider the anti-neutrino data/MC themselves. While the statistics are less, the observed discrepancy would automatically correspond to the average over the detector. This approach is currently under investigation.

7.2.4 Spill-in/out

If an IBD reaction occurs in the target volume close the boundary with the gamma-catcher there is a chance that the neutron escapes the target and get captured in the GC. This is called spill-out effect. At the same time, a neutron associated with an IBD event occuring in the gamma-catcher can wonder into the target and get captured on Gd. This effect is called spill-in. The two effects are known not to compensate each other precisely. The net

effect, or the "current" of IBD events, should be accounted for in order to correctly evaluate the amount of IBD interactions associated with the free protons in the target volume only. Monte-Carlo simulations for both anti-neutrino and mono-energetic 20 keV neutrons give consistent prediction of ≈6.5% spill-in current into the target region. This number, however, does not include the impact of the selection cuts, drastically different for the spill-in and "normal" IBD events. Neutrons produced in the GC find themselves in a more "friendly" environment, compared to the target neutrons that are agressively consumed by the Gd atoms. One would expect then the spill-in neutrons to live longer, compared to neutrons originating in the target, and hence be much more affected by the Δt cut. Figure 7.10 shows the fraction of events rejected by different time cuts separately for neutrons originating in the target and GC, confirming the expectation of stronger discimination against spill-in neutrons.

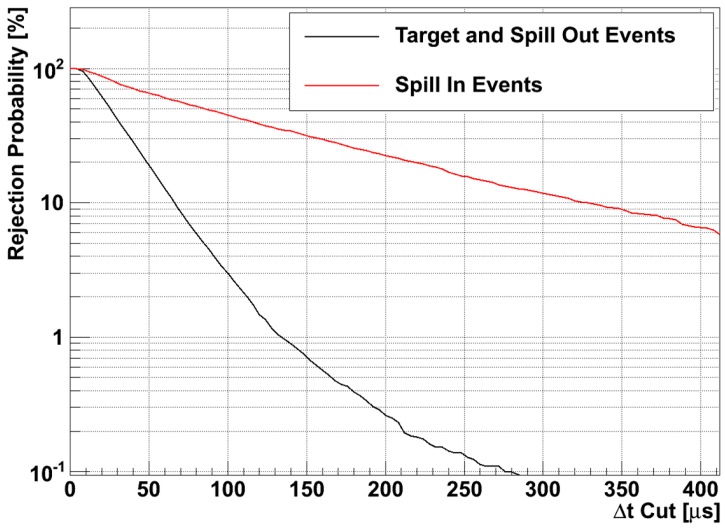

Figure 7.10: Rejection probability. Probability to reject a neutron is shown for different time cuts for neutrons originating in the target (black) and gamma-catcher (red) [76].

Along similar lines, all spill-in neutrons are captured relatively close to the boundary, where the effect of the gamma leakage is highest. Therefore, the average effiency of the 6 MeV Gd energy cut is smaller for a spill-in than it is for an "average" target neutron.

According to Monte-Carlo simulations [77], the effect of the [2, 100] μs time cut is to reduce the spill-in current from 6.5% to 3%. The Gd cut additionally reduces the spill-in current to 2.1%.

A completely different effect was investigated in [78], which used an alternative Monte-Carlo simulation that treats low energy neutron physics more accurately than our current Geant4 code does. Use of the TRIPOLI-4 code allowed to take into account effects of molecular bonds between carbon and hydrogen atoms. One of the apparent molecular effects is to increase the mean capture time on Gd (Figure 7.11).

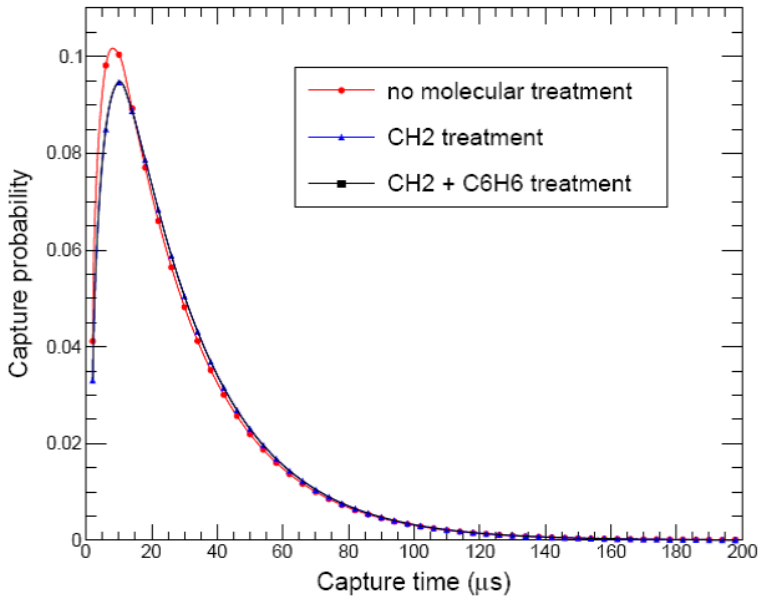

Figure 7.11: Capture time distribution for different molecular treatment options. Obtained using TRIPOLI-4 simulation [78]

Including the impact of the molecular bonds further decreases the apparent spill-in current and gives the final number of 1.37±0.06(stat)±0.37(syst)%. The difference between results including and excluding the molecular treatment is taken as a 2σ systematic error. Note that, as was mentioned earlier, the additional Geant4 library was developed by one of the collaborators to take into account the molecular effects, but was not used for the Monte-Carlo production for the first analysis. We, therefore, apply the normalization correction to the number of selected MC events to compensate for the lack of the molecular

bond treatment.

7.3 Prompt cut efficiency

The efficiency of the prompt 0.7 MeV cut is defined as the fraction of positron events above the cut, relative to the total number of positrons. While the minimum energy deposition associated with an IBD positron is 1.022 MeV, some of the events may have a lower value of reconstructed charge due to gamma leakage and resolution effects. This effect is small and can be quantified with the Monte-Carlo simulation alone. A more difficult question is the position of the hardware trigger threshold. If it is not low enough, the efficiency of detection of the low energy positrons may be decreased and, which is worse, be energy depenendent. As was described earlier 2.1.3, the data aquisition system is reading out the detector upon assertion of the hardware trigger. We, therefore, need to verify the position of the trigger threshold. In reality, the threshold is not a delta function, so we need to know the trigger efficiency curve and evaluate the efficiency as a function of reconstructed charge/energy.

7.3.1 Trigger threshold

The trigger curve was obtained by analysing the response of the trigger system as a function of the stretcher signal amplitude. As was mentioned in 2.1.3, the analogue sum of the PMTs signals is stretched before entering the trigger boards to ensure the overlap of individual PMTs pulses. The amplitude of the stretcher signal is therefore a proxy to the total energy of the event. Figure 7.12 shows a typical stretcher signal summed over all channels in one trigger group.

The trigger efficiency was calculated in the following steps [80]:

- Trigger release time position was determined inside the stretcher waveform
- Trigger efficiency was determined as a function of the stretcher amplitude at the trigger release time (Figure 7.13a)

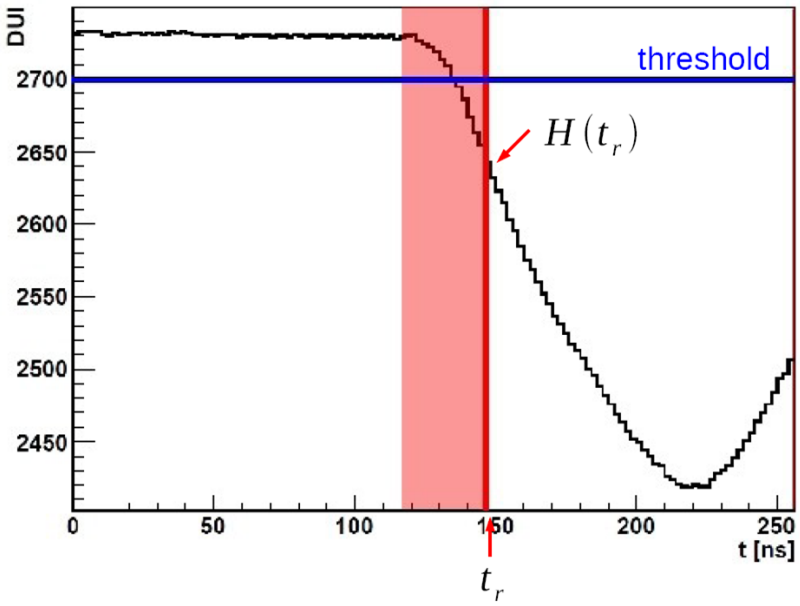

Figure 7.12: Waveform of a typical stretcher signal. The plotted distribution was summed over one of the two trigger groups. Position of the threshold and the trigger release time are shown. [79].

- The correlation between stretcher amplitude and the inner detector charge was mapped out (Figure 7.13b)

- Using the above two dependencies, the trigger efficiency as a function of inner detector charge was obtained

The efficiency curve obtained as described above is shown in Figure 7.14. The error bars include contributions from statistics, error on trigger release time, stability in time ("run time stability"), discrepancy between different trigger-board related methods, spread in the charge vs stretcher amplitude map due to different event types and reconstruction effects.

The method used above to determine the trigger efficiency involves analysis of the stretcher signal and trigger timing. A completely differnt approach is to use the calibration source data for a low energy gamma source and compare it to the Monte-Carlo prediction generated without trigger simulation. The deviation between the data and MC charge response in the low energy region provides a completely independent way to evaluate the trigger curve immediately as a function of reconstructed charge. The calibration data method may

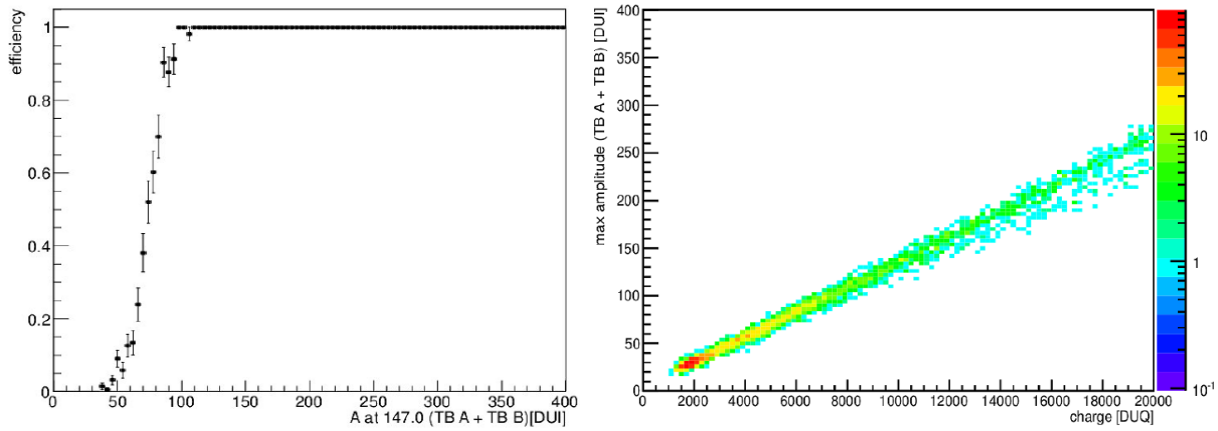

(a) Efficiency = f(stretcher amplitude)

(b) Stretcher amplitude = f(DUQ)

Figure 7.13: From stretcher efficiency to trigger efficiency. The plot shows trigger efficiency as a function of the stretcher signal amplitude and the map of the amplitude into the Inner Detector charge [80].

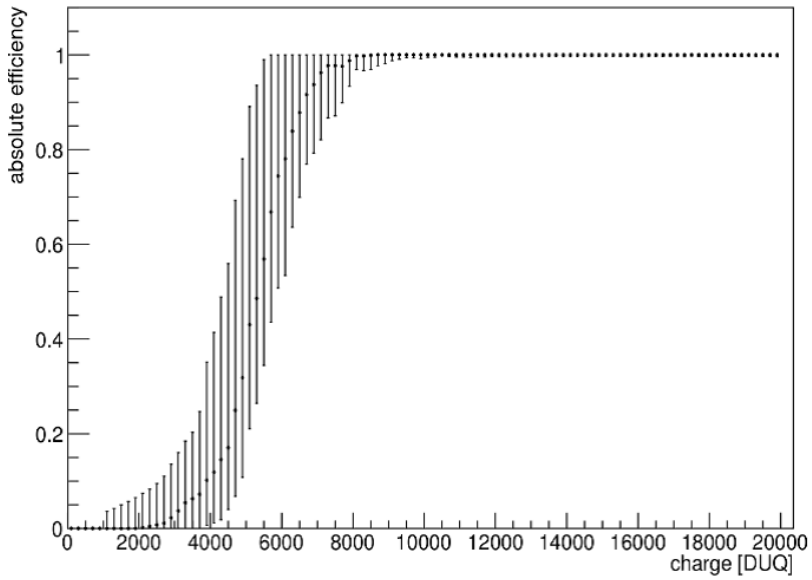

Figure 7.14: Trigger efficiency as a function of reconstructed charge [80].

be less accurate than the stretcher method due to lack of statistics, but the difference between the curves obtained by the two methods is a good way to evaluate the systematic error on the trigger efficiency. The trigger efficiency curve using the calibration source approach was obtained by the author of this thesis. To that end, the calibration data for the Cs137 source deployed at the detector center was used. Figure 7.15 shows the charge distribution in the data and MC. They were obtained in the following way:

- Muon veto and MQTQ cuts were applied to the calibration data run
- Same cuts were applied to a typical physics run
- The charge histogram for the physics run was normalized by the ratio of livetimes and subtracted from the calibration data charge histogram as a background
- The Monte-Carlo was generated without the trigger simulation
- The position and intergral of the data and Monte-Carlo full absorption peaks were made to match

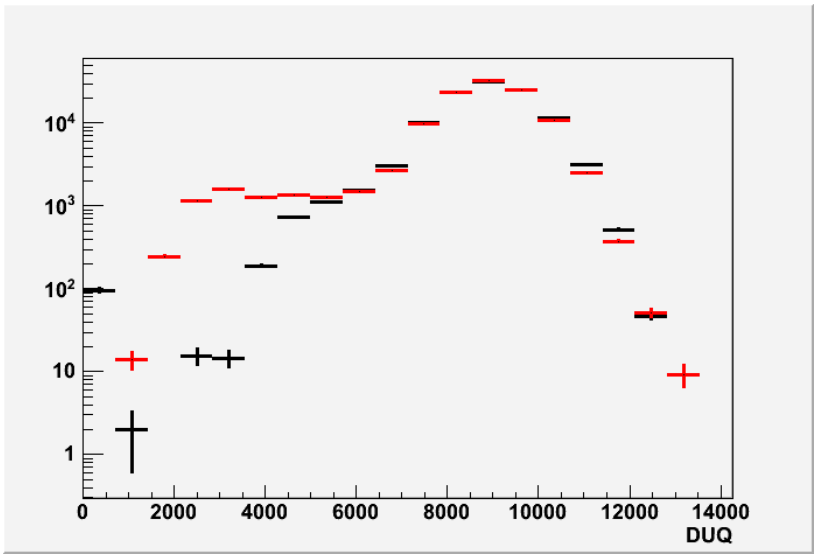

Figure 7.15: Charge distribution for Cs-137 source. The reconstructed charge distribution is shown for the data at the center (black) and MC (red).

Plotting the ratio of the bin content in the data and MC histograms, shown in Figure 7.15, demonstrates a clear trigger efficiency curve. Overlaying this curve with the one obtained by the stretcher method (Figure 7.16) shows the two results are consistent.

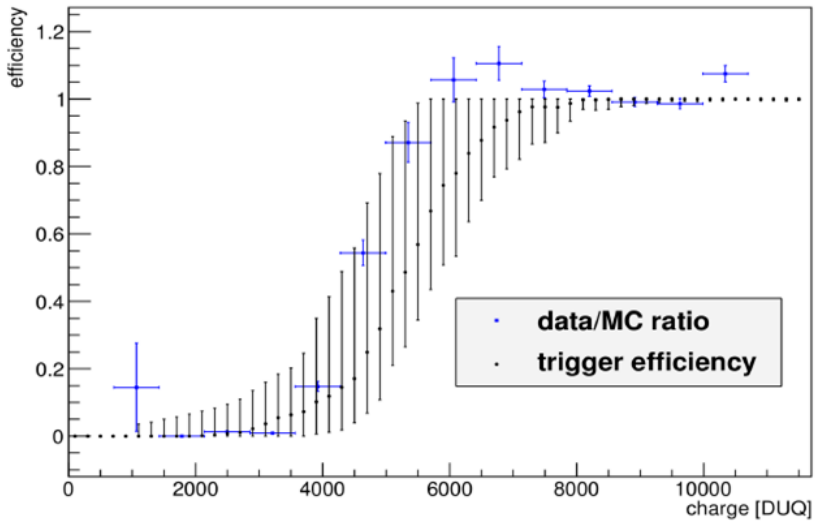

Figure 7.16: Stretcher versus source methods. Trigger efficiency is shown as determined using the stretcher amplitude method (black) and the calibration data method (blue). [80]

Taking the stretcher curve as the baseline, the trigger threshold (i.e. 50% efficiency) is reached at 0.35 MeV, and the efficiency at the prompt cut position (0.7 MeV) is 100%. The uncertainty of the curve at this energy is 0.4%, dominated by the run time stability [79]. Given the apparently low position of the trigger threshold, the prompt cut efficiency is evaluated with the Monte-Carlo and is found to be $> 99.9^{0}_{0.4}\%$.

As an illustration, Figure 7.17 shows the trigger curve overlaid with the charge distribution of the Ge-68 source at the target center (Ge-68 corresponds to the minimum positron signal in the detector).

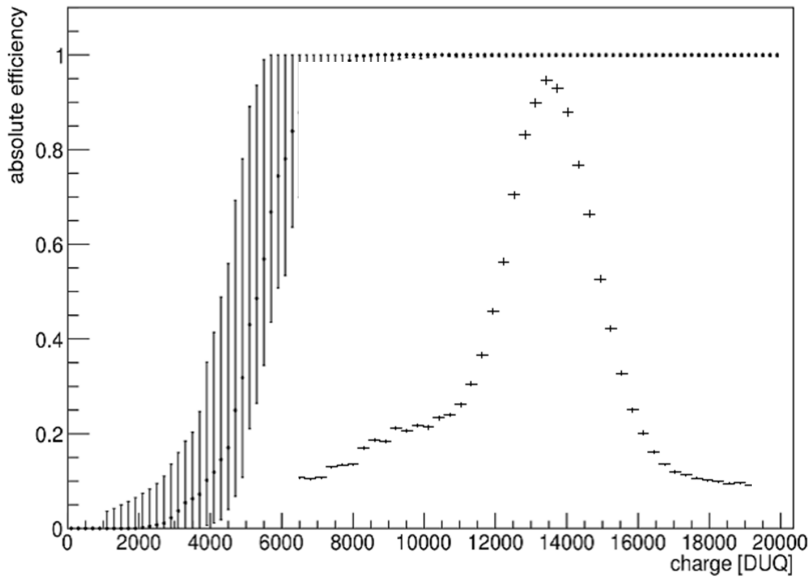

Figure 7.17: Trigger efficiency curve overlaid with the Ge-68 charge distribution.

7.4 Results of the selection

The physics data are accumulated in 1 hour increments (physics runs). After excluding the following bad runs:

- Runs affected by a high-voltage instability in one of the PMTs
- Runs with extremely high noise level from one of the PMTs
- Runs labeled as physics while the calibration system was running
- Other runs mistakenly mis-labeled as physics
- Runs accumulated while one of the FEE crates was turned off
- Runs shorter than 300 seconds for any reason

the total of 2594 runs were approved for the first Double Chooz analysis. Below is the series of figures that demonstrate results of the final selection:

1. Run time by day (Figure 7.18)

   The total run time used for the first analysis is 101.5234 days of data, collected from April 13th 00:00:00 to September 18th 11:00:00.

2. Muon veto time by day (Figure 7.19)

3. Delayed (neutron capture on Gd) energy peak (Figure 7.20)

   The fraction of captures on Gd cut is 86.0±0.6%, with 94.5±0.6% of Gd captures surviving the 6 MeV cut. The additional uncertainty associated with imperfect modeling of detector response as function of energy and position, is naturally included in the error matrix of the detector response, described later.

4. Prompt-Delayed time distribution (Figure 7.21)

   The efficiency of the time cut (from 2 to 100 μs) is 96.5±0.5%

5. Prompt-Delayed reconstructed distance (Figure 7.22)

6. Prompt-Delayed energy distribution (Figure 7.23)

7. The rate of the selected candidates by day (Figure 7.24),

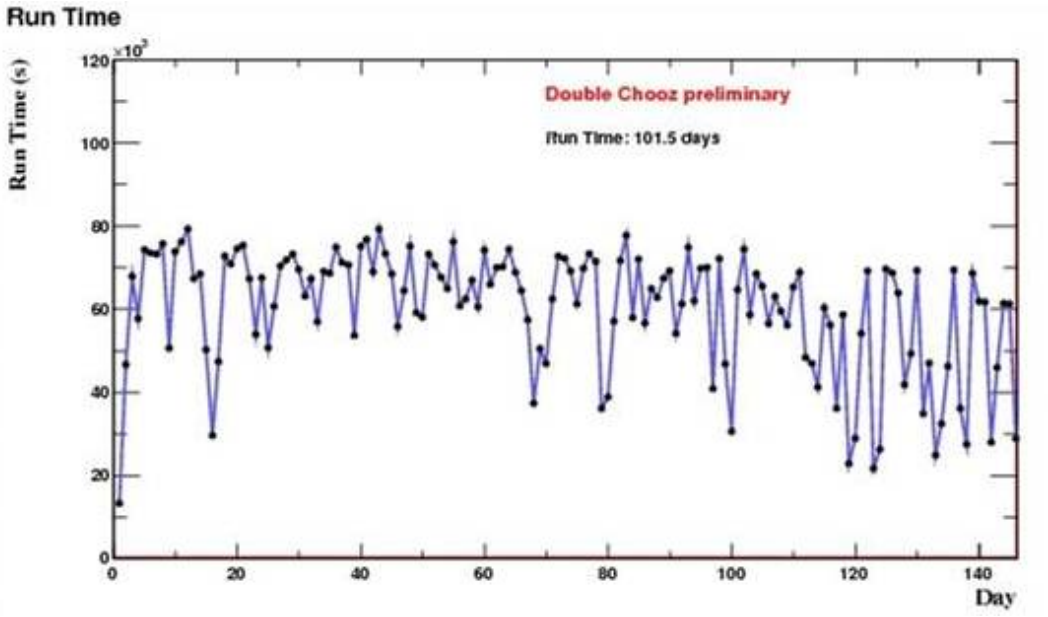

Figure 7.18: Run time.

Application of the selection criteria described above delivers total of 4121 neutrino candidates. These also include background events, which we estimate in the next section.

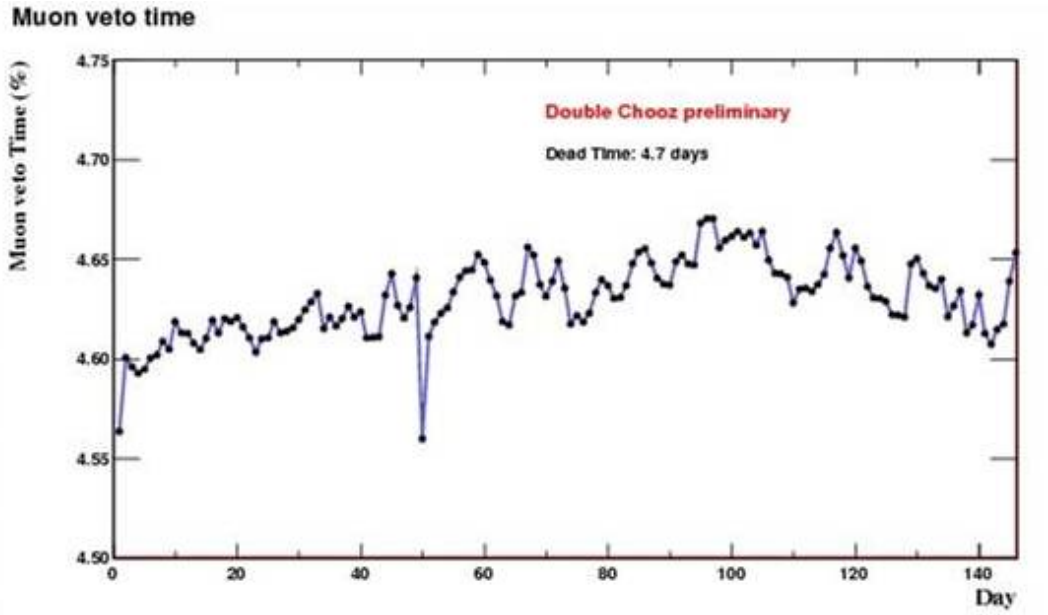

Figure 7.19: Dead time.

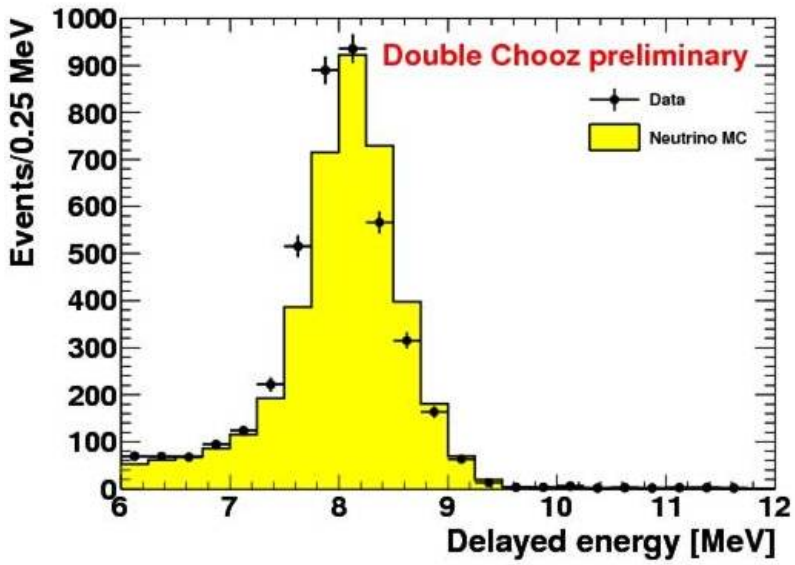

Figure 7.20: Gd neutron capture peak in the data (black) and MC (yellow).

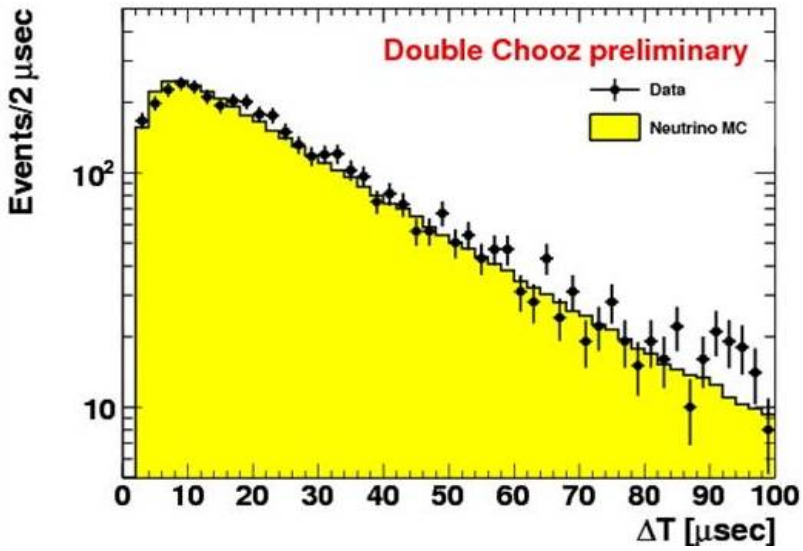

Figure 7.21: Inter-event time distribution in the data (black) and MC (yellow).

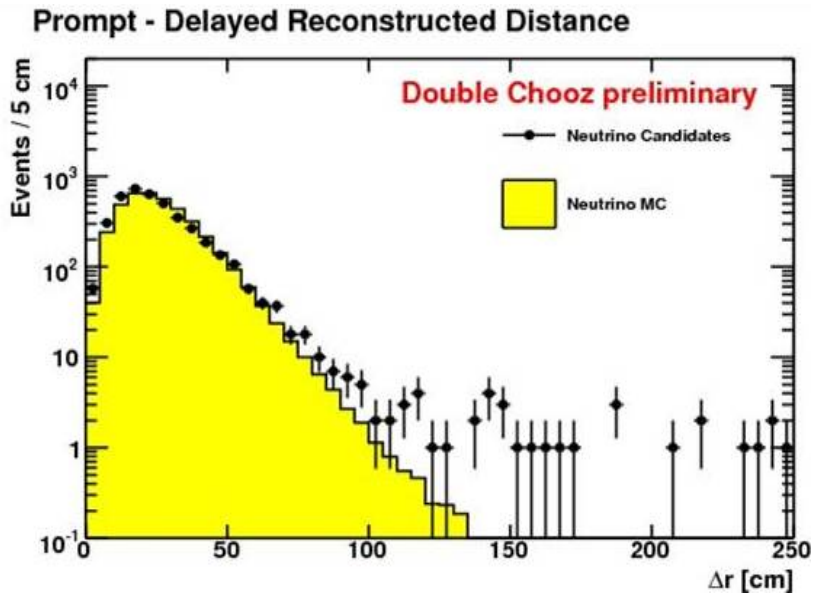

Figure 7.22: Inter-event distance. Distance between prompt and delayed event positions in the data (black) and MC (yellow). Note that the MC shown does not include backgrounds.

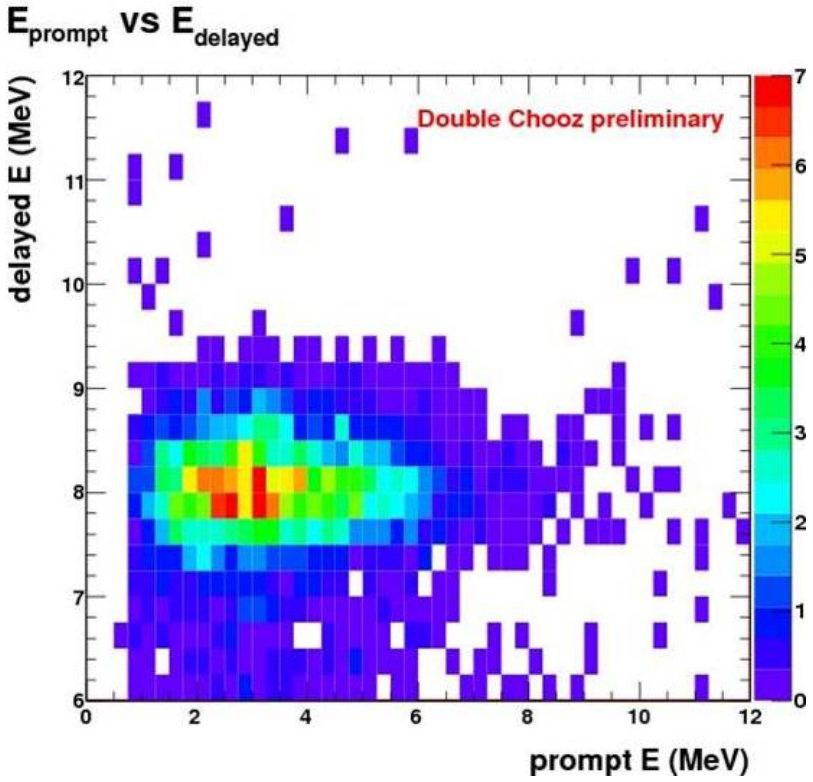

Figure 7.23: Prompt vs. Delayed energy for the selected candidates.

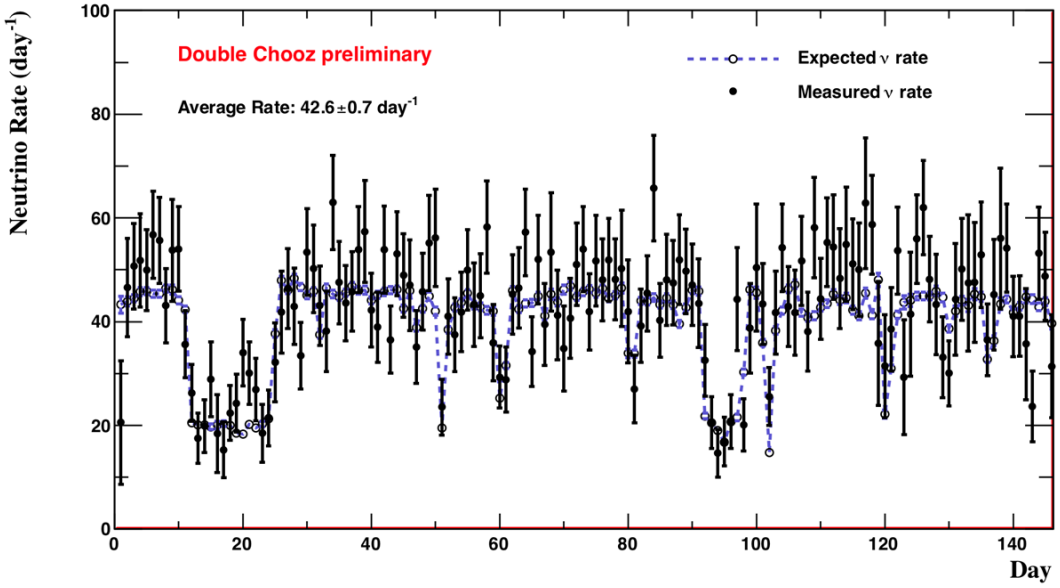

Figure 7.24: Rate of the selected candidates by day. Prediction does not include backgrounds.

7.5 Backgrounds

As was discussed in Section 1.4.1.1, the relevant backgrounds for a reactor experiment are accidental coincidences and correlated backgrounds, of which Li-9 and fast neutrons are the major ones.

7.5.1 Accidentals

Accidental backgrounds were already estimated during first comparison stage at the beginning of the first physics run (Section 4.2). Repeating the analysis using the final data set and taking advantage of the improved light noise rejection strategy, as well as more sophisticated selection criteria, results in even lower rates. Figure 7.25 and Figure 7.26 show the rates and spectra of the singles backgrounds in the prompt and delayed energy windows, respectively. Figure 7.27 shows the accidental rate and spectrum. The rates are lower than the ones quoted in the proposal, and the spectra show expected bumps corresponding to the K-40, Tl-208, and neutron capture on Gd lines. The rate of accidental coincidences obtained with the offtime method is 0.332±0.004 per day.

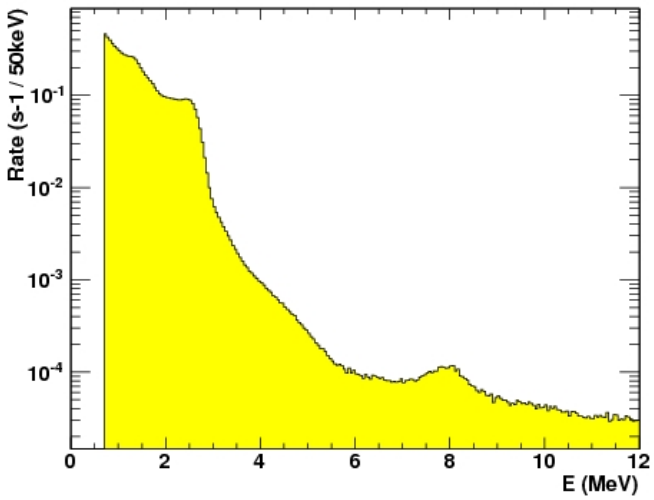

Figure 7.25: Spectrum of the singles background in the prompt energy window.

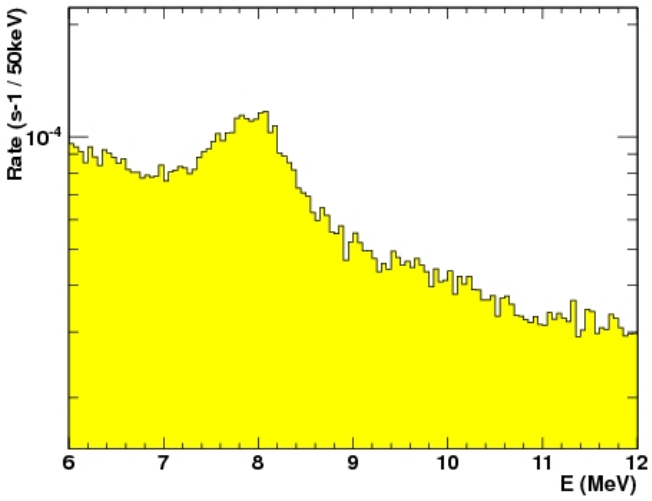

Figure 7.26: Spectrum of the singles background in the delayed energy window.

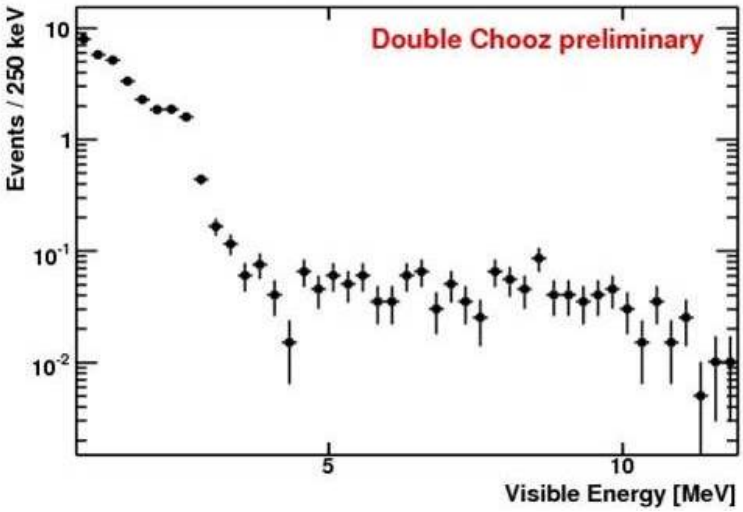

(a) Accidentals spectrum

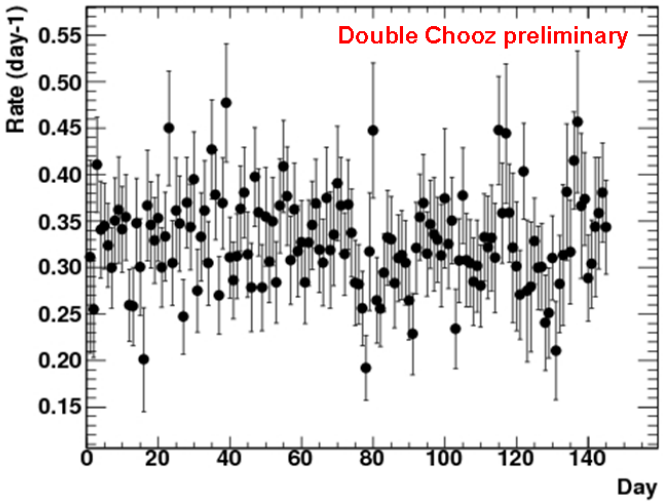

(b) Accidentals rate

Figure 7.27: Spectrum and daily rate of the accidentals backgrounds in the far detector.

7.5.2 Li-9

As was mentioned in Section 1.4.1.1, Li-9 is an isotope produced during muon spallation. It is unstable against beta decay and in 50% of cases emits a neutron, therefore mimicking an IBD coincidence. The half-life of Li-9 is 178.3 ms, making it difficult to employ the usual muon veto technique. One can, however, estimate the contamination of the selected IBD candidates sample by correlating the IBD coincidences with all preceeding muon-like energy depositions (triple coincidence). For a true neutrino event, the time distribution should be flat, while the Li-9 events should have the exponential time distribution with a decay constant of 257 ms. Performing this excercise results in a fit completely dominated by the flat distrubtion (Figure 7.28). Taking the fit result at the face value gives a negative best-fit estimate on the mean value of Li-9 events, with an upper limit of 342 Li-9 events (or less than 3.5 events per day).

From the experience of previous experiments, KamLAND in particular, we know that it is the more energetic, sometimes called "showering", muons that mostly contribute to the cosmogenic isotope production. Double Chooz, being a smaller detector, is less well equipped for identification of the showering muons, compared to KamLAND, but one can still attempt to descriminate against the lower energy muons by applying an energy cut. Repeating the triple coincidence fit while requiring the muon preceeding the IBD event to deposit at least 600 MeV of energy in the detector results in the clear exponential dependence (Figure 7.29). The number of Li-9 events from the fit with the lifetime fixed to the true value is 143±26 events. The unconstrained fit gives consistent result of 141±28 Li-9 events with best fit lifetime value of 236±64 ms. Repeating the fit with lifetime fixed to the values from 170 to 290 ms and showering thresholds from 400 to 750 MeV results in Li-9 rate estimates consistent within 20%.

Combining the two approaches we assume a central interval for the Li-9 rate estimate of 2.3±1.2 events per day, where the lower limit is the mean value minus 1 sigma error of the

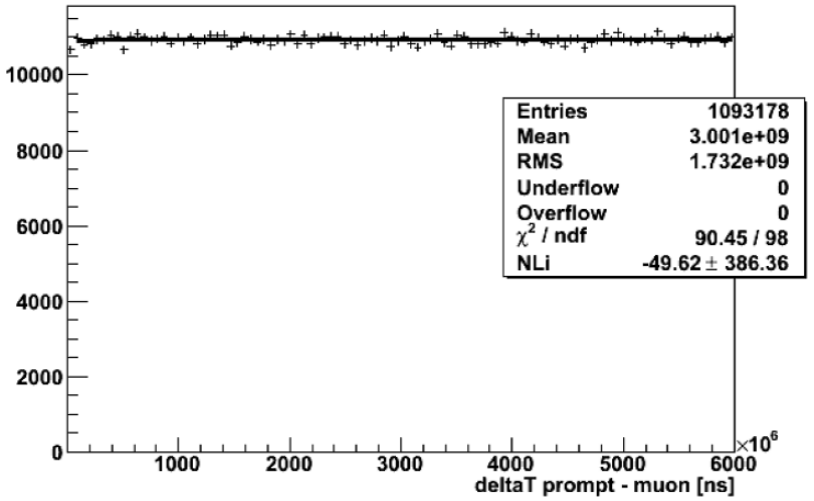

(a) Exponential fit

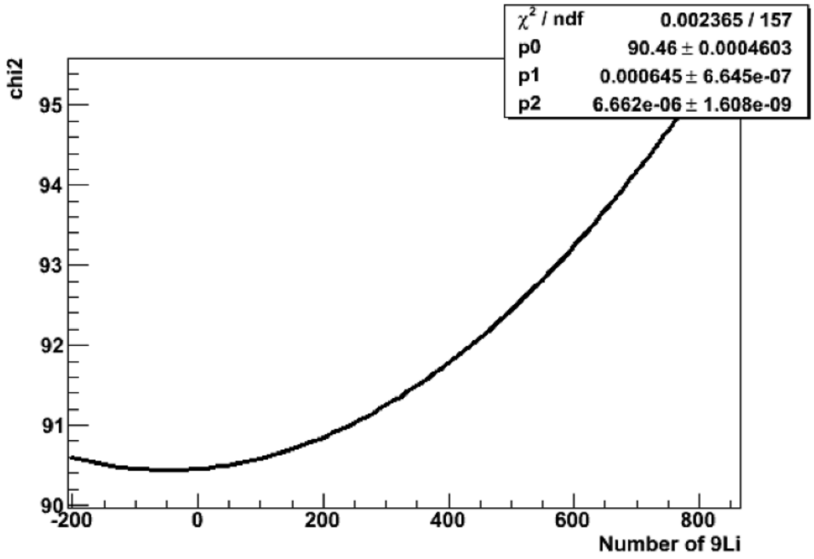

(b) Fit chi-square = f(Li-9 event count)

Figure 7.28: Estimate of the Li-9 event count. The estimate is obtained by an exponential fit to the inter-event time distribution between a muon and a prompt IBD candidate [83].

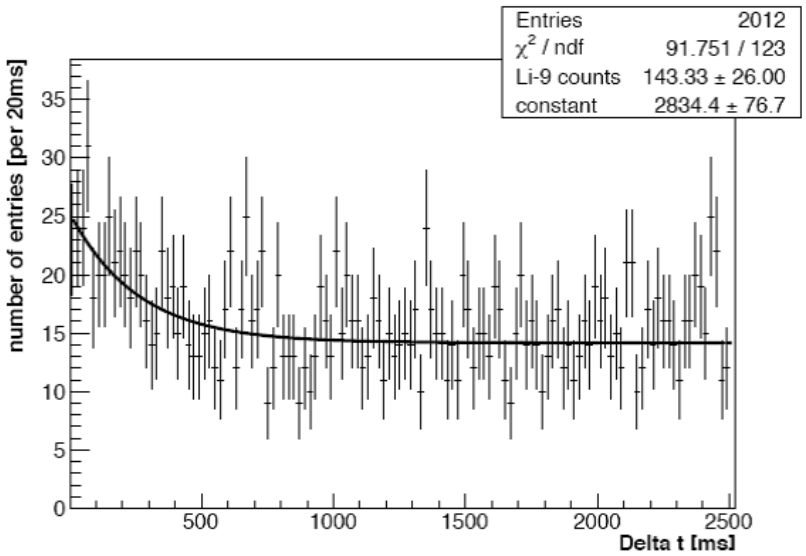

Figure 7.29: Exponential fit of the tripple coincidences. The fit is performed to the inter-event time distribution between a showering muon and a prompt IBD candidate [84].

showering muon analysis, and the upper limit is given by the first analysis, not employing any muon energy cuts.

Extracting the shape information on Li-9 from the data is not easy due to low statistics. Figure 7.30 shows the spectrum of Li-9 candidates obtained by separating neutrino-like events using time-since-last-muon cut (<0.7 s for Li-9 and 0.7-10 s for neutrino-like) and also requiring distance between the prompt IBD candidate and the preceeding muon track to be less than 0.5 m. At the same time, the prompt spectrum of Li-9 events can be modeled relatively accurately due to extensive studies of the Li-9 nucleus levels ([86]) and the available codes that calculate beta spectra. Figure 7.31 shows the theoretical Li-9 spectrum obtained using the code adapted from KamLAND's K-Beta library. This spectrum was used in the Monte-Carlo simulation of the Li-9 background and its uncertainty is assumed to be small compared to the rate error.

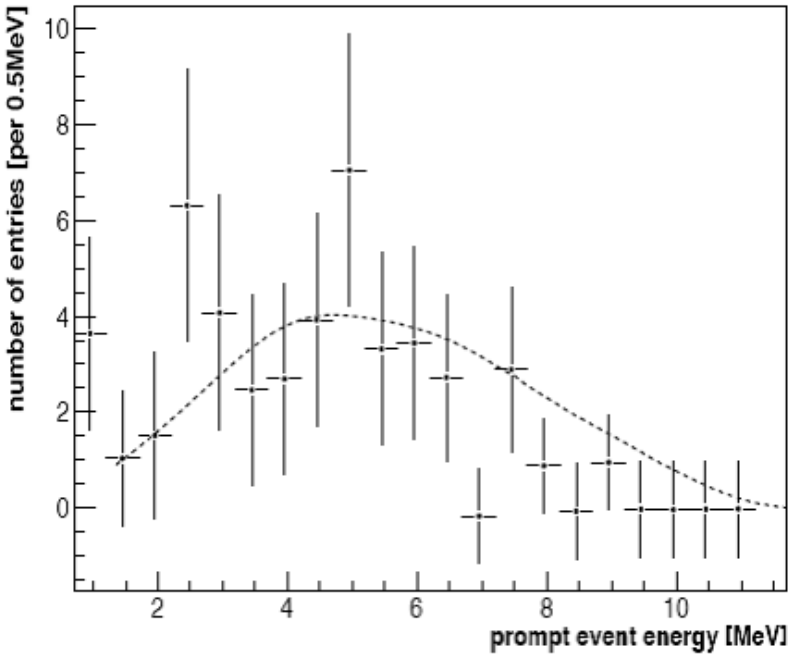

Figure 7.30: Li-9 prompt energy spectrum. The spectrum is extracted by separating neutrino candidates using time and distance from a muon track cuts. The Double Chooz spectrum (points) is superimposed with the published KamLAND spectrum of Li-9 and He-8 events (dashed line, [85]) showing good agreement.

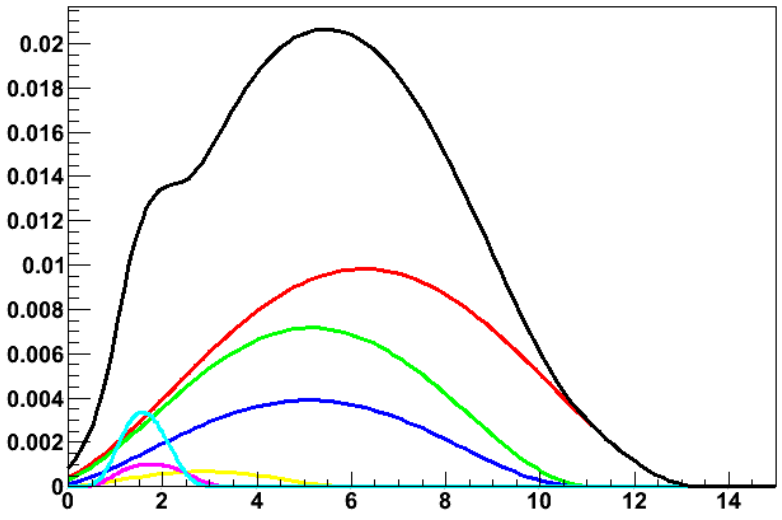

Figure 7.31: Beta spectrum of Li-9 events used in the MC. Different colors correspond to different decay branches (including branches that do not have a neutron in the final state). X axis is visible energy, MeV.

7.5.3 Fast neutrons

The fast neutrons are produced by the cosmic muons passing through or near the detector. They mimic the prompt part of an IBD event by depositing energy via recoil protons, and then get captured, faking the delayed part of the IBD. The fast neutrons enter the detector through the inner veto and can deposit energy there (which can also be combined with the energy deposited by the parent muon, if the latter partially traverses the region). To evaluate the fast neutron contribution, one of the approaches employed by Double Chooz was to perform the selection with the Inner Veto cut reversed, i.e. more than 10000 DUQ of charge was required to be deposited in the IV for the prompt event. This approach selects the fast neutrons that deposited enough energy on their way to the inner detector and, while may not provide the most reliable rate estimate, has an advantage that it directly obtains the prompt energy spectrum free of the IBD candidates in the low energy region and can therefore verify the spectrum shape. The resulting energy spectrum is flat in the high energy region, but contains a distinct bump around 5 MeV. Application of 6.6 μs inter-event time cut removes the peak, which suggests the peak is associated with Michel electrons. The vertex distribution of the prompt events, expected to be uniform for true fast neutrons, also demonstrates clustering of the events from the 5 MeV bump around the detector chimney - the likely way for stopping muons to sneak into the inner detector (Figure 7.32). These observations alert us to the fact that one needs to remove the stopped muon contamination from the rate calculations to avoid over-estimation of this background.

Repeating the analysis with the standard IBD cuts, but the extended prompt energy window, we find 164 events total in the region from 12 to 30 MeV. Separating the sample using vertex cut around the chimney and 6.6 μs inter-event time cuts, we arrive at an estimate of 59 stopped muon events and 105 "true" fast neutrons. Interpolating the numbers into the standard prompt energy window of 0.7 to 12 MeV, assuming flat energy spectrum, gives 0.68 events/day for the fast neutrons. To assign the error on the number we assume 100%

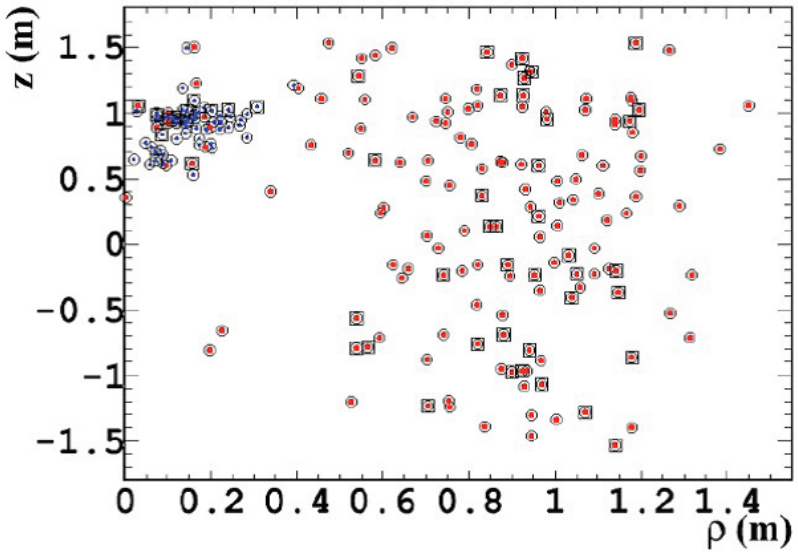

Figure 7.32: Reconstructed vertex distribution for fast neutrons candidates. Blue points show events with inter-event time less than 6.6 microsecond (consistent with a stopped muon). Red points are the remaining events (consistent with "true" fast neutrons. Squares indicate IV-tagged events [81].

uncertainty on the extrapolation of the stopped muon component, and further scale it up to account for a larger rate of IV tagged events in the low energy region. The fast neutron rate used in the first Double Chooz analysis is therefore 0.7±0.5 events/day. The last thing we need to do is to assign the shape error. While we know the excess of events around 5 MeV, observed in the IV tagged sample, is due to Michel electrons, we conservatevly take the bin-bin differences between the flat spectrum and the IV tagged spectrum as a fast neutron shape error (Figure 7.33). The corresponding error matrix will be shown in the final fit chapter.

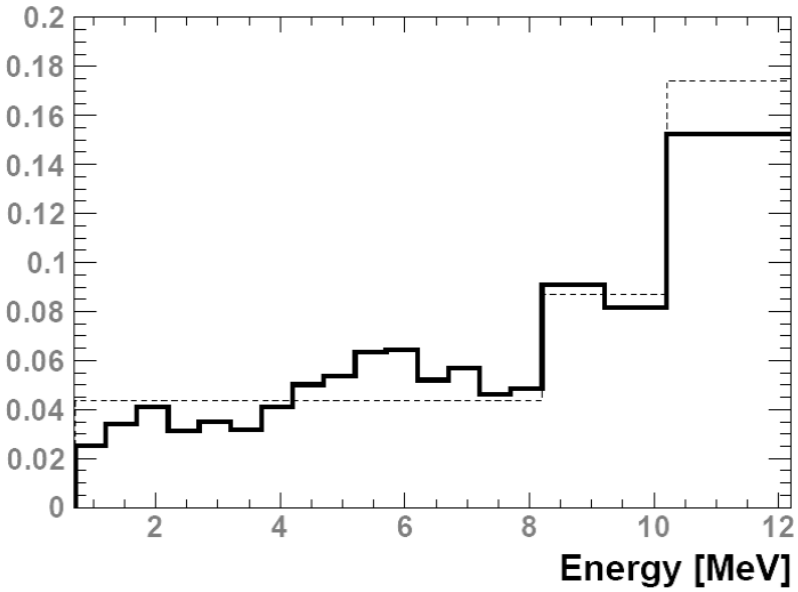

Figure 7.33: Fast neutrons energy spectra. A flat energy spectrum (dashed line), used in the final fit, and the spectrum of the IV tagged event sample (solid line), normalized to the fast neutron rate. Note that the final fit (uneven) binning is used. The difference between the two spectra is taken as an error on the fast neutron background shape [82].

7.5.4 Off-Off data

Double Chooz uses two existing cores of the CHOOZ nuclear reactor facility as a source of electron anti-neutrinos. Unlike other current reactor neutrino experiments, which use more cores, the Double Chooz has a non-negligible chance of acquiring data while all available reactor cores are turned off. In fact, between the beginning of the physics run and the release of the first analysis, both reactors cores happened to be offline for a period of one day. After the second reactor started to power down, three hours were allowed to pass to get rid of residual anti-neutrino emission before the analysis period started. The period lasted for a total of 23.5 hours until the power on one of the reactors begun to gradually ramp up. During the analysis period three events were recoreded that pass the selection cuts. The characteristics of the events are summarized below:

1. Li-9 candidate
    - Prompt event energy: 9.8 MeV
    - Delayed event energy: 8.0 MeV
    - Prompt-delayed distance: 16.4 cm
    - Prompt-delayed time: 4 μs
    - Closest showering muon characteristics: 739 MeV, 15.4 cm and 201 ms between the muon and the prompt event
2. Li-9 candidate
    - Prompt event energy: 4.8 MeV
    - Delayed event energy: 8.6 MeV
    - Prompt-delayed distance: 27.9 cm
    - Prompt-delayed time: 26 μs

- Closest showering muon characteristics: 627 MeV, 30.8 cm and 241 ms between the muon and the prompt event

3. Stopped muon candidate

   - Prompt event energy: 26.5 MeV
   - Delayed event energy: 7.6 MeV
   - Prompt-delayed distance: 79 cm
   - Prompt-delayed time: 2.2 μs
   - Closest showering muon characteristics: no showering muon candidates up to 17 s before the prompt

Observation of two Li-9 events in 23.5 hours is consistent with the estimate obtained using statistical analysis described above.

7.6 Prediction of the rate and spectrum of IBD events

As we saw previously (Section 1.4.1.1), to predict the rate of reactor anti-neutrinos one of the things one needs to know is the fission rates of the four main isotopes. In Double Chooz the fission rates and uncertainties were calculated using two different Monte-Carlo simulation codes of the reactor assemblies, DRAGON and MURE. The main differences between the two codes is that DRAGON uses the deterministic approach based on direct solution to the neutron transport equations, while MURE uses the random generation of a large neutron sample to solve the equations statistically (Monte-Carlo method) [87]. Another difference is that DRAGON models the fuel rod assembly in 2D, while Mure considers all dimensions. The performance of the two codes was compared to each other and further validated against the so-called Takahama benchmark. The 3rd reactor of the Takahama nuclear power station is a PWR reactor (as is CHOOZ) whose fuel composition was directly monitored over the course of three cycles by extracting the fuel elements and measuring the nuclide composition

using α-, γ-, and mass spectrometries [88] providing data on the isotope concentrations as a function of burn-up. The comparison demonstrated good performance of the codes against the Takahama benchmark [35].

In order to populate the fission rates error matrix, the results of the simulations were investigated as a function of variations in different input parameters:

- thermal power
- boron concentration
- water and fuel temperatures and densities
- energy released per fission
- geometrical parameters of the cores

The difference between results of the Monte-Carlo based and deterministic codes was also included. Figure 7.34 shows the fission rate prediction with error bars as the function of burn-up and an example of the break down of errors for one of the isotopes.

The changes in relative fission rates for different isotopes due to fuel evolution is a relatively slow process ($\sim$days), while the reactor power can be subject to rapid fluctuations ($\sim$minutes). It is therefore practical to simulate predictions for the fission rates with time granularity relevant for the fuel evolution changes, and then just rescale the absolute rate values by the reactor power data. The CHOOZ reactor power is monitored every minute via temperature in the primary loop, with weekly calibrations by enthalpic balance of the steam generators. Figure 7.35 shows the actual power history of the two CHOOZ reactor cores during the first physics run of the Double Chooz. A relative error of 0.46% is reported by EDF.

Once the rates are known, they can be converted into anti-neutrino spectra prediction. The original parameterizations based on the ILL measurements, discussed earlier 1.4.1.1, were recently re-evaluated by Mueller *et al.* ([89]) using the latest information from nuclear

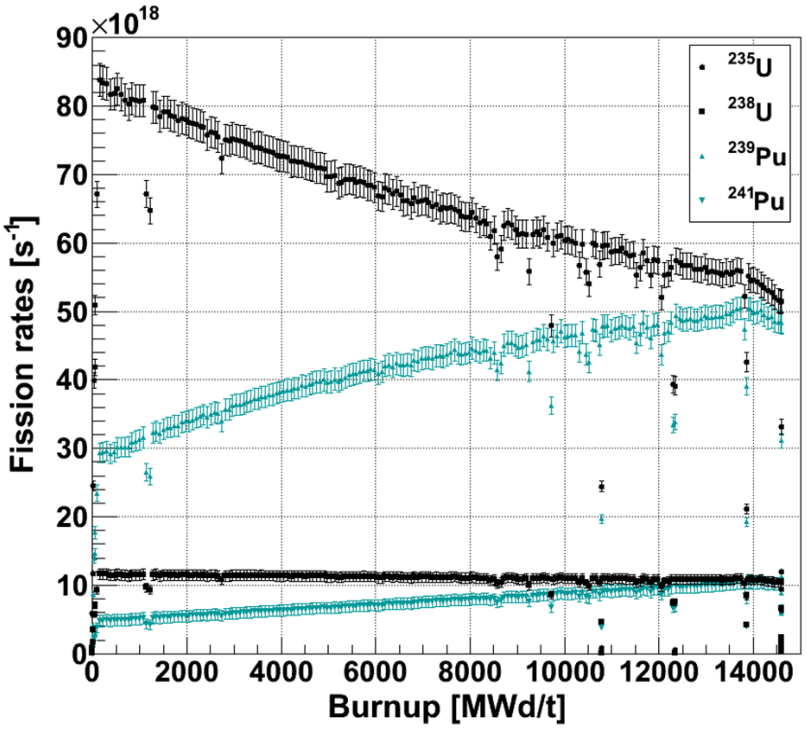

(a) Fission rates

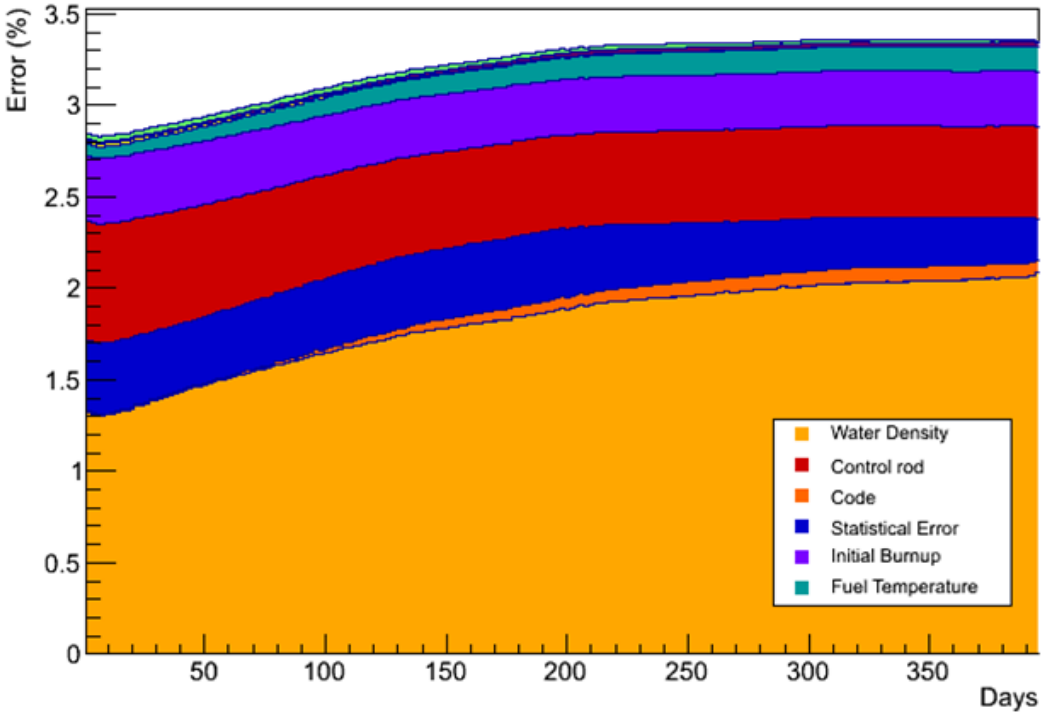

(b) U-235 errors

Figure 7.34: Fission rates uncertainties. (a) Errors on the predicted fission rates for the main fissile isotopes. (b) Contribution of different factors is shown for one of the isotopes. Other isotopes have similar behaviour.

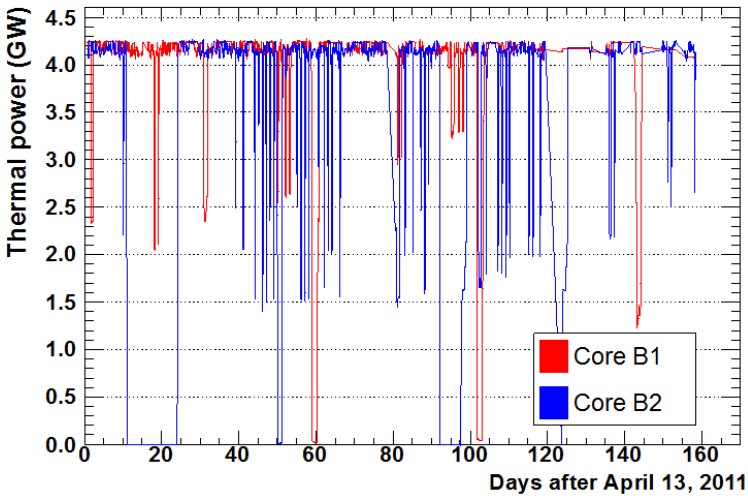

Figure 7.35: Thermal power of the two CHOOZ reactors as a function of time.

databases. While the uncertainties are similar to the ILL ones, the normalization is shifted by about +3% on average. Another recent re-evaluation performed by P.Huber ([90]) reports a consistent shift. For the first result we use the reference spectra based on the recent re-evaulation from [90] for U-235, Pu-239, and Pu-241 isotopes, and for U-238 we use the *ab initio* calculation from [89]. The non-equillbrium correction was applied following [90] to take into account the short irradiation time during the original ILL measurements. The details of the code used to produce the Monte-Carlo prediction of the anti-neutrino spectrum are described in [91]. Figure 7.36 shows the reference anti-neutrino spectra used in the prediction.

In principle, we now have all pieces needed to generate the anti-neutrino rate and spectrum as given by Equation (1.38). However, it is possible to reduce the total error by tying the mean cross-section per fission (Equation (1.39)) to the experimental value measured by Bugey-4 with only ≈1.4% uncertainty [92], instead of relying on the inherent normalisations of the conversion procedure:

$$\langle \sigma_f^{DC} \rangle = \langle \sigma_f^{Bugey} \rangle + \sum_j (\alpha_j^{DC} - \alpha_j^{Bugey}) \langle \sigma_f \rangle_j, \tag{7.5}$$

where the second term describes the correction due to different core inventories of the two

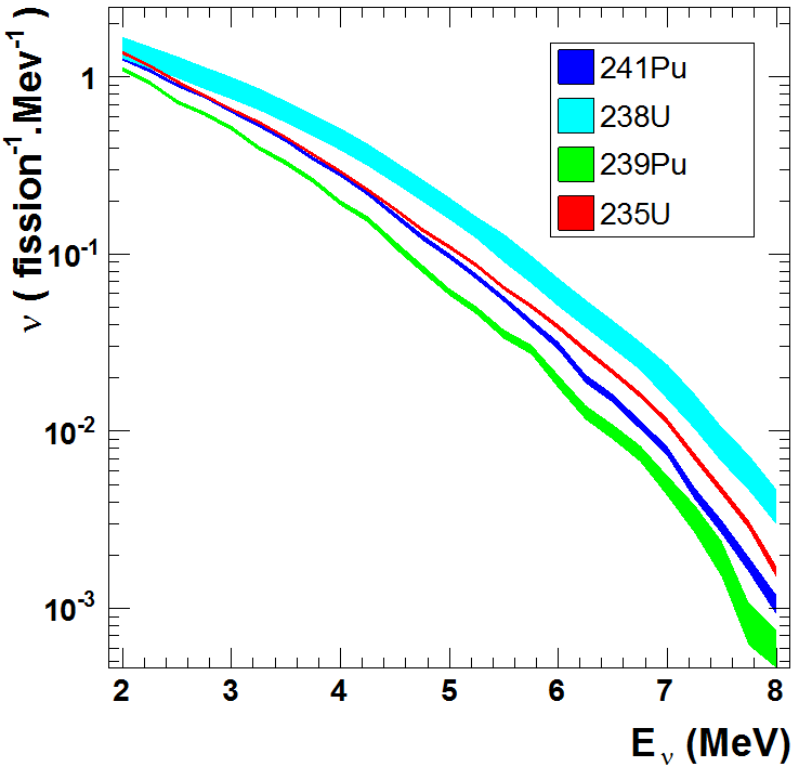

(a) Reference spectra

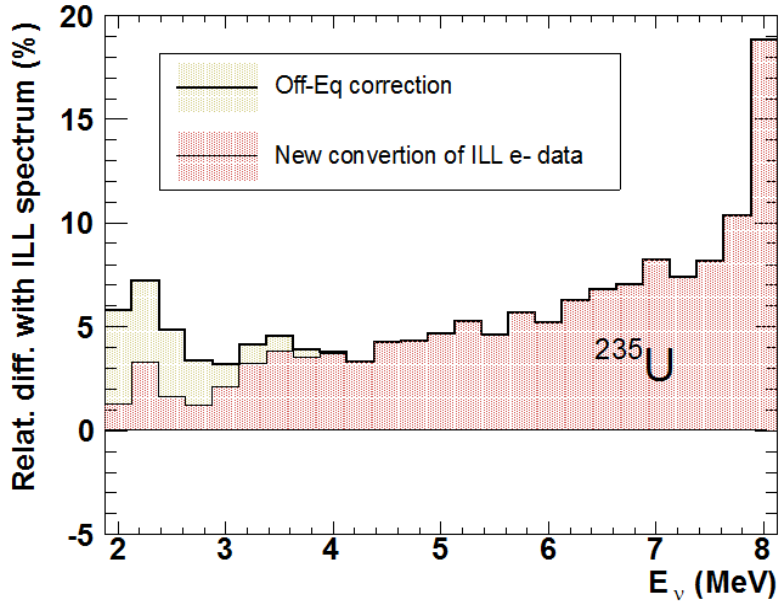

(b) Comparison to ILL

Figure 7.36: New reference anti-neutrino spectra. See text for details.

experiments. Using the Bugey-4 measurement as an "anchor point" decreases the overall contribution of the reactor related systematics to the first Double Chooz result from 2.7% to 1.7%. The relative contribution of different uncertainties to the prediction on the reactor rate is shown in Figure 7.37 [93]. The final step is to propagate the reactor related errors into the final fit reactor error matrix. This will be summarized in the corresponding section.

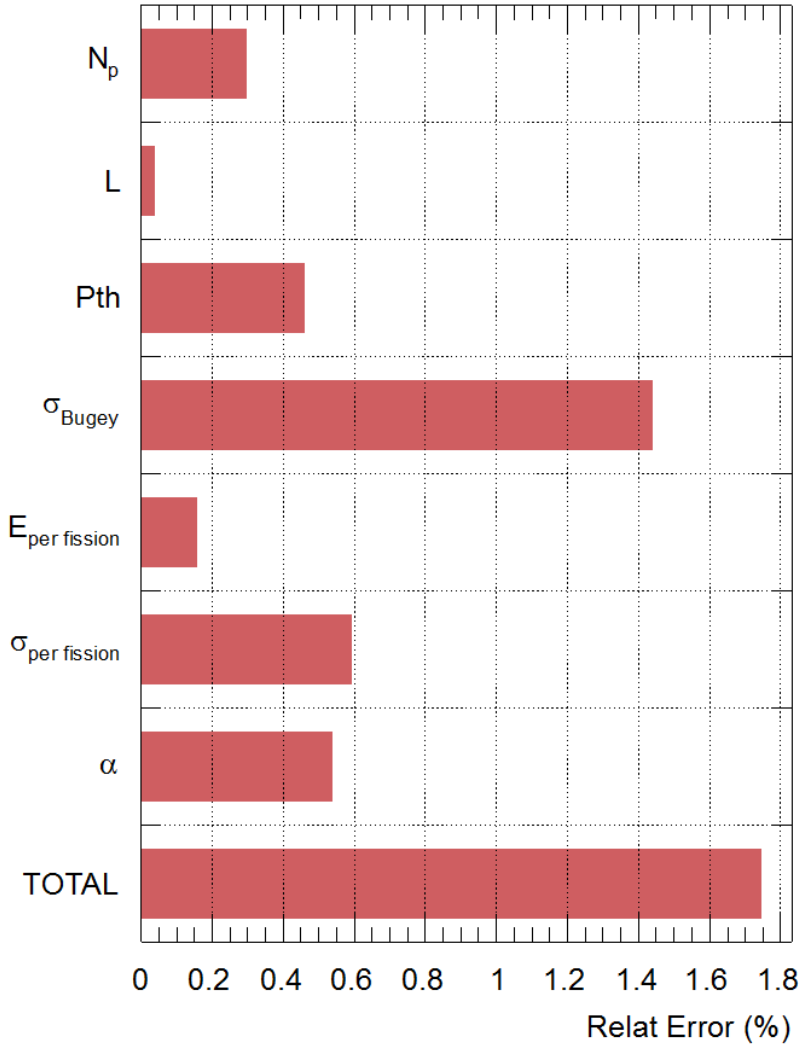

Figure 7.37: Break down of errors on the prediction of the reactor rate.

After the selection cuts, the MC correction factors, and the analysis framework were finalized, the reactor rates and power were unblinded to allow the final analysis. The time dependent numbers for the reactor power and fission rates were used to produce the Monte-

Carlo prediction (with a factor of 100 more statistics) for the anti-neutrino signal in the far detector assuming no oscillation. The total predicted number of the neutrino candidates for the two CHOOZ reactors was found to be 5334.7±93. The same selection cuts were then applied to the reconstructed Monte-Carlo events. After taking into account the following corrections:

- 95.47% correction due to the muon veto, which can be separated into three factors: 95.37% first order correction, 100.2% overlapping muon correction, and 99.9% impact on correlated events correction.
- 98% correction for the different fraction of captures on Gd
- 99.5% correction for the multiplicity cut
- 99.3% correction for the spill-in/out current

the prediction for the total number of signal events after the selection became 4010.2.

Chapter 8

Chi-square calculation with CUfits

In this chapter we describe the statistical approach used to analyse the first physics run data and the tool that implements the approach, to which the author of this thesis made one of the leading contrubitions.

8.1 Chi-square fits

In the first stage of the experiment we will perform a chi-square fit of the predicted visible spectrum to the data collected with the far detector. A general expression for the chi-square is shown below:

$$\chi^2 = \sum_{i,j} (Data_i - MC_i) M_{ij}^{-1} (Data_j - MC_j) \tag{8.1}$$

where $Data_{i(j)}$ is the number of observed events in prompt energy bin $i(j)$, $MC_{i(j)}$[1] is the number of expected events in bin $i(j)$, as predicted by Monte-Carlo simulation, and M^{-1} is the inverse of the total error matrix.

The total error matrix is a sum of several matrices, each corresponding to a particular source of systematic error. Note, that summing several covariance matrices is equivalent to adding errors in quadrature, hence individual matrices are assumed to represent independent

[1]Note, that the predicted number of events depends on the values of oscillation and other parameters

sources of errors.

An alternative way to include a systematic parameter in the fit is by adding a pull term to the chi-square equation. For the first final fit, Cluster United absorbed all systematic parameters in a covariance matrix.

The main components of the total error matrix are:

- Reactor rate and spectrum errors
- Uncertainty of detector response
- Statistical error
- Background rates and spectra

The author of this thesis made one of the leading contributions to calculation of the detector response error matrix for the first physics run. The process is described in details in the next chapter.

The total prediction $\mathrm{MC}_{i(j)}$ is a sum of predictions for the rate and spectra of individual reactors and backgrounds. In CUfits, the data can be provided either in the form of the final histogram or as an event tree. The Monte-Carlo prediction should be supplied in the form of the final fit event tree. The final fit tree format contains truth information, such as event type[2], true energy, emission and detection coordinates, etc., as well as the same reconstructed quanties available for the data. The histogram binning can be either provided by a user, or generated with one of the methods defined in the CUfits "utilities" namespace. The choices include the official Double Chooz first analysis binning and adaptive binning method, which will itself find the bin boundaries that satisfy the requirements on the minimum bin content and bin width, specified by a user. The histogram prediction will be automatically re-weighted by CUfits to reflect changes in the floating parameters. Currently, the code knows how to re-weight the events based on the following parameters:

[2]currently the following types are defined in the CUfits "physics" namespace: REACTOR1, REACTOR2, LI9, FASTN, ACCIDENTAL

- Oscillation variables (mixing angle and mass splitting)

  Note that the survival probability will be recalculated for each MC neutrino event individually, based on its true energy and distance between production point in the reactor core and the detection point in the detector.

- Rates of different event types separately

- Overall rate normalization

- Constant multiplier on the reconstructed energy variable

At any time a user can access the up-to-date total or individual prediction histograms. A typical user will interface with the code either interactively via the ROOT interpreter, or through a ROOT macro. The chi-square function will be produced by CUfits following user request based on the following inputs:

- List of detector objects and corresponding datasets (currently limited to single detector experiments)

- Optional list of parameters to be added as pull terms with corresponding errors

- Type of the fit (currently supported options are Rate, Shape, and Rate+Shape)

If a correlation matrix for the pull parameters is provided by the user, and found sound by CUfits, it will be converted into parameter covariance matrix and incorporated into the chi-square calculator. The final fit error matrix is provided as full inverted covariance matrix, either individually for each event type, or as a total matrix. CUfits performs basic sanity checks before accepting any matrix. The output chi-square function can then be used by the user, for example as an FCN function for the Minuit code. Upon completion of the fit, one can take advatange of several utility methods, such as plotting the residuals of the fit, the pull values, or the covariance ellipses for any pair of the floating parameters.

Let us consider a simple example of a chi-square formed between two two-bin histograms and a two-by-two error matrix. Apart from illustrating the basic concepts of covariance matrix and chi-square fits, it allows for an additional simple cross-check of the code.

8.2 Toy chi-square model

Let y_1, y_2 be the bin content of the data histogram, and x_1, x_2 the bin content of the MC histogram. Let n be a fractional normalization error, varied from 0 to 1, and a an absolute shape error, expressed in number of events squared.

The error matrix, including the statistical contribution[3] , is then given by:

$$M = \begin{bmatrix} x_1 + n^2 x_1^2 + a & x_1 x_2 n^2 - a \\ x_1 x_2 n^2 - a & x_2 + n^2 x_2^2 + a \end{bmatrix} \tag{8.2}$$

Note that normalization error is usually known as a fractional error, common for all bins. Hence the actual contribution of normalization error, in terms of number of events squared, will be generally different for different elements of the matrix, unless histogram has equal number of events in each bin.

The inverse of the matrix is:

$$M^{-1} = f \begin{bmatrix} x_2 + n^2 x_2^2 + a & -x_1 x_2 n^2 + a \\ -x_1 x_2 n^2 + a & x_1 + n^2 x_1^2 + a \end{bmatrix} \tag{8.3}$$

where f is the following factor:

$$f = \frac{1}{x_1 x_2 + x_1 n^2 x_2^2 + x_1 a + n^2 x_1^2 x_2 + n^2 x_1^2 a + x_2 a + n^2 x_2^2 a + 2 x_1 x_2 n^2 a} \tag{8.4}$$

[3]Note, that using predicted number of events for statistical error may result in fit instabilities or slower convergence, so data events are often used instead

To form the chi-square we also need the vector of the event shifts and its transpose:

$$V = \begin{bmatrix} y_1 - x_1 \\ y_2 - x_2 \end{bmatrix}, \quad V^T = \begin{bmatrix} y_1 - x_1 & y_2 - x_2 \end{bmatrix} \tag{8.5}$$

The explicit form for the chi-square is then given by:

$$\begin{aligned} \chi^2 &= V^T M^{-1} V \\ &= f \cdot [(y_1 - x_1)((x_2 + n^2 x_2^2 + a)(y_1 - x_1) + (-x_1 x_2 n^2 + a)(y_2 - x_2)) + \\ &\quad + (y_2 - x_2)((-x_1 x_2 n^2 + a)(y_1 - x_1) + (x_1 + n^2 x_1^2 + a)(y_2 - x_2))] \end{aligned} \tag{8.6}$$

Looking at the plot of the Equation (8.6) as a function of event shifts (Figure 8.1) we can make two simple observations:

1. The Chi-square is equal to zero if event shifts in each bin are zero, i.e. when the prediction matches data perfectly

2. Shape of the chi-square is parabolic in event shifts

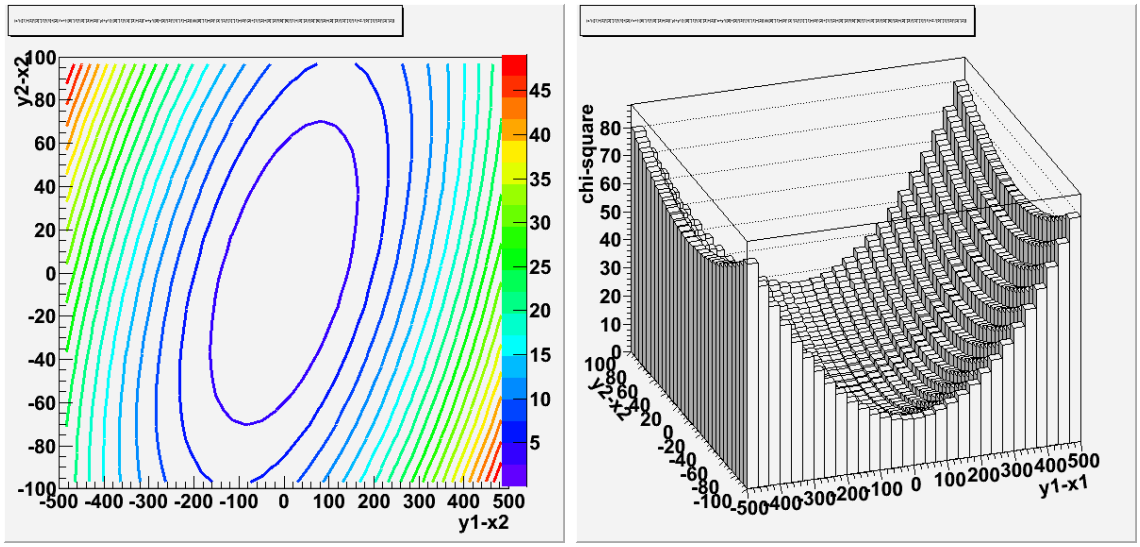

(a) contours (b) lego plot

Figure 8.1: Equation (8.6) plotted as a function of event shifts.

If we now play with the different values of normalization and shape error we can further conclude that

- When both systematic errors are zero, there is no correlation between two energy bins (Figure 8.2a)
- Normalization error introduces positive correlation (Figure 8.2c)
- Shape error introduces negative correlation (Figure 8.2b)
- A particular combination of normalization and shape errors exists such that the positive and negative correlations are canceled out, and the bins are effectively uncorrelated (Figure 8.2d)

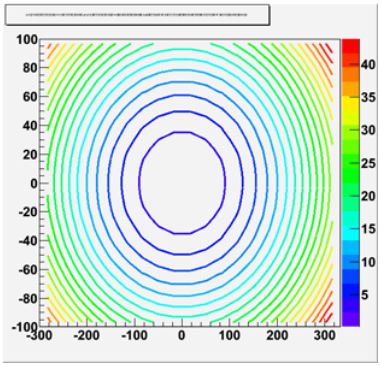

(a) stat errors only

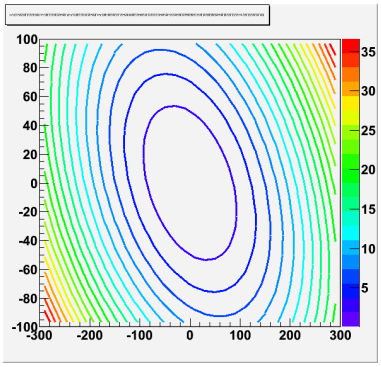

(b) shape error → anti-correlation

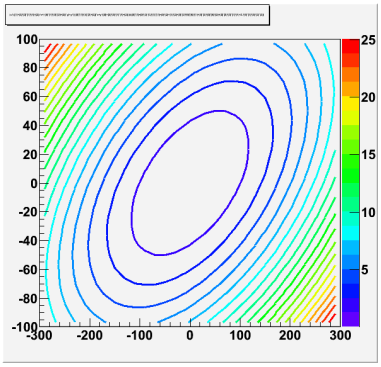

(c) norm error → correlation

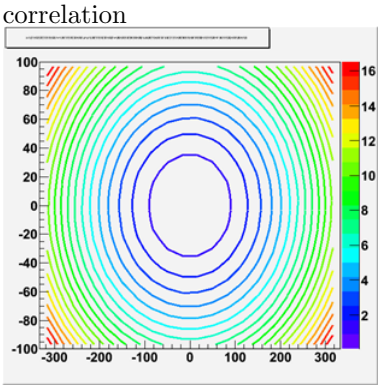

(d) norm and shape errors → decreased correlation

Figure 8.2: Impact of different types of error on correlation pattern.

Let's now plot the chi-square as a function of normalization and shape errors (Figure 8.3)

We can confirm that as the error level is scaled up, the chi-square value goes down. In other words, increasing the error can only worsen the sensitivity of the fit.

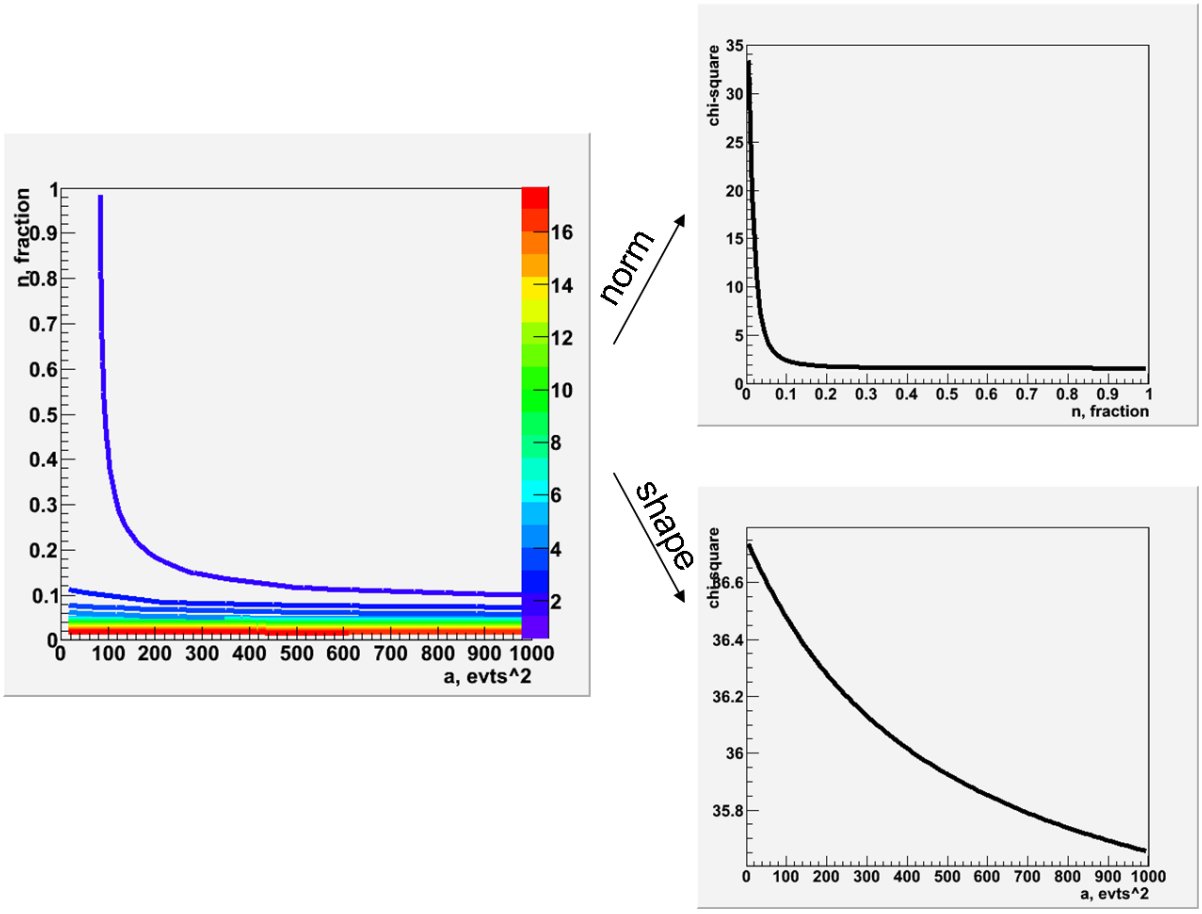

Figure 8.3: Chi-square as a function of normalization and shape errors. Contours of constant chi-square are shown on the left, projections on the normalization axis (at shape error equal zero) and to shape axis (at normalization error equal zero) are shown on the right.

For the last exercise, we plug in realistic numbers for the event shifts and systematic errors into both the analytical Equation (8.6) and the chi-square function provided by CUfits code, and compare the two chi-square values.

The prompt spectrum corresponding to roughly 180 days of data-taking was obtained using the DCNuGen2 anti-neutrino generator assuming no oscillations (red line on Figure 8.4). The spectrum was then re-weighted using the CUfits library to include oscillation signal ($sin^2(2\theta_{13}) = 0.17$, blue line in Figure 8.4)

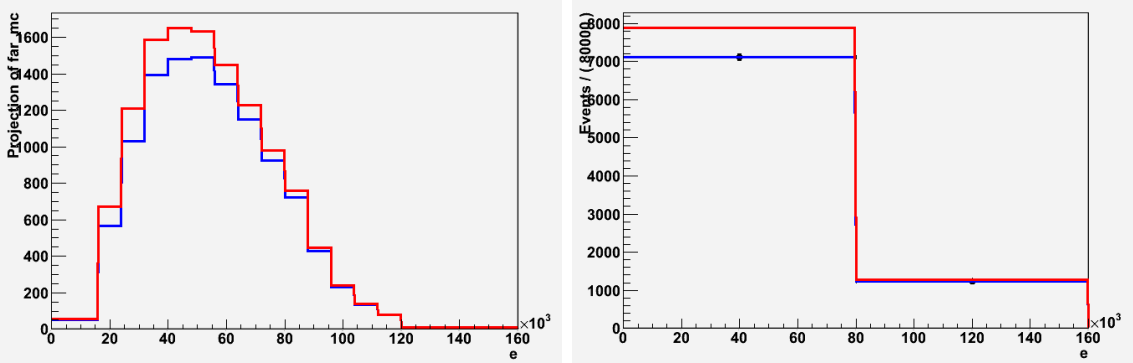

(a) prompt spectra (b) re-binned

Figure 8.4: Prompt spectra for non-oscillation (red) and oscillated (blue) cases.

According to the convention established earlier, the oscillated histogram is "Data", and the non-oscillated one is "MC". The two histograms were re-binned to contain only two bins (from 0 to 80e3, and from 80e3 to 1.6e5 DUQ). The corresponding number of events is as follows:

- $y_1 = 7108, y_2 = 1237$
- $x_1 = 7891, x_2 = 1288$

Table 8.1 shows the comparison between the chi-square values as suggested by the analytical Equation (8.6) and the CUfits code for a couple of realistic combinations of normalization and shape errors.

Shape error, evt^2	Norm error, %	χ^2 from 8.6	χ^2 from CUfits
0	0.	79.714	79.714
0	2.	20.158	20.158
2.49e4	2.5	11.416	11.416

Table 8.1: Comparison of chi-square values from analytical function and CUfits code.

Chapter 9

Error matrices

For the first Double Chooz result all sources of uncertainty were represented by the error matrices. This chapter describes the individual components included in the total error matrix, with particular attention given to the detector error matrix.

9.1 Detector response error matrix

As was described in Section 6.2, application of the correction functions removes dependence on the errors of the physical parameters in the Monte-Carlo simulation. The errors in the parameters of the correction functions were described by the error matrix (6.3), which was then enlarged to cover worse discrepancies between observed and predicted peak positions. We now need to propagate the parameter errors into the errors in the prediction of bin content of the prompt spectrum histogram used in the final fit. This is done as follows:

1. Draw a random parameter set from the enlarged parameter matrix
2. Perform candidate extraction on the common Monte Carlo event set, corrected according to the picked parameter values
3. Store the prompt energy distribution for the events that passed the selection

4. Repeat 300 times

5. Find the covariance matrix using the following estimator:

$$M_{ij} = \frac{1}{300} \sum_{n}^{300} (p_i^n - p_i^{cv})(p_j^n - p_j^{cv}), \tag{9.1}$$

where M_{ij} is the detector response covariance matrix, $p_{i/j}^{cv}$ is the i/j-th bin content obtained using default correction functions parameters, and $p_{i/j}^{n}$ is the i/j-th bin content obtained using n-th random parameter set

The detector covariance matrix was generated using the following criteria:

- Standard IBD candidate selection described earlier.
- Standard binning for the prompt spectrum:

  0.5 MeV-wide bins from 0.7 MeV to 8.2 MeV

  1.0 MeV-wide bins from 8.2 MeV to 10.2 MeV

  2.0 MeV-wide bin from 10.2 MeV to 12.2 MeV

- The combined set of anti-neutrino and Li-9 Monte Carlo events.

  The anti-neutrino set corresponds to the standard run list of unblinded data, with 100 times more statistics. The number of Li-9 events was chosen such that the ratio of events, selected using the central value parameters, was approximately the same as that observed in the data.

Since varying the parameters of the correction functions in effect changes the energy scale in the Monte-Carlo, a different number of events passes the selection cuts each time. Figure 9.1 shows the spread in the number of selected events between different random draws. Note that the RMS of the spread corresponds to the combined uncertainty of all energy selection cuts.

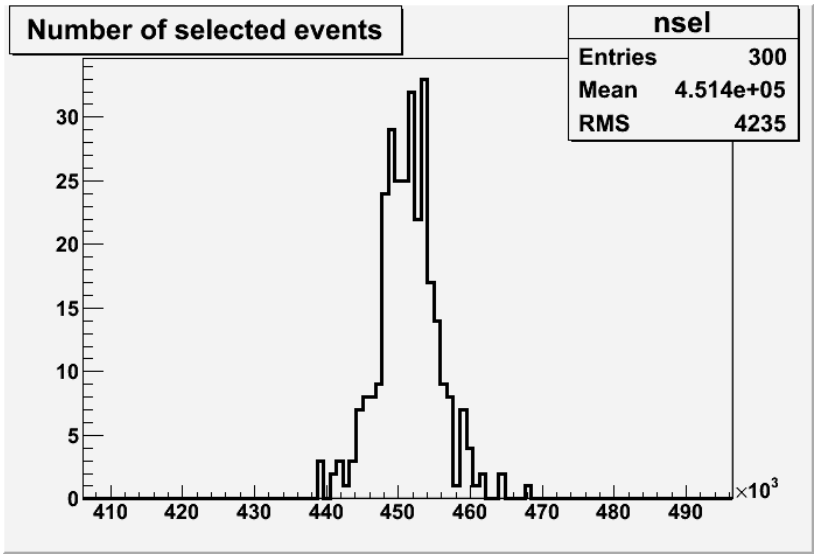

Figure 9.1: Spread in the number of selected events for various random parameter sets. The RMS of the distribution corresponds to the uncertainty of the energy selection cuts.

Figure 9.2 shows 10 prompt spectra obtained using different random parameter sets, along with the prompt spectrum obtained by averaging all random prompt spectra.

Figure 9.3 shows the fractional variance[1] and the determinant of the covariance matrix produced as described above as a function of the number of random draws.

The full and fractional covariance matrices are plotted in Figure 9.4.

Figure 9.5 shows the ratio of the first ten random correction functions to the central value correction.

[1]Equal to the sum of all matrix elements divided by the total number of predicted events

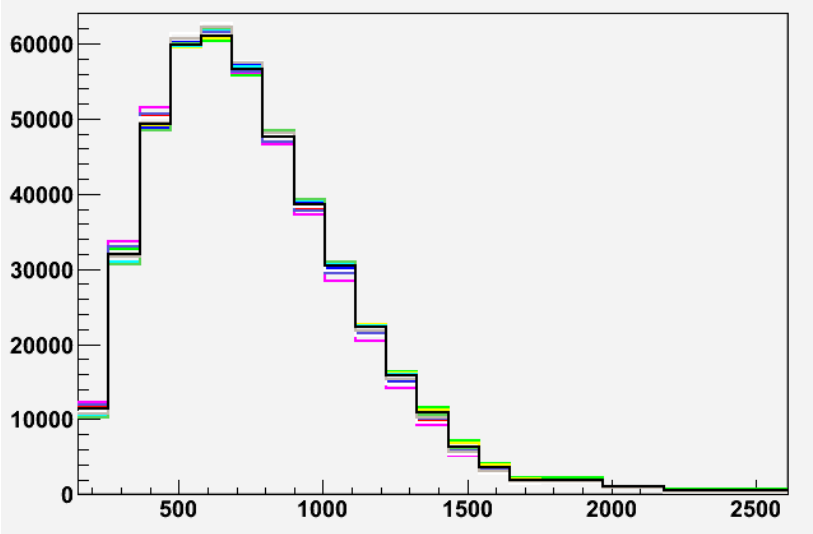

(a) First 10 prompt spectra corresponding to individual random draws

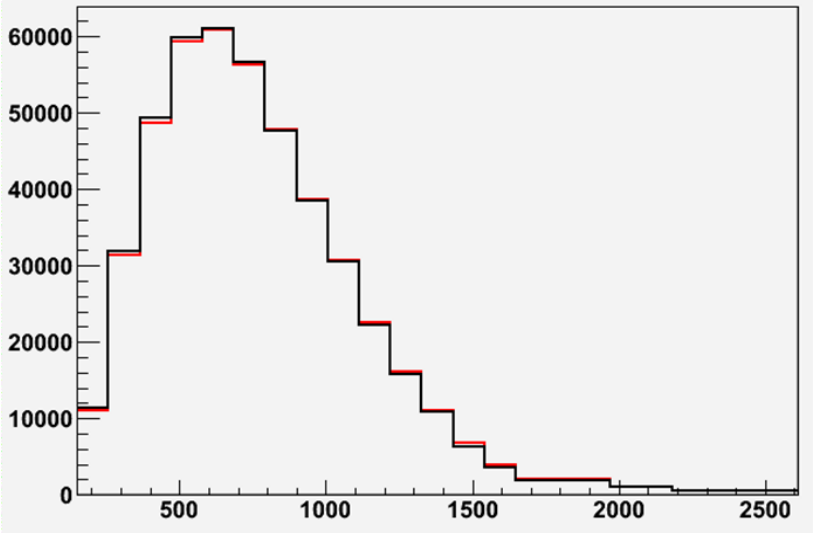

(b) Prompt spectrum (red) obtained by averaging all 300 random spectra

Figure 9.2: The prompt spectra of selected candidates. Different colors correspond to different parameter sets. Black corresponds to the central values of the correction function parameters.

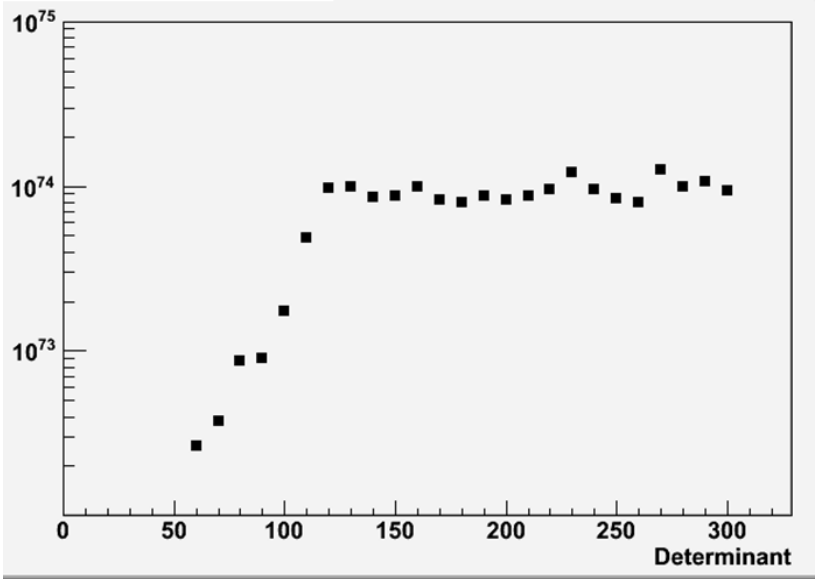

(a) Matrix determinant

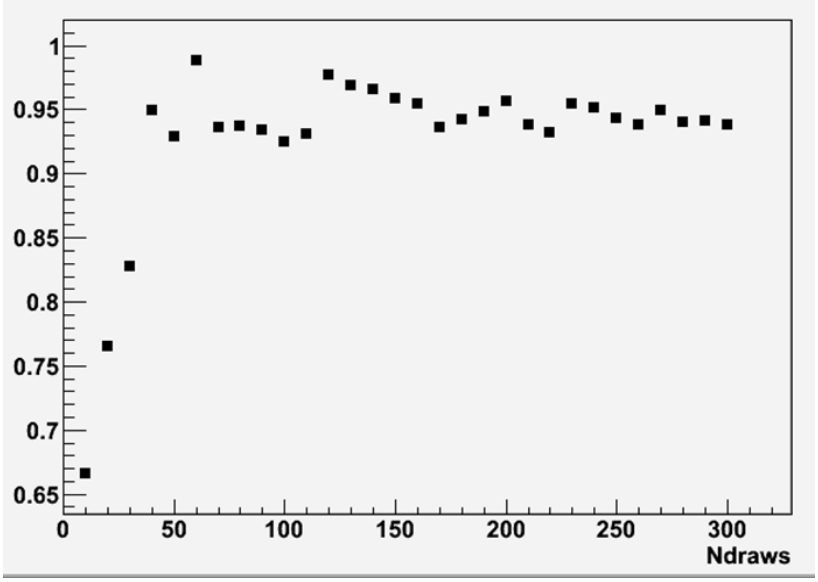

(b) Fractional variance

Figure 9.3: Parameters of the sample covariance matrix. The parameters are shown as a function of the number of random draws

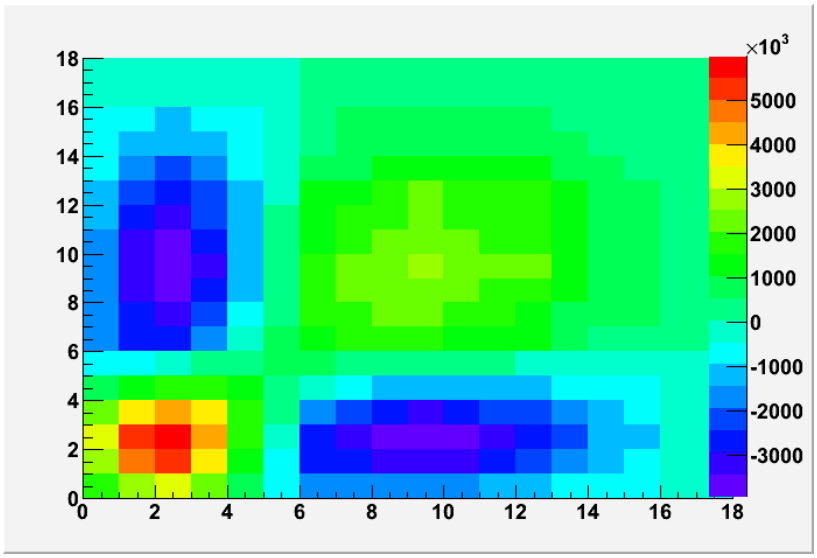

(a) Full matrix

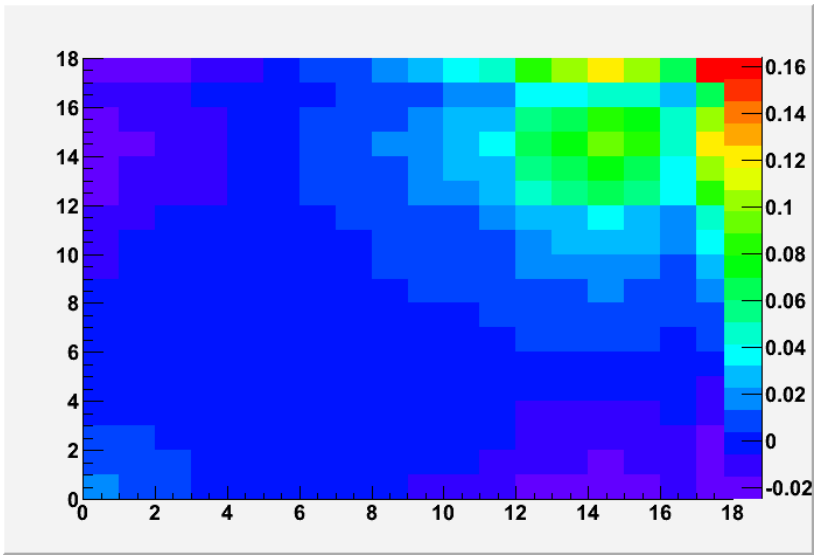

(b) Fractional matrix

Figure 9.4: The full and fractional covariance matrices. The X and Y axes are bin numbers. The full covariance matrix has units of event shifts squared.

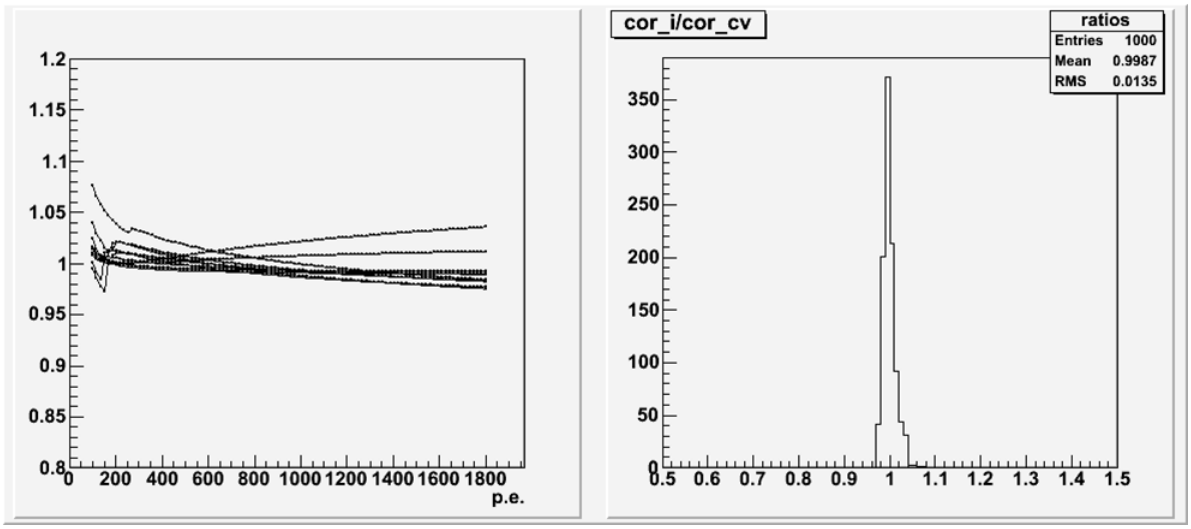

Figure 9.5: Impact of the wild draws. The ratios of the first 10 random correction functions to the central value correction as a function of the number of photoelectrons (left) and projected out (right). The impact of the wild draws can be seen as the increase in the included error at low energies.

9.2 Reactor matrix

[2] We first re-write Equation (1.38) for the case of a finite number of energy bins and using the mean cross-section per fission anchored by the Bugey-4 measurement (Equation (7.5)):

$$N_{k,t}^{exp} = \frac{\epsilon N_p}{4\pi} \sum_i \frac{P_i^{th}}{L_i^2 \langle E_f \rangle_i} \frac{\langle \sigma_f^{DC} \rangle_i}{\sum_j \alpha_{ij} \langle \sigma_f \rangle_j} \sum_j \alpha_{ij} \langle \sigma_f \rangle_{kj}, \tag{9.2}$$

where $\langle \sigma_f \rangle_{kj}$ is the mean cross-section in energy bin k, which can be calculated by multiplying the antineutrino reference spectrum for the corresponding isotope by the IBD crossection and averaging the product over the energy bin, $N_{k,t}^{exp}$ denotes the expected number of events in energy bin k at time t, i enumerates reactors and j enumerates fissile isotopes. To find the reactor error matrix we need to find the event shifts due to uncertain parameters in Equation (9.2) preserving existing correlations:

$$M_{kl}^{tot} = \delta N_k^{exp} \delta N_l^{exp}, \tag{9.3}$$

where k, l correspond to neutrino energy bins. We can separate out the matrices corresponding to independent parameters:

$$M_{kl}^{tot} = M_{kl}^{N_p} + M_{kl}^{\epsilon} + M_{kl}^{\sigma^{Bugey}} + M_{kl}^{\langle \sigma_f \rangle_{kj}} + \sum_i (M_{kl}^{\alpha_{ij}} + M_{kl}^{L_i} + M_{kl}^{P_i^{th}}) \tag{9.4}$$

The individual matrices are then constructed using the general expression for error propagation. In other words, if N^{exp} is a non-linear function of the variables $\vec{\mathbf{x}}$, in the first order:

$$M(N^{exp}) = JM(\vec{\mathbf{x}})J^T, \tag{9.5}$$

where J denotes the Jacobian matrix, or the matrix of partial derivates of N^{exp} with respect to $\vec{\mathbf{x}}$. The technical note [91] details the calculation of individual contributions to the total

[2] This section is based on the technical note [91]

reactor error matrix, including a summation of the errors for individual time periods, which in most cases are correlated in time. After the total matrix is calculated, the last step is to transform the matrix from neutrino energy into the positron energy. This is done in the following way [94]:

- A Monte Carlo prediction for the prompt spectrum was produced using the central-value parameters. A tree of selected candidates contains information for both true neutrino and reconstructed positron energies, so the central value prediction histograms are available in both cases.

- A random correlated set of event shifts was drawn from the reactor matrix and added to the central value prediction in terms of neutrino energy.

- For each random neutrino spectrum the corresponding spectrum in terms of reconstructed energy was obtained by re-weighting the central value histogram in terms of reconstructed energy by the ratio of the random neutrino spectrum to its own central value spectrum

- Total of $\sim$10k prompt spectra were so obtained

- The reactor matrix was reformulated in terms of the event shifts in the reconstructed energy histogram

The final reactor covariance matrix used in the first analysis is shown in Figure 9.6. [3]

[3]Just for fun we can argue that simply by looking at the matrix in Figure 9.6 we can see it contains mostly normalization error. It is apparent that 1D projections on both axes are very similar to each other and resemble the prompt energy spectrum, which suggests a constant fully correlated error is prevalent in the matrix

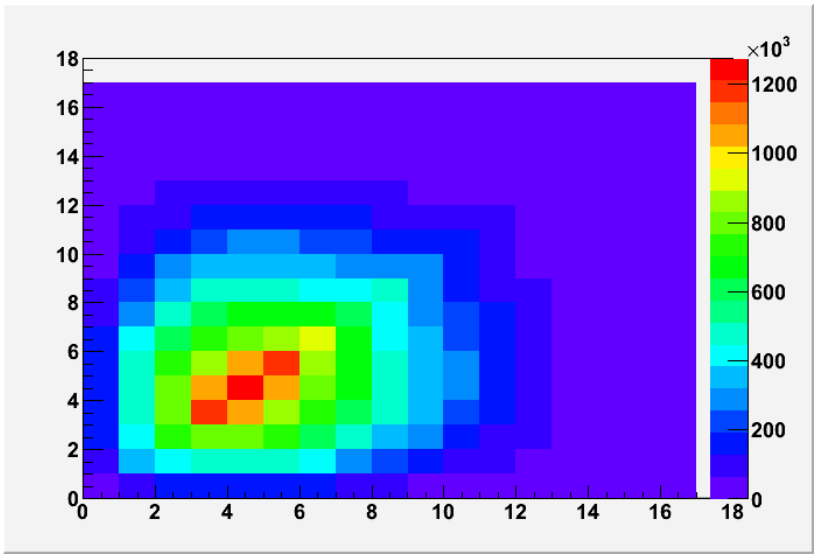

Figure 9.6: Full reactor matrix. The X and Y axes correspond to the energy bins. Color encodes event shifts squared.

9.3 Other matrices: backgrounds, efficiency, and statistical errors

The remaining error matrices are relatively straightforward to populate. The statistical error is included by a diagonal matrix with the diagonal elements corresponding to the bin content in the data histogram. In other words, Poisson errors on the observed spectrum are used as a statistical uncertainty. The efficiency and background rates errors are naturally represented by normalization matrices (i.e. taken as fully correlated between energy bins). The rate errors on the backgrounds are listed in the corresponding sections. The total efficiency error is calculated by adding in quadrature the individual normalization errors, which we summarize in Table 9.1.

Source	Uncertainty, %
Target #H	0.3
Trigger	0.4
Spill-in/out	0.4
Gd/(Gd+H)	0.58
Δt	0.5
Fraction of Gd in the delayed window	0.6
Total	1.1

Table 9.1: Error in the detector efficiency

The spectrum of the fast neutron background is assumed to be flat for the final analysis. The shape error is considered to be the difference between the flat spectrun and the spectrum obtained using the Inner Veto tag analysis, described in 7.5.3. The corresponding error matrix is shown in Figure 9.7

The matrices are expressed in terms of events squared. If a matrix is generated using a high statistics Monte-Carlo sample, as is often the case, it should be rescaled to the actual number of predicted events. Moreover, if not all types of events were used during matrix

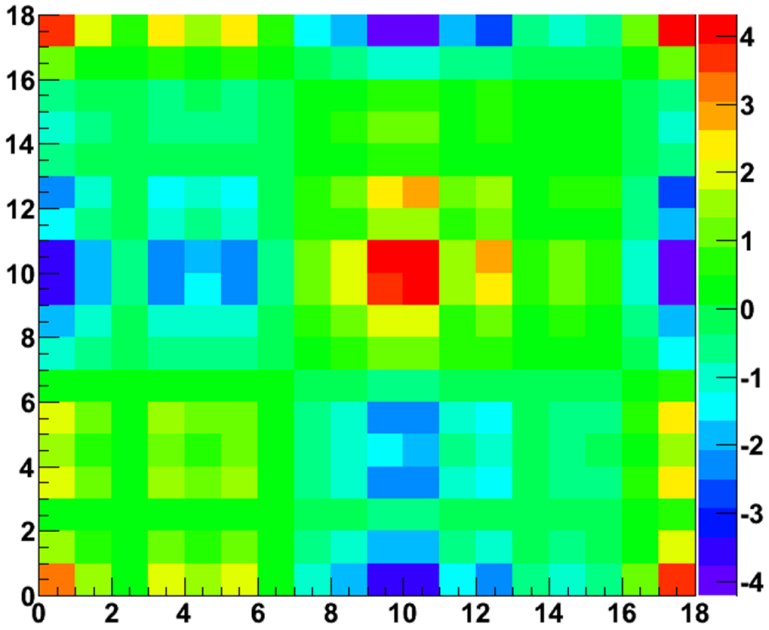

Figure 9.7: Fast neutron shape uncertainty. X and Y correspond to the energy bins. Color encodes event shifts squared.

generation[4], the better approach is to "fractionalize" the matrix and then rescale it using the bin content of the actual total prediction histogram. The fractional matrix is calculated as follows:

$$M_{ij}^{frac} = \frac{M_{ij}^{full}}{HS_i HS_j}, \tag{9.6}$$

where M^{frac} is the fractional matrix and M^{full} is the original full matrix, corresponding to the high statistics Monte-Carlo histogram, HS_i.

If only a sub-dominant event type is excluded from the matrix generation, the correlation pattern will be adequate, and the rescaling will restore the correct normalization:

$$M_{ij}^{final,full} = M_{ij}^{frac} F_i F_j, \tag{9.7}$$

where F_i is the total prediction histogram used in the final fit.

[4]For example, simulating accidentals is usually demanding in terms of CPU resources, while the spectrum can be accurately extracted from the data

For the rate-only fits one can still use the covariance matrix approach, but only the total variance of the matrix matters. By dividing the variance by the total number of predicted events, we get the fractional variance. Table 9.2 shows the fractional variances for all specified matrices, rescaled to the total prediction.

Source	Fractional variance, %
Statistical	1.56
Efficiency	1.1
Reactor	1.71
Detector	1.2
Accidentals	0.01
Fast neutrons	1.14
Li-9	2.73
Total	4.09

Table 9.2: Matrix fractional variances.

Chapter 10

Final fit

Putting all the pieces described in the previous chapters together, we can re-write Equation (8.1) in a more explicit form:

$$\chi^2 = \sum_{ij}(Data_i - (\sum_{R}^{Reactors} N_i^{\nu,R} + \sum_{b}^{Backgrounds} N_i^b))\times$$
$$(M_{ij}^{Reactor} + M_{ij}^{Detector} + M_{ij}^{Stat} + \sum_b^{Backgrounds} M_{ij}^b + M_{ij}^{Efficiency})^{-1} \times$$
$$(Data_j - (\sum_R^{Reactors} N_j^{\nu,R} + \sum_b^{Backgrounds} N_j^b)) \quad (10.1)$$

The prediction for the signal was generated with a high statistics Monte-Carlo simulation, as was the prediction for the Li-9 background. The fast neutron background was simulated assuming a flat spectrum, and for the accidentals the measured spectrum was used. The matrices were rescaled to the total prediction histogram, when necessary. As was mentioned earlier, for the first analysis the data was binned in 18 bin - the range from 0.7 to 8.2 MeV was covered in 0.5 MeV steps, from 8.2 to 10.2 MeV in 1 MeV steps, and from 10.2 to 12.2 MeV in a 2 MeV step.

10.1 Rate only and Rate+Shape results

As all systematic parameters are absorbed in the covariance matrix, we can directly plot the chi-square as a function of the oscillation amplitude. For the first analysis the mass splitting is fixed to the value reported by MINOS [95], assuming the normal hierarchy hypothesis, $\Delta m^2_{31} = \Delta m^2_{32} + \Delta m^2_{21} \approx 2.4^{0.12}_{0.12} \cdot 10^{-3} eV^2$. Figure 10.1 shows the chi-square (10.1) as a function of $sin^2(2\theta_{13})$. The minimum chi-square value of 24.84 corresponds to $sin^2(2\theta_{13})$=0.0849, and the value increases by 1 if $sin^2(2\theta_{13})$ is changed by 0.0509.

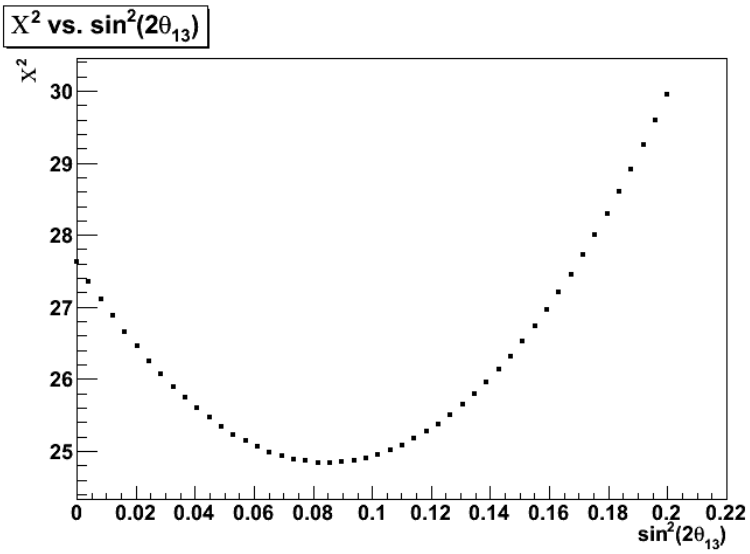

Figure 10.1: Chi-square curve for the first Double Chooz result.

Figure 10.2 shows the data prompt spectrum with the prediction superimposed.

The chi-square value of 24.84 with 17 degrees of freedom corresponds to the goodness-of-fit of 9.8%, which is reasonably consistent with statistical fluctuation and suggests the errors are not under-estimated.

If we ignore the spectral information, we get the chi-square curve shown in Figure 10.3. The minimum chi-square value corresponds to $sin^2(2\theta_{13})$=0.0934. The chi-square value increases by one if the value of $sin^2(2\theta_{13})$ is changed by 0.0785. As expected, the rate only result is less powerful due to its inability to constrain the backgrounds using shape

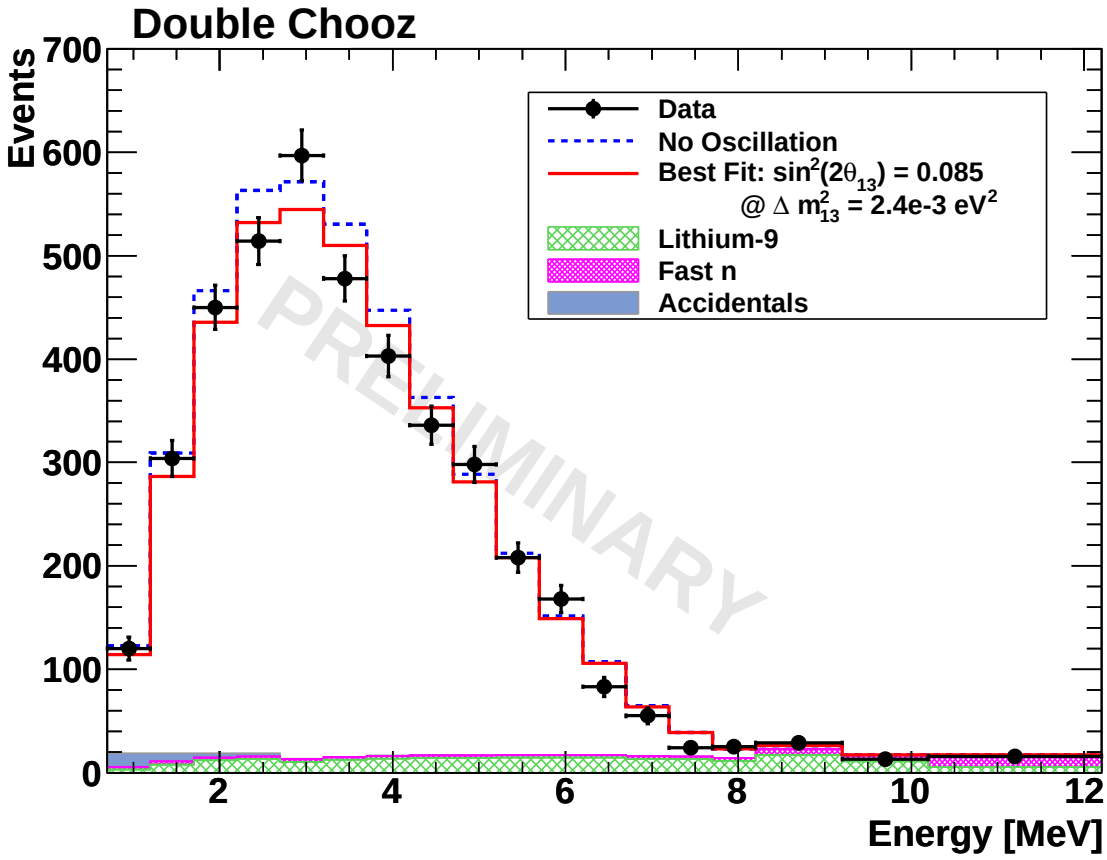

Figure 10.2: Prompt data spectrum. The data spectrum is superimposed with the no-oscillation and best-fit predictions. Background predictions are also shown.

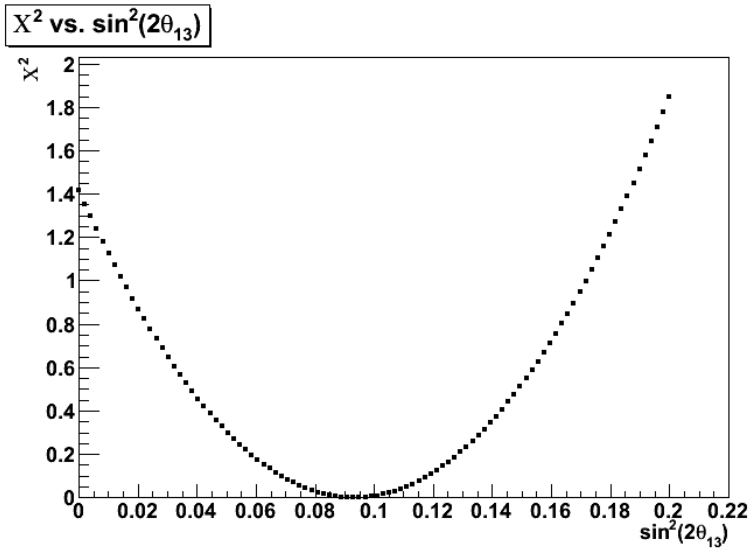

Figure 10.3: Chi-square curve for the first Double Chooz rate-only result.

information.

10.2 Frequentist studies

The two interesting questions we would like to answer are:

1. If the true value of the third mixing angle is zero, what is the probability of obtaining the result we have just presented?

2. What is the range of $sin^2(2\theta_{13})$ values corresponding to 90% C.L.

In an ideal situation, we could use the properties of the chi-square distribution to make the necessary statistical inference. In our case, however, the parameter of interest is close to the physical boundary and the errors can not be assumed to be perfectly Gaussian. In this case the chi-square probability density function (PDF) can not be blindly relied upon, so we employ the frequentist method to study the properties of our actual problem.[1]

10.2.1 Probability of zero

To find the probability of no-oscillation, we create a statistical sample in the following way:

- Generate a high statistics Monte-Carlo prediction assuming the true value of $sin^2(2\theta_{13})$=0
- Draw a random correlated set of event shifts from the total covariance matrix
- Create a toy prediction histogram by adding the random shifts to the central value prediction
- Repeat ∼10000 times

[1]The frequentist studies for the first result were performed by the author of this thesis.

For each simulated experiment we fit the histogram keeping the oscillation amplitude unconstrained and evaluate the test statistic:

$$\Delta\chi^2 = \chi^2(0) - \chi^2(sin^2(2\theta_{13})_{best}) \tag{10.2}$$

Following prescription of Feldman and Cousins [37], $sin^2(2\theta_{13})_{best}$ must be physically allowed, i.e. $sin^2(2\theta_{13})_{best} = \max(0,\ sin^2(2\theta_{13})_{bestfit})$. Figure 10.4 shows the distribution of $\Delta\chi^2$ for the ensemble of no-oscillation experiments. The total number of simulated experiments is 10000. We reject 1481 of the experiments because the Minuit reported the fit status as less than 3, indicating less-than-perfect convergence. We additionally reject 57 experiments that have unphysical (negative) $\Delta\chi^2$ values. The total number of simulated experiments considered is thus 8467. Evaluating the test statistic corresponding to the data fit (Figure 10.1) gives $\Delta\chi^2_{Data} = 2.79$. The total of 630 toy experiments have a test statistic at least as large as the value evaluated for the data, giving a 7.4% probability of no-oscillations.[2]

10.2.2 Confidence interval construction

We proceed to construct the frequentist belt[3] by creating statistical ensembles for different assumed values of oscillation amplitude. For each ensemble we evaluate the cut-off value that rejects 10% of simulated experiments with the largest $\Delta\chi^2$. Examples of distributions of test statistic and best fit oscillation amplitude for different true values of $sin^2(2\theta_{13})$ are shown on Figure 10.5. The best 90% of experiments have the best fit $sin^2(2\theta_{13})$ value within the boundaries highlighted in red. Plotting the boundary values for each ensemble, we obtain the confidence belt (Figure 10.6).

We then draw a vertical line corresponding to the data best fit $sin^2(2\theta_{13})$ value. The line intersects with the belt at two locations, thus providing an interval instead of a limit.

[2]Note that not using the two quality cuts to reject the misfit experiments changes the result by only 0.2%

[3]χ^2 asymptotically approaches -2ln(L). The $\Delta\chi^2$ therefore approaches the likelihood ratio, which is the test statistic used in the Feldman-Cousins ordering rule. However, we prefer not to rely on the asymptotic properties and only state that the frequentist interval is constructed using $\Delta\chi^2$ as an ordering rule.

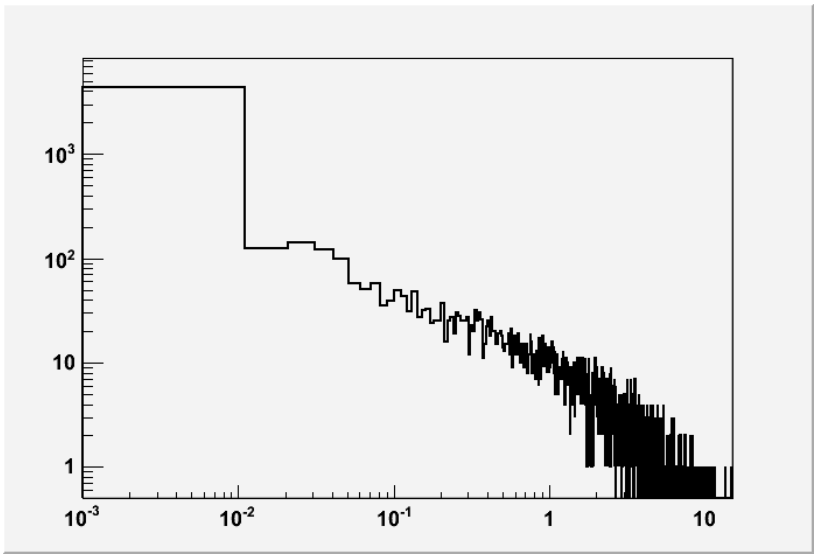

(a) Test statistic

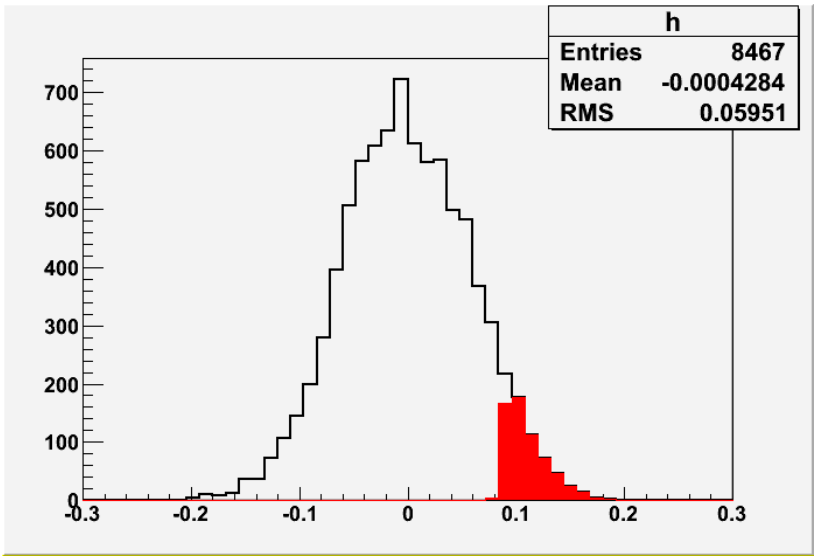

(b) Best fit values

Figure 10.4: Distribution of test statistic for simulated experiments. The test statistic and best fit oscillation amplitude values were obtained with simulated experiments containing no oscillation. Red highlights the toy experiments corresponding to test statistic values larger then 2.79.

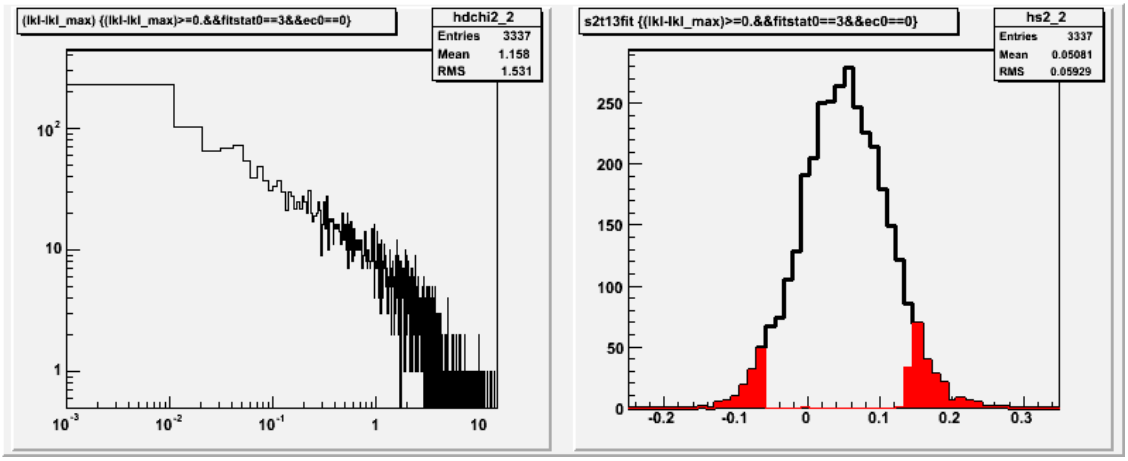

(a) $sin^2(2\theta_{13})$=0.05

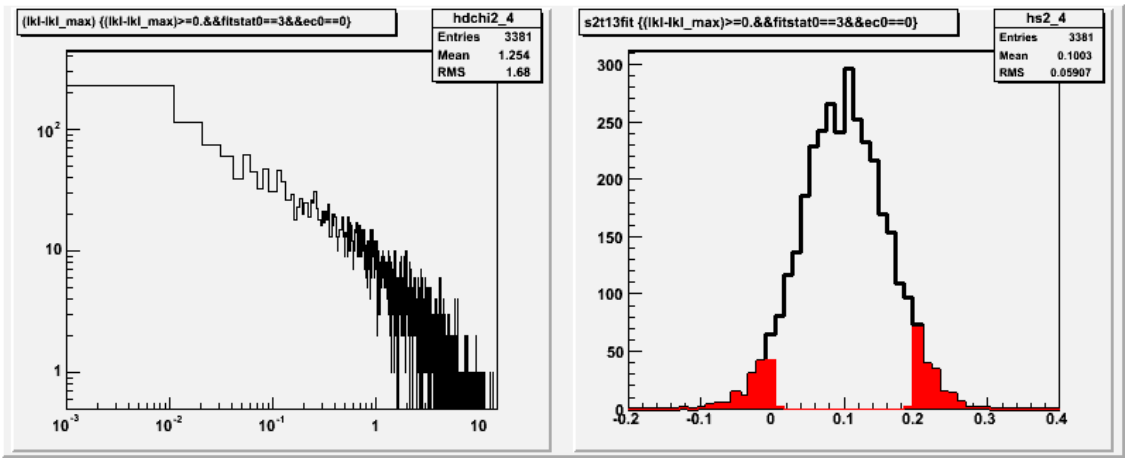

(b) $sin^2(2\theta_{13})$=0.10

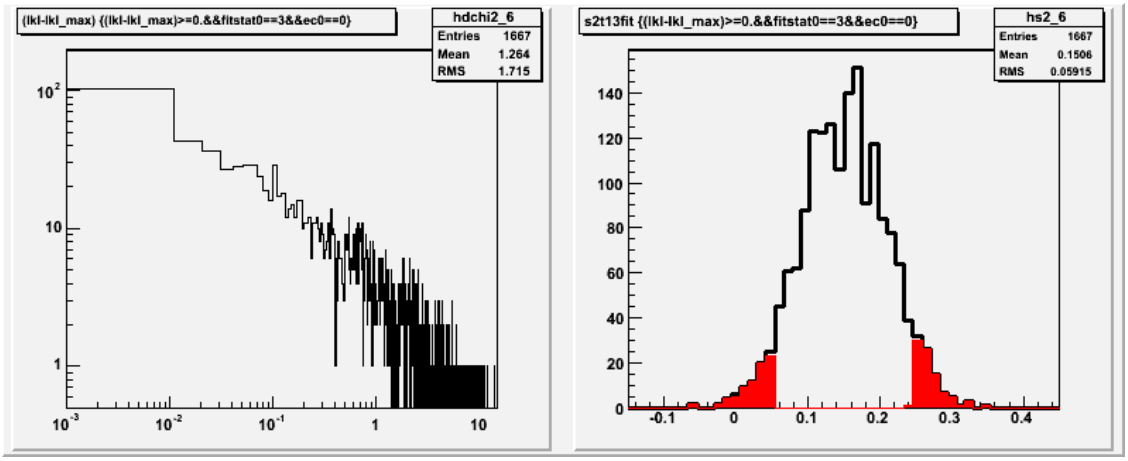

(c) $sin^2(2\theta_{13})$=0.15

Figure 10.5: Examples of test statistic distribution for three statistical ensembles. Red highlights the best fit values corresponding to simulated experiments with the worse 10% test statistic values. Note that the distribution of the best values is centered on the true value, indicating that the fitter is unbiased.

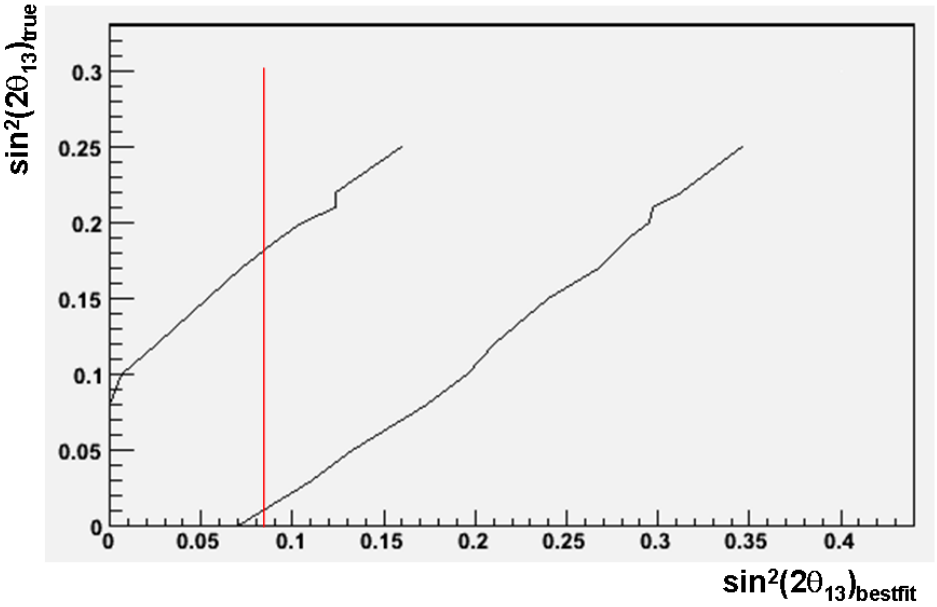

Figure 10.6: 90% C.L. frequentist belt.

Therefore, based on the first Double Chooz measurement, the 90% C.L. interval for the third mixing angle is:

$$sin^2(2\theta_{13}) \; \epsilon \; [0.0098, \; 0.1825] \text{ at } 90\% \text{ C.L.}$$

Chapter 11

Summary and conclusion

The first Double Chooz result presented at the LowNu conference[1]puts the $sin^2(2\theta_{13})$ at 0.085±0.051. The no-oscillation hypothesis is excluded at 92.6% confidence level. The frequentist interval is [0.0098, 0.1825] at 90% C.L.

In the two week period following the release of the first Double Chooz result, six papers appeared on the arXiv quoting it ([97, 98, 99, 100, 101, 102]).[2] This fact highlights the importance of improving our knowledge about the third mixing angle.

In the future, the Double Chooz will increase the accuracy of the measurement by accumulating more statistics and, when the near detector becomes operational, by reducing the reactor errors, as well as correlated detector errors. Improving the understanding of the detector response with careful calibrations and refined analysis methods will also be important for achieving the ultimate sensitivity of the experiment.

[1]6th International Workshop on Low Energy Neutrino Physics, 9-12 November, 2011, Seoul, South Korea

[2]In particular, Machado *et al* [100] combined the Double Chooz result with T2K and MINOS data resulting in exclusion of the zero value of $sin^2(2\theta_{13})$ at 3.3σ C.L. for both mass hierarchies

Bibliography

[1] M.E. Peskin and D.V. Schroeder. *An Introduction to Quantum Field Theory*. Addison-Wesley, 1995

[2] V.M. Emelianov. *Standard Model and Its Extensions* (in Russian). Physmatlit, 2007

[3] C.L. Cowan et al. Detection of the Free Neutrino: a Confirmation. *Science*, 124 (3212), July 1956

[4] E.Kh. Akhmedov and A.Yu. Smirnov. Paradoxes of Neutrino Oscillations. *arXiv:0905.1903v2*, 20 June 2009.

[5] M. Zrałek. From Kaons to Neutrinos: Quantum Mechanics of Particle Oscillations. *arXiv:hep-ph/9810543v1*, 30 October 1998

[6] S. Nussinov. Solar Neutrinos and Neutrino Mixing. *Phys. Lett. B*, 63 (1976) 201

[7] C.W. Kim. Neutrino Physics: Fundamentals of Neutrino Oscillations. *arXiv:hep-ph/960739v1*, 22 July 1996

[8] M. Beuthe. Oscillation of Neutrinos and Mesons in Quantum Field Theory. *arXiv:hep-ph/0109119v2*, 15 October 2002

[9] G.C. Branco and M.N. Rebelo. Leptonic CP Violation and Neutrino Mass Models. *New J. Phys.*, 7 (2005) 86

[10] Y. Fukuda et al. Atmospheric ν_{mu}/ν_e Ratio in the Multi-GeV Energy Range. *Phys. Lett. B*, 335 (1994) 237

[11] D. Casper et al. Measurement of Atmospheric Neutrino Composition With IMB-3 Detector. *Phys. Rev. Lett.*, 66 (1991) 2561

[12] K. Nakamura et al. [Particle Data Group]. *J. Phys. G*, 37 (2010) 075021

[13] A. Aguilar, et al. [LSND collaboration]. Evidence for Neutrino Oscillations From the Observation of $\bar{\nu_e}$ Appearance in a $\bar{\nu_\mu}$ Beam. *Phys. Rev. D* 64 (2001) 112007

[14] G.S. Karagiorgi. *Searches for New Physics at MiniBooNE: Sterile Neutrinos and Mixing Freedom*. Ph.D. thesis, MIT, 2010. FERMILAB-THESIS-2010-39

[15] G. Mention et al., The Reactor Antineutrino Anomaly. *arXiv:1101.2755v4*, 23 March 2011

[16] M. Apollonio et al. [CHOOZ collaboration]. Search for Neutrino Oscillations on a Long Base-Line at the CHOOZ Nuclear Power Station. *arXiv:hep-ex/0301017v1*, 13 Jan 2003

[17] F. Boehm et al. [Palo Verde collaboration]. *arXiv:hep-ex/0107009v1*, 4 Jul 2001

[18] S. Abe et al. [KamLAND collaboration]. *Phys. Rev. Lett.*, 100 (2008) 221803

[19] A. Gando et al. [KamLAND collaboration]. *arXiv:1009.4771v3*, 25 March 2011

[20] B.T. Cleveland et al. *Astrophys. J.*, 496 (1998) 505

[21] J.N. Abdurashitov et al. *Phys. Rev. C*, 80 (2009) 015807

[22] C. Arpesella et al. [Borexino collaboration]. *Phys. Rev. Lett.*, 101 (2008) 091302

[23] B. Aharmim et al. [SNO collaboration]. *Phys. Rev. Lett.*, 101 (2008) 111301

[24] B. Aharmim et al. [SNO collaboration]. *Phys. Rev. C*, 81 (2010) 055504

[25] J. Hosaka et al. [Super-Kamiokande collaboration]. *Phys. Rev. D* 73 (2006) 112001

[26] M. Gonzalez-Garcia, M. Maltoni, and J. Salvado. *arXiv:hep-ph/1001.4524v3*, 2010

[27] K. Abe et al. [T2K collaboration]. *arXiv:1106.1238v2*, 8 Jun 2011

[28] K. Abe et al. [T2K collaboration] *arXiv:1106.2822v2*, 25 Jul 2011

[29] P. Adamson et al. [Minos collaboration]. *arXiv:1108.0015v1*, 29 Jul 2011

[30] J. Maricic, for LBNE collaboration. *J. Phys.*, 259 (2010) 012038

[31] A.B. Sousa. Long-Baseline Neutrino Oscillation Experiments. *arXiv:1101.1125v2*, 5 March 2011

[32] D. Ayres et al. [NOνA collaboration]. Proposal to Build a 30 Kiloton Off-Axis Detector to Study $\nu_\mu \rightarrow \nu_e$ Oscillations in the NuMI Beamline. *arXiv:hep-ex/0503053v1* 30 Mar 2005

[33] K. Anderson et al. A New Nuclear Reactor Neutrino to Measure θ_{13} *arXiv:hep-ex/0402041v1*, 26 Feb 2004

[34] K.Schreckenbach, G.Colvin, W.Gelletly, and F.Von Feilitzsch. Determination of the Antineutrino Spectrum From ^{235}U Thermal Neutron Fission Products Up To 9.5 MeV. *Phys. Lett. B.* 160 (1985) 325

[35] C.L. Jones, et al. Reactor Simulation for Antineutrino Experiments Using DRAGON and MURE. *arXiv:1109.5379v1* 25 Sep 2011

[36] Z. Djurcic et al.. Uncertainties in the Anti-Neutrino Production at Nuclear Reactors. *arXiv:0808.0747v1*, 6 Aug 2008

[37] G. Feldman and R. Cousins. Unified Approach to the Classical Statistical Analysis of Small Signals. *Phys. Rev. D* 57 (1998) 3873

[38] P. Vogel. Analysis of the Antineutrino Capture on Protons. *Phys. Rev. D*, 29 (1984) 1918

[39] D. Franco, G. Consolati, and D. Trezzi. *arXiv:1011.5736v3*, 24 Feb 2011

[40] L.A. Mikaelyan and V.V. Sinev. Neutrino Oscillations at Reactors: What Next? *arXiv:hep-ex/9908047v1*, 11 Aug 1999

[41] Daya Bay collaboration. A Precision Measurement of the Neutrino Mixing Angle θ_{13} Using Reactor Antineutrinos at Daya Bay. *arXiv:hep-ex/0701029v1*, 15 Jan 2007

[42] J.K. Ahn et, al. [RENO collaboration]. RENO: an Experiment for Neutrino Oscillation Parameter θ_{13} Using Reactor Neutrinos at Yonggwang. *arXiv:1003.1391v1*, 6 Mar 2010

[43] Ed Blucher et al. Outer Veto Electronics and Test. *Double Chooz internal note*, DC-doc-1400-v3

[44] C. Buck. Number of Protons in Target and GC. *Double Chooz internal note*, DC-doc-3250-v1

[45] Th.A. Mueller, J.C. Barriere, and T. Lasserre. Target Protons Measurement Physics. *Double Chooz internal note*, DC-doc-1730-v2

[46] J.B. Birks Scintillation From Organic Crystals: Specific Fluorescence and Relative Response to Different Radiations. *Proc. Phys. Soc A*, 64 (1951) 874

[47] T. Matsubara et al. Development and Evaluation of 10-inch Photo-Multiplier Tubes for the Double Chooz Experiment. *arXiv:1104.0786*, 22 Mar 2011

[48] C. Bauer et al. Qualification Tests of 474 Photomultiplier Tubes for the Inner Detector of the Double Chooz Experiment. *arXiv:1104.0758*, 5 Apr 2011

[49] E. Caden Front End Electronics. *Double Chooz internal note*, DC-doc-2345-v2

[50] F.Ardellier et al. Double Chooz: A Search for the Neutrino Mixing Angle θ_{13}. *arXiv:hep-ex/0606025v4*, 30 Oct 2006

[51] B. Reinhold. *Development of a Level-1 Trigger and Timing System for the Double Chooz Neutrino Experiment*. Ph.D. thesis, RWTH Aachen, 2009

[52] A. Stüken Overview of the NuDAQ Trigger System. *Double Chooz internal note*, DC-doc-2509

[53] Measurements of Neutron Efficiency by Means of Cf-252 Chamber.

[54] J. Goon. Laser System Integration Readiness Review. *Double Chooz internal note*, DC-doc-2414-v6

[55] D.M. Kaplan, J.E. Kaplan, H.A. Rubin, and D. Underwood. Double Chooz LED Flasher Prototype. *Double Chooz internal note*, DC-doc-1721-v1

[56] P. Wahnon. Absolute Light Level Measurements of the Light Injection Calibration System: University of Sussex Undegraduate Project Report. *Double Chooz internal note*, DC-doc-1652-v1

[57] M. D'Agostino et al. Z-axis System Integration Readiness Review. *Double Chooz internal note*, DC-doc-2419-v2

[58] J. Maricic, E.A. Damon. Articulated Arm System Integration Readiness Review. *Double Chooz internal note*, DC-doc-2519-v2

[59] J. Maricic. Design Review for the Articulated Arm Deployment System for the Double Chooz Experiment. *Double Chooz internal note*, DC-doc-1418-v1

[60] J. Busenitz and I. Ostrovskiy. Optimization of Separation Between Guide Tubes and Target Wall. *Double Chooz internal note*, DC-doc-558-v1

[61] I. Ostrovskiy. Guide Tube Integration Readiness Review. *Double Chooz internal note*, DC-doc-887-v1

[62] I. Ostrovskiy and J. Busenitz. Summary of the Guide Tube Position in the Far Detector. *Double Chooz internal note*, DC-doc-1445-v2

[63] P. Novella, C. Palomares, and A. Cabrera. DCRecoPulse. Software and Algorithms for Pulse Reconstruction. *Double Chooz internal note*, DC-doc-649-v1

[64] Cluster United. First Analysis Comparison. *Double Chooz internal note*, DC-doc-2729-v2

[65] DCJapan analysis group. Standard Light-Noise Rejection. *Double Chooz internal note*, DC-doc-2835-v3

[66] Y. Abe, M. Ishitsuka, T. Matsubara, and T. Konno. Results of Timing Calibration and Status of IDLI System. *Double Chooz internal note*, DC-doc-2554-v1

[67] Y. Abe and M. Ishitsuka. Mean Gain and T0 Calibration Constants From IDLI for 3 Months of Data. *Double Chooz internal note*, DC-doc-3017-v1

[68] I. Stancu and Y. Sun. Measuring the Time Offsets in the Empty Detector. *Double Chooz internal note*, DC-doc-2145-v1

[69] Y. Sun. Update on RecoBAMA. *Double Chooz internal note*, DC-doc-2075-v3

[70] Y. Sun. QTLLK Study with New RecoPulse Algorithm. *Double Chooz internal note*, DC-doc-3075-v2

[71] M. Ishitsuke for Y. Abe. Check of Gain and T0 in Reprocessed Data. *Double Chooz internal note*, DC-doc-3205-v1

[72] G. Mention. Private communication

[73] M. Toups. MC Energy Scale Correction Functions Crosscheck. *Double Chooz internal note*, DC-doc-3360-v1

[74] Z. Djurcic et al. Neutron Efficiency Analysis Results. *Double Chooz internal note*, DC-doc-3364-v2

[75] A. Remoto. Energy Containment Studies. *Double Chooz internal note*, DC-doc-3299-v7

[76] C. Langbrandtner. *Background, Sensitivity, and Directionality Studies for the Double Chooz Experiment*. Ph.D. thesis, MPIK, 2011

[77] J. Haser and C. Langbrandtner. Status of Spill-in/out Studies. *Double Chooz internal note*, DC-doc-3246-v4

[78] T.A. Mueller. Spill-in/out Studies and Other Interesting Stuff About Neutron Physics. *Double Chooz internal note*, DC-doc-3031-v1

[79] M. Ishitsuka et al. Trigger Efficiency Task Force Report for the First Double Chooz Analysis. *Double Chooz internal note*, DC-doc-3261-v3

[80] A. Stŭken et al. Trigger Efficiency Task Force Summary. *Double Chooz internal note*, DC-doc-3247-v1

[81] A. Cabrera. Fast Neutron Measurement. *Double Chooz internal note*, DC-doc-3414-v1

[82] A. Franke and M. D'Agostino Fast Neutron Shape Systematics. *Double Chooz internal note*, DC-doc-3302-v2

[83] E. Conover. Cluster United Li-9 Background, *Double Chooz internal note*, DC-doc-3257-v2

[84] D. Greiner. Cosmogenics: 2nd Comparison Stage Results. *Double Chooz internal note*, DC-doc-3256-v1

[85] S. Abe et al. [KamLAND collaboration]. Production of Radioactive Isotopes Through Cosmic Muon Spallation in KamLAND. *Phys. Rev. C*, 81 (2010) 025807

[86] D.R. Tilley et al. Energy Levels of Light Nuclei A = 8, 9, 10. *Nucl. Phys. A*, 745 (2004) 155

[87] L. Winslow Simulation of Reactors for Antineutrino Experiments Using DRAGON. *arXiv:1109.6632v2*, 30 Sep 2011

[88] Y. Nakahara, K. Suyama, and T. Suzaki. *Technical Development on Burn-up Credit for Spent LWR Fuels*. ORNL/TR-2001/01

[89] Th.A. Mueller et al. Improved Predictions of Reactor Antineutrino Spectra. *Phys. Rev. C*, 83 (2011) 054615

[90] P. Huber. *Phys. Rev. C*, 84 (2011) 024617

[91] A.J. Franke, D. Lhuillier, C. Mariani, and M.Shaevitz. Event Generation and Uncertainty Propagation in DCRxtrTools Using the Bugey4 Anchor Point. *Double Chooz internal note*, DC-doc-3221-v3

[92] Y. Declais et al. Study of Reactor Antineutrino Interaction with Proton at Bugey Nuclear Power Plant. Phys.Lett.B338 (1994) 383

[93] D. Lhuillier Error Propagation in the Prediction of Antineutrinos Spectra. *Double Chooz internal note*, DC-doc-2671-v3

[94] A. Franke and A. Collin Propagating Antineutrino Spectrum Uncertainties to Reconstructed Positron Energy. *Double Chooz internal note*, DC-doc-3274-v2

[95] P. Adamson et al. [MINOS Collaboration]. Measurement of Neutrino Mass Splitting and Flavor Mixing by MINOS. *Phys. Rev. Lett.*, 106 (2011) 181801

[96] The Cluster United Final Fits Working Group. List of Systematics Uncertainty Sources. *Internal note*

[97] X. He and S.K. Majee. Implications of Recent Data on Neutrino Mixing and Lepton Flavor Violating Decays for the Zee Model. *arXiv1111.2293v1*, 9 Nov 2011

[98] M. Huang et al. Global Neutrino Data Analysis and the Quest to Pin Down $sin\theta_{13}$ in Different Mixing Matrix Parametrizations. *arXiv:1111.3175v1*, 14 Nov 2011

[99] P.A.N. Machado et al. Combining Accelerator and Reactor Measurements of θ_{13}; the First Result. *arXiv:1111.3330v1*, 14 Nov 2011

[100] K.N. Deepthi et al.. Neutrino Mixing Matrices with Relatively Large θ_{13} and with Texture One-Zero. *arXiv:1111.2781v2*, 15 Nov 2011

[101] B. Bhattacharya et al. Implications of Sterile Neutrios for Medium/Long-Baseline Neutrino Experiments and the Determination of θ_{13}. *arXiv:1111.4225v1*, 17 Nov 2011

[102] C. Giunti and M. Laveder. First Double-Chooz Results and the Reactor Neutrino anomaly. *arXiv:1111.5211v2*, 23 Nov 2011

[103] N.D. Gagunashvili. Comparison of Weighted and Unweighted Histograms. *arXiv:physics/0605123v1*, 15 May 2006

[104] J. Busenitz, Z. Djurcic, and I. Ostrovskiy. First Source Calibration in Double Chooz. *Double Chooz internal note*, DC-doc-2946

[105] F. James. *The Interpretation of Errors*, June 16, 2004

[106] C. Heimbach and M. Scott Dewey. *Calibration of AmBe Sources*. NIST Report of measurement, September 2008

Appendix A

Fabrication of the miniature AmBe sources

We report on the construction and performance of miniature AmBe calibration sources made for the Double Chooz experiment. The sources have an outer capsule of 2 mm in diameter. A typical source contains ∼50 μCi of Am-241 and emits ∼50 neutrons per second.

A.1 Motivation

Understanding the response of the detector to neutrons is a crucial part of the calibration program of any reactor neutrino experiment. AmBe neutron sources have been successfully used in different experiments (CHOOZ, Palo Verde, KamLAND) to study the neutron detection efficiency, and the neutron capture time distribution. Their advantage over Cf-252 sources are listed below:

- Definite neutron multiplicity

  Each alpha-decay of Am-241 can produce only one neutron. In contrast, Cf-252 emits ca. 3-4 neutrons per fission, which complicates the analysis, introduces an additional error due to the imperfect knowledge of average multiplicity (∼0.3%), and puts additional stress on the data acquisition system due to a rapid bursts of events occurring in a short time window.

- Longer half-life

  Am-241 has a half-life of 432 years, while Cf-252 has a half-life of 2.6 years, which may result in a significant decrease of activity during a typical duration of an experiment.

- A mono-energetic 4.43 MeV gamma that accompanies the neutron emission may provide an additional handle on the absolute neutron detection efficiency, and may also to improve understanding of the detector energy response in this energy range

In the Double Chooz experiment, the AmBe sources will be deployed inside sensitive regions, the target volume (TV) and the gamma catcher (GC), to measure the relative neutron detection efficiency, capture time distribution, and to study the spill-in and spill-out events.

During the gamma catcher calibrations, the source will be pushed by a wire through a guide tube that is permanently fixed inside the GC. The size of the tube was made as small as practical to reduce the effects of shadowing of scintillation light and absorption of emitted radiation. That, in turn, posed strict dimensional constraints on the size of the sources. In particular, the outer diameter should not exceed 2 mm. We were unable to locate a vendor for such small AmBe sources. In fact, to the best of our knowledge, a composite neutron source has never been made this small before.

A.2 Encapsulation design

The source design provides two levels of encapsulation and the interface with the deployment system. Below are a description, drawings, and pictures of the elements. The numerical results of the measurements described below correspond to the first of the several fabricated sources. Numbers for the other sources are presented in Table A.1. Pictures of the source's inner and outer capsule are shown in Figure A.1.

1. Inner capsule

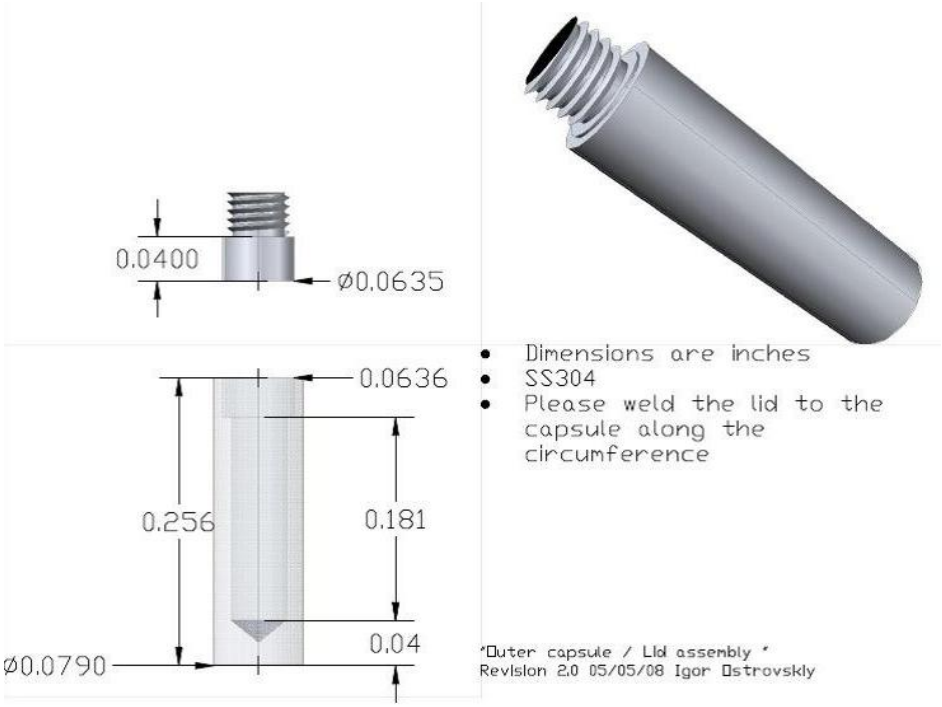

(a) Outer capsule and lid assembly

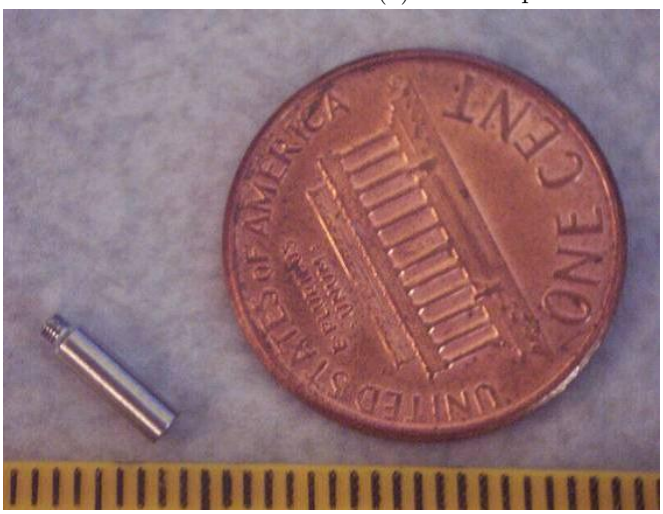

(b) AmBe source next to a penny

(c) AmBe source inner capsule (tungsten)

Figure A.1: Double Chooz AmBe source. Ruler notches are mm.

The inner capsule is made of tungsten to suppress the Am-241 59.5-keV gamma emission. The capsule has an outer diameter of 1.13±0.01 mm (1.12 mm close to the bottom, 1.14 mm closer to the top) and a height of 4.19±0.01 mm. It has a bore made by a drill 0.57±0.01 mm in diameter. The bore is approximately 4 mm deep. The weight of the inner capsule is 58.857 mg, as measured by a microbalance. The microbalance provides ±1 μg reproducibility. The absolute uncertainty was estimated to be around ±5% by comparing the measured weights with expectations based on known geometry and density. In particular, the weight of the inner capsule agrees with the geometrical estimate, based on the above numbers and known tungsten density to better than 5%.

2. Inner capsule lid

   For the first source, a stainless steel M0.5 screw was used as a lid for the inner capsule. It weighed 3.219 mg. After the Am/Be mixture was transferred into the inner capsule, the screw was dipped in an epoxy adhesive and placed to cover the capsule's bore. The following day, an additional drop of the epoxy was added on top of the inner capsule completely covering the screw's head and the top edges. The next day the assembly surface was gently worked with a needle file and wiped with a low lint tissue wiper (kimwipe) wetted with alcohol. The mass of the inner capsule, mixture, lid, and the epoxy was 62.677 mg.

   Note that for the subsequent sources a piece of steel wire was used instead of a screw. The wire bit was such that only a small tip was extending out when placed inside the bore. That allowed us to safely apply pressure on the short exposed piece of the wire and thus compress the mixture. This procedure resulted in a measurable increase of the neutron output per unit of Am-241 activity. The applied pressure was roughly estimated to be 10 atm, based on the cross-section of the wire and the applied force.

3. Outer capsule

The outer capsule was made of SS304 steel and was manufactured at Medical Micromachining Inc.[1] The outer diameter was 2.02±0.01 mm and the height was 6.50 mm.

4. Outer capsule lid

   The lid carries an additional task of interfacing the source with the wire source connector, which is important for providing the ability to inter-calibrate different volumes of different detectors with the same sources. The lid has the form of a cylindrical plug, 1.02 mm long and 1.60 mm in diameter, with a stem that has a milled M1.4x0.2 thread. The plug goes into the countersink on the outer capsule. The diameters are made to 5 microns tolerance to provide a perfectly aligned and concentric sliding fit. The outer capsule and the lid parts are mated.

After the inner capsule is put inside the outer capsule (head down), and the outer capsule lid is fitted in using a bench top lathe, the interface test is performed by gently screwing the assembly into the source connector and then screwing the protective cap on top of the assembly. This verifies the correctness of the assembly procedure and the good quality of the components. While the sliding fit is tuned to be relatively snug, extreme care should be exercised when handling the assembly before the parts are sealed by welding. After the interface test, the source assembly is welded shut at Andrews Hi-Tec electron beam welding facility [2]. The total mass of the source is 189.093 ± 1 μg (reproducibility) ± 5 % (estimate of the absolute uncertainty).

The mass of the outer capsule and the outer capsule lid, derived from the total mass of the source and the mass of the inner capsule assembly, is 126.4 mg. This agrees with the geometrical estimate to 2.5%.

[1] 1115 N Clay Street, Colfax WA 99111. www.medicalmicromachining.net
[2] 2447 Merced Ave, South El Monte, CA 91733. http://andrewshitec.blogpost.com

A.3 Mixture preparation and activity transfer

Am-241 isotope is available commercially in the US in a form of a nitrate or chloride solution. According to an informal communication with an Isotope Products chemist, a typical amount of a carrier (usually europium) is 1000 times the americium amount. The volume available for the mixture inside the inner encapsulation is about 750 nL. Fitting into that volume ∼100 μCi of Am/Eu with enough beryllium powder[3] may be problematic. This calls for either the isotope carrier separation (a known technology based on the ion exchange or extraction chromatography), or the use of a carrier-free Am-241 supply. We were able to obtain 1 mCi of pure Am-241 dioxide (2.96 Ci/g, radiochemical impurities $< 0.1\%$, Am-243 $< 0.02\%$) in the fine powder form at a price lower than 100 μCi of the nitrate solution. Beryllium powder, $> 99\%$, -325 mesh [4], was used.

To create the mixture, a small amount of beryllium powder was put inside the 0.5 mL ampoule containing the americium dioxide, then 0.3 mL of alcohol was added. Shaking did not have any effect due to the small diameter of the ampoule, so a plastic micropipette tip was used to stir the powders and concentrate the mixture on the bottom of the ampoule. After the alcohol evaporated, the stirring procedure was repeated.

Alcohol was then added again, and the mixture was stirred by a micropipette tip to create a short-lived suspension of Am/Be grains in the alcohol. Immediately afterward, 300 nL of Am/Be suspension was extracted with a micropipette and transferred into the inner capsule. After the alcohol was allowed to evaporate from the inner capsule, the mass of the capsule was measured with a microbalance to allow one to ascertain the mass of the AmO_2/Be mixture. The transfer procedure was repeated several times, until the necessary amount of mixture was transferred from the ampoule into the inner capsule.

The mass of the mixture was found to be 127 μg.

[3]The particle density of beryllium powder used to fabricate the sources was estimated to be ∼20 % of the bulk density

[4]This indicates that particles pass through a sieve with an opening size of 44 microns

A.4 Characterization and certification

The americium content was estimated at the University of Alabama using an HPGe detector by measuring 662.4 keV Am-241 line. The Cs-137 point calibration source was used to estimate the absolute efficiency for the used geometry. The estimated americium content, as measured in 2008, was 68 μCi of Am-241 alpha activity. The measurement was repeated in 2010, and the value of 65.7 μCi was found. The systematic uncertainty, mainly due to absolute detection efficiency, dead time, and absorption in the capsule, is believed to be of the order of 10%.

The neutron activity was estimated using BC-501 liquid scintillator counter. Another AmBe source, with practically the same geometry (but 2.5 mm outer diameter) and fabrication method was used as a calibration. The absolute neutron activity of this larger source was determined by NIST with 4% accuracy [106]. The estimated neutron activity of the first 2 mm AmBe source was 40 nps. Estimates for the other sources are shown in the Table A.1.

Based on the measured Am-241 content and the measured mass of the Am/Be mixture, the Am/Be atomic ratio of 1 to 140±10 was observed for the first source, or 99.3 atomic % of beryllium. At some point during fabrication of other sources, more beryllium was added to the ampoule, in an attempt to increase neutron output, so the ratio was not constant for all sources.

For the sources which had the Am/Be mixture compressed during fabrication, as described above, the neutron yield per unit of Am-241 activity reached 50% of the maximum value for commercially available sources.

To ensure the integrity and leak-tightness of the sources, the soak tests were performed as described below: the sources were cleaned and put inside one of two plastic bottles filled with 100 mL of 0.5 M nitric acid. The two bottles (labeled "sample" and "control"), with loose caps, were then put inside a pressure canister and pressurized to 20 psig. After three days, the bottles were removed from the pressure can. The solutions were poured into two

other clean bottles. The sample and control solutions were counted with the HPGe set-up for about a week each. No 59.5 keV signal was observed in the bottles. The sensitivity limit for the activity in the sample soak was estimated to be < 100 mBq of Am-241.

A year later, the AmBe sources were re-certified along with all other DC sources according to the ISO 9978 procedure described elsewhere. Again, no Am-241 signal was observed, and a similar limit was established.

Source ID	L_{inner}, in	D_{inner}, in	m, mg	A_{Am241}, μCi	A_n, nps
1	0.165	0.0445	i58.857 m0.127 s3.219 e126.4 a189.1	67	40
2	0.1655	0.044	i62.803 m0.325 d7.710 e71.006 a191.9	57	95
3	0.164	0.041	i56.353 m0.294 d9.536 e66.681 a197.7	56	86
4	0.1663	0.0435	i64.168 m0.135 s3.209 e68.016 a193.3	35	36
5	0.167	0.0435	i57.433 m0.269 d11.114 e69.276 a195.3	49	78
6	0.1675	0.0435	i57.338 m0.276 e70.417 a197.3	55	82
			i - inner capsl. m - mixture s/d - screw/wire bit e - i+m+s/d+epoxy a - complete source		

Table A.1: Parameters of the miniature AmBe sources.

Appendix B

Certification of the Cf-252 sources

All Double Chooz calibration sources have to be proved not to release radioactive isotopes under normal operation. To that end, soak tests were performed and the HPGe gamma spectrometer was used to establish satisfactory limits on released activity for all isotopes apart from Cf-252. Cf-252 does not have prominent mono-energetic gamma lines;[1] therefore, gamma spectrometers are less suited for certification of Cf-252 sources. At the same time, much smaller amounts of Cf-252 activity released in the sensitive region can be tolerated, compared to other sources, due to the correlated nature of the resulting background. For example, 100 mBq of Cf-252 activity translates into roughly 300 fissions per day, each having a roughly 5% chance of releasing one neutron. The associated correlated background of about 12 per day would dominate all other sources of backgrounds and significantly impair the experiment sensitivity.

In order to improve the certification limit on activity contained in the Cf-252 soak liquid, an alpha spectrometer was assembled. The alpha measurement is expected to improve the limit on contained activity, as compared to gamma spectroscopy:

- by a factor of 10 due to higher detector efficiency

[1] Cf-252 is an alpha emitter, with ca. 3% chance of undergoing fission. Approximately 3.7 neutrons are released with each fission, along with several gamma rays with broad energy spectrum averaging around 1 MeV and extending above 10 MeV

A typical HPGe detector has absolute efficiency of several percent, while typical alpha SSD achieves tens of percent

- by another factor of 30 due to branching ratios of alpha to fission decays

  $\alpha_{BR} = 96.9\%$

In addition, the alpha signal is expected to reside in a narrow energy window, as opposed to the wide gamma spectrum associated with the fission. Finally, the background of an alpha detector is typically very low in the energy range occupied by Cf-252 alpha particles. Therefore, naively, a factor of 100-1000 improvement is expected when in α measurement as compared to γ measurement.

B.1 Hardware

Since alpha particles are severely attenuated by air, the measurement had to be performed in a vacuum. To that end, a vacuum chamber was designed and manufactured at the machine shope of the UA department of physics. A Canberra's Passivated Implanted Planar Silicon detector (PIPS) was purchased[2], along with a matching pre-amplifier. A spectroscopy amplifier was also purchased from Ortec[3]. The PIPS detector had a 300 mm^2 area and a 100 μm entrance window. Pictures of the detector and the vacuum chamber are shown in Figure B.1.

B.2 Source preparation

Again, due to the short range of alpha particles, the 100 mL of the soak solution had to be transformed into a thin alpha source suitable for alpha spectrometry. The liquid solution was deposited onto a Teflon substrate using a commercially available intravenous injection

[2] www.canberra.com
[3] www.ortec-online.com

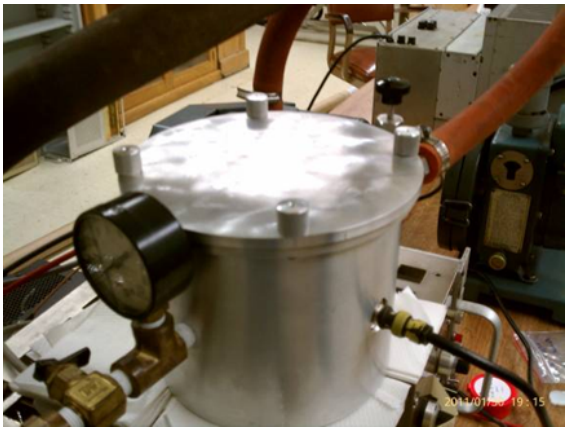

(a) Vacuum chamber

(b) PIPS detector

(c) Detector and source holder inside the chamber

Figure B.1: The alpha detector made for Cf-252 source certification.

line (IV). The IV line allowed for accurate adjustment of the drop rate, hence preventing overflows of the substrate. The substrate was seated on a hot plate, and both temperature and drop rate could be adjusted to provide the necessary transfer speed. This method was preferred over heating the bottle and allowing the solution to evaporate, since there was a fear that the latter would result in loss of activity due to precipitation on the walls of the bottle[4] The procedure was repeated using the control solution, obtained following the same soaking procedure but without sources inside. The substrate so obtained was used for background measurements. A picture of the source preparation set-up is shown in Figure B.2

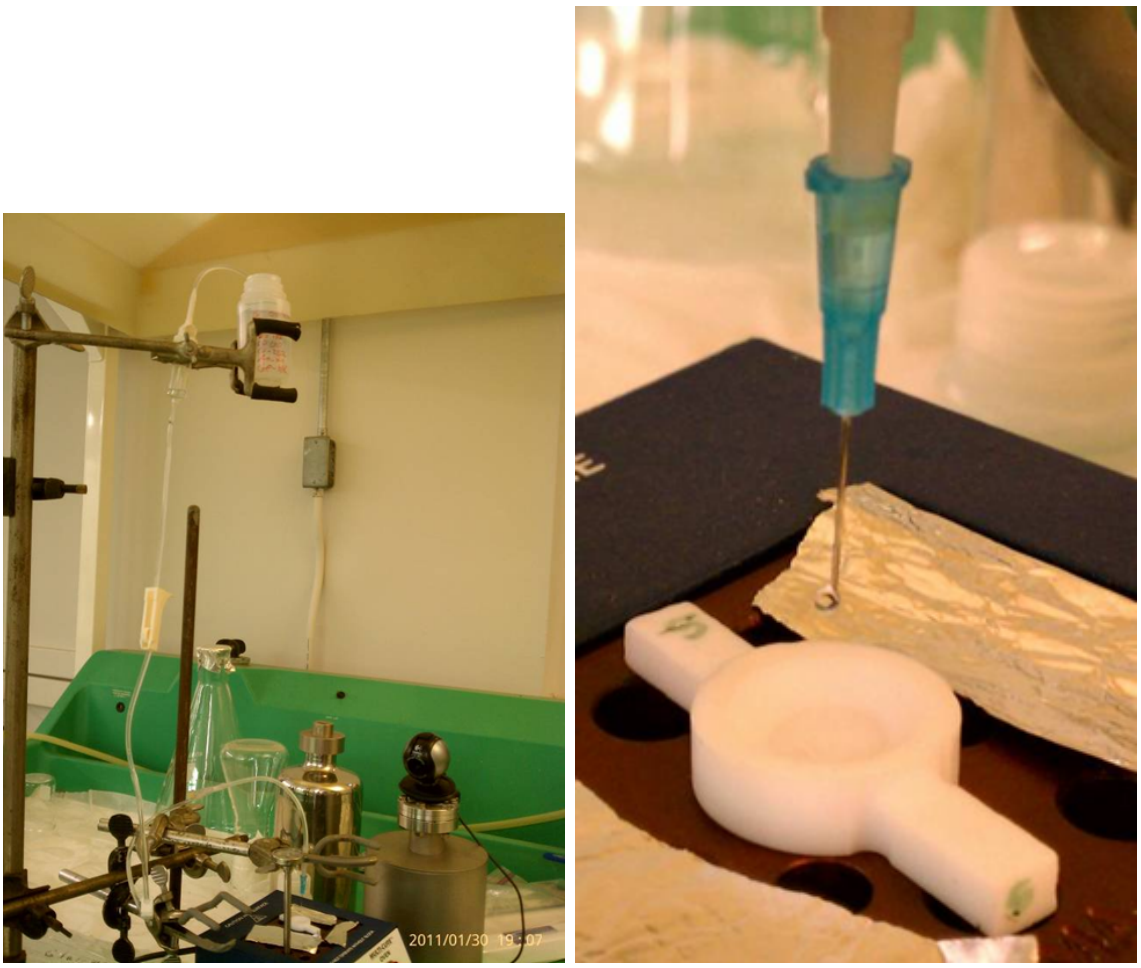

(a) Source preparation set-up

(b) IV line controls drop rate of soak solution on the substrate

Figure B.2: The source preparation set-up.

[4]Which is different from unavoidable microscopic sorption of isotopes on the walls, believed to be a small effect

It was still necessary to validate the ability of the procedure to transfer the Cf-252 activity, potentially present in the soak liquid, from the bottle to the substrate. It was also necessary to measure the efficiency of the transfer and the efficiency of the detector set-up. The above was achieved by injecting 10 μL of Cf-252 solution with known specific activity into a bottle of the same type, filled with 100 mL of weak acid solution, representative of the soak solution. The solution was transferred on the substrate to produce a reference source for the alpha detector set-up.

B.3 Measurement

Figure B.3a shows a spectrum obtained with the reference Cf-252 alpha source, prepared as described above. A clear signal of Cf-252 alphas is present proving the transfer procedure is effective. In other words, if there was any Cf-252 activity present in the soak bottle, we should see it in the prepared substrate.

The amount of Cf-252 deposited on the reference substrate is estimated to be about 1.4 Bq. The estimate is based on

1. The reported specific activity of the commercial Cf-252 solution, corrected for Cf-252 decay

2. The amount of Cf-252 solution injected into the bottle before transfer using a micro-syringe

3. The fraction of the soak-like solution deposited on the substrate

Comparing this estimate with observed event rate in the Cf-252 region of the alpha spectrum, defined here between 1930 and 2030 ADC channels, gives an estimate of the absolute efficiency of $\approx$11.4%

Zooming in on the Cf-252 alpha spectrum, we can fit the observed peaks to the known Cf-252 alpha lines to establish a rough energy scale (Figure B.3b) It is known from the vendor,

that Cf-252 solution contains other isotopes as contamination. This fact was ignored.

It is obvious that more careful analysis, higher statistics and improved source preparation would result in more accurate estimates of absolute efficiency and energy scale. However, due to the drastic increase in sensitivity, compared to gamma measurements, we can tolerate very large safety factors and still achieve our goal on the limit of Cf-252 activity in the soak sample. Therefore, spending more time on further improvements was considered unnecessary.

B.4 Results

To establish the limit on Cf-252 presence in the soak sample, both the control and the soak substrate were counted for about three days each. The data from the first day were discounted in both cases to allow radon-related activity to subside. The total collected livetime, as reported by the Maestro DAQ program, was $2.5 \cdot 10^5$ s for the control sample, and $2.1 \cdot 10^5$ s for the soak sample.

Figure B.4 shows the raw spectra for the control and soak samples. Zero counts were observed for both samples in the Cf-252 window, defined between ADC channels 1930 and 2030, based on the reference Cf-252 source data. This immediately translates into a Feldman-Cousins [37] upper limit of less than 2.44 Cf-252 alpha events in $2.1 \cdot 10^5$ s at 90% C.L. Plugging in numbers for branching ratio and efficiency estimates, together with the fraction of the soak liquid transferred onto the substrate, the measured limit on the Cf-252 activity in the source soak sample is

$$A_{Cf-252} < 6.5 \ \mu\text{Bq s.f, at 90\% C.L.}$$

Instead of carefully estimating the uncertainties due to absolute efficiency measurements and energy scale, which are believed to be of the order of 10 percent, we can assume a conservative safety factor of 10 or 100 and still have a stringent limit on the released activity.

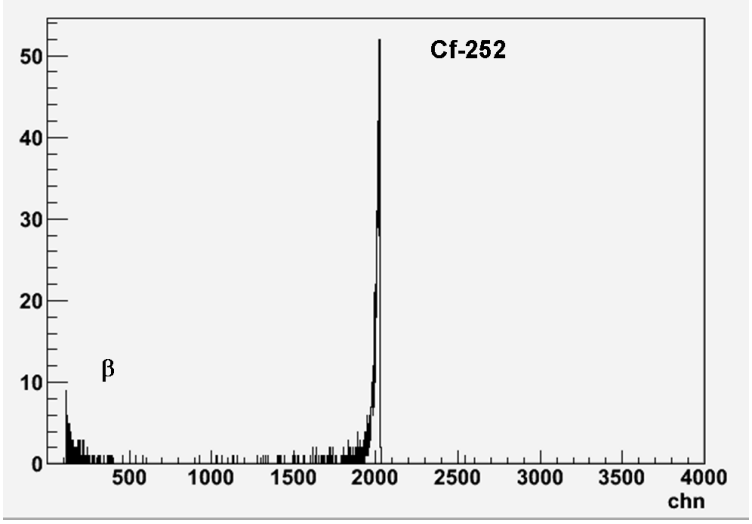

(a) Spectrum of the reference Cf-252 source. Decreasing DAQ threshold also allows one to see natural beta activity

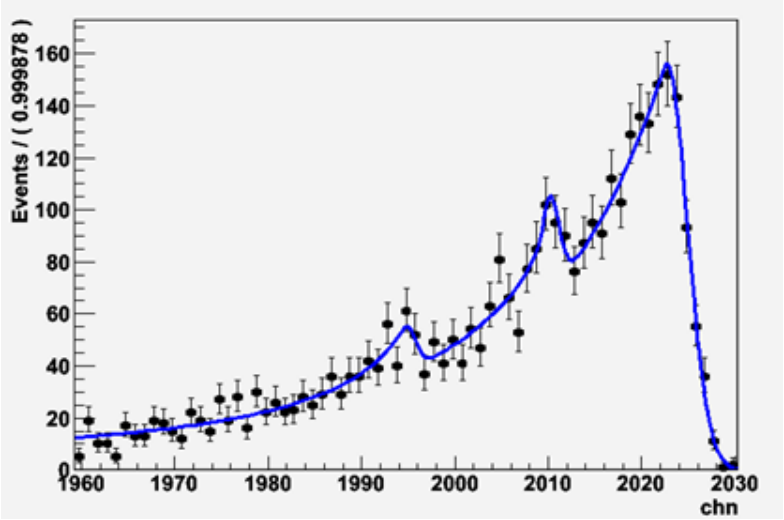

(b) Fit to the three main Cf-252 alpha particles. Contribution of contaminating isotopes is ignored.

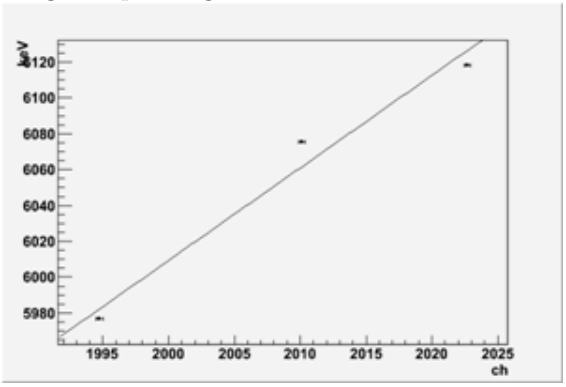

(c) Rough estimate of the energy scale

Figure B.3: Reference source spectra.

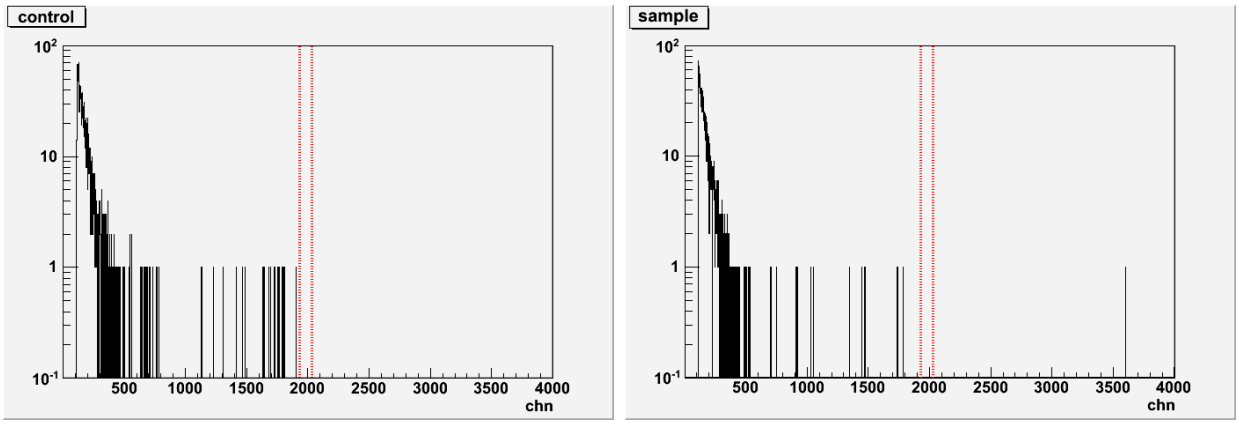

(a) Measured control sample spectrum

(b) Measured soak sample spectrum

Figure B.4: Spectra histograms for control and soak samples. The region of Cf-252 alphas is highlighted by red lines.

Appendix C

The guide tube

The list of the GT system components is presented in Table C.1

a) The steel part of the guide tube provides a rigid impenetrable source guide while occupying the minimum amount of space in a sensitive region of the detector. The GT path has a loop design to allow for recovery of a source in the case of the wire/source interface failure. Recovery is effected by pushing the loose source all the way through to the other end. The path allows one to effectively probe the detector response along the target volume boundary and along the equator. Details of the path optimization are described in [60] The steel part consists of three tubes with two bends each. Bending the whole steel part from one piece is not advisable because:

   - it requires the purchase and handling of 20-foot long steel tubes, which are more expensive and require a special oversize delivery truck
   - it is easier to make two accurate and coplanar bends on each of the three pieces, than six bends on one piece
   - a mistake in one bend requires the while tube to be re-made
   - it is easier and safer to insert a Teflon sleeve in three steps than all at once

   A dedicated bending table (Figure C.1) was made for forming the steel part of the GT.

Where	What	Material	Length and/or number	Comment
GC	“guide tube”	SS304 full hard	6 gauge (4.4/5.16 mm ID/OD) ≈6.2 m total	In 3 pieces connected by two Swagelok unions
GC, chimney, clean tent	“Teflon sleeve”	PTFE	9 gauge (3.0/4.0 mm ID/OD) ≈50 ft total	Only ≈6.2 m inside GC
GC	“sensor box”	SS304	≈14x8x5 cm	Has proximity sensor inside
GC	“Swageloks”	SS316	2 pcs ss-400-6, 5 pcs ss-400-1-2w	2 pcs to connect steel tubes, 5 pcs welded to the sensor box
GC	“fixtures”	GS0Z18	16 pcs	8 pcs glued to the acrylic vessels, 8 pcs attached to the GT
chimney, clean tent	“flexible tubing”	PTFE	6.35/4.76 mm (OD/ID). 3 tubes, ≈4 m each	2 tubes house Teflon sleeve, 3rd - sensor cables
chimney, clean tent	light tight tubes	Vinyl	13.5/9.5 mm (OD/ID). 3 tubes, Black	Protect from light leaks
bridge, clean tent	wire storage tube	PTFE	6.35/4.76 mm (OD/ID). 15 m	Store excess of the wire
clean tent	“wire driver”	various		

Table C.1: Guide tube components.

Calibration of the bending distances and spring-back angles was found to vary for different batches of the same size tubes, which may have been due to small differences in temper. The last calibration was performed on the same batch of the steel tubes that was used

in the far detector GT fabrication. An RMS deviation in lengths of the bended segments was found to be ca. 1mm in each direction.

Figure C.1: Picture of the guide tube installation jig on the bending table.

b) A Teflon sleeve guarantees guarantees smooth transition of a source capsule through the sensor box, Swageloks etc., and provides an additional disaster recovery option, as described in [61].

c) The sensor box (Figure C.3) achieves a substantial reduction of uncertainty in source position. In the original design, it housed two ring type inductive proximity sensors, which generated a signal when sources entered the sensitive detector. That provided absolute zero and scale calibration for wire driver encoders referenced directly to the part of the GT system being metrologically surveyed. However, the sensor box position close to the gamma catcher lid posed a risk of interference with the lid during installation, and given absence of accurate information about the lid dimensions, it was decided to mitigate the risk by reducing the size of the sensor box. As a consequence, the final sensor box contains only one position sensor, hence only zero calibration of the encoders is possible in the area of interest. In the future, it is envisaged that the second sensor will be installed outside of the sensitive area, a few meters away from the surveyed part of the tube, to recover the ability to control the encoder scale calibration, albeit with decreased

accuracy.

The sensor box is made of SS304, like the rest of the tubing embedded in the GC, and utilizes Swagelok connectors to attach to the steel parts of the guide tube below and flexible tubes above. Using steel allows mechanical robustness to be achieved while being as small as possible and hence decreasing shadowing and reducing the risk of interference with the lid (the box is positioned as close to the boundary of the sensitive detector as possible to minimize its impact on physics). Using acrylic would require much thicker walls (and hence the box would have to be positioned further away from the GC lid) to provide the same level of mechanical stability, which would undermine possible gains in terms of the reduced amount of absorption (there is not much gain in terms of shadowing either, as the sensor itself is not transparent). It is also reliable in terms of leak-tightness, which is necessary to isolate incompatible materials of the sensor from the scintillator liquid.

After the radio-assay revealed that the sensor box produced much thorium-related radiation, the emissions were traced down to the welding electrodes, which usually deliberately contain thorium, so the final sensor box was welded using special non-thoriated electrodes. The MC simulation incorporating the results of the radio-assay was used to estimate the possible contribution of the sensor box to the background and it was found to have a negligible impact on the single rate.

The effect of the sensor box on the position and shape of the charge distribution for the calibration source was estimated using MC simulation and found tolerable, though for the most demanding calibrations it is better to position the source at least few cm away from the box. In particular, a difference in the number of events in the full absorption peak of a low energy gamma source (Cs-137) observed with and without sensor box included in the simulation (Figure C.2) decreases from 15% 1 cm below the box to just 1% at 5 cm. The position of the full absorption peak was found to be 4% different from the no-box case 10 cm below the box, which was considered small enough to be

safely accounted for by the existing MC. Note that the study was conducted using the original sensor box design, which was almost twice as large as the final one, so the results are conservative. In conclusion, given its position at the very exit of the sensitive area, the advantage of improving the positional accuracy by providing zero calibration clearly outweighs everything else.

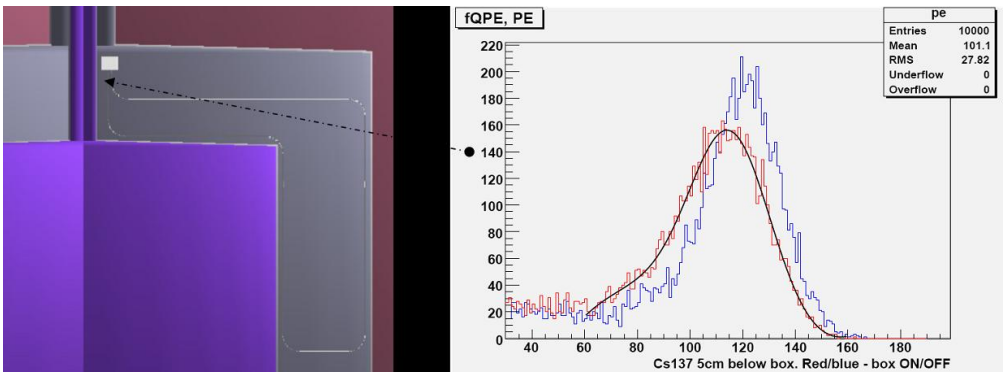

(a) Charge distribution from a low energy gamma source positioned below the sensor box with and without the box included in the simulation

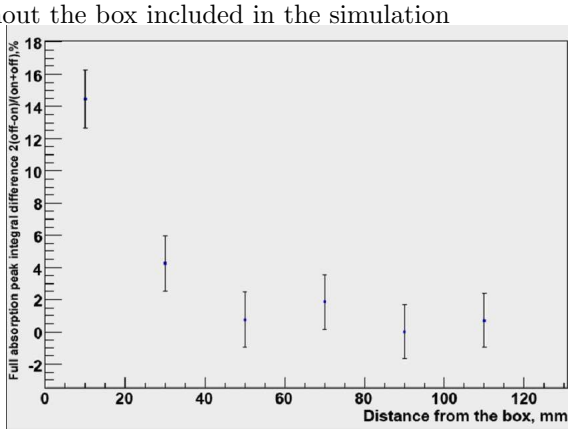

(b) Difference in number of events in full absorption peak as a function of distance from the sensor box

Figure C.2: Effects of the sensor box in the MC simulation.

When the capsule passes through the sensor, the latter issues a signal that causes the wire driver controller to stop the motor. The actual position of the capsule with respect to the bottom plate of the sensor box was calibrated to some 1-2 mm accuracy before welding the upper lid of the box shut, using the actual capsule and the wire driver. The stopping distance depends on the direction and the speed of the capsule. Only one configuration should be used for zero calibration during real deployments (the capsule

should be pulled down at a slow speed setting) but information for other regimes is available. The measurement was conducted using a digital caliper. Due to difficult access, the distance from the top edge of the capsule was measured, so a shift should be applied to convert the distance from the capsule edge to the center of activity.

During welding, nitrogen flow was used in between short welding steps to keep the box cool and ensure the safety of the sensor and the wires. Special non-thoriated electrodes were used to prevent an increased natural radioactivity rate from the box. After the sensor box was welded, it was successfully leak-tested using a helium mass spectrometer.

d) It was necessary to ensure a leak-tight connection for the guide tubes. We used Swagelok connectors since these offer a trusted way to provide a leak-tight connection between steel and plastic tubes. The connectors were custom ordered to avoid threads with standard silver plating and lubricants, which are not chemically compatible with the scintillator. Teflon ferrules were used to prevent damage to the tubing that could result in the obstruction of the path for the radioactive source, which could lead to dire consequences. Teflon ferrules are standard and were recommended for the application by Swagelok personnel (both in the USA and in Belgium offices).

   Two tests were performed on the full scale prototype of the guide tube to ensure leak tightness:

   - one end of the tube was shut and the other one was connected to a tap water supply (typically 4-5 bar) to ensure the absence of a gross leak
   - the tube was connected to the helium leak meter and evacuated, then helium gas was released near the the guide tube connections. No leaks were detected

e) The steel part of the GT system is fixed to the acrylic vessels using several acrylic fixations. The location of the fixations, along with required installation tolerances, are illustrated in Figure C.4.

Fixtures that are glued to the TV stiffener are called "clamps" (Figure C.6d). The radial positions of the two clamps supporting the sensor box, and vertical position of the clamp closest to the TV lid, are of particular importance and therefore require tighter tolerances. Fixtures that are glued on the target and gamma catcher walls are called "holes" and "slots" respectively (Figure C.6c and C.6b). These fixtures have an offset from the rib in the +X direction, as indicated in Figure C.4c. The fixtures matching the ones on the walls were installed on the steel part of the GT (Figure C.6a).

Notes:

- After discussions with the company manufacturing the acrylic vessels, Neotec, it was decided that only one fixture would be glued on the gamma catcher vessel and this would be done after the guide tube was installed. This was done because of the difficulties ensuring correct relative positions of the fixtures on the target and GC vessels
- An unexpected feature of the target vessel lid, a "lip", was discovered on the actual target It required a last minute modification of the guide tube path to avoid interference (Figure C.5), so the positions of the two clamping fixations were moved up
- A survey of the separation between the target and the GC vessels as installed showed a smaller distance between the two than originally expected, which was probably caused not by the smaller diameter of the gamma catcher as a whole, but rather by the shape irregularity of and immediately below the upper rim on top of the GC. To compensate for the observed smaller distance between the target and GC vessels, the path of the guide tube was decreased in this region, and to avoid any possible interference and stresses on the vessels, the slot type fixation (Figure C.6b) was enlarged to provide more slack

The fixtures provide an interface between the guide tube and the acrylic vessels. They

need to reliably attach the guide tube and mitigate possible stresses on the vessels. Stresses of the level of several Newtons are anticipated due to the tube's spring-back and wire transmittance. To test the reliability of the fixations, the following test was performed: a post was glued to an 8 mm acrylic plate (thickness of the target vessel) and annealed at 80 degrees Celsius for eight hours. The system was then submerged into DC-like scintillator and subjected to periodical stresses as shown in Figure C.7 More than 300000 cycles were completed with stress levels several times larger than anticipated in the actual system. No damage to the acrylic plate was observed.

The fixtures were glued to the target vessel of the far Double Chooz detector at the manufacturing facility in Bussang, France before installation of the guide tube (Figure C.11).

f) Flexible tubing serves three main goals:

- it protects the Teflon sleeve from kinking and denting
- it isolates sensor wires
- it allows normal operation of bellows.

PTFE 1/4" industrial wall tubing is used for the flexible tubes. It is important not to increase the length of the flexible tubes more than necessary, as increasing the total path of the wire decreases the reliability of the guide tube operation due to accumulation of resistance.

The flexible tubes are routed from the gamma-catcher, through the gamma-catcher flange, all the way into the calibration clean tent above the detector. Closing the gamma catcher flange was an important step (Figure C.13), and was completed without any damage to the tubes, as was confirmed by a dedicated test immediately after the IV lid was closed (Figure C.14).

g) Wire driver and dedicated software control program, motor, two encoders, and two sensors provide accurate positioning of the source capsule and safe operation of the GT system.

The driver has following connections:

- Right side. Special fitting for easy and secure connection of the Teflon sleeve (Figure C.8)
- Left side. Two fittings (different sizes) for connection of the wire housing tube. The spare fitting may be used to connect a nitrogen supply tube for anti-radon purging (alternately, nitrogen may be coupled to the second end of the Teflon sleeve)
- Back panel. USB interface for laptop connection and several electrical terminals for powering the motor (0-15V variable), the sensors (+15V), and various electronics (+5V). The driver comes with a dedicated power supply. The power supply requires a 1kW adapter for American voltage standard, 110V. The layout of the wire driver inside the clean tent is presented in Figure C.9

The tube exiting the wire driver on the left of Figure C.9 houses the guide wire. While it is possible to feed the wire exiting the driver back into the other end of the guide tube, the safest option is to house the excess in a separate tube (the storage tube) that is laid out as straight as possible. While only Teflon can be used for housing the wire itself (due to friction reasons), any other material may be employed as a protective cord cover to prevent people from tripping over. The only considerations to bear in mind while setting up the GT deployment post and the storage tube are:

- The total guide path should not be increased ($\approx$6 m of steel tubes and $\approx$ 4 m of flexible tubing from each end

  Note that during assembly, roughly five meters of flexible tubing were attached, just so the ends of the tubes could be safely handled as roughly as necessary, but the excess length should be cut out
- The number of bends along the path is minimized (no more than two after exiting the main chimney flange)

- The bending radius should be maximized (more than 30 cm preferably)

The "guide wire" itself consists of a 24-gauge (0.3/0.56 mm ID/OD) SS304 tube with a 0.009" spring wire inside. The tube provides necessary elasticity, while the wire inside prevents driver rollers from smashing the tube, significantly increasing its lifetime.

A dedicated wire fatigue test, pushing and pulling the wire through a series of bends for several kilometers, as well as routine operation of the full scale prototype, showed that under normal conditions (total length, number and radius of bends, undamaged Teflon sleeve, properly operated wire driver) the wire should be safe for a few years of deployments.

To attach the source connector (Figure 2.15), which provides the interface with calibration sources, the end of the wire is bent into a 2mm hook using miniature round-nose pliers. After the connector is threaded onto the wire, the hook is soldered shut using a solder appropriate for stainless steel. Apart from routine operation of the full scale prototype, a dedicated reliability test was performed by attaching a 2 kg weight to the hook. The hook was kept under this static load for about two years without showing any signs of failure (Figure C.10)

Before and after installation, a theodolite with an integrated laser distance meter was used to collect information about the dimensions and location of the guide tube with respect to the target vessel (Figure C.12). The result of this effort is described in detail in the note [62].

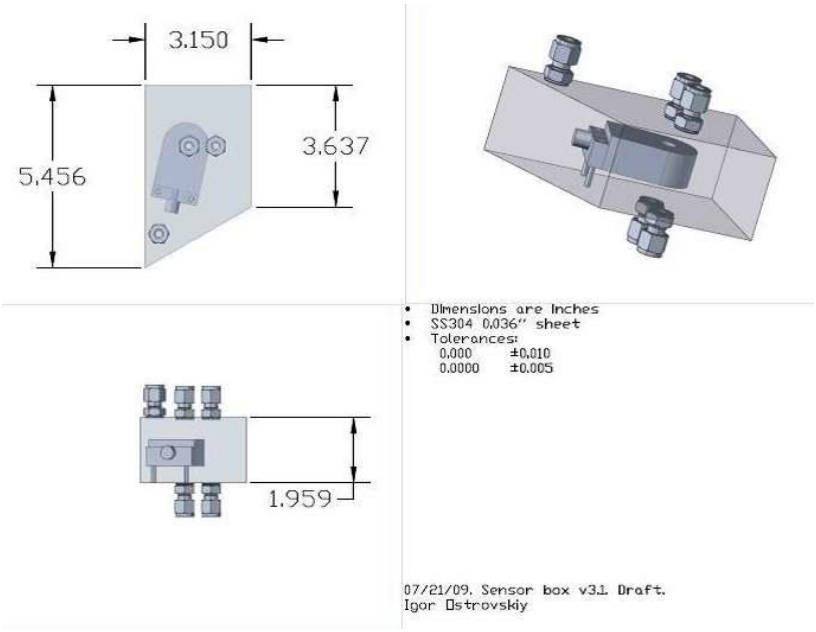

(a) Sensor box drawing

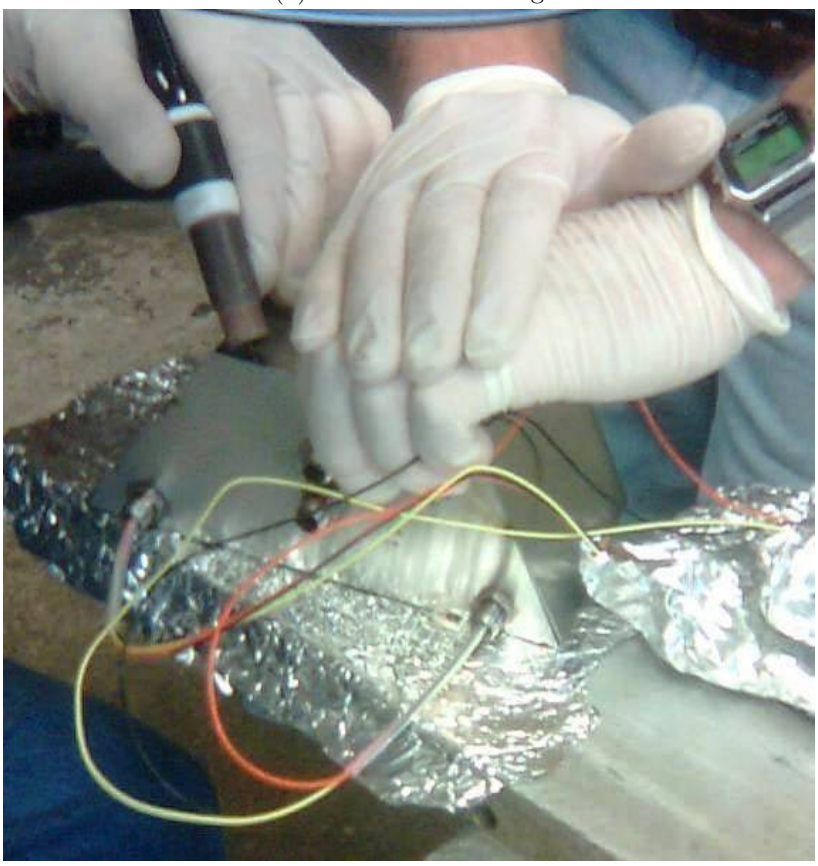

(b) Welding of the (original) sensor box. Gloves were used to ensure cleanliness

Figure C.3: The sensor box.

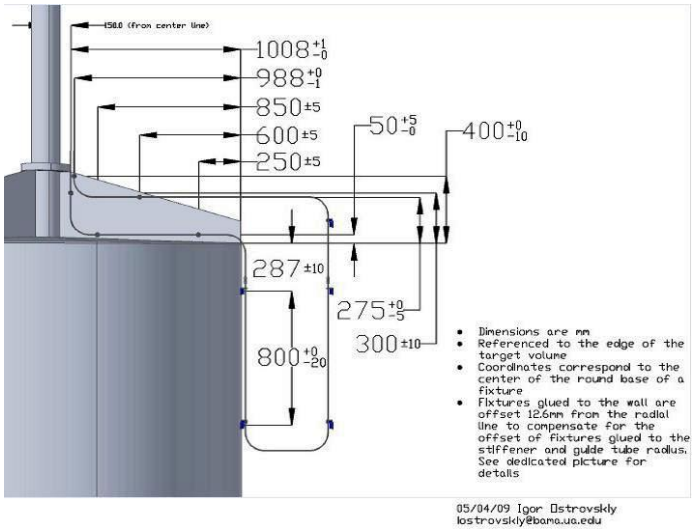

(a) Original fixation positions on the target

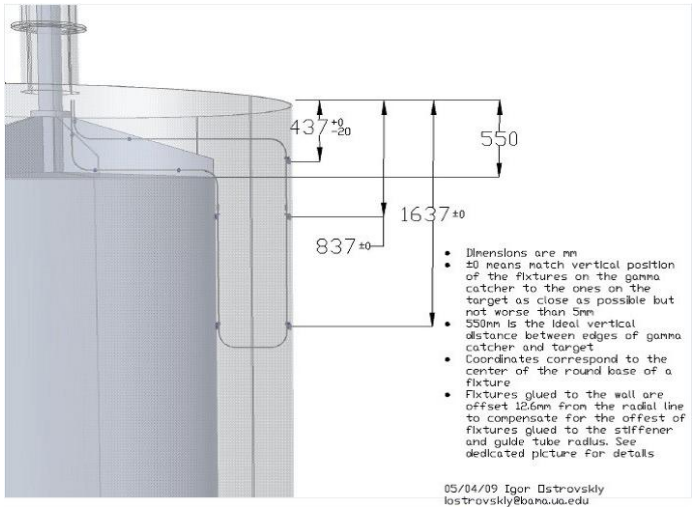

(b) Original fixation positions on the GC

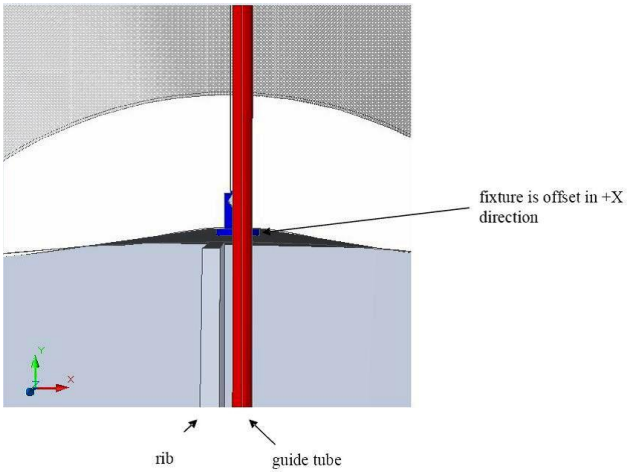

(c) Top view of the space between TV and GC, demonstrating the fixture offset with respect to the Y axis

Figure C.4: Original positions of the guide tube fixations.

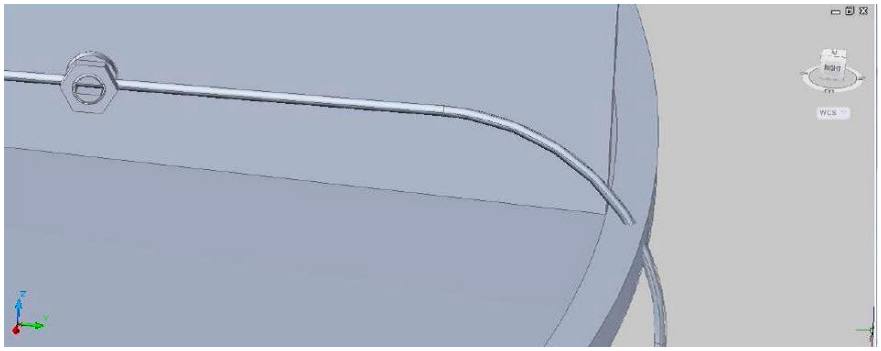

Figure C.5: The effect of the target lip on the original guide tube path.

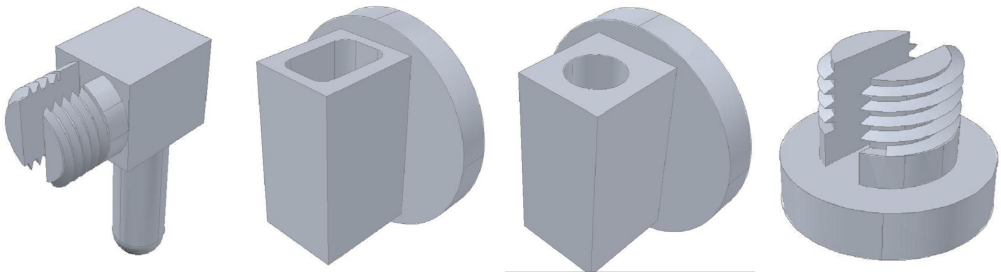

(a) pin (b) slot (c) hole (d) clamp

Figure C.6: Acrylic fixations.

(a) Spring test

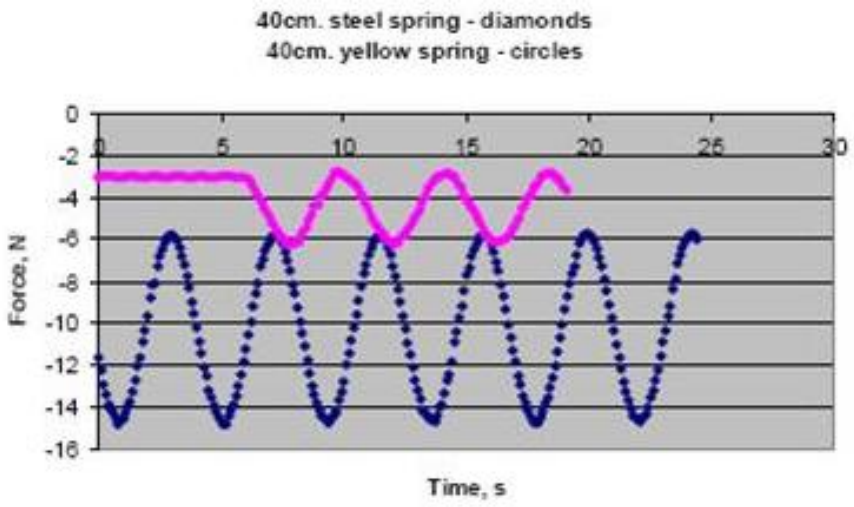

(b) Force level

Figure C.7: Stress testing an acrylic fixation.

Figure C.8: The push-to-connect fitting that connects the wire driver to the GT.

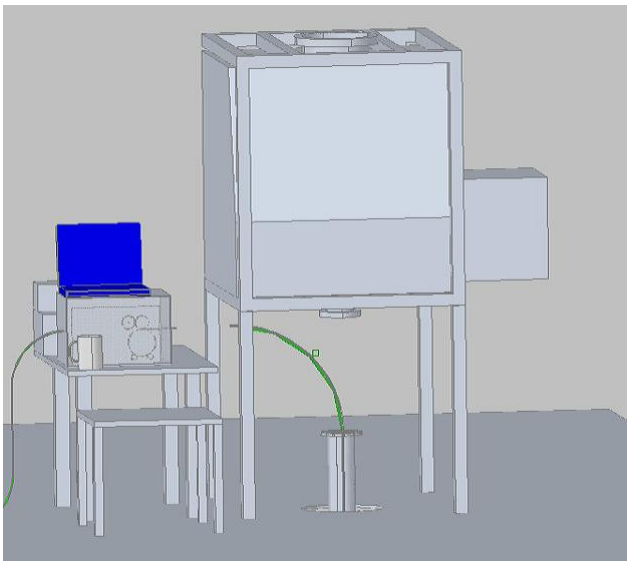

Figure C.9: Layout of the wire driver in the calibration clean tent. As conceived by the author in 2009. Compare with Figure 2.25. The glove box CAD model courtesy of Tim Classen.

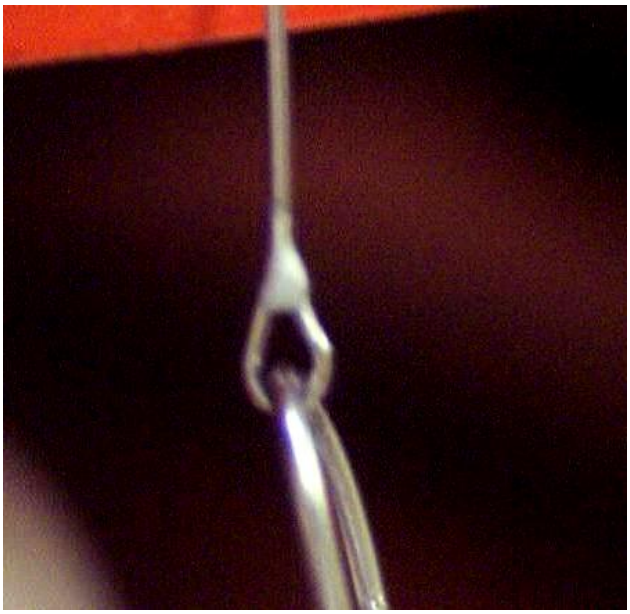

Figure C.10: The wire hook under a 2 kg load.

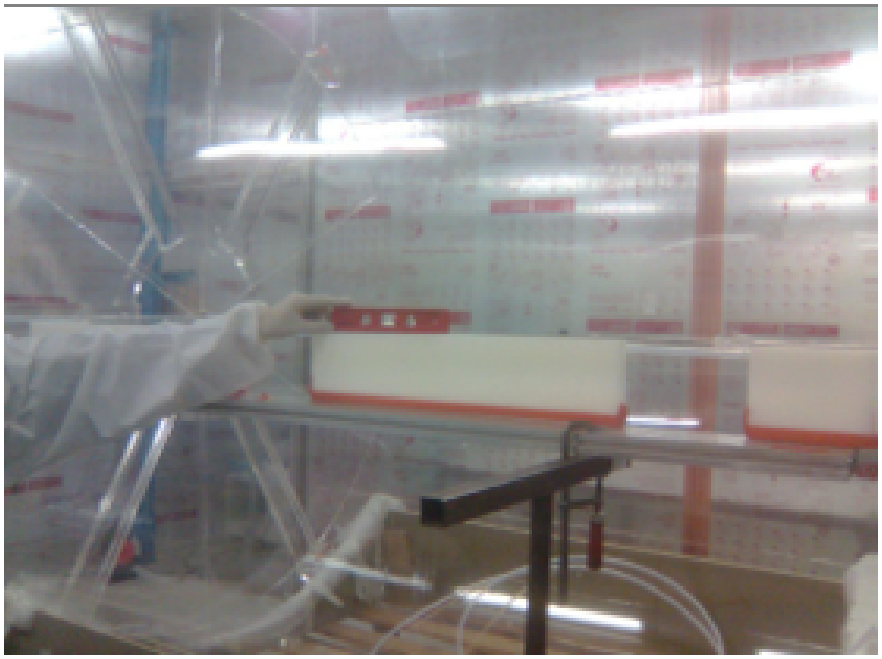

Figure C.11: Before gluing the guide tube fixations to the DC target vessel.

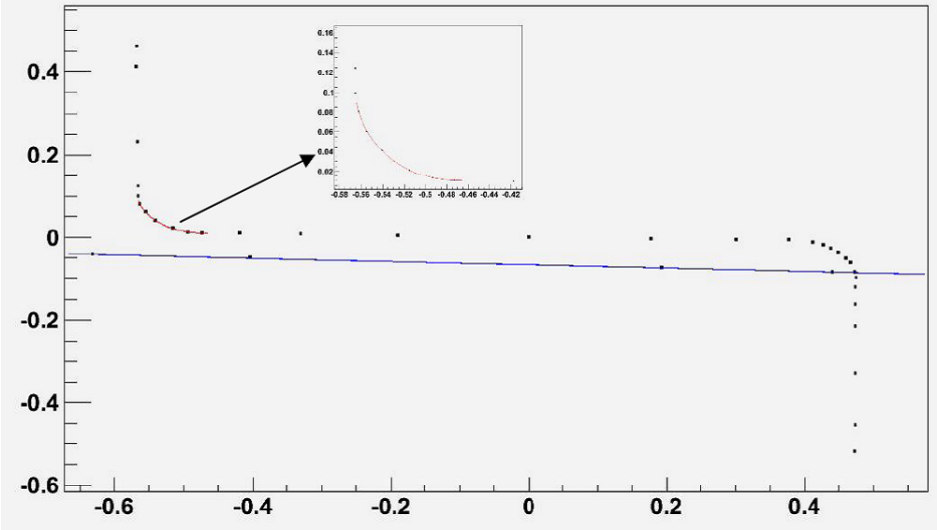

(a) Points surveyed on the part of the tube attached to the target stiffener. The blue line is a linear fit to the points surveyed on the target lid immediately under the stiffener. The red line is fitted to the points in the tube bend

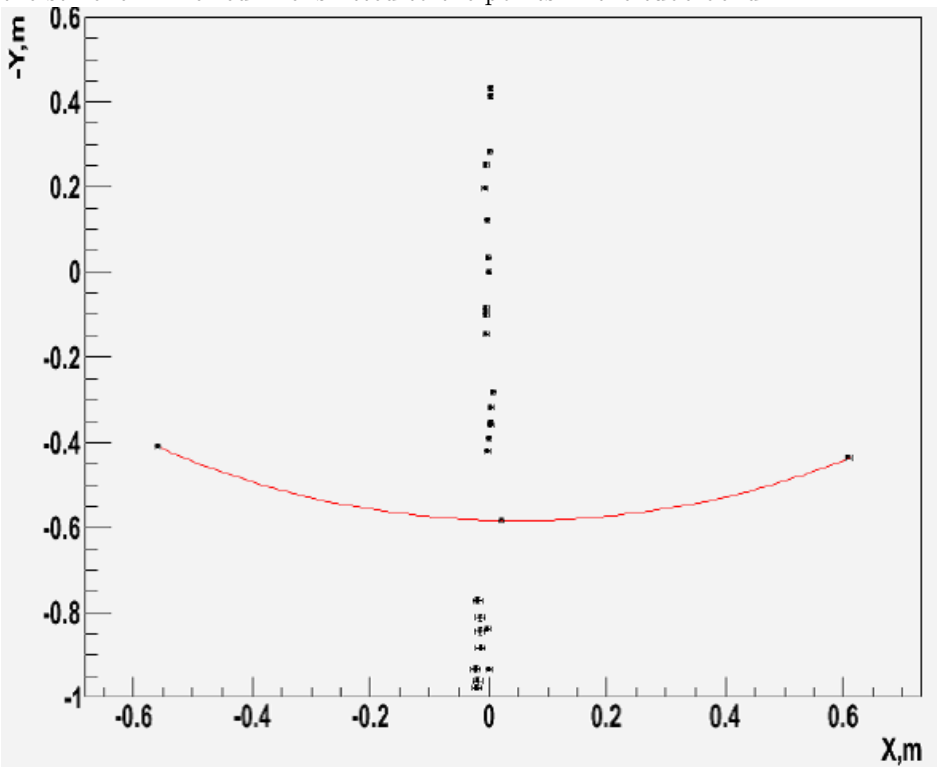

(b) Top view. The red line fits the points surveyed on the rim of the target vessel

Figure C.12: Survey data [62].

Figure C.13: Closing of the gamma-catcher flange. Herve de Kerret (left), Igor Ostrovskiy (middle), Patrik Perrin (right).

Figure C.14: Testing the GT on top of the inner veto lid. Frederic Dorigo (left), Igor Ostrovskiy (middle), Guillaume Mention (right).